UNIVERSITA' DEGLI STUDI DI VERONA

DIPARTIMENTO DI

NEUROSCIENZE, BIOMEDICINA E DEL MOVIMENTO

SCUOLA DI DOTTORATO IN SCIENZE DELLA VITA E DELLA SALUTE

DOTTORATO DI RICERCA IN

BIOMEDICINA MOLECOLARE, *curriculum* BIOCHIMICA

29° ciclo

Calcium sensor proteins in health and disease and their potential use in nanomedicine

S.S.D. BIO/10

Coordinatore: Prof.ssa Lucia De Franceschi

Tutor: Dott. Daniele Dell'Orco

Dottorando: Dott. Valerio Marino

Calcium sensor proteins in health and disease and their potential use in nanomedicine
Valerio Marino
Tesi di Dottorato
Verona, 8 febbraio 2017

University Of Verona

Abstract

University of Verona
Ph.D. Course in Biomolecular Medicine, 29th cycle

Doctor of Philosophy

Calcium sensor proteins in health and disease and their potential use in nanomedicine

by Valerio MARINO

Proteins are biomolecules involved in virtually every process occurring in cells, characterized by a sequence of amino acids, which confer them peculiar structural features implying specific functions. Ca^{2+}-sensor proteins are a family of proteins whose function is determined by structural changes occurring upon Ca^{2+}-binding, taking part in a wide range of physiological and pathological processes, among which muscle contraction and phototransduction. Unraveling the complex machinery behind these physiological processes is fundamental not only for the sake of expanding our knowledge, but also to understand which mechanisms are altered in inherited pathological conditions, in order to develop potential therapeutic approaches that may help relieving or treating these disorders. Protein therapy is one of the most promising potential treatments, allowing for the substitution of dysfunctional protein pool with physiological variants. Here, a collection of biochemical and biophysical studies focused on the physiological and pathological aspects of some Ca^{2+}-sensor proteins is presented, together with possible therapeutic implications in nanomedicine using CaF_2 nanoparticles (NP) as protein carriers. The combination of experimental and computational techniques revealed itself a complementary and exhaustive approach, allowing for a multiscale investigation of protein structural and functional properties. Indeed, the high-resolution structural information provided by Molecular Dynamics (MD) simulations and Protein Structure Network (PSN) analysis can be proficiently integrated into the biophysical and

biochemical experimental framework constituted by Circular Dichroism (CD) and fluorescence spectroscopy, Dynamic Light Scattering (DLS), Ca^{2+}-binding assays and enzymatic assays. Such integrated approaches allowed us to discover that mutations of the Neuronal Calcium Sensor (NCS) protein Guanylate Cyclase Activating Protein 1 (GCAP1) associated to retinal dystrophies did not necessarily altered protein Ca^{2+}-affinity, but rather that the pathological dysregulation of the target enzyme Guanylate Cyclase (GC) depended on more complex mechanisms, probably involving modified intramolecular communication. Moreover, PSN analysis of MD trajectories of GCAP1 highlighted that small conformational variations may strongly impact protein functionality, as the switch between activator and inhibiting states occurs through minor structural rearrangements subsequent to the Ca^{2+}/Mg^{2+} exchange in specific binding sites. This suggested again that the investigation of intramolecular communication may be the key to clarify unknown complex mechanisms of not only of Ca^{2+}-sensor proteins, but also of proteins belonging to different superfamilies.

Acknowledgements

Vorrei ringraziare:

il Dr. Daniele Dell'Orco per avermi fatto crescere sia scientificamente che umanamente negli ultimi 5 anni

i membri del gruppo DDO Giuditta, Alberto e Silvia per il loro aiuto e per aver reso le giornate in lab più divertenti

il Prof. Karl-Wilhelm Koch e tutti i membri del suo gruppo per avermi ospitato per 4 mesi nel loro laboratorio facendomi sentire parte di una grande famiglia internazionale

i miei amici che mi hanno supportato e sopportato, in particolare Gio, Mario, Taky, Luigi, Valy e Ciccio

Mamma, **Papà** e **Ilaria**, la nonna e gli zii per l'affetto dimostratomi

e infine **Alda** e **Daniele**

List of Figures

Contents

Dedicato alla mia fantastica moglie Alda e al nostro piccolo tesoro Daniele

Chapter 1

Introduction

1.1 Ca^{2+}-sensor proteins

Calcium (Ca^{2+}) is one of the most important and versatile metals in biological systems, as it is involved in several complex and diverse processes, spanning from bone mineralization, to muscle contraction, to signal transduction [1], to vision [2]. The importance of the Ca^{2+} ion calls for a class of proteins called the Ca^{2+}-binding protein family [3] which bind and release Ca^{2+} ions in response to variations in Ca^{2+} concentration. Although several Ca^{2+} binding motifs have been identified in Ca^{2+}-binding proteins, such as C2 [4], PERCAL, EGF-like [6], Dockerin [7], Cadherin [8] and S100 domains [9], most of the proteins belonging to this family share a structural motif which allows them to bind Ca^{2+} and other divalent cations, the EF-hand motif [10, 11]. This helix-loop-helix is composed by a stretch of 10 residues folded as an α-helix followed by a 12 residues loop with a consensus sequence of D-W-[DNS]-ILVFYW-[DENSTG]-[DNQGHRK]-GP-[LIVMC]-[DENQSTAGC]-x-x-[ED] [12] and another 10-residue α-helix where x stands for any residue, square brackets indicate one of the enclosed residues, curly brackets indicate all but enclosed residues. The coordination of Ca^{2+} ions occurs through a pentagonal bi-pyramidal geometry of negative charges provided by the side chains of residues in position 1, 3, 5 and 9, the backbone C=O of residue 7, a water molecule and residue 12, which is of crucial importance for Ca^{2+}-binding since it is the only amino acid responsible for a bidentate coordination [13]. Although EF-hands are highly selective for Ca^{2+}-binding, they are also capable of binding other divalent cations such as Zn^{2+}, Fe^{2+},Cu^{2+} and most importantly Mg^{2+}, which is present at

above-millimolar concentration in several tissues [14] including photoreceptor cells [15]. Indeed, Mg^{2+} ions can be bound four to five orders of magnitude more weakly with respect to Ca^{2+} ions through a octahedral geometry, in which residue 12 provides a monodentate coordination [16].

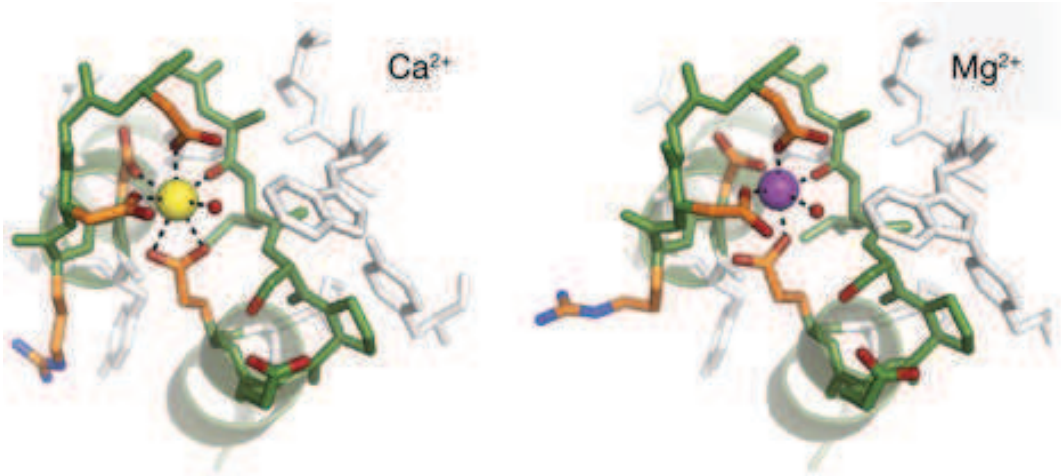

FIGURE 1.1: Ca^{2+} (left) and Mg^{2+} (right) coordination in EF-hands. Adapted from [17]

The reason for the low Mg^{2+}-affinity of EF-hands lies in the thermodynamical properties of binding, indeed the radius of Mg^{2+} increases 400-fold upon hydration, 16-fold higher respect to the increase shown by Ca^{2+}, meaning that Mg^{2+} binding requires a much higher energy [18]. The entropic contribution to the free energy is also one of the main factors influencing different calcium affinities exhibited by Ca^{2+}-binding proteins, as the presence of water molecules implied in ion hydration, rather than the coordination by a protein ligand, lowers Ca^{2+}-protein affinity. In this respect, the presence of specific residues in positions 9 and 12 [13] such as Glu or Gln instead of the shorter Asp or Asn residues is responsible for increasing Ca^{2+}-affinity, as Asp or Asn require an additional water molecule for the completion of the coordination sphere [19, 20]. This, for example, is also evident when comparing the sequence of the highest Ca2-affinity EF-hand (EF3) of human GCAP1 DVDGNGCI**D**RDE, whose affinity is around 80 nM [21], with the second-highest affinity EF-hand (EF3) of A. thaliana CaM1 DVDGDGQI**N**YEE, whose affinity is around 4.4 μM [22].

Ca^{2+}-binding proteins can be identified as Ca^{2+}-buffer proteins or Ca^{2+}-sensors, two

different classes of proteins which differ in their behavior upon ion binding. At odds with Ca^{2+}-buffer proteins, Ca^{2+}-sensors are in fact able to change their conformation. Ca^{2+}-sensor proteins can be classified as ubiquitous like Calmodulin or tissue-specific, like the Neuronal Calcium Sensor (NCS) family, which is entitled of regulating a variety of neuronal processes [23, 24, 25], among which phototransduction.

1.1.1 Phototransduction

Phototransduction is a complex cascade of processes that allows the conversion of a light stimulus to diverse biochemical signals which ultimately triggers vision in the visual cortex of the brain. This cascade starts inside rods and cones, specialized neuronal cells dedicated to scotopic and photopic vision respectively, which are located in the most external layer of neuronal cells of the retina.

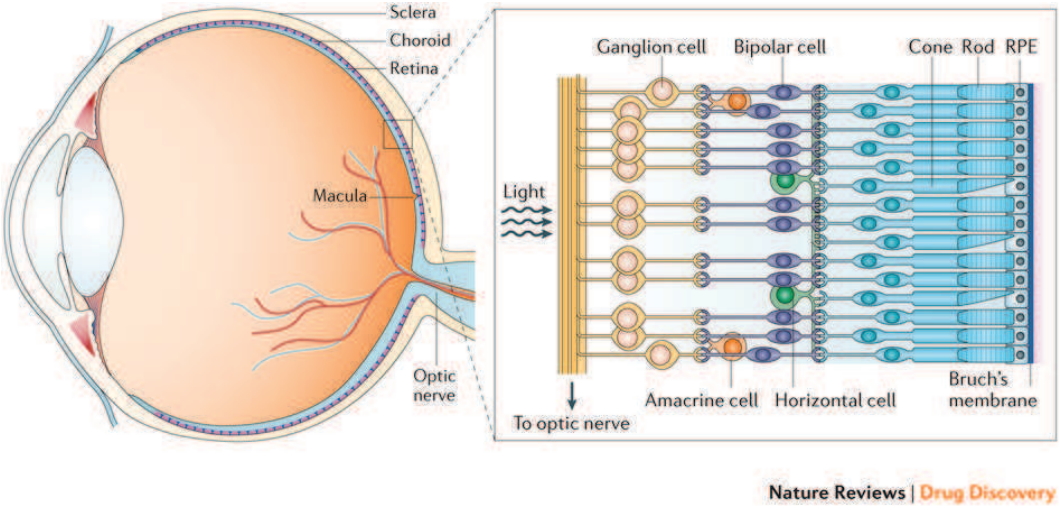

FIGURE 1.2: Retinal layers, from [26]

The phototransduction cascade is finely regulated by variations of the concentration of the two second messengers cGMP and Ca^{2+}, which are strictly dependent on one another. Several different NCS are therefore involved in different steps of the cascade, and in spite of the highly conserved sequence, each NCS has its specific physiological function [27].

When a photon is absorbed on the disc membranes by the G-protein coupled receptor Rhodopsin, the associated G-protein Transducin exchange GDP with GTP upon Rhodopsin binding, releasing its activated α-subunit to activate PDE6, which starts hydrolyzing cGMP to 5'-GMP. The drop in concentration of cGMP causes the closing of CNG-channels on the plasma membrane, preventing Na+ and Ca^{2+} ions from entering in the cytosol, which in combination with the simultaneous extrusion of Ca^{2+} ions by a Na+/Ca^{2+},K^{+} exchanger causes a drop of the intracellular Ca^{2+} concentration from 500-600 nM to 100 nM [28]. NCS detect this decrease of

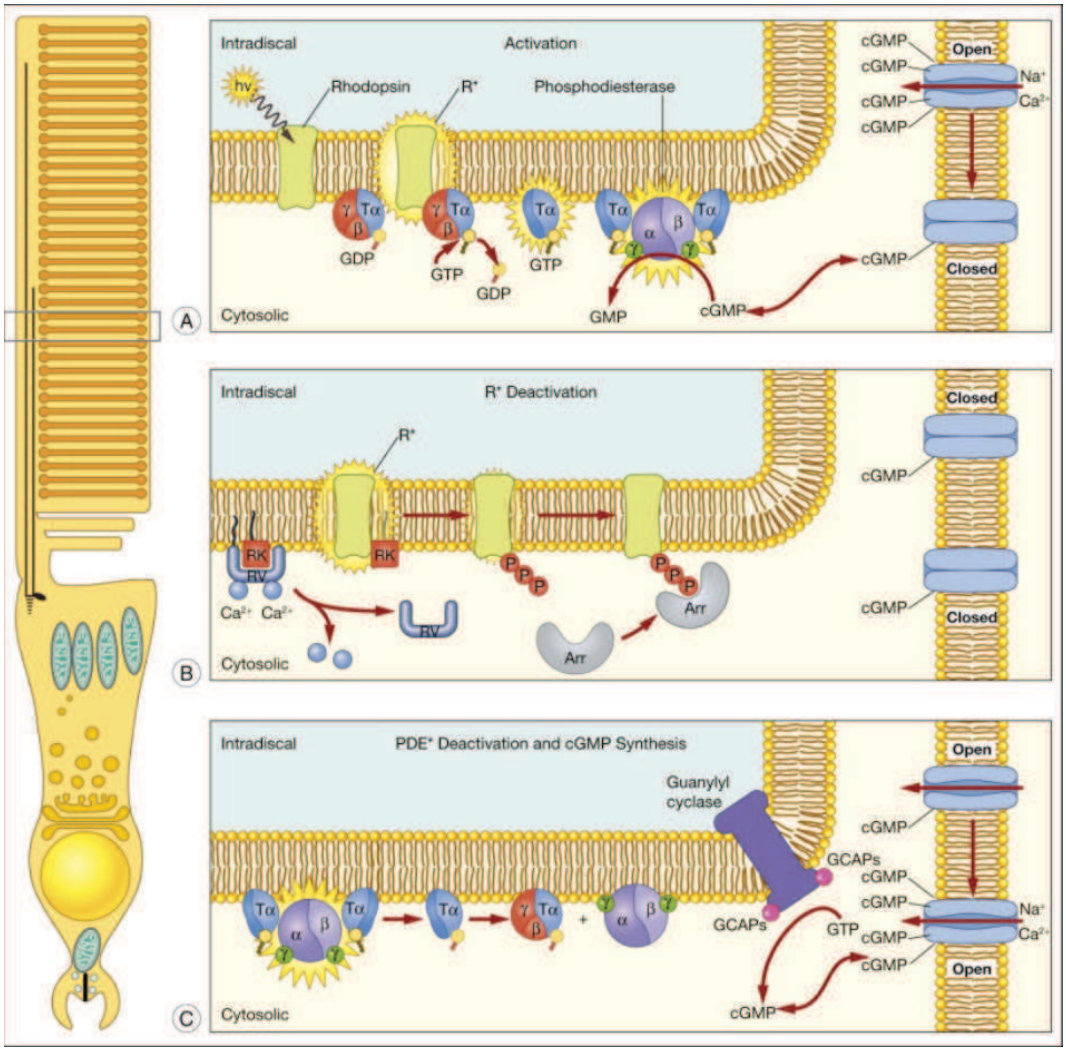

FIGURE 1.3: Main signaling mechanisms in phototransduction cascade. A) Rhodopsin activation, B) Recoverin-mediated Rhodopsin deactivation, C) GCAPs-mediated GC regulation, from [32]

the intracellular Ca^{2+} and exert their function as regulators of their specific molecular targets, that is CNG-channels in the case of CaM, rhodopsin kinase GRK1 in the case of Rec, and membrane-bound guanylate cyclases in the case of GCAPs [29, 30, 31].

1.1.2 GCAP1

GCAP1 is one of the three isoforms of GCAPs present in human photoreceptors and is a 23 kDa all α-helix protein composed by 4 EF-hand motifs arranged in two domains. Exception made for EF1, whose CPxG sequence impairs Ca^{2+}-coordination [33], all other EF-hands can bind 3 Ca^{2+} ions with sub-micromolar affinity and up to 2 Mg^{2+} ions in EF2 and putatively EF3 [**Paper 3**] [30] with sub-millmolar affinity. GCAP1 is involved in the Ca^{2+} mediated negative feedback mechanism of regulation of the GC, and has the peculiarity of being both activator and inhibitor of its target according to different Ca^{2+} levels [34], working in a Ca^{2+}-relay fashion with the cognate GCAP2 [35]. CNG-channels, restoring the high intracellular [Ca^{2+}] of the dark state.

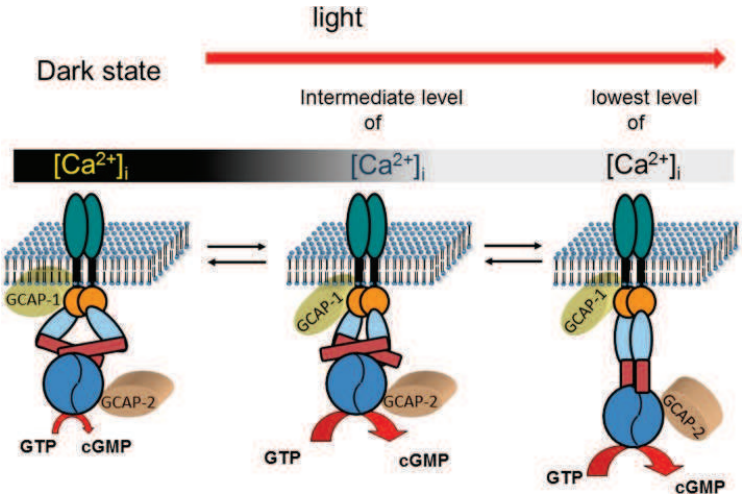

FIGURE 1.4: Ca^{2+}-relay mechanism, from [35]

Indeed, in the dark, when [Ca^{2+}] is high, GCAP1 acquires a conformation that prevents GC from synthesizing cGMP, thus keeping the catalytical activity below its basal value. When [cGMP] and [Ca^{2+}] drop as a consequence of the light stimulus, Ca^{2+} is released by GCAP1 EF-hands in decreased order of affinity (first EF4, then EF2, finally EF3), which then bind Mg^{2+} and switch to a conformation that activates GC. The newly synthesized cGMP can therefore replenish the intracellular pool to the concentration of 5 μM [36], allowing the opening of the The three-dimensional structure of GCAP1 in its Ca^{2+}-loaded form was solved via X-ray diffraction [37]

and was found not to be drastically different from the EF2-Mg^{2+} bound form [**Paper 3**], which was recently solved via NMR spectroscopy [38], nevertheless this subtle, yet significant conformational change is sufficient to switch on and off the target GC.

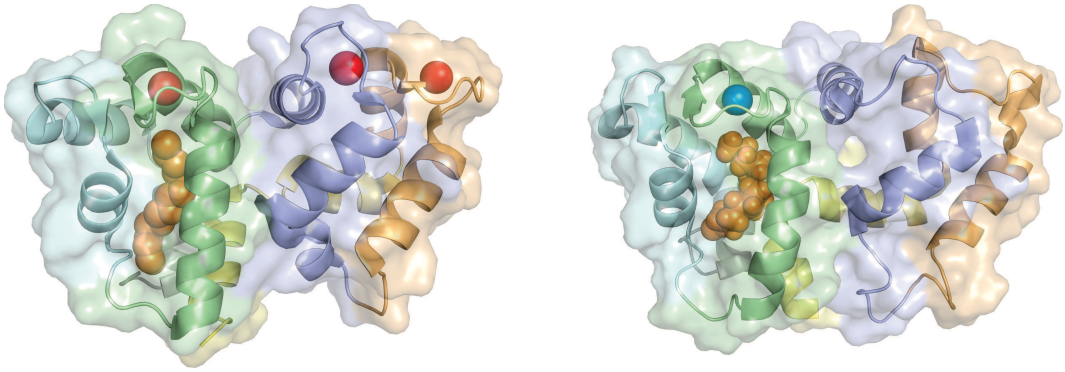

FIGURE 1.5: Three dimensional structure of Ca^{2+}-loaded (left) and Mg^{2+}-bound (right) myristoylated GCAP1. Protein backbone is represented as cartoons, myristoyl group is shown as orange spheres, Ca^{2+} ions are shown as red spheres, Mg/textsuperscript2+ ion is represented as a blue sphere. EF1 is colored in cyan, EF2 in green, EF3 in blue, EF4 in yellow, their molecular surface is shown in transparency.

The N-terminal myristoylation of GCAP1, a feature also shared by all other NCS, has a peculiar role in adjusting both the Ca^{2+}-sensitivity and the interaction with the target GC by mediating intramolecular communication between N and C domains [39, 40][**Paper 9**]. Unlike other NCS like Rec, the myristoyl group is always sequestered inside an hydrophobic crevice encompassing the N-domain and the C-terminus of the protein, even upon Ca^{2+}-binding.

1.1.3 Retinal dystrophy related GCAP1 mutations

GCAP1 is the only isoform associated with retinal dystrophies, a set of autosomal dominant degenerative pathologies ultimately leading to blindness. Retinal dystrophies can be classified in Macular Dystrophy, Cone Dystrophy and Cone-Rod Dystrophy, depending on the area of the retina and on the type of photoreceptor cells involved. The specific diagnosis of patients affected by retinal dystrophies is not trivial due to the heterogeneity of the symptoms [41, 42], as the clinical phenotype associated with these mutations is a combination of photophobia, nystagmus, reduction of visual acuity, color blindness, nyctalopia, hemeralopia and loss of central and peripheral vision. To this date, 15 missense mutation of have been identified in patients, namely P50L, L84F, E89K, Y99C, D100E/G, N104K, I107T, I143N/T, L151F, E155G/A, G159V, L176F, Y99C, L151F [41, 43, 44, 45, 46, 47, 48, 49, 50, 51, 52, 53, 54][**Paper 6**][**Paper 7**][**Paper 8**], and even though a precise pathological mechanism has not been identified, all these mutants exhibited alterations in the regulation of the GC resulting in its constitutive activation at physiological [Ca^{2+}]. Biochemical and biophysical investigations made by us and other research groups highlighted that most mutants had decreased Ca^{2+} affinity, but some variations like L84F and L176F showed wild type like affinity [**Paper 7**][**Paper 8**]. This suggested that the altered intramolecular communication from the ion binding sites, rather than merely their affinity for Ca^{2+}, was the main reason leading to the constitutive GC activation in the dark.

1.1.4 Recoverin

Recoverin is a 23 kDa all-α-helix prototypical NCS protein, with 4 EF-hand motifs arranged in two domains, two of which (EF2 and EF3) are Ca^{2+}-binding sites with micromolar affinity. Like other NCS, Rec is also myristoylated at the N-terminus, and the covalently attached myristoyl group, which is buried in an hydrophobic milieu in Ca^{2+}-free conditions, gets extruded from its pocket upon Ca^{2+}-binding, with the so-called "myristoyl-switch" mechanism [56, 28]. This conformational change allows Rec to exert its biological function, which take place during the recovery phase of the phototransduction cascade, where it regulates the target Rhodopsin Kinase GRK1. In the dark, when [Ca^{2+}] is elevated, Rec is in a "relaxed" Ca^{2+}-bound state, where the protein is anchored to the disc membrane by its myristoyl group and bound to GRK1 to inhibit the phosphorylation of Rhodopsin. When [Ca^{2+}] drops as a consequence of illumination, Rec switches its conformation to a "tense" state where the fatty acid is sequestered in an hydrophobic crevice, allowing Rec to diffuse in the cytosol. The dissociation of the Rec-GRK1 complex triggers the phosphorylation of Rhodopsin, leading to an increase of the affinity for Arrestin, which then replaces the α-subunit of Transducin, ultimately leading to the shutting down of the signal (Figure 3B).

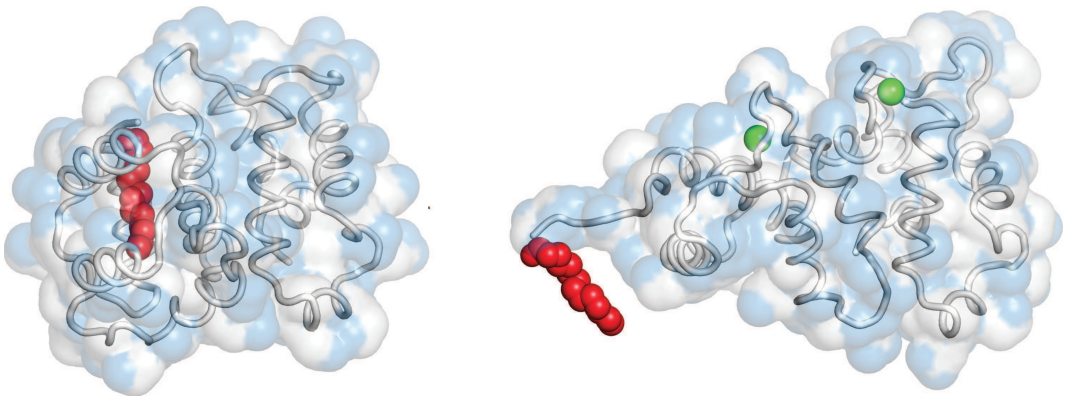

FIGURE 1.6: Three dimensional structure of apo (left) [57] and Ca^{2+}-loaded (right) [56] myristoylated Recoverin. Protein backbone is represented as grey tubes, myristoyl group is shown as red spheres, Ca^{2+} ions are shown as green spheres. The hydrophobic and hydrophilic Solvent Accessible Surfaces are shown in transparency in gray and blue respectively.

While Rec has been found to play a role only in Cancer-associated Retinopathies [58] and Recoverin-associated Retinopathies [59], it was tested as a prototypical Ca^{2+}-sensor protein for potential therapeutical applications of nanodevices [**Paper 1**] and for investigating the role of Mg^{2+} in the phototransduction cascade [**Paper 4**].

1.1.5 Calmodulin

Calmodulin is a ubiquitous 17 kDa all-αhelix protein considered the ancestor of the Calmodulin superfamily of Ca^{2+}-sensor proteins [60]. CaM is able to selectively recognize more than 300 different targets involved in several different biological processes, such as ion channels regulation, protein folding, apoptosis, cell motility, homeostasis and cytoskeleton development and functionality [61, 62]. Structural architecture of CaM is composed by four Ca^{2+}-binding EF-hand motifs arranged in two globular lobes connected by a flexible linker [63] with different Ca^{2+}-affinities, leading to an apparent affinity of a low micromolar order, usually increasing in the presence of a target protein[64]. In the absence of Ca^{2+} the two lobes acquire a tightly packed conformation [65], upon Ca^{2+} binding CaM exhibits an elevated degree of structural plasticity [66] making CaM, able to regulate different target proteins with selective interaction modes [67, 68], at odds with the aforementioned Ca^{2+} sensors Rec and GCAP1.

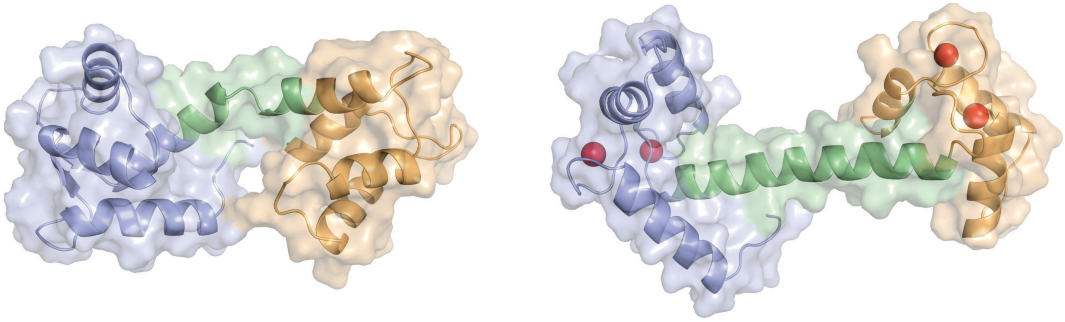

FIGURE 1.7: Three dimensional structure of apo (left) and Ca^{2+}-bound (right) CaM, secondary structure is represented in cartoon, Ca^{2+}-ions are represented as red spheres, N-term domain is colored in blue, C-term domain is in yellow, the linker region is in green.

Recently, an increasing number of heterogeneous pathologies have been found to be associated with CaM, spanning from cancer-related alterations of cell cycle and proliferation[69], to neurodegenerative diseases like Alzheimer's [70], to cardiovascular diseases [71, 72, 73, 74], raising interest as a potential target for nanodevice-mediated protein therapy.

1.2 Nanomedical applications for protein therapy

Gene therapy is one of most promising approaches for treating genetic disorders, but the difficulty of delivering and stably expressing the protein of interest, together with the potential risk of recombination-related side effects, is one major drawback. A safer alternative to this approach is the so called protein therapy, which consists in the delivery of folded and functional proteins to specifically targeted tissues, in order to replace the intracellular pool of mutated proteins which are the cause of the pathological phenotype [75]. In this context, nanodevices are one of the most promising tools thanks to their small size (<100 nm) and their high surface to volume ratio, which would allow high amounts of protein to be carried to a target tissue, cell, or even organelle [76]. Furthermore, nanodevices offer high versatility in terms of chemical composition, which allows these potential carriers to be specifically engineered in order to increase target specificity or to acquire useful features such as bioluminescence [77] and thermal sensitivity [78]. Several Ca^{2+}-sensor proteins have been found to be associated with inherited diseases, therefore different biocompatible nanodevices, namely liposomes and CaF_2 nanoparticles [79], have been tested for their suitability as Ca^{2+}-sensors carriers, by exploiting the physiological behavior of these proteins for binding and release [**Paper 1**][**Paper 2**]. Indeed liposomes with Rod-Outer-Segment like lipid composition were successfully applied for the delivery of encapsulated Rec inside rod cells, [80], in addition these liposomes were found to reversibly bind Rec on their surface presumably through to the myristoyl switch mechanism [**Paper 1**]. On the other hand, CaM and Rec were found to reversibly bind the matrix of lanthanide-doped, upconverting CaF_2 NP [81], supposedly through the coordination of Ca^{2+} ions belonging to the lattice by their EF-hands [**Paper 1**][**Paper 2**]. Binding is per se not sufficient for assessing the suitability of nanodevices as protein carriers, as a major requirement for this approach to be effective is the preservation of the native structure and functionality. Indeed, recent studies suggested that nanoparticle-bound proteins could be subjected to significant structural changes [82, 83] or unfolding [84] upon binding, which were found to be highly dependent on the chemical nature of the nanodevice and on the protein system [**Paper 1**][**Paper 2**].

Chapter 2

Methods

2.1 Expression and purification of recombinant proteins

Protein expression and purification is a necessary preliminary step of every *in vitro* biochemical an biophysical study, as different amounts of pure protein are required by different experimental techniques. Indeed, while some approaches like fluorescence spectroscopy or Surface Plasmon Resonance (SPR) need just few micrograms of protein, others like Isothermal Titration Calorimetry (ITC) or Nuclear Magnetic Resonance (NMR) employ several milligrams of sample, which have to possess a high percentage of purity in order to provide accurate and reliable data. Nowadays it is possible to express proteins in prokaryotic systems like *E. coli* and *B. subtilis* and eukaryotic systems like yeast or mammalian cells using recombinant DNA technique, or in *in vitro* systems. Recombinant DNA approach, which consists of the transformation of living systems using genetic material coming from different living system, was employed for the expression in *E. coli* strain BL21 DE3 of the Ca^{2+}-sensors studied in this thesis, namely CaM from *A. thaliana* and Rec and GCAP1 from *B. taurus*. *E. coli* is the most popular system for the expression of recombinant proteins because of its simplicity of transformation, rapid and low-cost growth [85, 86]. Moreover, the recent development of new bacterial strains, plasmidic vectors and protein tags provided tools to overcome most of the problems associated with recombinant protein expression, such as inclusion body formation, post-translational modifications, protein toxicity and mRNA instability

[85]. All previously presented Ca^{2+}-sensors presented in this thesis were indeed expressed recombinantly in *E. coli* BL21 DE3 strains transformed with different pET vectors. These vectors contain IPTG-induced T7 promoter [87], by far the best performing promoter with a recombinant protein expression up to 50% of total proteins [88], making T7-based pET vectors the most popular system used for heterologous expression in *E. coli* [89]. Purification of recombinantly expressed Ca^{2+}-sensors was achieved through Fast protein liquid chromatography techniques, which consist of the exploitation of biophysical properties of the proteins such as hydrophobicity, charge, size or biorecognition, for binding and eluting from specific chromatographic columns [90] differing in their resin content. Indeed CaM [91] and Rec [92] were purified through Hydrophobic Interaction Chromatography, while GCAP1 was purified after a combination of Anionic Exchange and Size Exclusion Chromatography [93].

2.2 CD spectroscopy

Circular dichroism spectroscopy is a low-resolution technique employed in the investigation of the structural properties of biomolecules [94], based on the absorption of circularly polarized light. The difference between the clockwise (R) and counter-clockwise (L) components of the circularly polarized light absorbed by chiral centers results in an elliptically polarized light, which gives information about the microenvironment of the chiral centers. CD spectroscopy can be proficiently used to retrieve some structural information about proteins [95, 96], indeed proteins have optically active chromophores such as the peptide bond, absorbing below 240 nm, aromatic sidechains, absorbing between 260 and 320 nm, and disulphide bonds which absorb weakly around 260 nm. Moreover, ligands and cofactors can also absorb ranging from 300 nm to the near infrared region [97], therefore this technique can be employed to investigate enzymatic reactions or conformational changes upon ligand binding. Since absorption below 240 nm is due mainly to the peptide bond, it is possible to obtain a fingerprint of the protein in terms of secondary structure type and content, as each type of secondary structure has its own typical far UV CD spectrum [Figure 2.1].

By deconvolving the far UV CD spectra is therefore possible to estimate the content of each type of secondary structure, using a variety of algorithms like K2d [98], CONTIN [99], and DICHROWEB [100, 101]. In the near UV region (260-320 nm) the three aromatic aminoacid sidechains are specifically absorbing at typical wavelengths, indeed Trp shows an absorption peak close to 290 nm with fine structure spanning to 305 nm, Tyr residues absorb between 275 and 282 nm, while Phe residues exhibit sharp bands with fine structure between 255 and 270 nm.

The signal arising from aromatic residues is greatly influenced by their number, mobility, position and environment, providing a low-resolution fingerprint of the protein that can be used for comparative studies. In addition, by monitoring variations of the CD signals upon titration with denaturing agents or by increasing the temperature it is possible to quantitatively estimate the stability of the native protein. While the structural information retrieved by CD spectra is not comparable to that of X-ray crystallography or NMR in terms of resolution, this technique is

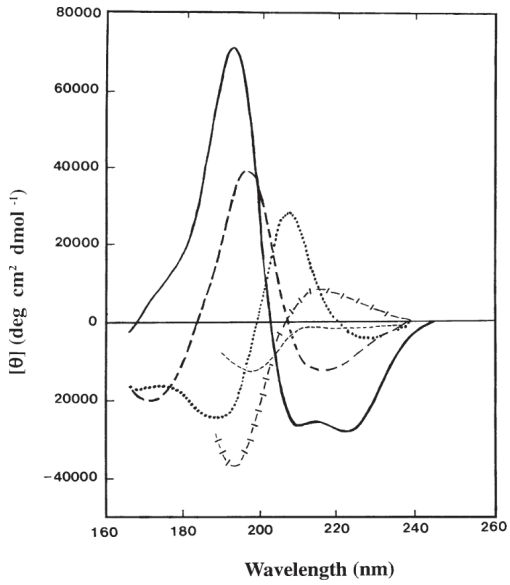

FIGURE 2.1: Examples of far UV CD spectra typical of α-helix (solid line), anti-parallel β-sheet(long dashed line), type I β-turn (dotted line), extended 3_1-helix or poly (Pro) II helix (cross dashed line), irregular structure (short dashed line), from [96]

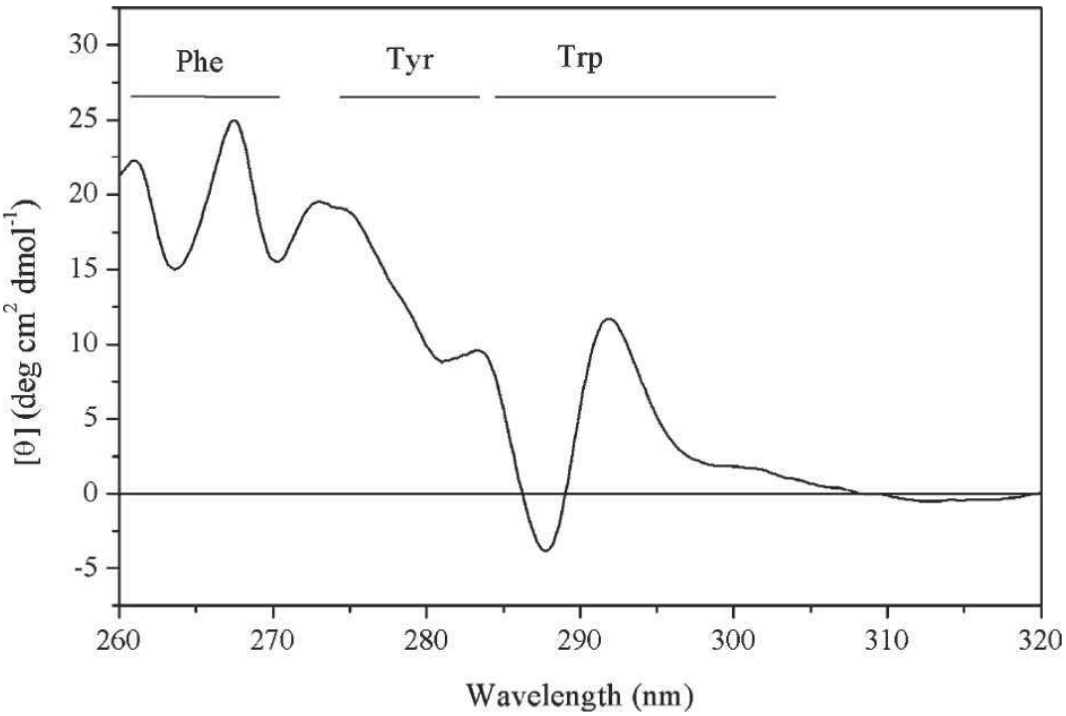

FIGURE 2.2: Example of Near UV CD spectrum, from [96]

far less demanding as far as measurement time and sample requirements are concerned. Indeed, CD spectroscopy allows to perform a comprehensive study of the structural features of a protein in less than 30 min, using roughly 1 mg of material and without destroying the sample. All these features make CD spectroscopy quite a useful technique when working with recombinant proteins which are difficult to express and purify with a low yield, especially when used in combination with other non-destructive techniques like Dynamic Light Scattering.

2.3 Fluorescence spectroscopy

Fluorescence is a luminescent process in which molecules are able to emit light upon excitation of the electronic states by external stimuli such as friction, chemical agents or light absorption. Molecules have a ground electronic state, characterized by a low energy, several excited electronic states at higher energies and many vibrational states in between. Excited electronic states can be reached by electrons when an external stimulus provides enough energy to fill the gap between the ground state and the excited state. The promoted electron, though, loses vibrational energy after collision with other molecules, reaching the lowest vibrational state of the excited electronic state, then the molecule reverts to the ground electronic state by emitting a photon [102]. The discovery of the fluorescence principle opened the door to a plethora of widely applied and sophisticated approaches to study biological processes. More specifically, this technique allowed to investigate the structure and dynamics of nucleic acids [103, 104], proteins [105, 106], and their interaction with other molecules such as substrates, cofactors and membranes. Proteins are ideal candidates for fluorescence studies due to the presence of delocalized electrons in the sidechain of aromatic residues Phe, Tyr and Trp, and the availability of several small chemical dyes like Cyanine or Alexa specifically developed.

Although all aromatic residues could be in principle used as intrinsic fluorescent probes, Trp is by far the most commonly used probe, as its indole group provides the highest absorbance, with a peak near 280 nm, and emission between 310 and 350 nm. Being the rarest aromatic aminoacid due to the metabolic cost of its synthesis [108], Trp fluorescence also provides somewhat detailed information of the microenvironment of precise regions of the proteins. This can be used not only to evaluate conformational changes [109] upon interaction with other molecular partners [110], but also to investigate the folding state of the protein. Indeed, like many other extrinsic fluorescent molecules, Trp residues are solvatochromic, as their properties in terms of quantum yield and the position of the emission or absorption bands strongly depends on their environment [111]. Denaturation or increased exposure to a polar solvent due to structural change cause a bathochromic

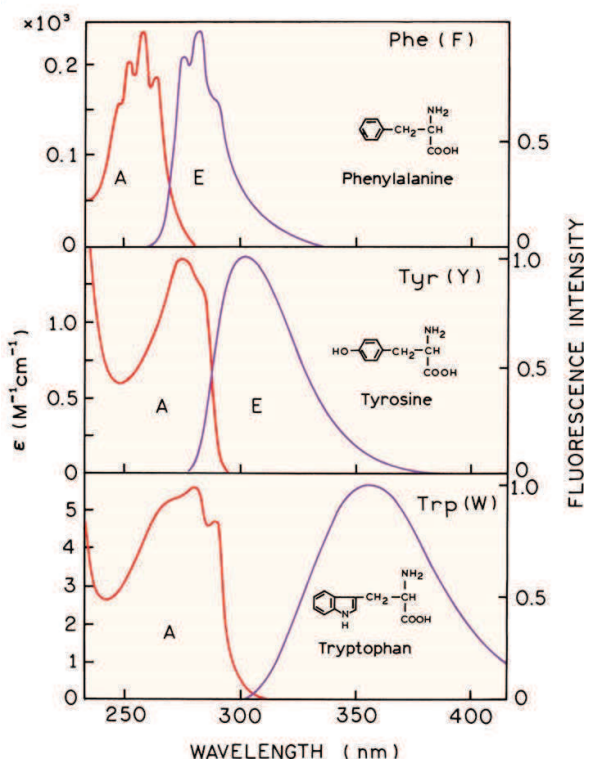

FIGURE 2.3: Fluorescence absorbance end emission spectra of aromatic aminoacids, from [108]

(red) shift of the maximal emission, whereas membrane embedding, or more generally a tighter packing of hydrophobic interactions surrounding Trp residues generate an hypsochromic (blue) shift to shorter wavelengths [112, 113]. Versatility is the main quality of fluorescence spectroscopy studies, since the possibility to employ either intrinsic or extrinsic fluorescent probes, combined with the investigation of anisotropy, Forster Resonance Energy Transfer and solvatochromism effects, allows the coverage of several structural aspects of biomolecules. In addition, fluorescence studies can be performed not only at steady state, but also monitoring the time dependence of fluorescence emission through lifetime and kinetic studies. Although fluorescence techniques are noninvasive, they are sensitive to autofluorescence interferences and each of the aforementioned approaches has different limitations. For example, FRET is suitable only for investigating short-range phenomena, fluorescence anisotropy suitability is dependent on the lifetime of the dye and on the properties of the proteic system studied, and intrinsic fluorescence measurements

could have a low spatial resolution due to the presence of several Trp residues [114].

2.4 Dynamic Light Scattering

Dynamic Light Scattering (DLS) also known as Photon Correlation Spectroscopy or Quasi-Elastic Light Scattering, is a widely used technique employed for the study of the dynamics of particles undergoing Brownian motion in colloidal solutions [115, 116]. DLS approach can therefore be applied for the estimation of the hydrodynamic properties of biomolecules like DNA [117], proteins [118, 119] and any nanosized-particle [120]. When a coherent and monochromatic light beam is shone onto a colloidal solution, where all particles are randomly moving according to Brownian motion, each particle behaves as a secondary source as the light wave gets scattered. The interference between the radiation scattered by the particles generates a time-fluctuating speckle pattern which depends on the diffusion coefficient of the particles. Small particles diffuse in liquid medium faster than large particles, resulting in more rapid fluctuations of the intensity of scattered light with respect to the slow fluctuation exhibited by large particles. The DLS technique is substantially based on the analysis of the fluctuations of the scattered intensity, which is performed by processing the signal with the autocorrelation technique, hence the synonym Photon Correlation Spectroscopy. Essentially, the correlation of the intensity of the scattered signal is monitored at increasing time intervals, yielding the autocorrelation function, which for a suspension of monodisperse, spherical particles, follows an exponential decay. The decay of the autocorrelation function is strictly related to the diffusion coefficient of the particles in suspension, as larger molecules have longer decay than smaller molecules. Therefore, using the Stokes-Einstein equation it is possible to obtain the equivalent sphere radius of the particles, which, for spherical particles, represents the hydrodynamic radius (R).

$$D = \frac{kT}{6\pi\eta R} \tag{2.1}$$

The only method recommended by the international standard ISO 13321 [121] to extract the particle size from DLS experiments performed on a population with a monomodal Gaussian distribution of size, such as proteins or nanodevices, is the

method of cumulants [122]. This method takes into account the mean and the variance of the population and allows to measure the polydispersity of the diffusion coefficient of the population, represented as polydispersity index, which is used to estimate the quality of the experimental sample object of the study.

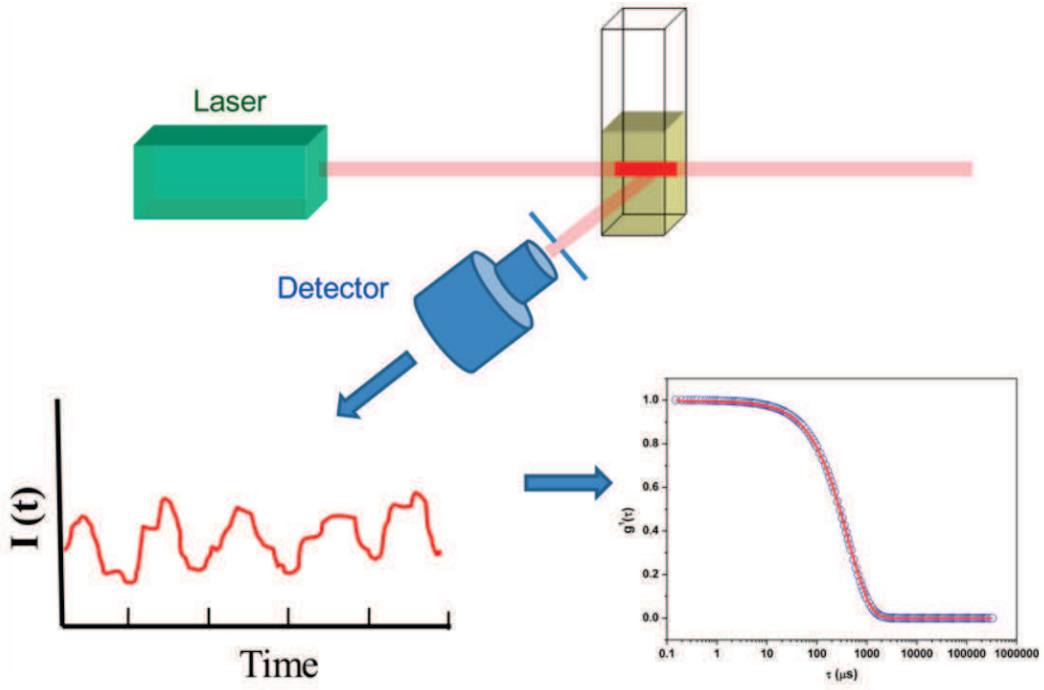

FIGURE 2.4: Dynamic Light Scattering principle, from [116]

The main advantages of this technique are the limited experimental time and quantity of sample, as a precise determination of the size of the particles can be achieved in less than 1 hour with less than 1 mg of protein or nanodevices. On the other hand, the sensitivity of the technique requires careful handling of the samples, which have to be preferably filtered through 0.2 μm filter in order to remove dust particles or oversize contaminants.

2.5 Chelator assay

The estimation of the Ca^{2+} affinity of Ca^{2+}-sensor protein ions can be achieved through different approaches, one of the most common is Isothermal Titration Calorimetry, based on the measurement of heat exchange upon ligand titration. This technique, though, can suffer from interferences due to the absorption or release of heat as a consequence of conformational changes, as would be the case for Ca^{2+}-sensor proteins in which, by definition, Ca^{2+}-binding is accompanied by structural variations. Therefore, other direct binding methods such as Circular Dichroism or fluorescence spectroscopy based titrations are more suitable for studying the Ca^{2+}-affinity of this family of proteins. Spectroscopy-based methods can give reliable and accurate results only when the population of Ca^{2+}-free and Ca^{2+}-bound proteins are significant, meaning that a protein concentration roughly equal to the dissociation constant is required. Nevertheless, spectroscopy-based direct binding methods do not allow to estimate Ca^{2+} smaller than 1 μM, therefore, in order to estimate high affinity constants, it is necessary to rely on other direct methods like Ca^{2+}-selective electrodes or measurement of bound ^{45}Ca, or on indirect methods. The chelator assay is one of the best performing indirect methods, and is based on the competition between a Ca^{2+}-sensor protein and a chromophoric Ca^{2+}-chelator [123] such as quin-2, 5,5'Br_2-BAPTA and 5N-BAPTA, whose fluorescence or absorbance strictly depends on Ca^{2+}-binding. The selectivity of Ca^{2+}-binding by these chromophoric chelators makes this technique particularly useful for studying NCS proteins like GCAPs, whose Ca^{2+}-affinity is affected by the presence of Mg^{2+} ions. While chelator assay experiments are relatively simple to perform, their interpretation is not trivial, as the estimation of macroscopic binding constants depends on the unraveling of several microscopic binding constants. Fortunately, CaLigator software [124] deals with the complexity of the system, leaving the user just with the determination of the total concentration of Ca^{2+}, protein and chelator in order to retrieve precise macroscopic binding constants for all possible binding sites. The only limitation of the method is that the affinity of each Ca^{2+} binding site has to be higher than that of the chelator, which can be overcome by a suitable choice of the chromophoric chelators, whose affinity span from low nanomolar to high micromolar range.

2.6 Molecular Dynamics simulations

The knowledge about structural properties of a protein is fundamental for the understanding of its function, in this regard the contribute given by X-ray crystallography and NMR spectroscopy has been invaluable. X-ray and NMR are, up to now, the only methods able to provide structural information at atomistic resolution, but the dynamic properties of the proteins of interest still remain largely unknown. Indeed, X-ray crystallography depicts only a frozen state of the protein, while NMR requires high protein concentration and sometimes not physiological experimental conditions. The progress in informatics, both in terms of computational resources and programming skills, led to the development of Molecular Dynamics (MD) simulations [125, 126], a method previously applied in theoretical physics and material science, to fill the lack of experimental tools for the investigation of biomolecules dynamics. This technique is able to combine both quantum mechanics and classical mechanics to monitor protein folding [127], and time evolution of biomolecules such as DNA, proteins and membranes [128] over relatively long time frames [129]. Pure quantum mechanics simulations are in principle the most accurate way to reproduce enzymatic reactions and biomolecules dynamics, but they are still computationally very demanding, therefore classical mechanics turned out to be a fair compromise between accuracy and feasibility, at least when dealing with proteins structural behavior. In classical MD simulations the trajectories of all atoms are calculated solving Newton's equations of motion, where forces acting on the particles and their potential energies are numerically calculated using molecular mechanics force fields. These force fields are empirical potentials consisting of a summation of bonded and non-bonded pair forces which represent approximations of quantum-mechanical effects through classical mechanics laws. Indeed stretching and bending of covalent interactions are modeled according to Hooke's law, torsional angles are modeled using a periodic function, electrostatics is represented by point charge Coulomb interactions, van der Waals interactions are approximated with the Lennard-Jones potential. Several programs dedicated to MD simulations like GROMACS [130], CHARMM [131] and AMBER [132] have their own force fields, which usually differ in the parametrization of the interactions and/or in the

specificity for biomolecules. Once the force field has been chosen and a three-dimensional structure of the protein is available, the workflow of MD simulations is well defined.

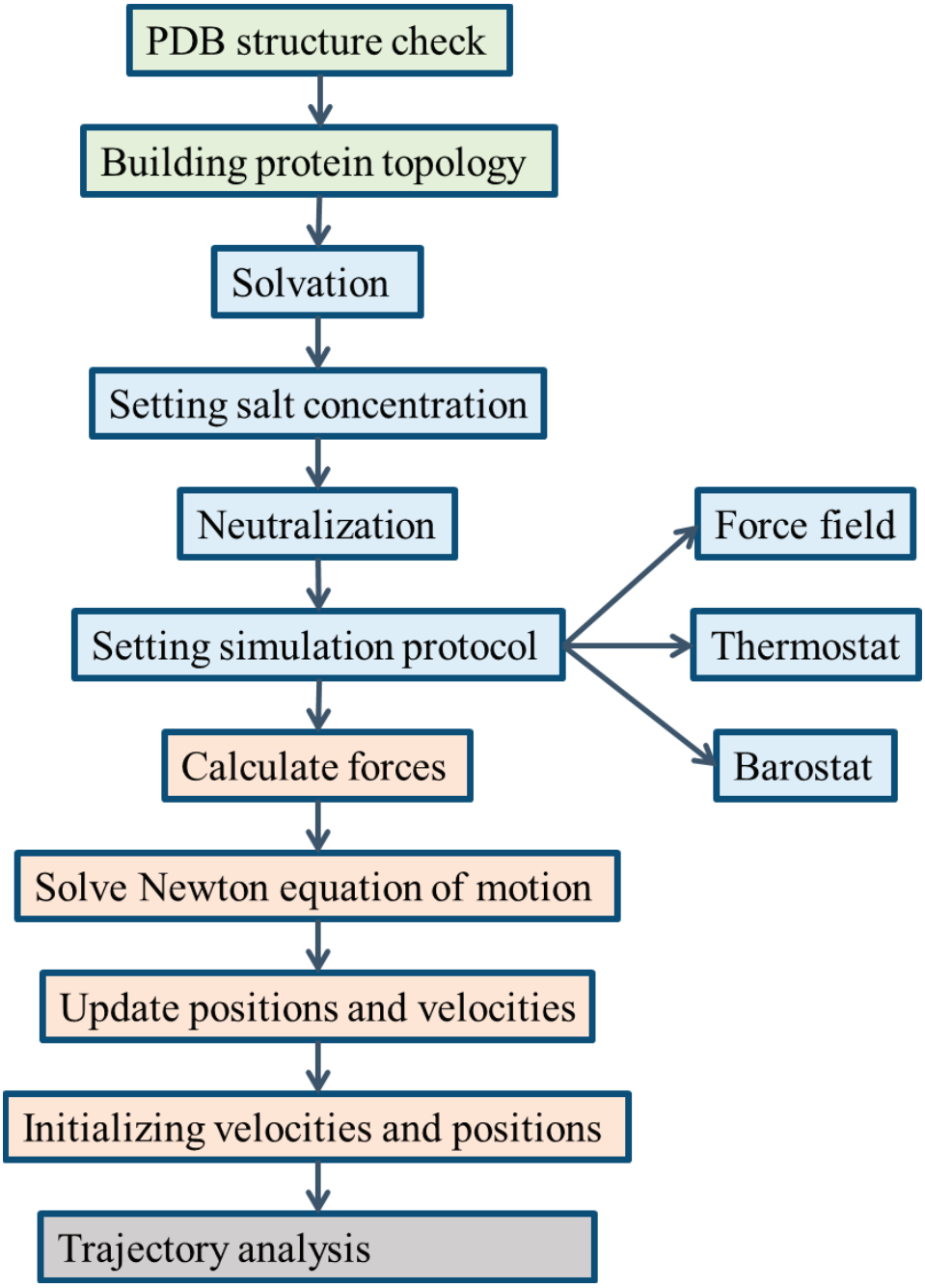

FIGURE 2.5: Molecular Dynamics simulations workflow

Unfortunately, MD simulations are very sensitive to the several initial parameters, such as structure, computational architecture, thermostatic and barometric controls, which make them intrinsically non reproducible. However, this obstacle can be overcome by running different replicas, whose consistency and reproducibility need to be assessed using Principal Component Analysis based approaches [133] such as cosine content [134] and Root-Mean Square Inner Product [135]. Consistent and exhaustive MD trajectories carry a huge amount of structural and energetic information representing several possible conformations of the simulated protein, which can be analyzed at different levels of accuracy and complexity. Among the most basic analyses that can be performed on a MD trajectory there are Root Mean Square Deviation and Root Mean Square Fluctuation (time-averaged RMSD) of α-carbons, which represent the global structural stability and the local flexibility, respectively. Another popular and useful analysis of MD trajectory is the estimation of the Solvent Accessible Surface of the protein or of specific residues, which represent the envelope of the center of a spherical molecule of water on the van der Waals surface. These indexes are indeed very informative for some Ca^{2+}-sensor proteins like CaM or Rec, which undergo major structural rearrangements upon Ca^{2+}-binding, while dynamical conformational studies of GCAP1 require more sophisticated approaches like, for example, the Protein Structure Network approach [136], to unveil the connection between GCAP1 subtle conformational changes and its regulation modes. MD simulations are a powerful tool for the investigation of protein dynamics and are also employed to refine or validate molecular restraints of NMR and X-ray structures, on which they strictly depend. The advantage over these techniques lies in the uniqueness of the dynamical information produced by MD simulations, which can be also considered as a disadvantage, as no experimental way of validating this information is yet available.

2.7 Protein Structure Network

Protein Structure Network (PSN) [137, 138] is a recent approach combining structural biology and network concepts, in which proteins are represented as graphs where residues are nodes and interactions between residues are edges. Such networks can be generated on crystallographic or NMR structures using geometrical constraints, indeed H-bond, electrostatic and hydrophobic interactions require particular distances and/or angles in order to occur. These PSN, though, are generated only on static structures or on a limited set of conformations derived from NMR experiments, lacking therefore of information about protein dynamics provided by MD simulations. Pyinteraph [139] revealed itself a valuable tool for combining protein dynamics and PSN, allowing not only to include dynamic information into PSN, but also providing quantitative tools for the evaluation of the persistence of each interaction. The size of the largest hydrophobic cluster of interaction is the most restrictive criterion for the evaluation [137] of the persistence threshold that can be used to refine PSN in order to include only persistent interactions. Once the PSN generated by persistent interactions has been created, the topological analysis of such PSN allows to identify the most connected amino acids in the network (hubs), which play a key role in maintaining the correct topology and, if mutated, are most likely to perturb global structure and functionality. Moreover, the PSN paradigm can be proficiently adopted to identify intramolecular communication pathways between distant regions of the protein, underlying allosteric mechanisms [140, 141] connected to protein dynamics. In order for a pathway between residues A and B to be significant for the sake of information transfer, the communication between them has to be robust, which means, according to the parsimony principle, that they are connected by a large number of shortest paths made by persistent interactions. Therefore, to investigate the preferential intramolecular communication routes between two residues belonging, for example, to a Ca^{2+}-binding site and target interface residue, we created the Communication Robustness (CR) index, defined as follows:

$$CR = \frac{\sigma AB \cdot l}{pT} \tag{2.2}$$

Where σAB is the number of shortest path of length l and pT is the persistence threshold previously used to generate the PSN. PSN analysis and CR index have been successfully employed to discover preferential communication routes in different regulatory states of GCAP1 as reported in **Paper 9**, but this approach can be virtually extended to any other Ca^{2+}-sensor protein.

Chapter 3

Introduction to the papers

This thesis work is composed by nine papers attached in appendix. Here is a brief summary of the results and the conclusions of each paper.

3.1 Paper 1: Nanodevice-induced conformational and functional changes in a prototypical calcium sensor protein.

Marino V, Astegno A, Pedroni M, Piccinelli F, Dell'Orco D. *Nanoscale*. **2014** Jan 7; *6(1)*:412-23. doi: 10.1039/c3nr04978g.
(published before the PhD period)

Nanodevices are one of the most promising tools for targeted protein therapy, since their high surface to volume ratio would allow to deliver high amounts of protein. Here we tested the suitability of liposomes and lanthanide-doped upconverting CaF_2 NP as nanocarriers of the prototypical NCS Rec. I performed all the experiments of this project as part of my Master Degree in Bioinformatics and Medical Biotechnology and in the following 9 months of internship. To prove the suitability of the nanodevices we had to assess the binding and the functionality of Rec while bound on the surface of the nanodevices, and in order to do so we used DLS, limited proteolysis, CD and fluorescence spectroscopy. We found that Rec was able to reversibly bind CaF_2 NP, probably via EF-hand motifs, and liposomes upon extrusion of the myristoyl group, even though the reversibility was more effective for

the latter. While liposomes preserved the structural features of Rec, allowing the triggering of the physiological Ca^{2+}-dependent myristoyl-switch, NP significantly perturbed the secondary and tertiary structure of Rec as well as its thermal stability, forcing Rec to acquire a conformation which impaired its capability to act as a Ca^{2+}-sensor protein. CaF_2 NP were therefore proven not to be suitable as Rec carriers, at odds with liposomes which fully preserved all physiological features of the NCS.

3.2 Paper 2: Structural plasticity of calmodulin on the surface of CaF_2 nanoparticles preserves its biological function.

Astegno A, Maresi E, Marino V, Dominici P, Pedroni M, Piccinelli F, Dell'Orco D. *Nanoscale*. **2014** Dec 21; *6(24)*:15037-47. doi: 10.1039/c4nr04368e.

Following the proof of concept presented in **Paper 1**, we tested the suitability of the same lanthanide-doped upconverting CaF_2 NP as carrier of the ubiquitous Ca^{2+}-sensor protein CaM. By means of DLS we were able to prove that also CaM was able to bind the NP with an ITC-estimated stoichiometric ratio of 1 NP: 120 CaM, consistent with the number of possible binding sites (144) on the surface of the NP assessed by geometrical approximations. My contribution to this project consisted of the experimental planning and the performing of the DLS and CD experiments. CD spectra showed that NP-bound CaM acquired a Ca^{2+}-bound like secondary and tertiary structure, meaning that the NP binding mode was presumably the same as the Ca^{2+}-binding mode, that is via the EF-hands motifs. Therefore, for a better understanding of the EF-hands involved in Ca^{2+}-binding and conformational changes upon NP interaction, we generated the double mutant E105Q-E141Q knocking out the Ca^{2+}-binding capability of EF3 and EF4. The lack of conformational changes detected upon NP or Ca^{2+} binding allowed us to identify the N-lobe, constituted by EF1 and EF2, as responsible for the physiological structural variations associated with Ca^{2+}-sensing. We also tested whether NP-bound CaM exhibited any residual capability of binding the target peptide from Gad1, such possibility was confirmed by CD spectroscopy, which highlighted that peptide binding was also Ca^{2+}-dependent. Finally we tested the residual functionality by enzymatic assay with Gad1, which was completely preserved as shown by the full activation of the enzyme, therefore proving the suitability of CaF_2 NP as carriers of CaM, at odds with what was reported for Rec in **Paper 1**. In conclusion, CaF_2 NP applicability as Ca^{2+}-sensors carriers was found to be dependent on the structural flexibility of the proteins. Indeed, the same structural plasticity which allows the recognition and

the regulation of several targets by CaM, compared to the single target of Rec, is probably the cause of the difference in the behavior of the two Ca^{2+}-sensors upon interaction with the NP.

3.3 Paper 3: Conformational changes in calcium-sensor proteins under molecular crowding conditions.

Sulmann S, Dell'Orco D, Marino V, Behnen P, Koch KW. *Chemistry*. **2014** May 26; *20(22)*:6756-62. doi: 10.1002/chem.201402146.

In this study we assessed by DLS and SEC the Ca^{2+}-induced variations of the hydrodynamic properties of several Ca^{2+}-sensor proteins, and compared them with Ca^{2+}-dependent SPR signals in order to discriminate different conformational changes. In detail we investigated the conformational changes of the ubiquitous Ca^{2+}-sensor CaM, and Troponin C, which is involved in Ca^{2+}-mediated muscle contraction. In addition, we studied two NCS involved in phototransduction, that is three different variants of Rec, namely non-myristoylated (nmRec), myristoylated (mRec) and myristoylated without the C-terminal region (mRec 2-190) and five variants of GCAP1, namely non-myristoylated (nmGCAP1), myristoylated (mGCAP1) and its retinal dystrophy-related mutants D100E, L151F and E89K. This comparative analysis allowed the investigation of the role of the N-terminal myristoylation in modulating the hydrodynamic variations of Rec and GCAP1 upon Ca^{2+}-binding. Moreover, the analysis of the effects of the C-terminal fragment of Rec and the point mutations of GCAP1 provided a comparative assessment of the sensitivity of the three experimental approaches. Indeed, while all three techniques measure the rearrangement of the water molecules belonging to the hydration shell of the proteins, DLS and SEC are solution techniques. The dextran-coated SPR chips instead mimic the physiological molecular crowding, which might affect structural and dynamical properties of protein hydration shell. For this project I performed DLS measurements and the relative data analysis, which highlighted a decrease of hydrodynamic diameter upon Ca^{2+}-binding for TnC, mGCAP1 and nmRec, or an increase, as was the case for CaM, mRec and nmGCAP1. These variations reflect the differences in hydrophobicity exhibited, for example, by apo and Ca^{2+}-bound Rec, where the increased exposure of hydrophobic surfaces upon Ca^{2+}-binding causes major rearrangements of the hydration shell. Interestingly, the presence of post-translational myristoylation had an opposite effect on the Ca^{2+}-dependent hydrodynamic size

variation of the two NCS Rec and GCAP1. By analyzing SPR, DLS and SEC measurements we could conclude that the change in the refractive index measured by SPR clearly correlated with the absolute value of the variation in the hydrodynamic size of the proteins. Moreover, this technique allowed to discriminate even small differences caused by point mutations in mGCAP1, providing further evidence of the sensibility of the approach and a fingerprint profile for each protein in conditions comparable to the physiological molecular crowding.

3.4 Paper 4: Structural effects of Mg^{2+} on the regulatory states of three neuronal calcium sensors operating in vertebrate phototransduction.

Marino V, Sulmann S, Koch KW, Dell'Orco D. *Biochim Biophys Acta*. **2015** Sep; *1853(9)*:2055-65. doi: 10.1016/j.bbamcr.2014.10.026.

Mg^{2+} is a divalent cation present in its free form at a concentration around 1 mM in photoreceptor cells [15] and it is involved in the regulation of several enzymes as well as a cofactor for ATP and GTP. The lack of major variations in the concentration of Mg^{2+} in photoreceptor cells led to the conclusion that it was not directly involved in the regulation of phototransduction cascade. NCS proteins though, are in principle capable to bind Mg^{2+} ions via the Ca^{2+}-binding EF-hands, especially when their Ca^{2+}-affinity is in the micromolar range. Therefore, in this project we investigated the effects that Mg^{2+} exerted on the structural properties of three NCS involved in phototransduction, namely GCAP1, GCAP2 and Rec, by means of CD and fluorescence spectroscopy, ITC and MD simulations. With the exception of the ITC measurements, all experimental and computational data were collected and analyzed by me. Rec was found to be slightly affected by Mg^{2+} in terms of secondary and tertiary structure, its physiological myristoyl switch was shown not to be triggered by Mg^{2+} ions, which in general mildly decreased the protein thermal stability with respect to the apo form. The secondary and tertiary structure of GCAP2 seemed to be affected by the presence of Mg^{2+}, ITC measurements allowed for the estimation of two binding sites, one with a physiologically relevant affinity of 320 uM and the other with a non-physiological affinity of 4.4 mM, similarly to what was previously reported for GCAP1. Nonetheless most of the investigations we performed on GCAP2 were intrinsically non reproducible, therefore suggesting that the role of the cation would be rather complex and possibly associated with different oligomeric states of GCAP2. GCAP1 was the most Mg^{2+}-affected NCS of this study, as both secondary and tertiary structures underwent small but significant changes in the presence of Mg^{2+}, which were known to be associated with

the activating form of the target GC. MD simulations highlighted the necessity of a Mg^{2+} ion in the EF2 motif for the stable and specific interaction with the target GC. Moreover they allowed us to identify a sequence of events that have to occur in order for GCAP1 to switch from the inhibiting to the activator state, namely the release of Ca^{2+} from EF4, the Ca^{2+}/Mg^{2+} exchange in EF2 and the release of Ca^{2+} from EF3.

3.5 Paper 5: Differential Nanosecond Protein Dynamics in Homologous Calcium Sensors.

Robin J, Brauer J, Sulmann S, Marino V, Dell'Orco D, Lienau C, Koch KW. *ACS Chem Biol*. **2015** Oct 16; *10(10)*:2344-52. doi: 10.1021/acschembio.5b00278.

GCAPs are able to specifically change conformation according to different Ca^{2+} concentrations triggering their switch from inhibitor to activator of the target GC. Here we studied the conformational dynamics of GCAP1 using the same approach that was successfully applied to investigate GCAP2 [142], that is time-resolved fluorescence spectroscopy. GCAP1 has 4 Cys residues located in different spatial regions, C18 and C29 belong to the entering helix of EF1 and are situated at the beginning and the end of the helix respectively, C106 is part of the Ca^{2+}-binding loop of EF3 and C125 lies in the loop connecting EF3 and EF4. To investigate in detail selected regions of the molecule, all but one Cys residues were mutated to Ala (CAAA, ACAA, AACA, AAAC), then the only remaining Cys residue was labelled with the fluorescent dye Alexa647 and subjected to the fluorescence studies. Fluorescence decay and anisotropy highlighted that C106 was the the most ion-affected residue in terms of increased lifetime and rotational correlation time. This implied a higher solvent exposure of C106 upon Ca^{2+} or Mg^{2+} dissociation, which was supported by the analysis of the diffusional dye motion. I collaborated to this project by running and analyzing all-atom Molecular Dynamics simulations in order to gain structural insights into the regions where the dye, which was not part of the simulations, would have been covalently bound. The increase of the distance between D168 and R178 (Figure 5), belonging respectively to the N-lobe (EF1 and EF2) and C-lobe (EF3 and EF4) highlighted a divergent motion of the lobes upon Ca^{2+}-binding. In addition, we identified three ideal planes representing EF1, EF3 and EF4 and monitored the amplitude of the angles between EF1-EF4 and EF3-EF4, resulting in a decrease of both angles upon Ca^{2+}-binding. Simulation derived data resulted to be in line with the experimentally deduced "twisted accordion" model of conformational dynamics, where Ca^{2+} induced the approach of two

lobes accompanied by the outward movement of the EF3 loop . This led to the conclusion that despite high structural similarity, NCS proteins are able to specifically recognize and regulate their target also thanks to peculiar protein dynamics.

3.6 Paper 6: Impact of cone dystrophy-related mutations in GCAP1 on a kinetic model of phototransduction.

Dell'Orco D, Sulmann S, Zägel P, Marino V, Koch KW. *Cell Mol Life Sci*. **2014** Oct; *71(19)*:3829-40. doi: 10.1007/s00018-014-1593-4.

In this study we investigated the effects that four GCAP1 mutants associated to Cone and Cone-Rod Dystrophies, namely E89K, D100E, L151F and G159V exerted on the structure and the functionality of the proteins, by means of CD spectroscopy, ITC and enzymatic assays. The experimental enzymatic parameters were then implemented in a previously published model of phototransduction in order to both predict the kinetics of the photoresponse in rod cells and to analyze the contribution of the other Ca^{2+}-sensor GCAP2 in shaping the cGMP synthesis. My contribution to this project consisted of the characterization of these mutants in terms of secondary and tertiary structure and their thermal stability, which were assessed by CD spectroscopy. All but E89K mutant showed small but significative differences in the CD spectra, both in the near and the far UV regions, in particular in the Ca^{2+} bound forms. E89K mutant instead exhibited major differences in the tertiary structure and a slight decrease of the thermal stability in the absence of Ca^{2+}. All data presented here allowed us to conclude that these mutants had a decreased catalytic efficiency with respect to that of the wild type, similarly to the Y99C mutant, for which electrophysiological recordings were available [55]. Therefore we were able to conclude that our photoresponse simulations were in line with experimental data, moreover we found a compensatory effect of GCAP2 in the regulation of the target GC, in line with the Ca^{2+}-relay model [35].

3.7 Paper 7: Two retinal dystrophy-associated missense mutations in GUCA1A with distinct molecular properties result in a similar aberrant regulation of the retinal guanylate cyclase.

Marino V, Scholten A, Koch KW, Dell'Orco D. *Hum Mol Genet.* **2015** Dec 1; *24(23)*:6653-66. doi: 10.1093/hmg/ddv370.

Here we presented a thorough characterization of the two recently found GCAP1 mutants I107T and L84F in spanish patients affected by Cone, Cone-Rod and Macular dystrophies, in terms of structure, thermal stability, Ca^{2+} affinity and functionality. These variants, which caused similar clinical phenotype, are in close proximity in terms of primary structure, but they belong to different lobes, indeed L84F is located at the end of the exiting helix of EF2, while I107T is a part of the Ca^{2+}-binding loop of EF3. With the exception of the enzymatic assays, all the experimental and computational data were collected and analyzed by me. CD spectroscopy highlighted a wild type-like secondary and tertiary structure for I107T, similar to those of the variants studied in **Paper 6**, while L84F exhibited a significantly different tertiary structure in the absence and in the presence of Ca^{2+} or Mg^{2+}. Both mutants showed three-phase thermal denaturation profiles in the absence of Ca^{2+} with decreased thermal stability with respect to the wild type, accompanied by an increase of the thermal stability in the Ca^{2+}-bound form, which was more pronounced for the L84F variation. Intrinsic Trp fluorescence approach was employed for the estimation of Ca^{2+} and Mg^{2+} affinity, highlighting that both mutants exhibited the same wild type-like biphasic behavior when switching from the apo to the Ca^{2+}-bound form. Interestingly, L84F variant showed that it could bind two Mg^{2+} ions at physiological Mg^{2+} concentration. While I107T showed a decreased Ca^{2+} affinity with respect to the wild type, similarly to most dystrophy related mutants [50], L84F surprisingly exhibited a wild-type like Ca^{2+} affinity and a positive cooperativity of binding in the presence of Mg^{2+}. Indeed it was possible to fit data from the chelator assay with a 2 or 3 binding site model without major differences in the macroscopic

binding constants, suggesting that probably EF2 was occupied by a Mg^{2+} ion and that Ca^{2+}-binding to EF3 increased Ca^{2+}-affinity in EF4. Molecular Dynamics simulations provided some mechanistic insights into the experimental evidences, highlighting that the higher thermal stability of the L84F variant was probably due to a tighter packing of the myristoyl moiety in the hydrophobic cleft, as shown by its lower solvent exposure. Moreover the EF3 Ca^{2+}-coordinating residues were found to be significantly less flexible in L84F mutant than the wild type in the Ca^{2+}-bound form, suggesting a long range intramolecular communication pathway between the myristoyl group and the C-lobe, in line with the previously described "myristoyl-tug" mechanism [39]. This suggested a deeper computational investigation of long-range allosteric mechanisms in GCAP1, which was performed in **Paper 9**. Despite all these structural and Ca^{2+}-affinity differences, both mutants exhibited functional features common to all other retinal dystrophy-related GCAP1 mutants and leading to a constitutive activation of the target GC. In conclusion, our data suggested that the alteration of intra-intermolecular communication mechanisms, rather than just the decreased Ca^{2+} affinity, could be responsible for the dysregulation of the GC by GCAP1 mutants associated with retinal dystrophies.

3.8 Paper 8: Dysfunction of cGMP signalling in photoreceptors by a macular dystrophy-related mutation in the calcium sensor GCAP1.

Vocke F, Weisschuh N, Marino V, Malfatti S, Jacobson SG, Reiff CM, Dell'Orco D, Koch KW. *Hum Mol Genet*. **2016** Dec 26. doi: 10.1093/hmg/ddw374.

In the last number of years an increasing number of retinal dystrophy-related GCAP1 mutants have been discovered. Here is the biochemical and biophysical characterization of the most recently identified L176F mutant by means of CD and fluorescence spectroscopy, DLS, enzymatic and chelator assays and Molecular Dynamics simulations. My contribution to this project consisted in the design and planning of CD and DLS experiments, as well as the running and analysis of MD simulations. Like the L84F mutant presented in **Paper 7**, L176F also didn't show any perturbations in its Ca^{2+}-affinity compared to the wild type, while it exhibited different tertiary structure, an increase in the hydrodynamic radius upon Ca^{2+} binding, higher affinity for the target GC and the highest activity of all mutants studied so far. The reason for this could be found in the intrinsic Trp fluorescence Mg^{2+} titrations, which showed 10 fold higher affinity for Mg^{2+} with respect to the wild type, meaning that probably this variant could bind 2 Mg^{2+} ions. To furtherly investigate this aspect we compared the trajectories resulting from MD simulations of the Ca^{2+}-loaded state as well as one/two Mg^{2+} ion-bound state of wild type GCAP1 and L176F variant. Results showed that not only the L176F variant was structurally more rigid than the wild type with two Mg^{2+} ions bound in EF2 and EF3, but also that the mutation had long-range allosteric effects on the distal EF4, which could explain the constitutive activation of the GC, at odds with the majority of the dystrophy-related variants, whose pathological mechanism was supposed to depend on the decreased Ca^{2+} affinity.

3.9 Paper 9: Allosteric communication pathways routed by Ca^{2+}/Mg^{2+} exchange in GCAP1 selectively switch target regulation modes.

Marino V, Dell'Orco D. *Sci Rep*. **2016** Oct 14; *6*:34277. doi: 10.1038/srep34277.

In this study we tried to shed some light on the mechanisms that allow GCAP1 to switch from activator to inhibitor of the target GC upon Mg^{2+}/Ca^{2+} exchange by running and analyzing five replicas of 200 ns all-atom Molecular Dynamics simulations. We therefore simulated the Ca^{2+}-loaded inhibiting state and the two possible activator states with Mg^{2+} bound to EF2 or EF2 and EF3, both with and without N-terminal myristoylation. In order to exhaustively sample the conformational space explored by MD simulations, we employed Principal Component Analysis (PCA)-based indexes to check the reproducibility and the consistency between replicas, such as cosine content, Root Mean Square Inner Product and PCA projections. All these combined indexes allowed us to consider the five replicas as one single 1 us consistent trajectory, which was then subjected to an analysis of the persistence of the noncovalent interactions between residues to generate a single Protein Structure Network (PSN) for each state representing the dynamic structural behavior. We then performed network analysis on each PSN to identify key residues with a high number of persistent interactions, finding that some hub residues like D100 or I143 were associated with retinal dystrophies mutations. To identify the preferential communication routes between EF-hands and the putative interface with the target GC, we created the Communication Robustness (CR) index that took into account the persistence threshold that generated the PSN, the number and the lenght of the shortest paths connecting selected residues according to the parsimony principle. The CR analysis was then performed on the residues of the putative GCAP1-GC interface and the representative Glu residues of each EF hand, finding that E38 and C29 were the most robustly communicating residues of the interface in specific states. We also analyzed the most probable pathways connecting the aforementioned residues with the EF-representative Glu residues using the Selective Betweenness index, which

allowed to highlight of specific intramolecular communication routes depending on the loading state of each EF-hand. Since the myristoyl group was found not to have many persistent interactions, we applied the CR criterion between the three functional EF-hands and compared the myristoylated and non myristoylated forms, finding that the acylic group was required in order to maintain the allosteric communication between EF2 and EF4, in line with the "myristoyl tug" mechanism [39]. In conclusion, our computational approach allowed us to understand that the switch between inhibitor and activator form of GCAP1 depended not only on the loading state of the EF-hands, but also on the intramolecular communication routes that transfer the information to the GCAP1-GC interface. Moreover, the identification of some hub residues as target of pathological mutations suggested that the dysregulation of the target GC could be due to the perturbation of the PSN, and therefore, of the communication routes. This led to the conclusion that this approach could be applied also to other NCS proteins to unveil intramolecular, and possibly intermolecular communication pathways.

Chapter 4

Conclusions

This thesis work combined experimental and computational techniques to investigate different aspects of structure-function relationship of Ca^{2+}-sensor proteins. In detail, the NCS GCAP1 was extensively studied both in health and disease conditions, from different standpoints: **Paper 4** deals with the structural determinants of the switch between its regulatory modes associated with Mg^{2+} and Ca^{2+} exchange and with the conformational effects of Mg^{2+} on other two NCS, namely GCAP2 and Rec. In **Paper 5** the Ca^{2+}/Mg^{2+} exchange of GCAP1 was investigated in terms of protein dynamics leading to the conformational switch from inhibitor to activator of the target GC. The structural and functional effects exerted by GCAP1 point mutations associated with retinal dystrophies are the subject of **Paper 6**, **Paper 7** and **Paper 8**. In particular, results from **Paper 7** and **Paper 8** highlighted a new perspective in GCAP1 pathological variants, that is that the molecular mechanism leading to the disease is not necessarily correlated to the decreased Ca^{2+}-affinity exhibited by some disease associated variants, but rather to the alteration of the intramolecular communication routes. This suggested the application of the PSN paradigm to MD simulations of GCAP1 as explained in **Paper 9**, in which the analysis of intramolecular communication pathways from the ion-binding sites to the target interface revealed long range allosteric communication routes specifically exhibited by the target-inhibiting and target-activating states. **Paper 3** is a comparative study of SEC, DLS and SPR techniques to investigate differences in hydrodynamic properties due to conformational changes upon Ca^{2+}-binding exhibited by Ca^{2+}-sensors, among which CaM, GCAP2 and different variants of GCAP1 and Rec. In this

work the sensitivity of SPR in detecting Ca^{2+}-induced conformational changes under molecular crowding conditions was assessed, indeed this approach has been proved to be able to discriminate even small conformational differences such as those associated with GCAP1 physiological states and its pathological mutants. Finally, **Paper 1** and **Paper 2** involve the suitability of liposome-based and CaF_2 NP-based nanodevices as Ca^{2+}-sensors carriers for potential nanomedical applications. Results from **Paper 1** show that liposomes preserved Rec physiological structural properties, while CaF_2 NP alter Rec conformation, impairing its Ca^{2+}-sensing ability. On the other hand, **Paper 2** suggests that the same CaF_2 NP preserve both CaM structure and functionality in terms of the ability to bind and regulate Gad target. Taken together, these papers indicate that CaF_2 exert protein-specific effects on Ca^{2+}-sensors, therefore suggesting further investigations. In conclusion, the combination of experimental and computational techniques provides a powerful framework for the investigation of structure/function relationship of Ca^{2+}-sensor proteins. Such approaches revealed themselves particularly useful for gaining multiscale insights into the molecular mechanisms leading to physiological processes, as well as their dysregulation associated to single residue mutations. Indeed, the biochemical and biophysical characterization of several GCAP1 variants highlighted similar clinical phenotypes in spite of different molecular properties, suggesting an association with the alteration of the intramolecular communication network. In this respect, the future application of the computational approach presented in **Paper 9** to GCAP1 variants may be helpful in identifying common patterns between dysfunctional communication networks. This could potentially provide the structural information needed to design compounds interfering with the inter/intramolecular interaction network of GCAP1, in order to restore the physiological regulation of the target enzyme GC.

Bibliography

[1] Calcium signalling: dynamics, homeostasis and remodelling. Berridge MJ, Bootman MD, Roderick HL. Nat Rev Mol Cell Biol. 2003 Jul;4(7):517-29.

[2] Local calcium signaling in neurons. Augustine GJ, Santamaria F, Tanaka K. Neuron. 2003 Oct 9;40(2):331-46.

[3] Calcium-binding proteins. Kretsinger RH. Annu Rev Biochem. 1976;45:239-66.

[4] The C2 domain calcium-binding motif: structural and functional diversity. Nalefski EA, Falke JJ. Protein Sci. 1996 Dec;5(12):2375-90.

[5] Identification of a novel calcium binding motif based on the detection of sequence insertions in the animal peroxidase domain of bacterial proteins. Santamaría-Hernando S, Krell T, Ramos-González MI. PLoS One. 2012;7(7):e40698.

[6] Key residues involved in calcium-binding motifs in EGF-like domains. Handford PA, Mayhew M, Baron M, Winship PR, Campbell ID, Brownlee GG. Nature. 1991 May 9;351(6322):164-7.

[7] Solution structure of a type I dockerin domain, a novel prokaryotic, extracellular calcium-binding domain. Lytle BL, Volkman BF, Westler WM, Heckman MP, Wu JH. J Mol Biol. 2001 Mar 30;307(3):745-53.

[8] Cadherins: a molecular family important in selective cell-cell adhesion. Takeichi M. Annu Rev Biochem. 1990;59:237-52.

[9] The S100 protein family. Kligman D, Hilt DC. Trends Biochem Sci. 1988 Nov;13(11):437-43.

[10] The EF-hand family of calcium-modulated proteins. Persechini A, Moncrief ND, Kretsinger RH. Trends Neurosci. 1989 Nov;12(11):462-7.

[11] Evolution of EF-hand calcium-modulated proteins. II. Domains of several subfamilies have diverse evolutionary histories. Nakayama S, Moncrief ND, Kretsinger RH. J Mol Evol. 1992 May;34(5):416-48.

[12] http://prosite.expasy.org/prosite.html

[13] Structures and metal-ion-binding properties of the Ca2+-binding helix-loop-helix EF-hand motifs. Gifford JL, Walsh MP, Vogel HJ. Biochem J. 2007 Jul 15;405(2):199-221.

[14] Regulation of cellular magnesium. Romani AM, Scarpa A. Front Biosci. 2000 Aug 1;5:D720-34.

[15] Free magnesium concentration in salamander photoreceptor outer segments. Chen C, Nakatani K, Koutalos Y. J Physiol. 2003 Nov 15;553(Pt 1):125-35.

[16] Structural analysis, identification, and design of calcium-binding sites in proteins. Yang W, Lee HW, Hellinga H, Yang JJ. Proteins. 2002 May 15;47(3):344-56.

[17] Structural coupling of the EF hand and C-terminal GTPase domains in the mitochondrial protein Miro. Klosowiak JL, Focia PJ, Chakravarthy S, Landahl EC, Freymann DM, Rice SE. EMBO Rep. 2013 Nov;14(11):968-74.

[18] Calcium Binding Proteins. Permyakov E, Kretsinger RH. Wiley 2011

[19] Crystal structure of a high-affinity variant of rat alpha-parvalbumin. Lee YH, Tanner JJ, Larson JD, Henzl MT. Biochemistry. 2004 Aug 10;43(31):10008-17.

[20] Metal ion binding properties and conformational states of calcium- and integrin-binding protein. Yamniuk AP, Nguyen LT, Hoang TT, Vogel HJ. Biochemistry. 2004 Mar 9;43(9):2558-68.

[21] Effects of Ca2+, Mg2+, and myristoylation on guanylyl cyclase activating protein 1 structure and stability. Lim S, Peshenko I, Dizhoor A, Ames JB. Biochemistry. 2009 Feb 10;48(5):850-62.

[22] Biochemical and biophysical characterization of a plant calmodulin: Role of the N- and C-lobes in calcium binding, conformational change, and target interaction. Astegno A, La Verde V, Marino V, Dell'Orco D, Dominici P. Biochim Biophys Acta. 2016 Mar;1864(3):297-307.

[23] Neuronal calcium sensor proteins: generating diversity in neuronal Ca2+ signalling. Burgoyne RD. Nat Rev Neurosci. 2007 Mar;8(3):182-93.

[24] Sense and specificity in neuronal calcium signalling. Burgoyne RD, Haynes LP. Biochim Biophys Acta. 2015 Sep;1853(9):1921-32.

[25] Neuronal Calcium Sensor Proteins. Philippov P, Koch KW. Nova Biomedical 2006.

[26] Current status of pluripotent stem cells: moving the first therapies to the clinic. Kimbrel EA, Lanza R. Nat Rev Drug Discov. 2015 Oct;14(10):681-92.

[27] Structural diversity of neuronal calcium sensor proteins and insights for activation of retinal guanylyl cyclase by GCAP1. Lim S, Dizhoor AM, Ames JB. Front Mol Neurosci. 2014 Mar 17;7:19.

[28] Phototransduction in vertebrate rods and cones: molecular mechanisms of amplification, recovery and light adaptation. Pugh EN Jr, Lamb TD. In: Stavenga DG, DeGrip WJ, Pugh EN Jr (eds) Handbook of biological physics, vol 3. Elsevier Science BV, Amsterdam, pp 183–255 2000

[29] Ca(2+)-modulated vision-linked ROS-GC guanylate cyclase transduction machinery. Koch KW, Duda T, Sharma RK. Mol Cell Biochem. 2010 Jan;334(1-2):105-15.

[30] Mg2+/Ca2+ cation binding cycle of guanylyl cyclase activating proteins (GCAPs): role in regulation of photoreceptor guanylyl cyclase. Dizhoor AM,

Olshevskaya EV, Peshenko IV. Mol Cell Biochem. 2010 Jan;334(1-2):117-24.

[31] Ca2+-dependent control of rhodopsin phosphorylation: recoverin and rhodopsin kinase. Senin II, Koch KW, Akhtar M, Philippov PP. Adv Exp Med Biol. 2002;514:69-99.

[32] Structure and Function of Rod and Cone Photoreceptors. Jeannie Chen, Alapakkam P. Sampath, in Retina (Fifth Edition), 2013.

[33] Molecular structure and target recognition of neuronal calcium sensor proteins. Ames JB, Lim S. Biochim Biophys Acta. 2012 Aug;1820(8):1205-13. doi: 10.1016/j.bbagen.2011.10.003.

[34] Regulation of photoreceptor membrane guanylyl cyclases by guanylyl cyclase activator proteins. Dizhoor AM, Hurley JB. Methods. 1999 Dec;19(4):521-31.

[35] A calcium-relay mechanism in vertebrate phototransduction. Koch KW, Dell'orco D. ACS Chem Neurosci. 2013 Jun 19;4(6):909-17.

[36] Photoreceptor specific guanylate cyclases in vertebrate phototransduction. Koch KW, Duda T, Sharma RK. Mol Cell Biochem. 2002 Jan;230(1-2):97-106.

[37] Stabilizing function for myristoyl group revealed by the crystal structure of a neuronal calcium sensor, guanylate cyclase-activating protein 1. Stephen R, Bereta G, Golczak M, Palczewski K, Sousa MC. Structure. 2007 Nov;15(11):1392-402.

[38] Structure of Guanylyl Cyclase Activator Protein 1 (GCAP1) Mutant V77E in a Ca2+-free/Mg2+-bound Activator State. Lim S, Peshenko IV, Olshevskaya EV, Dizhoor AM, Ames JB. J Biol Chem. 2016 Feb 26;291(9):4429-41.

[39] Calcium-myristoyl Tug is a new mechanism for intramolecular tuning of calcium sensitivity and target enzyme interaction for guanylyl cyclase-activating

protein 1: dynamic connection between N-fatty acyl group and EF-hand controls calcium sensitivity. Peshenko IV, Olshevskaya EV, Lim S, Ames JB, Dizhoor AM. J Biol Chem. 2012 Apr 20;287(17):13972-84.

[40] Effects of Ca2+, Mg2+, and myristoylation on guanylyl cyclase activating protein 1 structure and stability. Lim S, Peshenko I, Dizhoor A, Ames JB. Biochemistry. 2009 Feb 10;48(5):850-62.

[41] Involvement of the calcium sensor GCAP1 in hereditary cone dystrophies. Behnen P, Dell'Orco D, Koch KW. Biol Chem. 2010 Jun;391(6):631-7.

[42] Genes and mutations in autosomal dominant cone and cone-rod dystrophy.Kohl S, Kitiratschky V, Papke M, Schaich S, Sauer A, Wissinger B.Adv Exp Med Biol. 2012;723:337-43.

[43] Ca(2+)-binding proteins in the retina: from discovery to etiology of human disease. Sokal I, Li N, Verlinde CL, Haeseleer F, Baehr W, Palczewski K. Biochim Biophys Acta. 2000 Dec 20;1498(2-3):233-51.

[44] Autosomal dominant cone and cone-rod dystrophy with mutations in the guanylate cyclase activator 1A gene-encoding guanylate cyclase activating protein-1. Downes SM, Holder GE, Fitzke FW, Payne AM, Warren MJ, Bhattacharya SS, Bird AC. Arch Ophthalmol. 2001 Jan;119(1):96-105.

[45] GCAP1 (Y99C) mutant is constitutively active in autosomal dominant cone dystrophy. Sokal I, Li N, Surgucheva I, Warren MJ, Payne AM, Bhattacharya SS, Baehr W, Palczewski K. Mol Cell. 1998 Jul;2(1):129-33.

[46] A novel GCAP1 missense mutation (L151F) in a large family with autosomal dominant cone-rod dystrophy (adCORD). Sokal I, Dupps WJ, Grassi MA, Brown J Jr, Affatigato LM, Roychowdhury N, Yang L, Filipek S, Palczewski K, Stone EM, Baehr W. Invest Ophthalmol Vis Sci. 2005 Apr;46(4):1124-32.

[47] A novel mutation (I143NT) in guanylate cyclase-activating protein 1 (GCAP1) associated with autosomal dominant cone degeneration. Nishiguchi KM, Sokal I, Yang L, Roychowdhury N, Palczewski K, Berson

EL, Dryja TP, Baehr W. Invest Ophthalmol Vis Sci. 2004 Nov;45(11):3863-70.

[48] Disease progression in autosomal dominant cone-rod dystrophy caused by a novel mutation (D100G) in the GUCA1A gene. Nong E, Lee W, Merriam JE, Allikmets R, Tsang SH. Doc Ophthalmol. 2014 Feb;128(1):59-67.

[49] Novel GUCA1A mutations suggesting possible mechanisms of pathogenesis in cone, cone-rod, and macular dystrophy patients. Kamenarova K, Corton M, García-Sandoval B, Fernández-San Jose P, Panchev V, Avila-Fernández A, López-Molina MI, Chakarova C, Ayuso C, Bhattacharya SS. Biomed Res Int. 2013;2013:517570.

[50] Calcium binding, structural stability and guanylate cyclase activation in GCAP1 variants associated with human cone dystrophy. Dell'Orco D, Behnen P, Linse S, Koch KW. Cell Mol Life Sci. 2010 Mar;67(6):973-84.

[51] Constitutive activation of photoreceptor guanylate cyclase by Y99C mutant of GCAP-1. Possible role in causing human autosomal dominant cone degeneration. Dizhoor AM, Boikov SG, Olshevskaya EV. J Biol Chem. 1998 Jul 10;273(28):17311-4.

[52] Mutations in the GUCA1A gene involved in hereditary cone dystrophies impair calcium-mediated regulation of guanylate cyclase. Kitiratschky VB, Behnen P, Kellner U, Heckenlively JR, Zrenner E, Jägle H, Kohl S, Wissinger B, Koch KW. Hum Mutat. 2009 Aug;30(8):E782-96.

[53] Identification and functional consequences of a new mutation (E155G) in the gene for GCAP1 that causes autosomal dominant cone dystrophy. Wilkie SE, Li Y, Deery EC, Newbold RJ, Garibaldi D, Bateman JB, Zhang H, Lin W, Zack DJ, Bhattacharya SS, Warren MJ, Hunt DM, Zhang K. Am J Hum Genet. 2001 Sep;69(3):471-80.

[54] Novel GUCA1A mutation identified in a Chinese family with cone-rod dystrophy. Huang L, Li S, Xiao X, Jia X, Sun W, Gao Y, Li L, Wang P, Guo X, Zhang Q. Neurosci Lett. 2013 Apr 29;541:179-83.

[55] The Y99C mutation in guanylyl cyclase-activating protein 1 increases intracellular Ca2+ and causes photoreceptor degeneration in transgenic mice. Olshevskaya EV, Calvert PD, Woodruff ML, Peshenko IV, Savchenko AB, Makino CL, Ho YS, Fain GL, Dizhoor AM. J Neurosci. 2004 Jul 7;24(27):6078-85.

[56] Molecular mechanics of calcium-myristoyl switches. Ames JB, Ishima R, Tanaka T, Gordon JI, Stryer L, Ikura M. Nature. 1997 Sep 11;389(6647):198-202.

[57] Sequestration of the membrane-targeting myristoyl group of recoverin in the calcium-free state. Tanaka T, Ames JB, Harvey TS, Stryer L, Ikura M. Nature. 1995 Aug 3;376(6539):444-7.

[58] Pathological roles of recoverin in cancer-associated retinopathy. Ohguro H, Nakazawa M. Adv Exp Med Biol. 2002;514:109-24.

[59] Recoverin-associated retinopathy: a clinically and immunologically distinctive disease. Whitcup SM, Vistica BP, Milam AH, Nussenblatt RB, Gery I. Am J Ophthalmol. 1998 Aug;126(2):230-7.

[60] Calmodulin: a prototypical calcium sensor. Chin D, Means AR. Trends Cell Biol. 2000 Aug;10(8):322-8.

[61] Calcium signaling: a tale for all seasons. Carafoli E. Proc Natl Acad Sci U S A. 2002 Feb 5;99(3):1115-22.

[62] Novel aspects of calmodulin target recognition and activation. Vetter SW, Leclerc E. Eur J Biochem. 2003 Feb;270(3):404-14.

[63] Structure of calmodulin refined at 2.2 A resolution. Babu YS, Bugg CE, Cook WJ. J Mol Biol. 1988 Nov 5;204(1):191-204.

[64] Solution structure of calmodulin bound to the target peptide of endothelial nitric oxide synthase phosphorylated at Thr495. Piazza M, Taiakina V, Guillemette SR, Guillemette JG, Dieckmann T. Biochemistry. 2014 Mar 4;53(8):1241-9.

[65] Solution structure of calcium-free calmodulin. Kuboniwa H, Tjandra N, Grzesiek S, Ren H, Klee CB, Bax A. Nat Struct Biol. 1995 Sep;2(9):768-76.

[66] Genetic polymorphism and protein conformational plasticity in the calmodulin superfamily: two ways to promote multifunctionality. Ikura M, Ames JB. Proc Natl Acad Sci U S A. 2006 Jan 31;103(5):1159-64.

[67] Structural basis for calmodulin as a dynamic calcium sensor. Zhang M, Abrams C, Wang L, Gizzi A, He L, Lin R, Chen Y, Loll PJ, Pascal JM, Zhang JF. Structure. 2012 May 9;20(5):911-23.

[68] The ever changing moods of calmodulin: how structural plasticity entails transductional adaptability. Villarroel A, Taglialatela M, Bernardo-Seisdedos G, Alaimo A, Agirre J, Alberdi A, Gomis-Perez C, Soldovieri MV, Ambrosino P, Malo C, Areso P. J Mol Biol. 2014 Jul 29;426(15):2717-35.

[69] The many faces of calmodulin in cell proliferation, programmed cell death, autophagy, and cancer. Berchtold MW, Villalobo A. Biochim Biophys Acta. 2014 Feb;1843(2):398-435.

[70] Calmodulin levels in blood cells as a potential biomarker of Alzheimer's disease. Esteras N, Alquézar C, de la Encarnación A, Villarejo A, Bermejo-Pareja F, Martín-Requero A. Alzheimers Res Ther. 2013 Nov 7;5(6):55.

[71] Calmodulin mutations associated with recurrent cardiac arrest in infants. Crotti L, Johnson CN, Graf E, De Ferrari GM, Cuneo BF, Ovadia M, Papagiannis J, Feldkamp MD, Rathi SG, Kunic JD, Pedrazzini M, Wieland T, Lichtner P, Beckmann BM, Clark T, Shaffer C, Benson DW, Kääb S, Meitinger T, Strom TM, Chazin WJ, Schwartz PJ, George AL Jr. Circulation. 2013 Mar 5;127(9):1009-17.

[72] Mutations in calmodulin cause ventricular tachycardia and sudden cardiac death. Nyegaard M, Overgaard MT, Søndergaard MT, Vranas M, Behr ER, Hildebrandt LL, Lund J, Hedley PL, Camm AJ, Wettrell G, Fosdal I, Christiansen M, Børglum AD. Am J Hum Genet. 2012 Oct 5;91(4):703-12.

[73] Calmodulin mutations associated with long QT syndrome prevent inactivation of cardiac L-type Ca(2+) currents and promote proarrhythmic behavior in ventricular myocytes. Limpitikul WB, Dick IE, Joshi-Mukherjee R, Overgaard MT, George AL Jr, Yue DT. J Mol Cell Cardiol. 2014 Sep;74:115-24.

[74] Calmodulin mutations causing catecholaminergic polymorphic ventricular tachycardia confer opposing functional and biophysical molecular changes. Søndergaard MT, Sorensen AB, Skov LL, Kjaer-Sorensen K, Bauer MC, Nyegaard M, Linse S, Oxvig C, Overgaard MT. FEBS J. 2015 Feb;282(4):803-16

[75] Specific Protein Therapy. Henderson VE. Can Med Assoc J. 1922 Nov;12(11):821.

[76] The potential environmental impact of engineered nanomaterials. Colvin VL. Nat Biotechnol. 2003 Oct;21(10):1166-70.

[77] Upconversion luminescence of monodisperse CaF2:Yb(3+)/Er(3+) nanocrystals. Wang G, Peng Q, Li Y. J Am Chem Soc. 2009 Oct 14;131(40):14200-1.

[78] NIR-to-NIR two-photon excited CaF2:Tm3+,Yb3+ nanoparticles: multifunctional nanoprobes for highly penetrating fluorescence bio-imaging. Dong NN, Pedroni M, Piccinelli F, Conti G, Sbarbati A, Ramírez-Hernández JE, Maestro LM, Iglesias-de la Cruz MC, Sanz-Rodriguez F, Juarranz A, Chen F, Vetrone F, Capobianco JA, Solé JG, Bettinelli M, Jaque D, Speghini A. ACS Nano. 2011 Nov 22;5(11):8665-71.

[79] Lanthanide doped upconverting colloidal CaF_2 nanoparticles prepared by a single-step hydrothermal method: toward efficient materials with near infrared-to-near infrared upconversion emission. Pedroni M, Piccinelli F, Passuello T, Giarola M, Mariotto G, Polizzi S, Bettinelli M, Speghini A. Nanoscale. 2011 Apr;3(4):1456-60.

[80] Effective delivery of recombinant proteins to rod photoreceptors via lipid nanovesicles. Asteriti S, Dal Cortivo G, Pontelli V, Cangiano L, Buffelli M, Dell'Orco D. Biochem Biophys Res Commun. 2015 Jun 12;461(4):665-70.

[81] Upconverting luminescent nanomaterials: application to in vivo bioimaging. Hilderbrand SA, Shao F, Salthouse C, Mahmood U, Weissleder R. Chem Commun (Camb). 2009 Jul 28;(28):4188-90.

[82] Structural changes in apolipoproteins bound to nanoparticles. Cukalevski R, Lundqvist M, Oslakovic C, Dahlbäck B, Linse S, Cedervall T. Langmuir. 2011 Dec 6;27(23):14360-9.

[83] Protein structural changes induced by glutathione-coated CdS quantum dots as revealed by Trp phosphorescence. Gabellieri E, Cioni P, Balestreri E, Morelli E. Eur Biophys J. 2011 Nov;40(11):1237-45.

[84] How do proteins unfold upon adsorption on nanoparticle surfaces? Pan H, Qin M, Meng W, Cao Y, Wang W. Langmuir. 2012 Sep 4;28(35):12779-87.

[85] Strategies for production of active eukaryotic proteins in bacterial expression system. Khow O, Suntrarachun S. Asian Pac J Trop Biomed. 2012 Feb;2(2):159-62.

[86] Recombinant protein expression in Escherichia coli: advances and challenges. Rosano GL, Ceccarelli EA. Front Microbiol. 2014 Apr 17;5:172.

[87] Strategies to optimize protein expression in E. coli. Francis DM, Page R. Curr Protoc Protein Sci. 2010 Aug;Chapter 5:Unit 5.24.1-29.

[88] Use of bacteriophage T7 RNA polymerase to direct selective high-level expression of cloned genes. Studier FW, Moffatt BA. J Mol Biol. 1986 May 5;189(1):113-30.

[89] Protein production and purification. Structural Genomics Consortium.; China Structural Genomics Consortium.; Northeast Structural Genomics Consortium., Gräslund S, Nordlund P, Weigelt J, Hallberg BM, Bray J, Gileadi O,

Knapp S, Oppermann U, Arrowsmith C, Hui R, Ming J, dhe-Paganon S, Park HW, Savchenko A, Yee A, Edwards A, Vincentelli R, Cambillau C, Kim R, Kim SH, Rao Z, Shi Y, Terwilliger TC, Kim CY, Hung LW, Waldo GS, Peleg Y, Albeck S, Unger T, Dym O, Prilusky J, Sussman JL, Stevens RC, Lesley SA, Wilson IA, Joachimiak A, Collart F, Dementieva I, Donnelly MI, Eschenfeldt WH, Kim Y, Stols L, Wu R, Zhou M, Burley SK, Emtage JS, Sauder JM, Thompson D, Bain K, Luz J, Gheyi T, Zhang F, Atwell S, Almo SC, Bonanno JB, Fiser A, Swaminathan S, Studier FW, Chance MR, Sali A, Acton TB, Xiao R, Zhao L, Ma LC, Hunt JF, Tong L, Cunningham K, Inouye M, Anderson S, Janjua H, Shastry R, Ho CK, Wang D, Wang H, Jiang M, Montelione GT, Stuart DI, Owens RJ, Daenke S, Schütz A, Heinemann U, Yokoyama S, Büssow K, Gunsalus KC. Nat Methods. 2008 Feb;5(2):135-46.

[90] HPLC and FPLC. Recent progress in the use of automated chromatography systems for resolution of pancreatic secretory proteins. Göke B, Keim V. Int J Pancreatol. 1992 Apr;11(2):109-16.

[91] Production of recombinant plant calmodulin and its use to detect calmodulin-binding proteins. Liao B, Zielinski RE. Methods Cell Biol. 1995;49:487-500.

[92] Senin II, Fischer T, Komolov KE, Zinchenko DV, Philippov PP, Koch KW (2002) Ca^{2+}-Myristoyl Switch in the Neuronal Calcium Sensor Recoverin requires different function of Ca^{2+}-binding sites, The Journal of Biological Chemistry 277(52):50365-50372

[93] Identification of a domain in guanylyl cyclase-activating protein 1 that interacts with a complex of guanylyl cyclase and tubulin in photoreceptors. Schrem A, Lange C, Beyermann M, Koch KW. J Biol Chem. 1999 Mar 5;274(10):6244-9.

[94] Biomolecular studies by circular dichroism.Dodero VI, Quirolo ZB, Sequeira MA.Front Biosci (Landmark Ed). 2011 Jan 1;16:61-73.

[95] Structural characterization of recombinant therapeutic proteins by circular dichroism. Bertucci C, Pistolozzi M, De Simone A. Curr Pharm Biotechnol. 2011 Oct;12(10):1508-16.

[96] How to study proteins by circular dichroism. Kelly SM, Jess TJ, Price NC. Biochim Biophys Acta. 2005 Aug 10;1751(2):119-39.

[97] Circular Dichroism: Principles and Applications. Berova N, Nakanishi K, Woody RW. Wiley-VCH 2000, 877 pp.

[98] Evaluation of secondary structure of proteins from UV circular dichroism spectra using an unsupervised learning neural network. Andrade MA, Chacón P, Merelo JJ, Morán F. Protein Eng. 1993 Jun;6(4):383-90.

[99] Estimation of globular protein secondary structure from circular dichroism. Provencher SW, Glöckner J. Biochemistry. 1981 Jan 6;20(1):33-7.

[100] DICHROWEB: an interactive website for the analysis of protein secondary structure from circular dichroism spectra. Lobley A, Whitmore L, Wallace BA. Bioinformatics. 2002 Jan;18(1):211-2.

[101] DICHROWEB, an online server for protein secondary structure analyses from circular dichroism spectroscopic data. Whitmore L, Wallace BA. Nucleic Acids Res. 2004 Jul 1;32(Web Server issue):W668-73.

[102] [Uber den mechanisms des photolumineszenz von Farbstoffphosphore. Jäblonski A. Z Phys. 94 (1935), pp. 38–46

[103] Fluorescence studies of nucleotides and polynucleotides. I. Formycin, 2-aminopurine riboside, 2,6-diaminopurine riboside, and their derivatives. Ward DC, Reich E, Stryer L. J Biol Chem. 1969 Mar 10;244(5):1228-37.

[104] Fluorescence studies of DNA and RNA structure and dynamics. Millar DP. Curr Opin Struct Biol. 1996 Jun;6(3):322-6.

[105] Application of fluorescence spectroscopy for determining the structure and function of proteins. Jiskoot W, Hlady V, Naleway JJ, Herron JN. Pharm Biotechnol. 1995;7:1-63.

[106] Ultraviolet fluorescence of the aromatic amino acids. Teale FW, Weber G. Biochem J. 1957 Mar;65(3):476-82.

[107] Fluorescence technologies for monitoring interactions between biological molecules in vitro. Deshayes S, Divita G. Prog Mol Biol Transl Sci. 2013;113:109-43

[108] Principles of Fluorescence Spectroscopy. Lakowicz JR. Springer 2006

[109] Toward understanding tryptophan fluorescence in proteins. Chen Y, Barkley MD. Biochemistry. 1998 Jul 14;37(28):9976-82.

[110] Fatty acid binding to plasma albumin. Spector AA. J Lipid Res. 1975 May;16(3):165-79.

[111] Mechanisms of tryptophan fluorescence shifts in proteins. Vivian JT, Callis PR. Biophys J. 2001 May;80(5):2093-109.

[112] Monitoring protein interactions and dynamics with solvatochromic fluorophores. Loving GS, Sainlos M, Imperiali B. Trends Biotechnol. 2010 Feb;28(2):73-83.

[113] Fluorescence-polarization spectrum and electronic-energy transfer in tyrosine, tryptophan and related compounds. Weber G. Biochem J. 1960 May;75:335-45.

[114] Homogeneous fluorescence readouts for miniaturized high-throughput screening: theory and practice. Pope AJ, Haupts UM, Moore KJ. Drug Discov Today. 1999 Aug;4(8):350-362.

[115] Dynamic light scattering of biopolymers and biocolloids. Schurr JM. CRC Crit Rev Biochem. 1977 Nov;4(4):371-431.

[116] Making sense of Brownian motion: colloid characterization by dynamic light scattering. Hassan PA, Rana S, Verma G. Langmuir. 2015 Jan 13;31(1):3-12.

[117] Dynamic light scattering studies of internal motions in DNA. II. Clean viral DNAs. Thomas JC, Allison SA, Schurr JM, Holder RD. Biopolymers. 1980 Aug;19(8):1451-74.

[118] Dynamic light scattering studies of ribonuclease. Wang CC, Cook KH, Pecora R. Biophys Chem. 1980 Jun;11(3-4):439-42.

[119] Dynamic light scattering as a relative tool for assessing the molecular integrity and stability of monoclonal antibodies. Nobbmann U, Connah M, Fish B, Varley P, Gee C, Mulot S, Chen J, Zhou L, Lu Y, Shen F, Yi J, Harding SE. Biotechnol Genet Eng Rev. 2007;24:117-28.

[120] Dynamic light scattering measurement of nanometer particles in liquids. Pecora R. J Nanopart Res. 2000 2:123-131

[121] Particle Size Analysis - Photon Correlation Spectroscopy; International Standard ISO 13321:1996(E); International Standards Organization: Geneva, Switzerland, 1996.

[122] Analysis of Macromolecular Polydispersity in Intensity Correlation Spectroscopy: The Method of Cumulants. Koppel DE. J.Chem. Phys.1972,57, 4814-4820.

[123] Calcium binding to proteins studied via competition with chromophoric chelators. Linse S. Methods Mol Biol. 2002;173:15-24.

[124] Measurement of Ca2+-binding constants of proteins and presentation of the CaLigator software. André I, Linse S. Anal Biochem. 2002 Jun 15;305(2):195-205.

[125] Los Alamos report LA-1940. Fermi E, Pasta J, Ulam S. 1955

[126] Studies in Molecular Dynamics. I. General Method. Alder BJ, Wainwright TE. J. Chem. Phys. 1959 31 (2): 459.

[127] Computer simulation of protein folding. Levitt M, Warshel A. Nature. 1975 Feb 27;253(5494):694-8.

[128] Dynamics of folded proteins. McCammon JA, Gelin BR, Karplus M. Nature. 1977 Jun 16;267(5612):585-90.

[129] The birth of computational structural biology. Levitt M. Nat Struct Biol. 2001 May;8(5):392-3.

[130] GROMACS 4: Algorithms for Highly Efficient, Load-Balanced, and Scalable Molecular Simulation. Hess B, Kutzner C, van der Spoel D, Lindahl E. J Chem Theory Comput. 2008 Mar;4(3):435-47.

[131] CHARMM: the biomolecular simulation program. Brooks BR, Brooks CL 3rd, Mackerell AD Jr, Nilsson L, Petrella RJ, Roux B, Won Y, Archontis G, Bartels C, Boresch S, Caflisch A, Caves L, Cui Q, Dinner AR, Feig M, Fischer S, Gao J, Hodoscek M, Im W, Kuczera K, Lazaridis T, Ma J, Ovchinnikov V, Paci E, Pastor RW, Post CB, Pu JZ, Schaefer M, Tidor B, Venable RM, Woodcock HL, Wu X, Yang W, York DM, Karplus M. J Comput Chem. 2009 Jul 30;30(10):1545-614.

[132] The Amber biomolecular simulation programs. Case DA, Cheatham TE 3rd, Darden T, Gohlke H, Luo R, Merz KM Jr, Onufriev A, Simmerling C, Wang B, Woods RJ. J Comput Chem. 2005 Dec;26(16):1668-88.

[133] Essential dynamics of proteins. Amadei A, Linssen AB, Berendsen HJ. Proteins. 1993 Dec;17(4):412-25.

[134] Convergence of sampling in protein simulations. Hess B. Phys Rev E Stat Nonlin Soft Matter Phys. 2002 Mar;65(3 Pt 1):031910.

[135] On the convergence of the conformational coordinates basis set obtained by the essential dynamics analysis of proteins' molecular dynamics simulations. Amadei A, Ceruso MA, Di Nola A. Proteins. 1999 Sep 1;36(4):419-24.

[136] Intra and inter-molecular communications through protein structure network. Vishveshwara S, Ghosh A, Hansia P. Curr Protein Pept Sci. 2009 Apr;10(2):146-60.

[137] Small-world communication of residues and significance for protein dynamics. Atilgan AR, Akan P, Baysal C. Biophys J. 2004 Jan;86(1 Pt 1):85-91.

[138] Small-world view of the amino acids that play a key role in protein folding. Vendruscolo M, Dokholyan NV, Paci E, Karplus M. Phys Rev E Stat Nonlin Soft Matter Phys. 2002 Jun;65(6 Pt 1):061910.

[139] PyInteraph: a framework for the analysis of interaction networks in structural ensembles of proteins. Tiberti M, Invernizzi G, Lambrughi M, Inbar Y, Schreiber G, Papaleo E. J Chem Inf Model. 2014 May 27;54(5):1537-51.

[140] Two pathways mediate interdomain allosteric regulation in pin1. Guo J, Pang X, Zhou HX. Structure. 2015 Jan 6;23(1):237-47.

[141] Integrating atomistic molecular dynamics simulations, experiments, and network analysis to study protein dynamics: strength in unity. Papaleo E. Front Mol Biosci. 2015 May 27;2:28.

[142] Probing the Ca(2+) switch of the neuronal Ca(2+) sensor GCAP2 by time-resolved fluorescence spectroscopy. Kollmann H, Becker SF, Shirdel J, Scholten A, Ostendorp A, Lienau C, Koch KW. ACS Chem Biol. 2012 Jun 15;7(6):1006-14.

Nanoscale

PAPER

Nanodevice-induced conformational and functional changes in a prototypical calcium sensor protein†

Cite this: *Nanoscale*, 2014, **6**, 412

Valerio Marino,[a] Alessandra Astegno,[b] Marco Pedroni,[bc] Fabio Piccinelli[bc] and Daniele Dell'Orco*[ad]

Calcium (Ca^{2+}) plays a major role in a variety of cellular processes. Fine changes in its concentration are detected by calcium sensor proteins, which adopt specific conformations to regulate their molecular targets. Here, two distinct nanodevices were probed as biocompatible carriers of Ca^{2+}-sensors and the structural and functional effects of protein–nanodevice interactions were investigated. The prototypical Ca^{2+}-sensor recoverin (Rec) was incubated with 20–25 nm CaF_2 nanoparticles (NPs) and 70–80 nm liposomes with lipid composition similar to that found in photoreceptor cells. Circular dichroism and fluorescence spectroscopy were used to characterize changes in the protein secondary and tertiary structure and in thermal stability upon interaction with the nanodevice, both in the presence and in the absence of free Ca^{2+}. Variations in the hydrodynamic diameter of the complex were measured by dynamic light scattering and the residual capability of the protein to act as a Ca^{2+}-sensor in the presence of NPs was estimated spectroscopically. The conformation, thermal stability and Ca^{2+}-sensing capability of Rec were all significantly affected by the presence of NPs, while liposomes did not significantly perturb Rec conformation and function, allowing reversible binding. NP-bound Rec maintained an all-helical fold but showed lower thermal stability and high cooperativity of unfolding. Our analysis can be proficiently used to validate the biocompatibility of other nanodevices intended for biomedical applications involving Ca^{2+}-sensors.

Received 17th September 2013
Accepted 14th October 2013

DOI: 10.1039/c3nr04978g

www.rsc.org/nanoscale

Introduction

Calcium (Ca^{2+}) triggers and regulates a broad variety of cellular and physiological processes and acts as an important second messenger in many biochemical pathways.[1] The detection of Ca^{2+} is performed by sensor proteins, which adopt specific conformations in response to fine changes in intracellular [Ca^{2+}].[2] Among Ca^{2+}-sensor proteins, neuronal calcium sensors (NCS) are mostly localized in the neuronal tissue, although their expression has been detected also in other tissues.[3,4] A prototypical NCS is recoverin (Rec), a sensor belonging to the EF-hand superfamily, which is involved in the regulation of the biochemical events occurring in photoreceptor cells upon light exposure. The post-translational myristoylation at the N-terminus allows Rec to act as a regulator of the signalling cascade as [Ca^{2+}] drops during the phototransduction process.[5,6] Specifically, the binding of Ca^{2+} triggers the protein structural transition from a "tense" (T), compact conformation in which the myristoyl group is sequestered in a hydrophobic pocket to a "relaxed" (R), more extended conformation, in which the myristoyl moiety is solvent-exposed (Fig. 1). Exposure of the myristic group is accompanied by an overall augmented hydrophobicity of the protein surface and provides an anchor that binds Rec to the photoreceptor disc membranes, thus permitting the regulation of the rhodopsin kinase activity.[5,7] This switch mechanism constitutes a functional hallmark for myristoylated Rec (mRec) and the physico-chemical details have long been investigated.[7,8] Interestingly, mRec binds two Ca^{2+} ions with moderate affinity (apparent $K_D \sim 17$–18 μM),[9,10] while the non-myristoylated variant (nmRec) has two binding sites with significantly higher affinity ($K_{D1} = 0.11$ μM, $K_{D2} = 6.9$ μM).[9]

It is well established that distortion in the cell Ca^{2+}-homeostasis may lead to severe diseases. In particular, hereditary cone dystrophies represent a severe class of disorders that correlate with mutations in genes coding for NCS proteins, which can eventually lead to impaired vision and blindness.[11–15] In order to rescue the physiological levels of second messengers including Ca^{2+}, a novel approach could be the direct delivery of well-defined and precisely structured proteins into the cell to

[a]*Department of Life Sciences and Reproduction, Section of Biological Chemistry, University of Verona, Verona, Italy. E-mail: daniele.dellorco@univr.it; Fax: +39-045-802-7170; Tel: +39-045-802-7637*

[b]*Department of Biotechnology, University of Verona, Verona, Italy*

[c]*Solid State Chemistry Laboratory, University of Verona, Verona, Italy*

[d]*Center for BioMedical Computing, University of Verona, Verona, Italy*

† Electronic supplementary information (ESI) available: Supplementary figures, methods and tables. See DOI: 10.1039/c3nr04978g

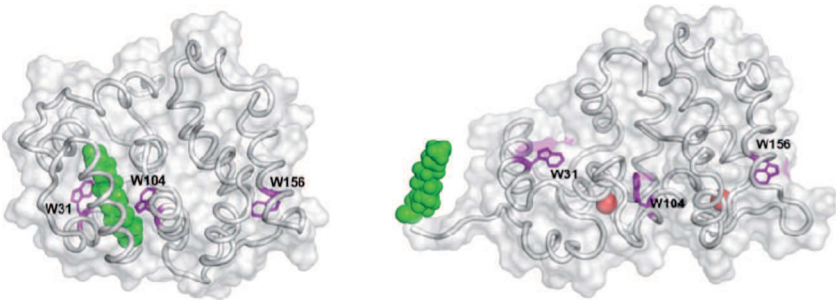

Fig. 1 Three-dimensional structure of myristoylated recoverin in its Ca^{2+}-free (left) and Ca^{2+}-bound (right) forms, corresponding to the T and R states, respectively. The backbone is represented by gray cartoon tubes, the myristic moiety by green spheres, and the two Ca^{2+} ions by red spheres. The three Trp residues are represented by purple sticks and labeled, while the molecular surface is shown in transparency. Solvent-accessible surface areas (ASA) for each Trp in the absence and in the presence of Ca^{2+} are: W31 (49.4 $Å^2$ to 58.6 $Å^2$); W104 (0 $Å^2$ to 12.6 $Å^2$); W156 (2.6 $Å^2$ to 33.3 $Å^2$); structural data are from NMR average structures (left: PDB entry 1IKU; right: PDB entry 1JSA).

replace the dysfunctional protein, hence avoiding some of the potential problems of gene therapy. Ideally, the means of delivery should minimally perturb the proteins to be carried in order to keep them fully functional. For the sake of protein delivery, nanodevices (NDs) may offer unique opportunities in that the high surface to volume ratio would ensure high amounts of protein carried by devices of relatively small volumes. It is however fundamental to assess the effects that the ND exerts on the protein conformation and function upon interaction. Indeed, very recent lines of evidence suggest that nanoparticles (NPs) may lead to significant structural changes and even unfolding of proteins bound to the particle surface.[16–19]

Among the most promising nanoscale devices for nanomedicine purposes, lanthanide-doped upconverting NPs have raised considerable attention in the last few years because of their capacity to be multiphoton-excited with near infra-red (NIR) light and generate emission at higher energies spanning the UV to the NIR, a feature that can be exploited in a variety of bioimaging and biomedical goals.[20–26] Particularly promising are CaF_2 NPs,[27] which can be synthesized by a single-step hydrothermal method and coated by citrate, thus ensuring appropriate dispersion in water environments.[28] In particular, CaF_2 NPs doped with luminescent lanthanide ions can be used as multifunctional nanoprobes for highly penetrating fluorescence, which can be exploited together with the fluorescence thermal sensitivity property.[29] Moreover, they showed no toxicity in tests performed with HeLa cells, thus setting the basis for biocompatible carrier systems that can conveniently exploit the upconversion phenomenon.[29]

In this work, we explored the possibility to use CaF_2 NPs and lipid nanovesicles as convenient carriers of Ca^{2+} sensors for biomedical purposes. We investigated the effects that the interaction with the ND exerted on the structural and functional properties of both mRec and nmRec and evaluated the residual capability of the protein to act as a Ca^{2+}-sensor in the presence of the ND. Our results show that CaF_2 NPs significantly alter the structural and functional properties of both mRec and nmRec, which significantly decrease their sensitivity to free Ca^{2+}. The interaction between the protein and the particles is not mediated by the citrate coating NPs, thus suggesting a direct electrostatic interaction that alters the size of the protein as well as its secondary and tertiary structures. NP-bound mRec and nmRec showed a significantly lower thermal stability and the unfolding profile was found to be highly cooperative, independent of the presence of free Ca^{2+}. Liposomes on the other hand did not significantly perturb protein secondary and tertiary structures, and the capability to work as a Ca^{2+}-sensor in their presence was preserved.

The partial reversibility of binding to CaF_2 NPs observed for mRec and the specific conformational features observed suggest that the interaction with the particle surface induces a structure that is significantly different from the respective equivalent in solution. While Ca^{2+}-sensing is greatly altered, the novel conformation is completely folded and perhaps associated with novel functions to be explored in future studies.

Results and discussion

Ca^{2+}-dependent structural changes in myristoylated and non-myristoylated Rec

Binding of two Ca^{2+} ions to mRec showed distinct spectroscopic features, which represent the hallmarks of the myristoyl-switch mechanism. Far UV-CD spectra showed the typical pattern of an all-α protein, with two minima at 208 and 222 nm (Fig. 2A). In line with previous findings,[30] we observed that the binding of Ca^{2+} leads to a significant decrease of the minimum at 222 nm with substantially unaltered intensity at 208 nm, thus causing the $\theta_{222}/\theta_{208}$ ratio to switch from 0.77 in the apo-form to 0.87 in the Ca^{2+}-bound form (Table 1). CD spectroscopy in the near UV region allows monitoring of the asymmetric environment of the aromatic residues, which was observed to significantly change upon Ca^{2+}-binding in the case of mRec (Fig. 2B).

As observed in previous studies,[31] metal binding caused the ellipticity to drastically decrease mostly in the tyrosine (Tyr) and tryptophan (Trp; W) bands, while only a minor change was observed in the phenylalanine (Phe) region. The fluorescence spectrum (Fig. 2C) arising mostly from the intrinsic fluorescence of three Trp residues (W31, W104 and W156) showed a 7 nm red-shift (329 nm to 336 nm) of the maximum wavelength (Table 1) and a moderate quenching of the signal, as already found in previous studies.[32] This is in line with the increased

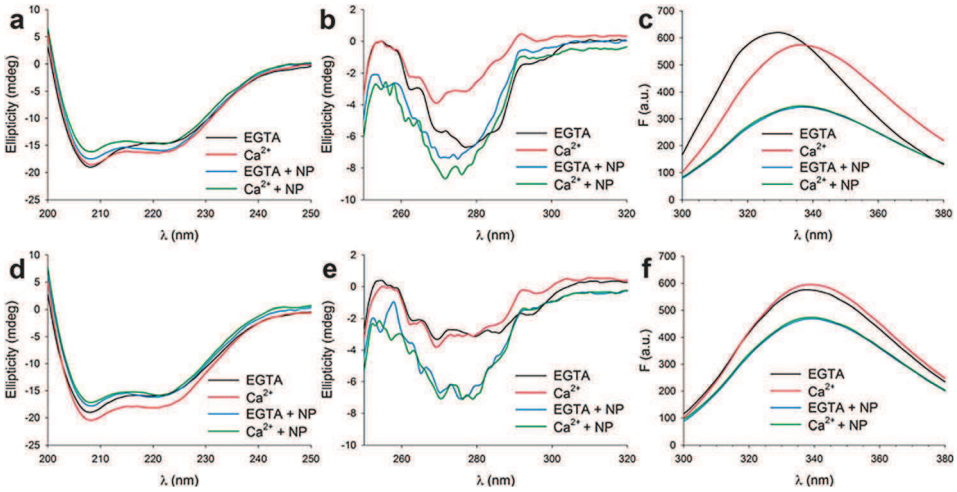

Fig. 2 Structural changes occurring in mRec and nmRec upon binding of Ca^{2+} and upon interaction with CaF_2 NPs. All measurements were performed at $T = 25$ °C in 5 mM Tris–HCl pH 7.5, 150 mM KCl buffer. (a) Far-UV CD spectra of 6.3 μM mRec in the presence of equal amounts (46 μM) of saturating EGTA or Ca^{2+}, both isolated and incubated with 1 mg mL^{-1} CaF_2 NPs. (b) Near-UV CD spectra of 31.4 μM mRec in the presence of equal amounts (230 μM) of saturating EGTA or Ca^{2+}, both isolated and incubated with 5 mg mL^{-1} CaF_2 NPs. (c) Intrinsic Trp fluorescence emission spectrum ($\lambda_{exc} = 290$ nm) of 0.78 μM mRec in the presence of equal amounts (5.8 μM) of saturating EGTA or Ca^{2+}, both isolated and incubated with 125 μg mL^{-1} CaF_2 NPs. (d) Far-UV CD spectra of 5.8 μM nmRec in the presence of equal amounts (46 μM) of saturating EGTA or Ca^{2+}, both isolated and incubated with 1 mg mL^{-1} CaF_2 NPs. (e) Near-UV CD spectra of 29.3 μM nmRec in the presence of equal amounts (230 μM) of saturating EGTA or Ca^{2+}, both isolated and incubated with 5 mg mL^{-1} CaF_2 NPs. (f) Intrinsic Trp fluorescence emission spectrum ($\lambda_{exc} = 290$ nm) of 0.73 μM nmRec in the presence of equal amounts (5.8 μM) of saturating EGTA or Ca^{2+}, both isolated and incubated with 125 μg mL^{-1} CaF_2 NPs. The $\theta_{222}/\theta_{208}$ ratio for all forms and the wavelengths of maximal emission are reported in Table 1.

solvent-exposure of hydrophobic residues upon occurrence of the myristoyl switch during the Ca^{2+}-binding process, in particular structural data confirm that all three Trp residues (W31, W104 and W156) become significantly exposed (Fig. 1). The significant variations observed in mRec conformation upon saturation with Ca^{2+} were confirmed also by dynamic light scattering (DLS) measurements (Fig. S1A;† see also Table 2 and Fig. 4D and E), which revealed a ~0.3 nm increase in the hydrodynamic diameter. The overall increase in mRec hydrodynamic size was postulated earlier[7] and appears to be in line with the radius of gyration and solvent-accessible surface area as determined by comparing the average NMR structures of the apo[8] and Ca^{2+}-bound[5] forms. Overall, our spectroscopic data are consistent with a significant conformational change in mRec secondary and tertiary structures upon Ca^{2+}-binding, compatible with the myristoyl switch mechanism.

The non-myristoylated form of the same protein (nmRec) showed different spectroscopical features (Fig. 2). While the overall fold is clearly all-α, in this case both minima detected by far UV-CD spectroscopy (Fig. 2D) at 208 and 222 nm became more negative upon Ca^{2+}-binding, leading to a less pronounced variation in the $\theta_{222}/\theta_{208}$ ratio, which switched from 0.83 in the apo-form to 0.88 in the Ca^{2+}-bound form (Table 1). The overall different spectral shape of the Ca^{2+}-bound form compared to mRec was previously observed in other NCS that do not undergo a myristoyl switch,[12,30] and can be attributed to an increased compactness of the protein in the presence of Ca^{2+}.[12] Along the same line, the variation in the tertiary structure was less prominent for nmRec (Fig. 2E) compared to mRec (Fig. 2B), and the changes mostly concerned the Trp and Tyr regions. Differences were detected also in the Trp-fluorescence spectrum (Fig. 2F and Table 1), which showed a modest (1 nm) red-shift

Table 1 Biophysical parameters of mRec and nmRec in the absence and in the presence of nanodevices (LP stands for ROS-like liposomes)

	+EGTA				+Ca^{2+}			
	$\theta_{222}/\theta_{208}$ [a] (n)	T_m [b] (°C)	H_c [c]	λ_{max} flu [d] (nm)	$\theta_{222}/\theta_{208}$ (n)	T_m (°C)	H_c	λ_{max} flu (nm)
mRec	0.77 (5)	73.1	15.0	329	0.87 (5)	78.8	10.7	336
nmRec	0.83 (5)	73.8	7.8	338	0.88 (5)	79.4	11.5	339
NP + mRec	0.91 (5)	66.4	21.9	336	0.91 (5)	65.4	23.9	336
NP + nmRec	0.90 (5)	68.6	19.4	339	0.92 (5)	68.1	19.2	339
LP + mRec	0.77 (5)	—	—	330	0.92 (5)	—	—	338
LP + nmRec	0.84 (5)	—	—	339	0.92 (5)	—	—	340

[a] Ratio between ellipticity at 222 and 208 nm; n stands for number of replicates in each experiment. [b] Melting temperature obtained by fitting the experimental curve to a 4 parameter Hill sigmoid (see eqn (1) in Methods). [c] Hill coefficient. [d] Wavelength at which fluorescence emission is maximal upon excitation at $\lambda = 290$ nm.

Table 2 Hydrodynamic diameter measurements by dynamic light scattering. d: hydrodynamic diameter, σ: standard error, n: number of repetitions, pdI: polydispersity index

	+ EGTA		+ Ca^{2+}	
	$d \pm \sigma$ (nm) (n)	pdI	$d \pm \sigma$ (nm) (n)	pdI
mRec	5.22 ± 0.02 (20)	0.43	5.52 ± 0.02 (19)	0.37
nmRec	5.57 ± 0.06 (12)	0.51	5.3 ± 0.08 (13)	0.49
CaF_2 NP	25.4 ± 0.2 (15)	0.08	27.61 ± 0.17 (15)	0.14
LP[a] (mRec)	71.6 ± 0.7 (6)	0.14	72.3 ± 0.7 (8)	0.12
LP[b] (nmRec)	78.6 ± 0.5 (10)	0.08	78.0 ± 0.5 (10)	0.08
NP + mRec	28.0 ± 0.2 (19)	0.13	29.29 ± 0.17 (18)	0.13
NP + nmRec	28.9 ± 0.2 (21)	0.17	32.7 ± 0.3 (20)	0.16
LP + mRec	74.2 ± 2.5 (7)	0.21	77.4 ± 0.6 (8)	0.11
LP + nmRec	78.9 ± 0.8 (8)	0.08	79.1 ± 0.6 (8)	0.08

[a] Liposomes used in experiments with mRec. [b] Liposomes used in experiments with nmRec.

and an increase of intensity in the presence of saturating Ca^{2+}, substantially in line with previous findings.[32] Interestingly, DLS measurements showed the co-presence of two populations, a monomeric form with hydrodynamic diameter decreasing upon Ca^{2+}-binding (~−0.27 nm, see Table 2 and Fig. S1C†) and a higher order oligomer likely comprising 5–7 units that behaved independent of Ca^{2+}. While intensity peaks corresponding to higher order oligomers were detected both for mRec and nmRec in DLS experiments, their effective weight on the photon correlation signal is modest due to the $1/d^6$ scaling of scattered light intensity. Indeed, according to number and volume distributions of the same molecular species only monomeric forms were detected (data not shown). Thus, we may conclude that mRec and nmRec behave in an opposite way upon binding of Ca^{2+}, the latter decreasing its hydrodynamic size at variance with the first one. An opposite behaviour of the two Rec variants was similarly found in a very recent study using surface plasmon resonance.[33]

Effects of CaF_2 nanoparticles on Rec structure and stability

The same spectroscopic characterization performed with isolated proteins was done in the presence of CaF_2 NPs. Working with a suitable NP concentration is necessary to distinguish between spectroscopic signals arising from the unbound proteins and those relative to NP-bound ones. According to a simple geometric model of Rec–NP interaction (see Methods and ESI†) we calculated the maximum number of bound Rec for a ~30 nm diameter NP to be ~244, thus after fixing the NP concentration we kept the corresponding protein concentration below this theoretical maximum in all the experiments, working under conditions at which the signal arising from the protein was clearly detectable.

Interestingly, the structural features of mRec significantly changed in the presence of NPs (Fig. 2). The presence of saturating free Ca^{2+} led to lower dichroism in the far UV-CD region (Fig. 2A), at odds with the isolated protein and likely indicative of a loss of protein compactness upon interaction with the NP. The spectrum however showed a very similar shape for NP-bound mRec independent of the presence of free Ca^{2+}, as quantitatively demonstrated by the same $\theta_{222}/\theta_{208}$ ratio (0.91 in both cases, Table 1). This value is similar to that observed for the Ca^{2+}-bound form of both mRec and nmRec (~0.88, Table 1). Thus, the secondary-structural features in the presence of NPs are incompatible with those typical of the myristoyl switch, although under every tested condition the protein clearly showed a characteristic all-α folding. Along the same line, near UV-CD spectra in the presence of CaF_2 NPs showed a tertiary structure hallmark significantly different from that of the isolated protein. In detail, while the Trp region was very similar to that of the apo mRec (Fig. 2B), Tyr and Phe bands showed a remarkable difference in their fine structure and increased signal. The tertiary structure appeared to be less affected by the presence of saturating free Ca^{2+} compared to the isolated protein and overall, the presence of CaF_2 NPs yielded more prominent differences in the spectrum of Ca^{2+}-bound forms.

Since the CaF_2 NPs used in this study were coated with citrate, we further tested whether the interaction was mediated by citrate rather than occurring through the CaF_2 matrix. The presence of K–citrate even at high concentration did not prevent the occurrence of the myristoyl switch (Fig. S2A†), moreover the $\theta_{222}/\theta_{208}$ ratio and the near-UV spectra (Fig. S2B and Table S1†) were all very similar to those of mRec in the absence of citrate (see Fig. 2A and B). The citrate coating therefore did not perturb the interaction of Rec with the NP, and was probably fully replaced by the protein milieu.

Very minor differences were detected in the intrinsic Trp fluorescence spectra (Fig. 2C) in the presence and in the absence of Ca^{2+}. A hardly detectable blue shift of the maximum wavelength was observed upon saturation with Ca^{2+} and comparison with the unbound protein highlighted a quenching of the signal and a microenvironment of Trp residues similar to that of the Ca^{2+}-bound isolated protein (λ_{max} = 336 nm, Table 1). DLS experiments showed that mRec binds NPs both in the presence and in the absence of free Ca^{2+}, and the changes in the hydrodynamic diameter of the NP–protein complex were 2.6 nm and 1.7 nm respectively (see Table 2, Fig. S1B,† 4D and E).

Similar to mRec, incubating nmRec with CaF_2 NPs led to significant structural changes. The secondary structure of NP-bound nmRec was comparable to the unbound condition (Fig. 2D) although a lower dichroism signal is likely indicative of decreased compactness. Similar $\theta_{222}/\theta_{208}$ ratios were observed in the absence (0.90) and in the presence (0.92) of Ca^{2+} (Table 1), thus indicating a very similar secondary structure compared to the myristoylated form when bound to the NP surface. Also similar to mRec, ellipticity in the near-UV range substantially increased in the presence of NPs (Fig. 2E) showing minor differences in the Trp bands and small but significant differences in the Phe and Tyr regions. The intrinsic Trp fluorescence spectrum (Fig. 2F) was virtually identical in the presence or in the absence of saturating Ca^{2+} and beside a very minor increase in fluorescence intensity in the presence of saturating Ca^{2+}, no shift in the maximum wavelength was observed (Table 1). DLS experiments showed that also nmRec binds NPs both in the presence and in the absence of free Ca^{2+}, and changes in the hydrodynamic diameter of the NP–protein complex were more

significant compared to the myristoylated variant (3.5 nm and 5.1 nm, respectively; see Table 2, Fig. S1D,† 4D and E).

Overall, these findings suggest that the interaction with CaF_2 NPs causes dramatic changes in the secondary and tertiary structures of both mRec and nmRec. In particular, our data clearly show that the myristoyl switch does not occur in the presence of CaF_2 NPs. It is worth noting that the interaction occurs under all the tested conditions, as proved by: (a) the spectroscopic evidence, which ensures the presence of only minimal amounts of unbound protein, and (b) the size determination by DLS, which shows that the thickness of the protein coating on the NP varies between 1.7 nm and 5.1 nm (Table 2), depending on the protein and the presence or absence of free Ca^{2+}.

Further information as to the structural features of NP-bound Rec was obtained by limited proteolysis experiments. Limited proteolysis is a useful tool for detecting protein flexibility,[34] since the sensitivity to protease digestion differs significantly between folded regions and unfolded regions, such as flexible loops. Even for proteins with known structures, limited proteolysis can provide important information about folding intermediates.[35] The presence or absence of a bound ligand can affect the susceptibility of a protein segment to proteases, thus resulting in either increased or decreased accessibility. Limited proteolysis has been applied to investigate both the structural effects induced by the binding of small ligands such as Ca^{2+} ions[36] as well as changes in protein structure and dynamics upon binding to nanoparticles.[16] The proteolysis patterns of mRec and nmRec in the absence and in the presence of NPs are shown in Fig. 3A.

Tryptic treatment with 2 mM Ca^{2+} (lanes 1 and 2) and 2 mM EGTA (lanes 5 and 6) led to different digestion profiles for mRec and nmRec; such a treatment was more effective on nmRec. In particular, in the presence of 2 mM EGTA (lanes 5 and 6) nmRec became very sensitive to trypsin digestion, leading to the accumulation of a ~15 kDa fragment, while mRec proteolysis was appreciably slowed down and no lower molecular mass fragments were detected by SDS-PAGE. This could indicate that exposed sites in the non-myristoylated protein are more protected in the myristoylated one. In the presence of NPs the electrophoretic patterns of both nmRec and mRec were characterized by the prevalence of a band with a very high molecular weight, most likely representing protein–NP complexes, with only a faint band corresponding to the full length Rec. Under these conditions the digestion profiles of nmRec and mRec are identical both with Ca^{2+} (lanes 3 and 4) and EGTA (lanes 7 and 8), supporting our previous conclusion that CaF_2 NPs inhibit the occurrence of the myristoyl-switch of mRec under the investigated conditions. Proteins are probably "spread" on the surface of the NP, thus exposing hydrophobic residues in a Ca^{2+}-independent manner. Moreover, while the presence of NPs seems to be ineffective in mRec proteolysis, it apparently protects nmRec from proteases in the presence of EGTA. In particular, for nmRec mixed with particles, only one protein band was visible with no accumulation of the 15 kDa tryptic fragment (lanes 6 *versus* lanes 8), indicating that sites exposed in the free protein are protected in the NP-bound protein.

The biophysical analysis was completed by the comparison of the thermal denaturation profiles of isolated proteins and

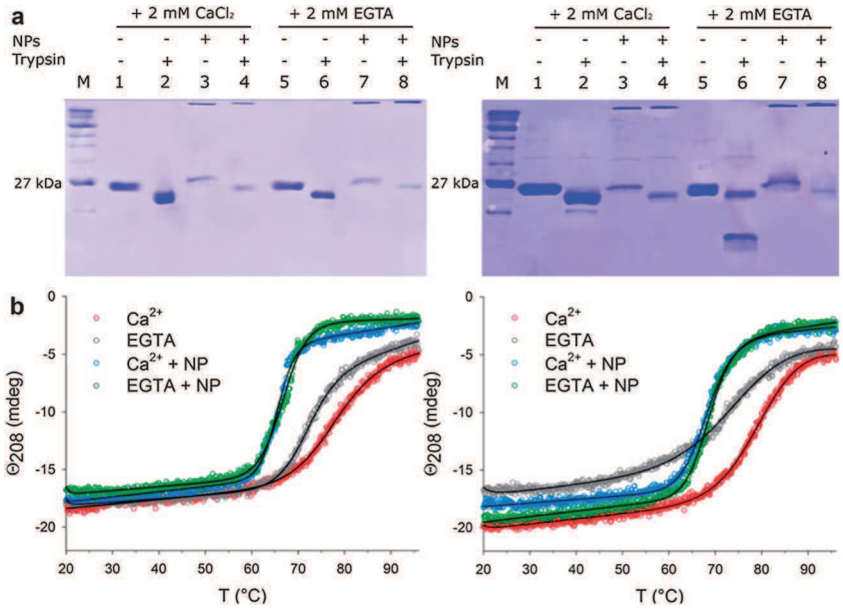

Fig. 3 Analysis of limited proteolysis patterns and thermal denaturation profiles of mRec and nmRec in the presence and in the absence of CaF_2 NPs. (a) Left: limited proteolysis of mRec in the presence of 2 mM $CaCl_2$ or 2 mM EGTA: undigested (lanes 1 and 5), digested by TPCK–trypsin 1 : 100 (lanes 2 and 6), undigested in the presence of NPs (mRec–NP 200 : 1) (lanes 3 and 7), digested by TPCK–trypsin 1 : 100 in the presence of NPs (mRec–NP 200 : 1) (lanes 4 and 8). Lane (M) is the protein ladder. Right: identical analysis for nmRec. (b) Thermal denaturation profiles of ~6 μM mRec (left) and nmRec (right) in the presence of equal amounts (46 μM) of EGTA or Ca^{2+}, both with or without incubation with 1 mg mL^{-1} CaF_2 NPs. Thermal denaturation was followed by monitoring the ellipticity signal at 208 nm over the 20–96 °C temperature range. Quantitative data obtained by fitting the experimental curve to a sigmoidal function are reported in Table 1.

NP–protein complexes in the presence and in the absence of Ca^{2+} (Fig. 3B), obtained by heating the system up to 96 °C. Thermal denaturation profiles of mRec (Fig. 3B) presented a typical sigmoidal shape which was satisfactorily fitted by a Hill function (see Methods and ESI†). The melting temperature increased by about 5.7 °C upon binding of Ca^{2+}, indicative of the typical stabilizing effect of the cation. This value is in partial disagreement with the results reported by Permyakov *et al.*[31], who measured by thermal scanning microcalorimetry an increase of 15 °C. The different technique employed for scanning as well as the overall conditions might partially explain such discrepancy. The melting process showed higher cooperativity in the apo-form (Table 1), and far UV-CD spectra recorded after cooling down the denatured sample to 25 °C showed a minimal residual structure both in the presence and in the absence of Ca^{2+}, however the typical secondary structure was lost (results not shown). Very interestingly, incubation with CaF_2 NPs led to significantly different thermal denaturation profiles (Fig. 3B). Thermal stability turned out to be independent of the presence of free Ca^{2+} and about 7 °C lower compared to the isolated protein in the absence of Ca^{2+}, respectively 13 °C lower in the presence of Ca^{2+} (Fig. 3B and Table 1). Moreover, the unfolding process occurred with remarkably higher cooperativity (Table 1). A similar result was observed for nmRec (Fig. 3B and Table 1). Here as well Ca^{2+} increased the thermal stability of the unbound protein, but the presence of CaF_2 NPs led to highly cooperative unfolding profiles which were substantially identical to one another, independent of the presence of free Ca^{2+}. The NP–protein complex was slightly more stable ($\Delta T_m \sim 2$–3 °C) in the case of nmRec compared to mRec (Table 1). The fact that for both mRec and nmRec the Hill coefficient was significantly higher in the presence of NPs suggests that the structure of the NP-bound protein is less "conformationally dynamic" compared to the equivalent in solution, and the thermal denaturation process indeed spans a narrower range of conformational states resulting in a highly cooperative transition.

Effects of CaF_2 nanoparticles on Rec Ca^{2+}-sensing

We further investigated whether the binding of Rec to CaF_2 NPs was reversible, that is, if the protein could be released from the particle surface in the presence of saturating free Ca^{2+} or in its complete absence. Fig. 4A–C show the results of our DLS experiments, in which injections of small volumes of saturating Ca^{2+} and/or EGTA were performed in pre-incubated mixtures of protein and ND. Interestingly, the binding of mRec to the NP was found to be only partially reversible (Fig. 4A): injection of saturating Ca^{2+} followed by injection of saturating EGTA led to a modest change in hydrodynamic diameter (~0.5 nm), which is however lower compared to the change induced in the NP–mRec complex by the presence of Ca^{2+} (~1.3 nm). Unlike mRec, nmRec resulted to be more tightly bound to the NP's surface (Fig. 4B): in fact, the same procedure did not lead to a decrease of the hydrodynamic diameter after the second injection, but it rather caused a further increase of the overall size (+0.6 nm). We point out that from our DLS data it is not possible to clearly distinguish between variations in the hydrodynamic diameter solely due to changes in conformation of the bound protein and changes due to a shifted equilibrium between bound and

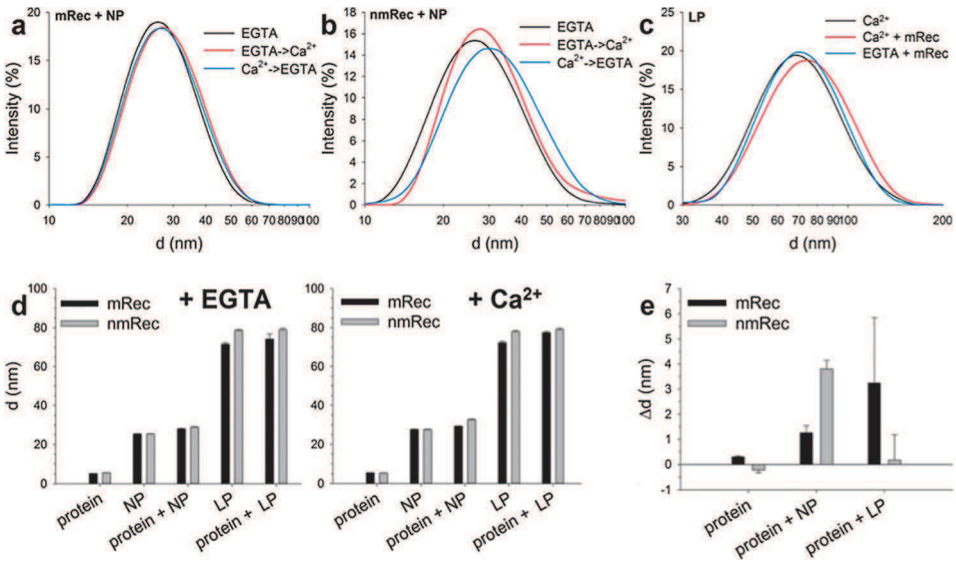

Fig. 4 Results from dynamic light scattering experiments. (a–c) Reversibility tests for Rec-ND binding monitored by DLS. Plots are reported as size distributions for each complex. (a) Size profiles for 1 mg mL^{-1} CaF_2 NPs incubated with 8 μM mRec in the presence of 100 μM EGTA (black line) and after two subsequent injections leading to 233 μM free Ca^{2+} (red line) and 222 μM EGTA (blue line). (b) Same conditions as in (a) obtained for nmRec. (c) Size profiles for 20 nM ROS-like liposomes (~70 nm diameter) in the presence of 240 μM free Ca^{2+} (black line), incubated with 27 μM mRec (red line) and after injection leading to 1 mM EGTA (blue line). (d–e) Hydrodynamic diameter measurements of proteins, NDs and protein–ND complexes and dependence on free Ca^{2+}. (d) Hydrodynamic diameter measured by DLS in the presence of saturating EGTA (left) and saturating Ca^{2+} (right); bars stand for standard errors. (e) Effects of free Ca^{2+} on the size of proteins and protein–ND complexes as measured by $\Delta d = d^{Ca^{2+}} - d^{EGTA}$. Error bars report on errors calculated by error propagation procedures, LP stands for ROS-like liposomes.

unbound proteins. The significantly different behaviour observed by DLS for mRec (Fig. 4A) and nmRec (Fig. 4B) in contrast with the similar spectroscopic features of the NP-bound proteins (Fig. 3) suggests that the binding mechanism is strictly protein-dependent, and the myristoyl moiety plays a significant role in allowing binding/release of the NCS from the NP's surface.

While informative as to the general behaviour of NP–Rec complexes in the presence of saturating Ca^{2+} as well as in its complete absence, in an "on–off" fashion, DLS experiments did not thoroughly probe the residual capability of mRec/nmRec to act as NCSs in the presence of the NP. We therefore performed Ca^{2+} titrations in the nM to mM range and monitored the intrinsic Trp fluorescence of the protein in the presence and in the absence of CaF_2 NPs (Fig. 5). Fluorescence emission at the wavelength corresponding to the maximum intensity at low Ca^{2+} ($F^{\lambda_{max}}$) from mRec showed a typical sigmoidal trend (Fig. 5A), and reached its half-maximal value (K_D^{app}) at 40.9 μM [Ca^{2+}]. This value is higher compared to the apparent affinity for Ca^{2+} of mRec (~18 μM (ref. 9 and 10)), which is reasonable since rather than directly studying the binding process we monitored the effect of Ca^{2+}-binding on the protein conformation, ultimately responsible for the fluorescence signal.

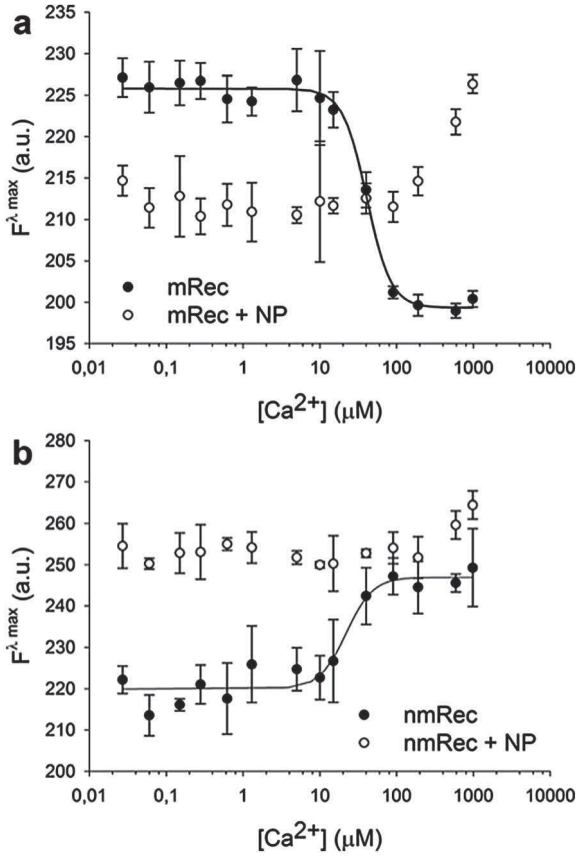

Fig. 5 Ca^{2+}-sensing capability of Rec in the presence and in the absence of CaF_2 NPs. Titration experiments were performed in the 27 nM to 980 μM [Ca^{2+}] range by monitoring the intrinsic Trp fluorescence emission ($\lambda_{exc} = 295$ nm in all the experiments). (a) Ca^{2+} titration of 0.8 μM mRec isolated (full circles) and incubated with 135 μg mL^{-1} CaF_2 NPs (empty circles). Fluorescence emission ($F^{\lambda_{max}}$) was monitored at $\lambda_{em} = 329$ nm for the unbound protein and at $\lambda_{em} = 336$ nm in the presence of CaF_2 NPs. Four replicates were accumulated and results are shown as average ± standard deviation. Data points collected for the unbound protein were fitted according to a Hill function leading to $K_D^{app} = 40.9$ μM and a Hill coefficient $H = 2.8$. (b) Ca^{2+}-titration of 0.8 μM nmRec isolated (full circles) and incubated with 135 μg mL^{-1} CaF_2 NPs (empty circles). Maximum fluorescence emission was monitored at $\lambda_{em} = 338$ nm for the unbound protein and at $\lambda_{em} = 339$ nm in the presence of CaF_2 NPs. Four replicates were accumulated and results are shown as average ± standard deviation. Data points collected for the unbound protein were fitted according to a Hill function leading to $K_D^{app} = 22.1$ μM and a Hill coefficient $H = 2.5$.

The same reasoning applies to nmRec (Fig. 5B), for which $K_D^{app} = 22.1$ μM, higher than the apparent affinity for Ca^{2+} ($K_{D1} = 0.11$ μM, $K_{D2} = 6.9$ μM).[9] It is worth noting that, while for mRec $F^{\lambda_{max}}$ decreased with increasing [Ca^{2+}], in line with the augmented hydrophobicity of the Ca^{2+}-bound protein, the opposite trend was observed for nmRec, thus $F^{\lambda_{max}}$ increased with increasing [Ca^{2+}]. This is in line with previous reports.[7,8,33]

Incubating mRec and nmRec with CaF_2 NPs resulted in very different trends for $F^{\lambda_{max}}$. Neither form of the protein was able to respond normally to Ca^{2+} and remained "blocked" up to high concentrations ([Ca^{2+}] > 200 μM; Fig. 5A and B). After the prolonged plateau, $F^{\lambda_{max}}$ monotonically increased in both cases in a similar manner, although at high [Ca^{2+}] the change in $F^{\lambda_{max}}$ was more apparent for mRec than for nmRec (Fig. 5A and B). Therefore, in the presence of NPs, the Ca^{2+}-sensing capability of both mRec and nmRec was highly compromised, suggesting that both proteins were blocked in a specific conformation up to relatively high [Ca^{2+}], after which proteins did partially respond to Ca^{2+}. The increase in fluorescence emission at high concentrations of Ca^{2+} observed for mRec might reflect the partial release of the protein from the NP surface observed in DLS experiments (Fig. 4A). Overall, this scenario appears fully compatible with the previous evidence from spectroscopic, DLS and limited proteolysis experiments.

Effects of ROS-like liposomes on Rec structure and stability

We tested whether completely different NDs exerted any structural and functional effects on Rec by creating nanovesicles with the same lipid composition as that found in rod-outer segment (ROS) discs within vertebrate photoreceptors. Far UV-CD spectra of mRec in the presence of ~70 nm liposomes (Fig. S5A†) were very similar to those of the unbound protein (Fig. 2A), as shown by comparable $\theta_{222}/\theta_{208}$ ratios observed in the absence (0.77) and in the presence (0.92) of saturating Ca^{2+} (Table 1). Despite the noise due to the comparable size of the liposomes and the wavelength of the incident light, near UV-CD spectra (Fig. S5B†) were also very similar to those of the unbound protein, except for minor differences in the fine structure observed for the Tyr and Trp bands. Fluorescence spectra also showed high similarity with respect to the isolated protein, and a 8 nm red-shift accompanied by intensity quenching was observed in this case too (Fig. S5C†), although both maxima were slightly red-shifted. Interestingly, DLS experiments proved that mRec-bound liposomes in the presence of saturating Ca^{2+} (Fig. 4C and Table 2) led to a ~5.2 nm

increase in the size of the complex, which was almost completely reversible upon addition of saturating EGTA (Fig. 4C). In the absence of Ca^{2+} (*i.e.* 240 μM EGTA), however, the size of the complex did not significantly change within the experimental error (Table 2), compatible with a very low propensity of apo mRec to bind liposomes. The situation was slightly different for nmRec, as the presence of ROS-like liposomes did not significantly alter the secondary structure (Fig. S5D†), thus resulting in similar $\theta_{222}/\theta_{208}$ ratios as those of the unbound protein (0.84 in the absence and 0.92 in the presence of saturating Ca^{2+}, Table 1), while slight changes in optical activity were observed in the near UV range (Fig. S5E†), where fine spectral structures appeared corresponding to all three aromatic bands, both in the presence and in the absence of saturating Ca^{2+}. On the other hand, the behaviour comparable to that of the unbound protein was observed in the intrinsic Trp fluorescence emission (Fig. S5F†), the main differences being a 1 nm instead of 2 nm red-shift and a more prominent increase of intensity.

The observed differences are not likely to be due to a stable binding between nmRec and liposomes, as DLS experiments could not detect any significant variation of the hydrodynamic size of the liposomes in the presence of proteins, independent of the presence of saturating EGTA or Ca^{2+} (Table 2 and Fig. S3†). They are likely due to excluded volume effects and a balance between long-range electrostatic effects induced by liposomes and transient contacts between the protein and the liposome surface.

Overall, these results show that ROS-like liposomes work as suitable "anchors" for Ca^{2+}-bound mRec, which mimic biological membranes and unlike CaF_2 NPs do not prevent the protein from functioning as a NCS *via* the myristoyl switch mechanism. This interpretation seems to be completely in line with previous findings.[37] In this respect, liposomes could be used as suitable carriers for mRec in a biological context. On the other hand, nmRec did not show significant interactions with the liposomes under the tested conditions.

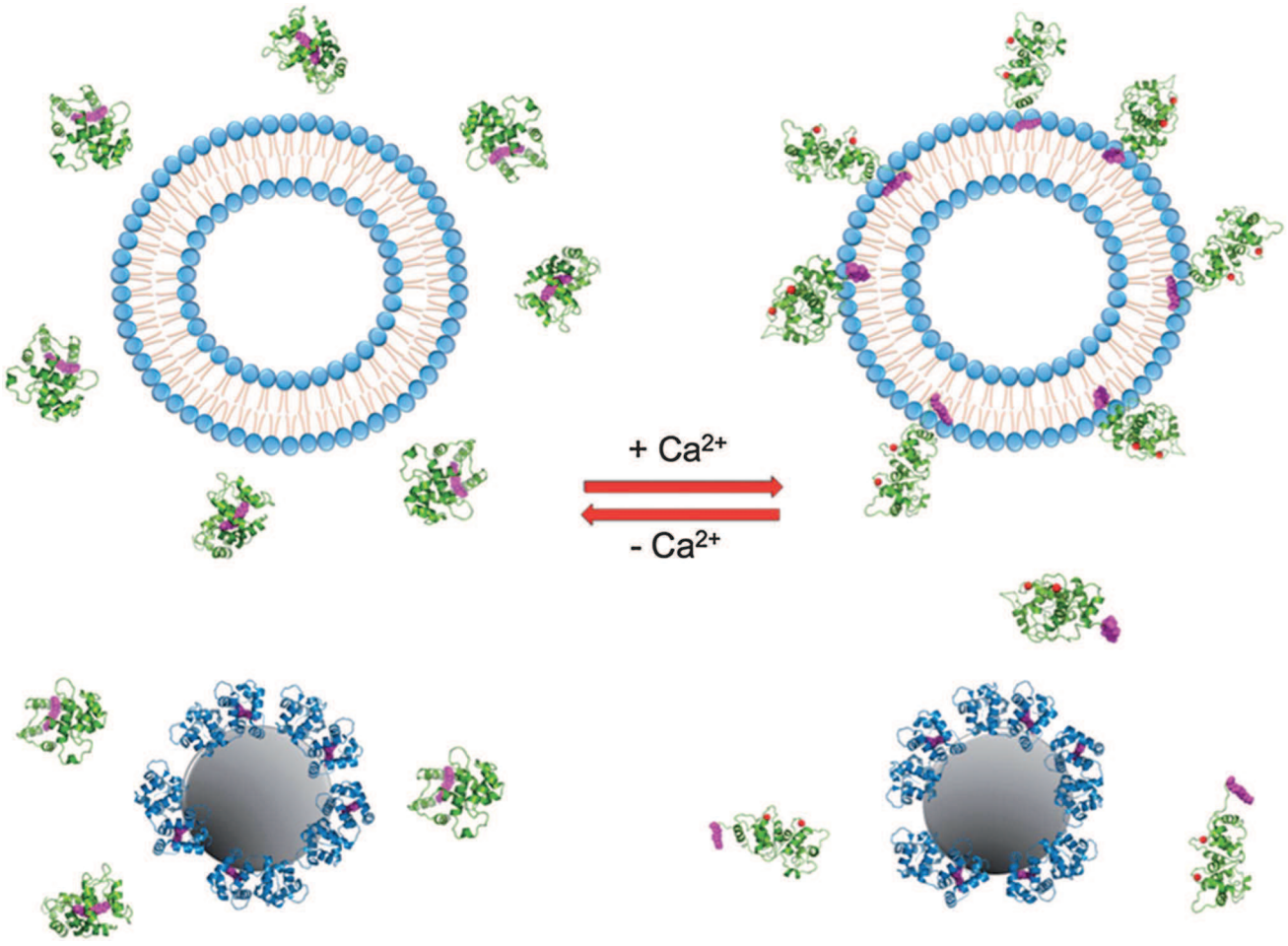

Fig. 6 Schematic representation of the interaction between mRec and liposomes (top) and CaF_2 NPs (bottom). On the left is depicted the situation at low free Ca^{2+}, while on the right that at saturating Ca^{2+}. Top: the protein (green cartoon) is free in solution in its apo T-state and does not interact with the liposome. When Ca^{2+} increases and binds to mRec (right: red spheres represent Ca^{2+} ions) the myristic group (magenta) is exposed and serves as an anchor to bind to the liposome surface. The process is fully reversible. Bottom: in the presence of CaF_2 NPs, mRec binds tightly to the particle surface independent of free Ca^{2+}, adopting a new conformation (blue cartoons) that differs from both the T and R one, and which does not respond to free Ca^{2+}. Only the unbound protein responds normally and may undergo the T to R reversible transition.

Free Ca^{2+}-dependence of ND-Rec hydrodynamic size

In this work we investigated the interaction of Rec in both its myristoylated and non-myristoylated forms with two significantly different types of NDs, namely CaF_2 NPs and liposomes with a ROS-like lipid composition. We found that the interaction generally depends on both the presence of post-translational modification in the protein and the presence or absence of free Ca^{2+} in solution. Fig. 4D–E summarize the results obtained by DLS (Table 2): mRec, whose size increased by ~0.3 nm upon Ca^{2+} binding (Fig. 4D), apparently binds CaF_2 NPs independent of the presence of free Ca^{2+} in solution as clearly shown by the increase in the hydrodynamic diameter of the complex observed both in the presence of Ca^{2+} and EGTA (Table 2). The increase in size though depends on the free Ca^{2+}, being 2.6 nm in the absence of Ca^{2+}, and 1.7 nm increase in the presence of free Ca^{2+} in solution. In contrast, nmRec decreased in size by ~0.3 nm upon Ca^{2+} binding, however when it was incubated with CaF_2 NPs, it increased the hydrodynamic diameter of the particles by 3.5 nm in the absence of free Ca^{2+} and by 5.1 nm in the presence of free Ca^{2+} in solution. Interestingly, free Ca^{2+} affects the hydrodynamic size of the protein–ND complex in a protein-specific way (Fig. 4E). High free Ca^{2+} led to significantly thicker coating of CaF_2 NPs by nmRec compared to mRec, as clearly assessed by comparing the difference in the hydrodynamic diameter ($\Delta d = d^{Ca^{2+}} - d^{EGTA}$) of the NP–protein complex in the presence of Ca^{2+} and in the presence of EGTA (Δd = 3.8 nm for nmRec and 1.3 nm for mRec; Fig. 4E). It is unclear whether this is due to a higher propensity of nmRec to form aggregates already in solution (see Fig. S1A†) or, more likely, to a not well-defined surface phenomenon involving the coating by multiple protein layers.

A different situation was observed when proteins were incubated with ROS-like liposomes. While no significant interaction with nmRec was observed either in the presence or in the absence of free Ca^{2+} (Fig. 4E, S3† and Table 2), incubation with mRec at high free Ca^{2+} increased the hydrodynamic diameter of the liposomes by 3.2 nm (Fig. 4E). In the absence of free Ca^{2+}, however, the hydrodynamic diameter showed high variance (Table 2 and Fig. 4E) indicative of a more polydisperse suspension (Table 2). Overall, this is compatible with a stabilizing effect of free Ca^{2+} on liposome–mRec interaction, which is reflected by the significantly lower polydispersity index (Table 2).

Conclusion

Our data show that both CaF_2 NPs and liposomes interact with mRec and nmRec, however the interaction strongly depends on the specific ND. Fig. 6 schematically summarizes our findings on mRec. In the absence of free Ca^{2+} (Fig. 6, top left), most of the protein is present in solution in its apo-form (T), and does not interact with the vesicle. Under conditions of saturating Ca^{2+} however, the myristoyl switch mechanism occurs, thus leading to the Ca^{2+}-bound form (R) and to the exposure of the myristic group, which allows the protein to stably bind to the liposome surface. The extent of binding is directly regulated by the fully preserved capability of mRec to detect Ca^{2+}, and the association process can be reversed if the free Ca^{2+} is chelated (see Fig. 4).

A completely different scenario applies to the molecular process in the presence of CaF_2 NPs (Fig. 6, bottom). Upon incubation with particles, mRec sticks to the NP surface adopting a conformation (blue cartoons in Fig. 6) that differs from both the R and T ones. This tight interaction prevents mRec from functioning as a Ca^{2+} sensor, at least up to high Ca^{2+} concentrations (see Fig. 5). However, the NP-bound protein is not unfolded at all. It rather adopts a new, highly helical conformation that exposes hydrophobic residues in a manner that partly resembles the R-form, and the binding is partially reversible. A similar scheme applies to nmRec in the presence of CaF_2 NPs, but the interaction with CaF_2 NPs appears even tighter and irreversible. Moreover, no significant interaction occurs with liposomes.

In conclusion, liposomes could be used as suitable surface carriers of mRec in a biological context to preserve the protein structure and functional properties. On the other hand, CaF_2 NPs seem to induce a different conformation to the protein, stabilizing a state that is greatly independent of the levels of free Ca^{2+} and suggesting a direct interaction between the Ca^{2+}-binding motifs of the protein and the CaF_2 matrix, which seems to be the case both for mRec and nmRec. The specific mode of interaction is currently unknown, and together with the novel biological functions, it will be the object of future studies.

Experimental

Protein expression and purification

Myristoylated and nonmyristoylated Rec were expressed essentially as reported,[10,38] with some modifications elucidated in the ESI.†

Nanoparticle synthesis, structural and spectroscopic characterization

The synthesis procedure of lanthanide doped CaF_2 NPs was similar to the method developed by some of us.[29] Details are provided in the ESI.†

Preparation of liposomes

Liposomes were prepared as described previously[10] and is reported in the ESI.†

Limited proteolysis

26.5 μg of nmRec or mRec were mixed with nanoparticles (Rec–NP 200 : 1) in 5 mM Tris–HCl pH 7.5, 150 mM KCl, 1 mM DTT and 2 mM $CaCl_2$ or 2 mM EGTA and incubated for 1 h at 25 °C. Particle–protein mixtures were treated with TPCK–trypsin 1 : 100 (w/w). For each protein a control sample without any protease was studied in parallel. After 30 minutes the digestion reaction was stopped by rapid addition of reducing sample buffer and boiling for 5 min. Then, proteolysis pattern was visualized by SDS-PAGE on a 15% gel and Coomassie blue staining.

Dynamic light scattering experiments

DLS measurements were performed with a Zetasizer Nano-S (Malvern Instruments) using a polystyrene low volume disposable sizing cuvette (ZEN0112). Viscosity and refractive index were set to be 0.8872 cP and 1.330 (default values for water), the temperature was set to 25 °C with 2 min equilibration time. The measurement angle was 173° backscatter and the analysis model was set to multiple narrow modes. For each measurement a minimum of 7 determinations were performed, each consisting of 13–15 repetitions. Buffers (5 mM Tris–HCl, 150 mM KCl pH = 7.5, adjusted with $CaCl_2$ or EGTA), were filtered through a Jet Biofilm 0.22 mm membrane, while protein-only solutions were filtered through an Anotop 10 filter (Whatman, 0.02 μm).

Circular dichroism spectroscopy and thermal denaturation profiles

Circular dichroism (CD) spectroscopy studies were performed with a Jasco V-710 spectropolarimeter equipped with a Peltier type thermostatted cell holder. Both near-UV (250–320 nm) and far-UV spectra (200–250 nm) were recorded at 25 °C at a scan rate of 50 nm min^{-1}, a bandwidth of 1 nm and an integration time of 4 s. Five spectra accumulations were averaged for each sample, and the spectrum of the buffer (with or without NP or liposomes) was considered as a blank and subtracted. For recording far-UV spectra the protein concentration was 5–7 μM in 0.1 cm cuvettes, while for near-UV spectra it was 29–32 μM in 1 cm cuvettes. Far-UV spectra were recorded in the presence of either 45–50 μM EGTA or Ca^{2+} while near-UV spectra were recorded in the presence of either 230 μM EGTA or Ca^{2+}.

Thermal denaturation of Rec both isolated and in the presence of CaF_2 NPs was monitored between 20 °C and 96 °C using the same conditions and concentration range as for the far-UV spectra measurements. The ellipticity signal at 208 nm (θ_{208}) was recorded at a scan rate of 1°C min^{-1} and a response time of 4 s, using a 0.1 cm quartz cuvette. Thermally denatured samples were cooled down to 25 °C and, after 5–15 min, a far-UV CD spectrum was recorded to check for residual structures (results not shown).

The analysis of thermal denaturation curves was performed for each sample assuming a two-state transition process. By monitoring θ_{208} as a function of the temperature it was possible to quantitatively describe the fraction of folded and unfolded protein under different conditions. No complete unfolding was achieved for Rec under any experimental condition, as shown by the residual CD signal after thermal denaturation. Data were fitted according to two functions, one accounting for the variation of the Gibbs free energy (see ref. 12, results not shown), and another one consisting of a 4-parameter Hill sigmoid:

$$y = b_n + \frac{|b_n - b_u| T^H}{{T_m}^H + T^H} \quad (1)$$

where b_n is the baseline value (θ_{208}) of the native protein, b_u is the baseline value of the unfolded protein, T is the temperature, H is the Hill coefficient and T_m is the melting temperature. Results from the two fitting procedures were comparable in terms of T_m and eqn (1) was used throughout this work for quantitative comparisons.

Fluorescence spectroscopy and Ca^{2+}-titrations

The emission fluorescence spectra were recorded between 300 and 380 nm at 25 °C in 1 cm quartz cuvette using a Jasco FP-750 spectrofluorimeter, after excitation at 290 nm, at a scan rate of 60 nm min^{-1}. The excitation and emission bandwidth were set to 5 nm. The collected data were obtained by subtracting the signal of NPs or liposomes to an average of three accumulations. The protein concentration for all fluorescence spectra measurements was ~1 μM in the presence of ~6 μM EGTA or Ca^{2+}.

Ca^{2+} buffers used in fluorescence titration experiments were prepared as described previously.[39] The solutions used for the fluorescence titration experiments were: (1) carefully decalcified 5 mM Tris–HCl 150 mM KCl pH = 7.5; (2) $CaCl_2$ at variable concentrations; and (3) 1 mM EGTA, whose pH was adjusted to 7.5 by addition of KOH. Free Ca^{2+} concentration for each titration point was calculated according to the Ca–EGTA NIST software (http://www.maxchelator.stanford.edu/CaEGTA-NIST.htm), by fixing T = 25 °C, pH = 7.5 and ionic strength = 0.15 M. By mixing the three solutions, the final Ca^{2+} concentration for each point was varied in the 27 nM to 980 μM range. In each titration experiment the protein concentration was 0.8 μM while that of NPs was 135 μg mL^{-1}. Ca^{2+} titration experiments were performed by monitoring the maximal Trp fluorescence emission (λ_{ex} = 295 nm) at the lowest free Ca^{2+} concentration (27 nM), which is expected to change according to the increasing saturation of the protein by Ca^{2+}. The corresponding λ_{max} values in every case are reported in Fig. 6.

Estimation of the size-dependent protein coverage of the ND surface and concentration adjustments

The maximum number of proteins bound to each ND depends on the total surface accessible to proteins and on the fraction of the ND surface occupied by a bound protein. Based on the simplest geometric model of interaction and considering all the objects as rigid spheres, the maximal stoichiometric protein–NP ratio to ensure a minimal presence of unbound proteins in solution is:

$$N_{Rec}^{max} = \frac{4\pi(r_{ND} + r_{Rec})^2}{\pi {r_{Rec}}^2} \quad (2)$$

where N_{Rec}^{max} is the maximum number of Rec molecules that can occupy the surface of the ND, r_{ND} is the radius of the ND and r_{Rec} is the radius of Rec. In other words, the geometric problem is that of occupying the augmented surface area of a sphere by N_{Rec}^{max} circles, each of area $\pi {r_{Rec}}^2$.

Also, assuming that the density of CaF_2 NPs is equal to that of bulk CaF_2 (ρ = 3.18 g cm^{-3}), the molecular weight of CaF_2 NPs (NP in eqn (3)) was calculated as follows:

$$MW_{NP} = \frac{4\pi {r_{NP}}^3}{3} \rho_{CaF_2} N_A \quad (3)$$

For example, in the presence of NPs of 30 nm diameter, $N_{Rec}^{max} = 244$ and the molecular weight of CaF_2 NPs is 27×10^6 g mol^{-1}. For near UV CD spectra with a reasonable signal-to-noise ratio, approximately 30 μM (0.7 mg mL^{-1}) Rec is required, so that 0.12 μM is the concentration of saturating CaF_2 NPs (3.2 mg mL^{-1}) that, under the maximal binding geometric assumption, guarantees to keep the amount of free Rec low.

Liposomes differ from NPs in terms of geometrical properties, as the former can be modeled as a spherical bilayer of thickness h whereas the latter can be modeled as a full sphere. The molecular weight of lipids making the ROS-like liposomes ($MW_{ROS} = 756.725$ Da) was calculated using a weighted mean of the molecular weight of each lipid ($MW_{PC} = 790.2$ Da, $MW_{PE} = 748.1$ Da, $MW_{PS} = 814.1$ Da, $MW_{Cho} = 386.7$ Da). The number of lipid molecules in a unilamellar liposome is given by:

$$N_{tot} = \frac{4\pi\left(\frac{d}{2}\right)^2 + 4\pi\left(\frac{d}{2} - h\right)^2}{a} \quad (4)$$

where d is the diameter of the liposome, h is the thickness of the bilayer (5 nm) and a is the head group area of a lipid molecule. Assuming that the head group area of the ROS-like lipid mixture is equal to that of PC (0.71 nm^2), the molar concentration of liposomes that can be obtained when rehydrating a certain amount of lipids in a specific volume of aqueous buffer (c_{lipid} in mg mL^{-1}) is:

$$M_{LP} = \frac{c_{lipid}}{N_{tot} MW_{ROS}} \quad (5)$$

Thus, if 2 mg lipids are rehydrated in 2.6 mL aqueous buffer, the molar concentration M_{LP} of liposomes expected is 20 nM. Knowing the M_{LP} allows the determination of the stoichiometric relationship between liposomes and dissolved Rec, under the assumption of maximal geometric binding. The maximum number of Rec bound to 80 nm liposomes is $N_{Rec}^{max} = 1471$ (see eqn (2)), therefore the maximum concentration of Rec bound to a suspension of 0.77 mg mL^{-1} liposomes is 29.4 μM. Since the hydrodynamic diameter of liposomes varied between 70 and 80 nm, in order to ensure stoichiometric excess of protein binding sites on ROS-like liposomes over free, unbound Rec, 0.77 mg mL^{-1} liposomes and 25 μM Rec concentration were chosen for DLS and near UV spectra measurements, whereas a 1 : 5 dilution was chosen for recording far UV spectra (0.15 mg mL^{-1} LP and 5 μM Rec) and a 1 : 80 dilution was chosen for recording fluorescence spectra (0.18 μg mL^{-1} LP and 0.3 μM Rec).

Acknowledgements

We would like to thank P. Dominici (University of Verona) for the encouragement in the initial phase of this work and for the continuous support. Plasmids for protein expression were a kind gift from K. W. Koch (University of Oldenburg). This work was supported by funds from the Italian Ministry for Research and Education *via* departmental funds (FUR2011DDO and FUR2012DDO).

References

1 M. J. Berridge, P. Lipp and M. D. Bootman, *Nat. Rev. Mol. Cell Biol.*, 2000, **1**, 11–21.
2 E. A. Permyakov and R. H. Kretsinger, *Calcium Binding Proteins*, Wiley, 2011.
3 R. D. Burgoyne, *Nat. Rev. Neurosci.*, 2007, **8**, 182–193.
4 P. P. Philippov and K. W. Koch, *Neuronal Calcium Sensor Proteins*, Nova Science Publishers, Inc., 2006.
5 J. B. Ames, R. Ishima, T. Tanaka, J. I. Gordon, L. Stryer and M. Ikura, *Nature*, 1997, **389**, 198–202.
6 E. N. Pugh Jr and T. D. Lamb, *Phototransduction in Vertebrate Rods and Cones: Molecular Mechanisms of Amplification, Recovery and Light Adaptation*, Elsevier Science B.V., 2000.
7 D. Dell'Orco, M. Muller and K. W. Koch, *Chem. Commun.*, 2010, **46**, 7316–7318.
8 T. Tanaka, J. B. Ames, T. S. Harvey, L. Stryer and M. Ikura, *Nature*, 1995, **376**, 444–447.
9 J. B. Ames, T. Porumb, T. Tanaka, M. Ikura and L. Stryer, *J. Biol. Chem.*, 1995, **270**, 4526–4533.
10 I. I. Senin, T. Fischer, K. E. Komolov, D. V. Zinchenko, P. P. Philippov and K. W. Koch, *J. Biol. Chem.*, 2002, **277**, 50365–50372.
11 P. Behnen, D. Dell'Orco and K. W. Koch, *Biol. Chem.*, 2010, **391**, 631–637.
12 D. Dell'Orco, P. Behnen, S. Linse and K. W. Koch, *Cell. Mol. Life Sci.*, 2010, **67**, 973–984.
13 A. M. Dizhoor, S. G. Boikov and E. V. Olshevskaya, *J. Biol. Chem.*, 1998, **273**, 17311–17314.
14 F. Doonan, M. Donovan and T. G. Cotter, *Invest. Ophthalmol. Visual Sci.*, 2005, **46**, 3530–3538.
15 V. B. Kitiratschky, P. Behnen, U. Kellner, J. R. Heckenlively, E. Zrenner, H. Jagle, S. Kohl, B. Wissinger and K. W. Koch, *Hum. Mutat.*, 2009, **30**, E782–E796.
16 R. Cukalevski, M. Lundqvist, C. Oslakovic, B. Dahlback, S. Linse and T. Cedervall, *Langmuir*, 2011, **27**, 14360–14369.
17 H. Pan, M. Qin, W. Meng, Y. Cao and W. Wang, *Langmuir*, 2012, **28**, 12779–12787.
18 E. Gabellieri, P. Cioni, E. Balestreri and E. Morelli, *Eur. Biophys. J.*, 2011, **40**, 1237–1245.
19 D. H. Tsai, F. W. Delrio, A. M. Keene, K. M. Tyner, R. I. Maccuspie, T. J. Cho, M. R. Zachariah and V. A. Hackley, *Langmuir*, 2011, **27**(6), 2464–2477.
20 F. Vetrone, R. Naccache, A. Juarranz de la Fuente, F. Sanz-Rodriguez, A. Blazquez-Castro, E. M. Rodriguez, D. Jaque, J. G. Sole and J. A. Capobianco, *Nanoscale*, 2010, **2**, 495–498.
21 S. Jiang, Y. Zhang, K. M. Lim, E. K. Sim and L. Ye, *Nanotechnology*, 2009, **20**, 155101.
22 E. I. Altinoglu, T. J. Russin, J. M. Kaiser, B. M. Barth, P. C. Eklund, M. Kester and J. H. Adair, *ACS Nano*, 2008, **2**, 2075–2084.
23 C. Vinegoni, D. Razansky, S. A. Hilderbrand, F. Shao, V. Ntziachristos and R. Weissleder, *Opt. Lett.*, 2009, **34**, 2566–2568.
24 S. A. Hilderbrand, F. Shao, C. Salthouse, U. Mahmood and R. Weissleder, *Chem. Commun.*, 2009, 4188–4190.

25 M. Wang, C. C. Mi, W. X. Wang, C. H. Liu, Y. F. Wu, Z. R. Xu, C. B. Mao and S. K. Xu, *ACS Nano*, 2009, **3**, 1580–1586.
26 F. Wang, D. Banerjee, Y. Liu, X. Chen and X. Liu, *Analyst*, 2010, **135**, 1839–1854.
27 G. Wang, Q. Peng and Y. Li, *J. Am. Chem. Soc.*, 2009, **131**, 14200–14201.
28 M. Pedroni, F. Piccinelli, T. Passuello, M. Giarola, G. Mariotto, S. Polizzi, M. Bettinelli and A. Speghini, *Nanoscale*, 2011, **3**, 1456–1460.
29 N. N. Dong, M. Pedroni, F. Piccinelli, G. Conti, A. Sbarbati, J. E. Ramirez-Hernandez, L. M. Maestro, M. C. Iglesias-de la Cruz, F. Sanz-Rodriguez, A. Juarranz, F. Chen, F. Vetrone, J. A. Capobianco, J. G. Sole, M. Bettinelli, D. Jaque and A. Speghini, *ACS Nano*, 2011, **5**, 8665–8671.
30 R. E. Hughes, P. S. Brzovic, A. M. Dizhoor, R. E. Klevit and J. B. Hurley, *Protein Sci.*, 1998, **7**, 2675–2680.
31 S. E. Permyakov, A. M. Cherskaya, L. A. Wasserman, T. I. Khokhlova, I. I. Senin, A. A. Zargarov, D. V. Zinchenko, E. Y. Zernii, V. M. Lipkin, P. P. Philippov, V. N. Uversky and E. A. Permyakov, *J. Proteome Res.*, 2003, **2**, 51–57.
32 S. Ray, S. Zozulya, G. A. Niemi, K. M. Flaherty, D. Brolley, A. M. Dizhoor, D. B. McKay, J. Hurley and L. Stryer, *Proc. Natl. Acad. Sci. U. S. A.*, 1992, **89**, 5705–5709.
33 D. Dell'Orco, S. Sulmann, S. Linse and K. W. Koch, *Anal. Chem.*, 2012, **84**, 2982–2989.
34 S. Dokudovskaya, R. Williams, D. Devos, A. Sali, B. T. Chait and M. P. Rout, *Structure*, 2006, **14**, 653–660.
35 A. Fontana, P. P. de Laureto, B. Spolaore, E. Frare, P. Picotti and M. Zambonin, *Acta Biochim. Pol.*, 2004, **51**, 299–321.
36 S. Pedigo and M. A. Shea, *Biochemistry*, 1995, **34**, 1179–1196.
37 C. Lange and K. W. Koch, *Biochemistry*, 1997, **36**, 12019–12026.
38 I. I. Senin, K. W. Koch, M. Akhtar and P. P. Philippov, *Adv. Exp. Med. Biol.*, 2002, **514**, 69–99.
39 R. Tsien and T. Pozzan, *Methods Enzymol.*, 1989, **172**, 230–262.

Nanoscale

PAPER

View Article Online
View Journal

Cite this: DOI: 10.1039/c4nr04368e

Structural plasticity of calmodulin on the surface of CaF_2 nanoparticles preserves its biological function†

Alessandra Astegno,*[a] Elena Maresi,[a] Valerio Marino,[b] Paola Dominici,[a] Marco Pedroni,[a] Fabio Piccinelli[a] and Daniele Dell'Orco*[b]

Nanoparticles are increasingly used in biomedical applications and are especially attractive as biocompatible and biodegradable protein delivery systems. Herein, the interaction between biocompatible 25 nm CaF_2 nanoparticles and the ubiquitous calcium sensor calmodulin has been investigated in order to assess the potential of these particles to serve as suitable surface protein carriers. Calmodulin is a multifunctional messenger protein that activates a wide variety of signaling pathways in eukaryotic cells by changing its conformation in a calcium-dependent manner. Isothermal titration calorimetry and circular dichroism studies have shown that the interaction between calmodulin and CaF_2 nanoparticles occurs with physiologically relevant affinity and that the binding process is fully reversible, occurring without significant alterations in protein secondary and tertiary structures. Experiments performed with a mutant form of calmodulin having an impaired Ca^{2+}-binding ability in the C-terminal lobe suggest that the EF-hand Ca^{2+}-binding motifs are directly involved in the binding of calmodulin to the CaF_2 matrix. The residual capability of nanoparticle-bound calmodulin to function as a calcium sensor protein, binding to and altering the activity of a target protein, was successfully probed by biochemical assays. Even if efficiently carried by CaF_2 nanoparticles, calmodulin may dissociate, thus retaining the ability to bind the peptide encompassing the putative C-terminal calmodulin-binding domain of glutamate decarboxylase and activate the enzyme. We conclude that the high flexibility and structural plasticity of calmodulin are responsible for the preservation of its function when bound in high amounts to a nanoparticle surface.

Received 31st July 2014,
Accepted 11th October 2014

DOI: 10.1039/c4nr04368e

www.rsc.org/nanoscale

Introduction

Calcium (Ca^{2+}) is a ubiquitous intracellular messenger responsible for controlling numerous cellular processes in a wide range of organisms.[1] Cells respond to an extra-cellular stimulus by a transient change in intracellular Ca^{2+} concentration which, in turn, is sensed by an array of Ca^{2+}-binding proteins or Ca^{2+}-sensors that are able to adapt their shape so as to recognize their molecular partners.[2] Among these, calmodulin (CaM) is probably the most prototypical member, which acts as a Ca^{2+} messenger in all eukaryotic cells, recognizing more than 300 different protein partners involved in various fundamental biological mechanisms[3,4] such as cell motility, cytoskeleton architecture and function, growth, proliferation, metabolic homeostasis, ion transport, protein folding, and apoptosis. CaM is a small (~17 kDa), highly conserved, acidic protein with two globular domains (N- and C-domains or lobes) connected by a flexible spacer.[5] Each domain contains a pair of Ca^{2+}-binding motifs called EF-hands and binds two Ca^{2+} ions in a cooperative manner. The apparent affinity of CaM for Ca^{2+} is in the range of 10^{-6}–10^{-7} M and can increase in the presence of the target protein.[6] Notably, the N- and C-lobes differ in their affinity for Ca^{2+}, showing an apparent K_d of approximately 10 μM and 1 μM, respectively,[7,8] and adopt different conformations depending on the presence of Ca^{2+}. In the absence of Ca^{2+}, the two lobes adopt a closed conformation formed by a bundle of helices that are packed against each other, and most of the hydrophobic residues are shielded from the solvent.[9] Ca^{2+} binding to each globular domain leads to substantial alterations in the interhelical angles within the EF-hands to produce a more open conformation.[10] This results in the exposure of hydrophobic sites that bind to and activate a large number of target proteins. CaM displays a high degree of conformational plasticity, both at the level of individual

[a]Department of Biotechnology, University of Verona, Verona, Italy. E-mail: alessandra.astegno@univr.it; Fax: +39-045-802-7929; Tel: +39-045-802-7955
[b]Department of Life Sciences and Reproduction, Section of Biological Chemistry, University of Verona, Verona, Italy. E-mail: daniele.dellorco@univr.it; Fax: +39-045-802-7170; Tel: +39-045-802-7637

† Electronic supplementary information (ESI) available: Supplementary methods and figures. See DOI: 10.1039/c4nr04368e

amino acid side chains and of the orientation of entire domains, allowing for target proteins to evolve specific modes of CaM interaction and regulation during Ca^{2+} sensing.[11,12]

In the last few years, the central role of CaM and different Ca^{2+}/CaM-dependent systems in controlling several physiological processes and disease-associated conditions has clearly emerged. Altered CaM-dependent cell cycle regulation and proliferation have been described in tumor cells, and targeting of CaM and/or CaM-dependent systems has been considered a valid strategy for therapeutic intervention in cancer.[13] Moreover, recently discovered CaM point mutations associated with arrhythmogenic human pathologies[14] and the recent finding that CaM levels are significantly increased in Alzheimer's disease[15] suggest that several physiological conditions and diseases other than cancer may involve Ca^{2+}/CaM messenger systems, thus highlighting the importance of CaM as a target for new therapeutic approaches.

As one of the developing areas of nanomedicine, increasing interest has been dedicated to nanoparticle (NP) systems as carriers for protein delivery. NPs are expected to offer several advantages over more traditional devices, such as improved protein stability, protection from proteases, cell targeting, and bioavailability. Moreover, nanodevices are small enough to enter almost all areas of the body, including cells and organelles, potentially leading to a new approach to medicine.[16] Our group has previously investigated the possibility to use CaF_2 NPs as suitable carriers of Ca^{2+}-sensor proteins, analyzing the interaction between the prototypical neuronal calcium sensor recoverin and the nanodevices.[17] CaF_2 NPs are easily obtained by means of a straightforward synthetic protocol and were found to be biocompatible, showing no evidence of toxicity in experiments performed on HeLa and mesenchymal cells.[18] Moreover, CaF_2 NPs doped with suitable trivalent rare earth ions are efficient luminescent nano-probes, a feature that could be conveniently exploited for various bioimaging applications.[18]

CaF_2 NPs were found to significantly alter the structural and functional properties of recoverin and decrease its sensitivity to free Ca^{2+}, thus suggesting novel biological functions induced by the particle. These novel features seem to be related to the nature of these particles, which are constituted by a CaF_2 matrix that could be specifically recognized by the Ca^{2+}-sensor protein.

In order to devise a carrier system with broad biomedical or biotechnological applicability, it is important that surface-bound proteins retain their structural and functional properties. In this work, the suitability of CaF_2 NPs as nanocarriers of a model Ca^{2+}-sensor protein, namely the calmodulin isoform 1 (CaM1) from *A. thaliana*, has been investigated. For this purpose, as a direct probe of the biological functionality of the CaM–NP complex, the pyridoxal 5-phosphate (PLP)-dependent enzyme glutamate decarboxylase (Gad1) was used, which catalyzes the α-decarboxylation of L-glutamate to γ-aminobutyrate (GABA). A unique feature of plant Gad is the presence of a CaM-binding domain at its C-terminus, making it the best characterized metabolic enzyme regulated by Ca^{2+}/CaM in plants.

In this work, it was found that the binding of CaM1 to CaF_2 NPs is fully reversible and occurs with physiologically-relevant affinity. Using site-specific mutagenesis, we investigated the role of EF-hand motifs as possible sites for CaM1–NP interaction, and the effect of NPs on the Gad1–CaM1 complex activity and spectral properties has been evaluated.

Results and discussion

To investigate the interaction between CaM1 and NPs and its effect on Gad1 activation, the recombinant protein corresponding to CaM1, which represents the canonical CaM isoform, was utilized. The primary structure of *A. thaliana* CaM1 is highly conserved among plant CaMs identified in *Hordeum vulgare*, *Medicago sativa*, and *Petunia hybrida*, as well as very similar to those found in mammals (89% identity to vertebrate CaMs). Moreover, the canonical 12-amino acid loop of the CaM EF-hand motif, which binds Ca^{2+} with a pentagonal bipyramidal geometry including seven coordination sites, is strongly conserved (Fig. 1a and b). This conservation between plant and animal CaMs is not surprising since CaM is thought to be essential for eukaryotic cell function. A major difference in the primary structure with mammalian CaMs is the presence in plant CaMs of a cysteine residue at position seven in the 12-amino acid loop of the first EF-hand.

The synthesized CaF_2 NPs possess the fluorite-like crystal structure. They crystallize with a cubic structure of 5.46 Å unit cell length.[19] Each Ca^{2+} ion is surrounded by eight fluoride anions (as depicted in Fig. 1c for the red colored Ca^{2+} ion) and each fluoride anion is surrounded by four Ca^{2+} ions. Within the unit cell there are four Ca^{2+} and eight F^- ions and the distance between two nearest neighbour Ca^{2+} ions is 3.86 Å. As the CaF_2 NPs are capped with the citrate anion, several Ca^{2+} ions on the surface of the material are bound both to the fluoride anions and to the carboxylic group of the capping agent.

Thermodynamics of CaM1–NP interaction

Isothermal titration calorimetry (ITC) was used to investigate the affinity and thermodynamic parameters that accompany the binding of CaM1 to NPs. Raw data of CaM1-binding to CaF_2 NPs at 25 °C are shown in Fig. 2. The subsequent addition of CaM1 to CaF_2 NPs results in a pattern of exothermic binding spikes, characterized by the thermodynamic parameters shown in Table 1. The exothermicity of calorimetry peaks is believed to be due to the strong interaction between NPs and the protein. The data fitted well to a single process. Thus, interprotein interaction is not involved in binding and protein association appears to occur without any significant degree of cooperativity. The association constant was estimated to be $\sim 4.9 \times 10^5$ M^{-1}, corresponding to an apparent affinity of ~2 μM. The binding of CaM1 to NPs appears to be an enthalpically driven process, with the large, favorable value

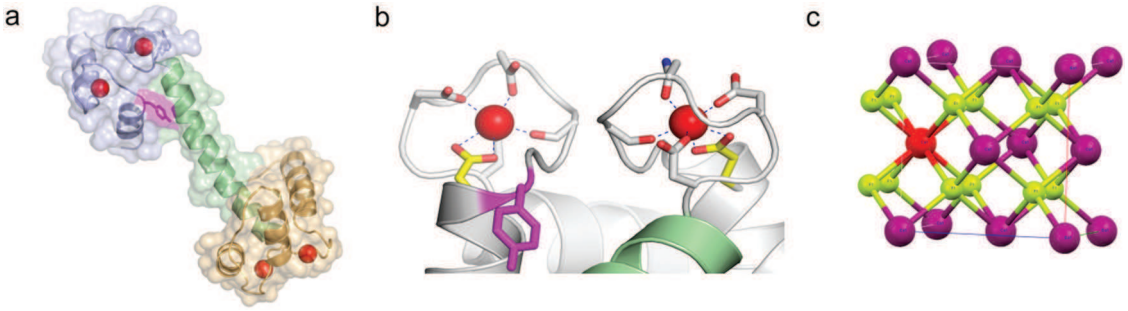

Fig. 1 Structural details of CaM1 from *A. thaliana* and of CaF_2 NPs. (a) Cartoon representation superimposed in transparency to the molecular surface representation highlights the typical architecture of CaM. The N-term lobe is shown in light orange, the linker region in light green, and the C-terminal lobe in light blue. The four Ca^{2+} ions, each bound to an EF-hand motif, are represented by red spheres while the unique Tyr residue (Y139) is represented by magenta sticks. (b) Close-up of the coordination of two Ca^{2+} ions (red spheres) at the C-terminal domain by five oxygens from carboxylic groups of acidic residues in each EF-hand motif (represented by sticks), a backbone carbonyl oxygen (represented by sticks) and a water molecule (not shown). The two Glu residues providing bidentate ligands and the target of mutagenesis (E105 and E141) are shown in yellow, and Tyr139 is represented by magenta sticks. Secondary structure elements from the C-terminal domain are represented by gray cartoons, while the visible portion of the linker region is represented by light green cartoons. (c) Detail of the CaF_2 unit cell: for the red colored Ca^{2+} ion the full coordination environment is shown. The figure was prepared with the software PyMol (The PyMOL Molecular Graphics System, Version 1.5.0.4, Schrödinger, LLC (a and b)) and the Mercury computer program for crystal structure visualisation, provided by CCDC (c).

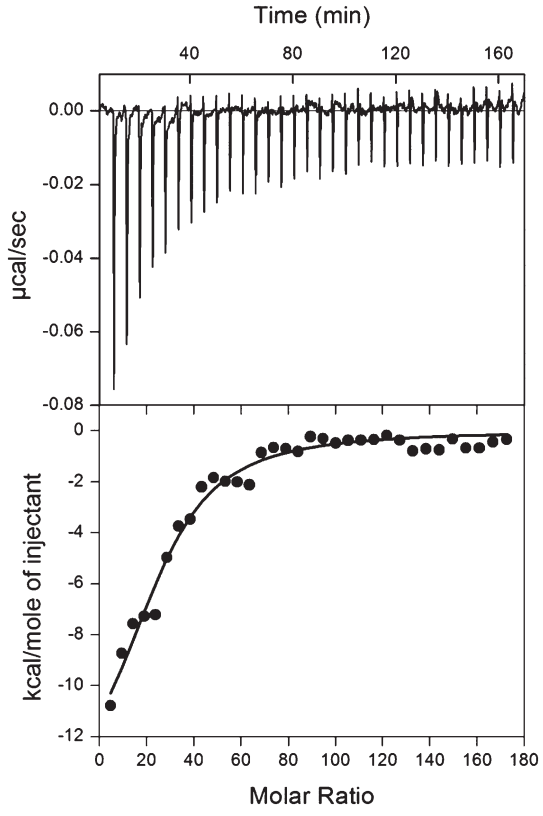

Fig. 2 ITC data for CaM1 in solution with CaF_2 NPs in decalcified 5 mM Tris-HCl and 150 mM KCl, pH 7.5, at 25 °C. The particle concentration in the cell (0.2 mL) was 240 nM, and the protein concentration in the syringe was 190 μM. The upper panel shows the raw data, and the bottom panel shows the plot of heat flow per mole of titrant (CaM1) *versus* the molar ratio (CaM1 : NP) at each injection together with a fit using a one-site binding model.

of the ΔH term that dominates over ΔS, thus suggesting that polar interactions are primarily responsible for CaM1–NP binding. The complete saturation of heat signal was observed at a CaM1 to NP molar ratio of ~120, which is consistent with the theoretical maximum number of bound CaM1 of ~144 for a ~25 nm diameter NP obtained by a previously described[17] simple geometric model of CaM1–NP interaction, where all objects are considered to be rigid spheres.

The parameter values obtained from the fitting process were only marginally affected by subtraction of the blank titration (CaM1 into buffer), and the reported values are without subtraction as the total concentration of CaM1 in the blank titration does not correspond to the free concentration of CaM1 obtained in the particle-binding experiments.

Ca^{2+}-dependent structural changes in CaM1 in the presence and absence of NPs

The shape of the far-UV CD spectrum (250–200 nm) of CaM1 from *A. thaliana* is very similar to that of bovine CaM for both the Ca^{2+}-free (apo) and Ca^{2+}-saturated (holo) forms[20,21] (Fig. 3a). This indicates that the overall secondary structure content of the two CaMs is very similar, which is expected given the very high sequence identity between the two proteins. The far-UV CD spectra of both the apo- and holo-forms have two minima at 208 and 222 nm indicating that the protein contains substantial α-helical structure. In the presence of saturating concentrations of Ca^{2+}, a major conformational change takes place causing an increase in the negative bands at 208 and 222 nm leading to a switch in the $\theta_{222}/\theta_{208}$ ratio from 0.91 in the apo-form to 0.94 in the Ca^{2+}-bound form (Table 2). In the literature, this change has been explained as an increase in the α-helical content, due to re-orientation/distortion of the α-helices[22] or a change in protein compactness upon Ca^{2+} binding.[23] The latter suggestion is

Table 1 Thermodynamics parameters involved in the binding between CaM1 and CaF_2 NPs, derived from ITC measurements[a]

	K_A (10^5 M^{-1})	ΔH (kcal mol^{-1})	Stoichiometry	ΔS (cal mol^{-1} K^{-1})	$\Delta G°$ (kcal mol^{-1})	n
CaM1 : NPs	4.9 ± 0.5	−21.72 ± 5.39	28.29 ± 3.61	−47.77 ± 18.97	−7.76 ± 0.06	6

[a] Weighted average and standard deviations are from n measurements. The ΔS and the $\Delta G°$ values were calculated from $\Delta H - T\Delta S = -RT \ln K_A$.

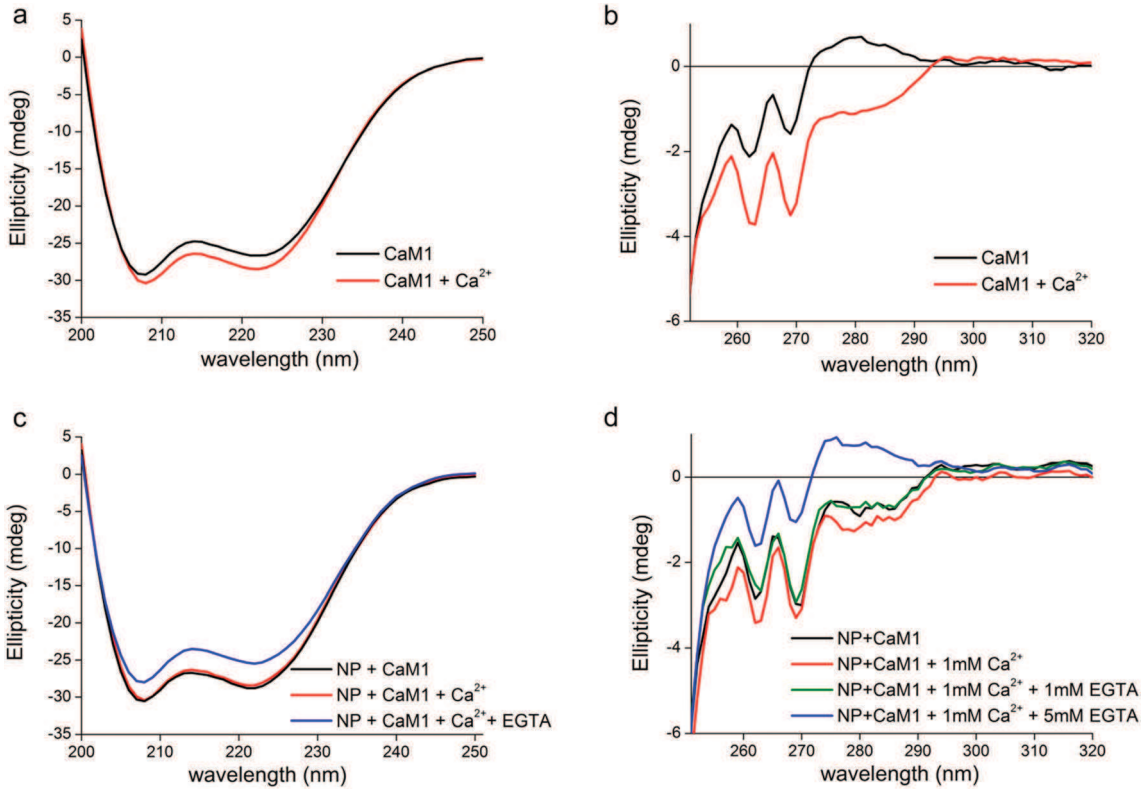

Fig. 3 Far- and near-UV CD spectra of CaM1 in the presence and absence of CaF_2 NPs. All measurements were performed at 25 °C in 5 mM Tris-HCl, pH 7.5, and 150 mM KCl buffer. (a) and (c) Far-UV CD spectra of 12 μM CaM1 in the presence of 1 mM Ca^{2+} or 1 mM EGTA, alone (a) and incubated (c) with 1.4 mg mL^{-1} CaF_2 NPs. (b) and (d) Near-UV CD spectra of 60 μM CaM1 in the presence of 1 mM Ca^{2+}, or 1 mM and 5 mM EGTA alone (b) and incubated (d) with 7 mg mL^{-1} CaF_2 NPs.

Table 2 The $\theta_{222}/\theta_{208}$ ratio of CaM1 in the absence and presence of NPs

	θ_{208} (mdeg)	θ_{222} (mdeg)	$\theta_{222}/\theta_{208}$
CaM1	−29.23	−26.67	0.91
CaM1 + Ca^{2+}	−30.39	−28.50	0.94
NP + CaM1	−30.56	−28.82	0.94
NP + CaM1 + Ca^{2+}	−30.44	−28.43	0.93
NP + CaM1 + EGTA	−28.00	−25.48	0.91

consistent with NMR data comparing apo- and holo-CaM, showing that the α-helical contents of the two states are similar.[10] It is also compatible with recent surface plasmon resonance studies[24] that showed variations in the compactness of CaM upon Ca^{2+} binding.

Thermal denaturation of CaM1 was further investigated by ramping the temperature from 20 °C to 96 °C at a rate of 1 °C min^{-1} and monitoring the ellipticity signal at 208 nm (θ_{208}). Under these conditions, apo-CaM1 is denatured at 60 °C and above. As already reported in ref. 25 addition of Ca^{2+} leads to stabilization of the structure of CaM1 where even at 90 °C, the protein retains evidence of a partially folded state (see Fig. S1†). Interestingly, incubation with CaF_2 NPs yielded thermal denaturation profiles that were very similar to one another independent of the presence of free Ca^{2+} and to the isolated protein profile in the presence of Ca^{2+} (Fig. S1†).

Fig. 3b shows the near-UV CD spectra of CaM1 in the apo-form and in the presence of added Ca^{2+}. CD spectroscopy in the near-UV region (320–250 nm) allows monitoring the asymmetric environment of aromatic residues, which was observed to change significantly upon Ca^{2+}-binding. *A. thaliana* CaM1 contains no tryptophan, nine phenylalanine residues, and a single tyrosine, which lies at position 139 in the "loop" of Ca^{2+}-binding site 4 (Fig. 1).

As observed for other CaMs,[26] the prominent decrease in ellipticity at 262 and 268 nm upon Ca^{2+} binding, as well as the shoulder at 255 nm, is attributed to phenylalanine residues that are equally distributed in the N (5) and C (4) domains. The broad unresolved negative band above 273 nm in the Ca^{2+}-saturated protein can be attributed to the single tyrosine residue in the C-terminal half of the molecule. Metal binding causes a sign inversion of the dichroic signal previously observed also in *Neurospora* CaM,[27] spinach CaM,[28] zucchini CaM,[29] and *Drosophila melanogaster* CaM,[26] which all possess only one tyrosine residue. In the presence of EGTA, both near- and far-UV CD spectra of CaM1 were identical to that of apo-CaM1, confirming the high level of both protein and buffer decalcification (data not shown).

Far- and near-UV CD spectroscopy was also used to determine whether the same structural changes occurred upon CaM1–NP interaction (Fig. 3c and d). In the far-UV, CD spectra are more negative in the presence of NPs and become almost indistinguishable in shape and intensity from those of the Ca^{2+}-saturated free protein (see Fig. 3a). The spectra showed a very similar shape for NP-bound CaM1, independently of the presence of free Ca^{2+}, as quantitatively demonstrated by the same $\theta_{222}/\theta_{208}$ ratio (0.94 *versus* 0.93 respectively, Table 2). This value is identical to that observed for the Ca^{2+}-bound form of CaM1 (0.94, Table 2). Thus, NPs induced the protein to acquire a Ca^{2+} like conformation. Interestingly, upon removal of free calcium by EGTA, the spectrum showed a shape that was very similar to that of Ca^{2+}-free CaM1, as is evident from the identical $\theta_{222}/\theta_{208}$ ratio (0.91 in both cases, Table 2). This suggests that the binding of CaM1 to NPs, both in the presence and absence of Ca^{2+}, is almost completely reversible upon addition of saturating concentrations of EGTA. Reversibility of the association between CaM1 and NPs was further demonstrated by dynamic light scattering (DLS) experiments in the presence of saturating concentrations of Ca^{2+} and EGTA (Fig. S2†).

Along the same lines, near-UV CD spectra in the presence of CaF_2 NPs were very similar to those of the Ca^{2+}-bound protein, and upon addition of EGTA a behavior comparable to that of the apo-protein was observed (Fig. 3d). We used 5 mM EGTA for the near-UV spectra to maintain the same excess of EGTA over CaM1 used in the far-UV experiments (~83-fold excess). All these data seem to suggest that the interaction between the CaF_2 matrix and CaM1 is mediated by the same CaM1 Ca^{2+}-binding sites involved in the binding of free Ca^{2+} ions to the unbound protein.

Role of C-terminal domain Ca^{2+} binding sites in CaM1–NP interactions

To investigate whether EF-hand motifs are directly involved in the binding of CaM1 to CaF_2 NPs, a CaM1 mutant was prepared with a Ca^{2+} binding capacity limited to the N-lobe by substituting the negatively charged glutamate residues at position 12 (Glu105 and Glu141) in both the EF-hand motifs at the C-terminal domain to neutral glutamine residues. Sequence comparisons of EF-hand Ca^{2+}-binding sites from other proteins reveal that the glutamate at position 12 is one of the most conserved residues within the EF-hand motif.[30] The carboxylate group of this residue is unique as it provides two ligands for the Ca^{2+} ion, suggesting a critical role in Ca^{2+}-binding (Fig. 1). It was decided to remove the Ca^{2+} binding sites at the C-terminal domain, since in mammalian CaM1 Ca^{2+}-binding affinities are different for the N- and C-terminal lobes, with the latter having a 3- to 10-fold higher affinity for Ca^{2+}. The residual capability of the mutant protein to interact with NPs was further probed by CD spectroscopy. Interestingly, the spectra of the isolated mutant did not show the Ca^{2+} induced changes in the near-UV region typical of the wild-type (wt) protein. Indeed, when treated with the same amount of Ca^{2+} and EGTA used for the wt, the CaM1 variant exhibited CD spectra that were identical both in shape and intensity (Fig. 4a). Moreover, in the presence of NPs the near-UV spectra were very similar to those of the protein in the absence of NPs, both with saturating concentrations of Ca^{2+} and EGTA (Fig. 4b). Taken together, this suggests that there is a direct interaction between the Ca^{2+}-binding motifs of the protein and the CaF_2 matrix. However, the absence of significant variations in the CD spectra of the mutant in the absence and presence of NPs can be ascribed to either a weaker interaction between the mutant protein and the NP compared to the wt protein, to

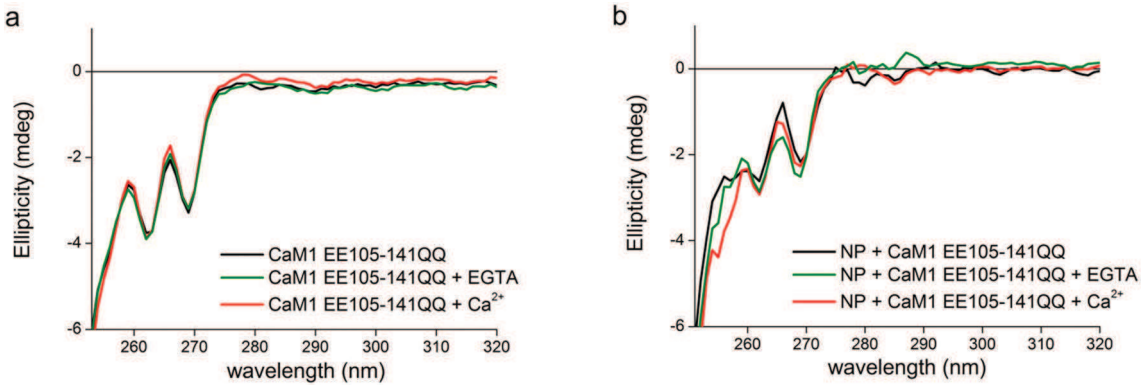

Fig. 4 Near-UV CD spectra of CaM1 EE105-141QQ double mutant. Near-UV CD spectra of 60 μM CaM1 mutant in the presence of 1 mM Ca^{2+} or 1 mM EGTA alone (a) and incubated (b) with 7 mg mL^{-1} CaF_2 NPs.

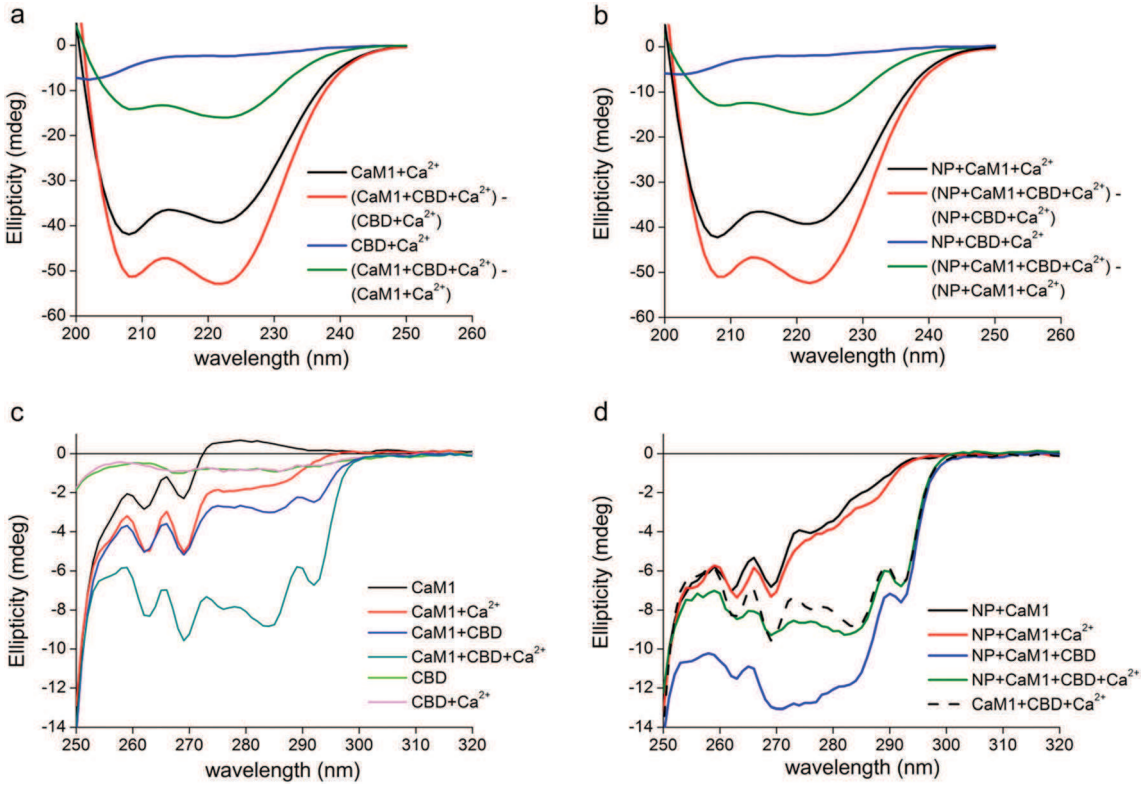

Fig. 5 Far- and near-UV CD spectra of CaM1, CBD peptide and CaM1–CBD complex in the presence of Ca^{2+} with and without CaF_2 NPs. All measurements were performed at 25 °C in 5 mM Tris-HCl, pH 7.5, and 150 mM KCl buffer. (a) and (b) Far-UV CD spectra of 12 μM CaM1 and 24 μM peptide in the presence of 1 mM Ca^{2+}, alone (a) and incubated (b) with 1.4 mg mL^{-1} CaF_2 NPs. (c) and (d) Near-UV CD spectra of 60 μM CaM1 and 120 μM peptide in the presence of 1 mM Ca^{2+}, alone (c) and incubated (d) with 7 mg mL^{-1} CaF_2 NPs.

a minor conformational change in the tertiary structure of the mutant upon Ca^{2+}-binding, or both. ITC data (Fig. S3†) support the former hypothesis, as addition of the CaM1 mutant to CaF_2 NPs under the same experimental conditions used for the wt protein (see Fig. 2) exhibited a profile that was not ascribable to a binding event in terms of both heat change and signal intensity.

The high affinity of CaM1 for the CaF_2 NPs may be partly explained by the high local concentration of the Ca^{2+} ion (~41 M, within the crystal, see Supplementary methods in ESI†). Presumably, upon interaction between CaM1 and CaF_2 NPs, the capping agent is replaced by the donating groups of the protein. This hypothesis is supported by our previous study, in which the same type of NPs were shown to bind recoverin despite the presence of citrate as a capping agent.[17] In particular, the geometric environment of the Ca^{2+} ions on the surface, involved in the bond with CaM1, should be constituted by several donating oxygen atoms from the residues of the EF-hand motif and by several fluoride anions from the fluorite matrix.

Binding of CaM1 to Gad1 CaM binding domain (CBD) peptide

Since Gad1 is a CaM-binding protein, comparing the capacity of CaM1 to interact with Gad1 binding domain (CBD) in the presence and absence of NPs would be informative regarding the residual ability of NP-bound CaM1 to bind to its target. The ability of CaM1 to bind the Gad1 CBD was thus assessed by CD spectroscopy. Previous small-angle X-ray scattering (SAXS) analysis demonstrated a 1 : 2 CaM1 : peptide stoichiometry for the interaction,[31] and the binding of the CBD peptide to CaM1 in the presence of Ca^{2+} was thus investigated under the same conditions.

It has been established that CaM-binding peptides adopt an amphipathic helix conformation when binding to Ca^{2+}-saturated CaM1.[32–34] As shown in Fig. 5, the far-UV CD spectrum of the isolated CBD peptide in the presence of Ca^{2+} suggests that the peptide was not folded in a distinct structure (Fig. 5a). When the peptide was incubated with CaM1, however, the interaction led to significant structural rearrangements of both CBD and CaM1 (Fig. 5a and Table 3). An intense dichroic signal with two negative peaks at 208 and 222 nm was observed (Fig. 5a, green line), suggesting that upon interaction with CaM1 the peptide adopted the typical α-helical conformation observed with other interacting peptides. Interestingly, the intensity of the signal arising from CaM1 also increased upon interaction with the peptide (Fig. 5a, red line, and Table 3), indicating that a helical fold with increased ellipticity distinguished the formation of the

Table 3 The $\theta_{222}/\theta_{208}$ ratio of CaM1 in the presence and absence of CBD and NPs

	θ_{208} (mdeg)	θ_{222} (mdeg)	$\theta_{222}/\theta_{208}$
CaM1 + CBD	−52.85	−49.95	0.94
CaM1 + CBD + Ca^{2+}	−56.11	−55.31	0.98
(CaM1 + CBD) − CBD	−47.70	−47.30	0.99
(CaM1 + CBD + Ca^{2+}) − (CBD + Ca^{2+})	−51.24	−52.87	1.03
(CaM1 + CBD) − CaM1	−12.56	−13.19	1.05
(CaM1 + CBD + Ca^{2+}) − (CaM1 + Ca^{2+})	−14.15	−15.97	1.13
NP + CaM1 + CBD	−55.55	−54.58	0.98
NP + CaM1 + CBD + Ca^{2+}	−55.16	−54.30	0.98
(NP + CaM1 + CBD) − (NP + CBD)	−50.95	−52.41	1.03
(NP + CaM1 + CBD + Ca^{2+}) − (NP + CBD + Ca^{2+})	−50.98	−52.37	1.03
(NP + CaM1 + CBD) − (NP + CaM1)	−13.25	−15.24	1.15
(NP + CaM1 + CBD + Ca^{2+}) − (NP + CaM1 + Ca^{2+})	−12.89	−15.01	1.16

complex as compared to individual spectra of CaM and CBD. Moreover, the shape of the spectra referring to the complex also differed from that of the individual components, as demonstrated by the $\theta_{222}/\theta_{208}$ ratio, which for CaM1 increased from 0.94 (Table 2) to 0.98 (Table 3) in the presence of the CBD peptide and Ca^{2+}, approaching the ~1.02 values observed for coiled-coil motifs.[35,36] Such a value was fully reached for the spectra obtained by subtracting: (i) the spectrum of the CaM1 alone from that in complex with CBD peptide (Fig. 5a, green line; $\theta_{222}/\theta_{208}$ = 1.13, Table 3); (ii) the spectrum of CBD peptide alone from that in complex with CaM1 (Fig. 5a, red line; $\theta_{222}/\theta_{208}$ = 1.03, Table 3). Thus, the binding between CaM1 and the CBD peptide induced a tight interaction between the constituting α-helices, which in certain regions may coil together like the strands of a rope. It should be noticed that the same experiments performed in the absence of free Ca^{2+} led to similar results, with lower spectral intensities (Table 3), indicating a substantial role of free Ca^{2+} in facilitating and stabilizing the interaction between CaM1 and the CBD peptide (Fig. S4†). Indeed, we cannot exclude that resuspension of lyophilized peptides induced a small but significant contamination with free Ca^{2+}.

Results from near-UV CD spectroscopy are in agreement with those in the far-UV (Fig. 5c). The CBD peptide, either in the presence or absence of Ca^{2+}, did not show a well defined tertiary structure (green and pink curves); however, when the peptide was incubated with CaM1 the interaction became apparent even in the absence of Ca^{2+} or in the presence of a small contamination with Ca^{2+} induced by the resuspension of lyophilized peptides. The complex showed a conformation (dark blue curve) similar to that of the Ca^{2+}/CaM1 (red curve), with appreciable differences ascribable to the band of Tyr139. When saturating Ca^{2+} was added, drastic changes over the entire spectral range were clearly detected (cyan curve), implying important conformational changes involving both the phenylalanine and tyrosine bands, as suggested by the significantly increased signal and the onset of finer band structure, especially in the region around Tyr139.

The same experiments were performed in the presence of NPs (Fig. 5b and d). Overall, the results obtained in the far-UV region were similar to those obtained in the absence of NPs and in the presence of saturating Ca^{2+} (compare Fig. 5a and b). Considering the spectral shape and intensity, the presence of NPs was found to mimic that of free Ca^{2+}, as almost identical intensities and $\theta_{222}/\theta_{208}$ ratios were obtained, compared to those in the absence of NPs but in the presence of saturating free Ca^{2+} (Table 3). Moreover, adding saturating Ca^{2+} to the suspension in the presence of NPs affected neither the intensity nor the shape of any spectra (Table 3).

Interesting results were obtained from CD spectroscopy in the near-UV region when the interactions between CaM1 and the CBD peptide were investigated in the presence of NPs (Fig. 5d). When no free Ca^{2+} was added to the suspension, a large dichroic signal was observed with local maxima that only partly reflected those observed in other cases (dark blue line). This suggests that at low Ca^{2+} the peptide might interact with CaM1 and/or the NP, resulting in an overall different tertiary structure, at least considering the local environment of phenylalanine residues and that of Tyr139. However, in the presence of saturating free Ca^{2+} the spectrum (green line) was similar to that observed in the absence of NPs (black dashed line in Fig. 5d or cyan line in Fig. 5c), and specific features of the spectral pattern such as a local maximum at 290 nm were clearly present.

Overall, results from CD experiments suggest a virtually complete capability of CaM1 to bind the CBD peptide even when bound to NPs, and to undergo the required conformational switches that are triggered or enhanced by free Ca^{2+} in a structurally correct and reversible manner.

Effect of NPs on Gad1 activity and spectral properties

CD experiments in the presence of Gad1 CBD provide information about the ability of both NP-bound and unbound CaM1 to bind the target in the presence of saturating Ca^{2+}. However, they cannot thoroughly probe the residual capability of CaM1 to act as a sensor protein that transduces Ca^{2+} signals by binding to and altering the activity/function of a target protein. To investigate this aspect, Gad1 activity was measured in the presence of CaM1–NP complexes. Gad1 is a cytosolic enzyme that exhibits a dual regulation: pH regulation, with a maximum activity at pH 5.8, and a Ca^{2+}/CaM1 activation at neutral pH. We tested Gad1's ability to perform a decarboxylation reaction in the presence of CaM1 and NPs at pH 7.5, where it is influenced mostly by CaM1.[31] Interestingly, at this pH, CaM1 previously incubated with NPs is still able to cause Gad1 activation in a similar manner to the effect observed in the absence of NPs and restores an activity profile comparable to that of the Gad1–CaM1 complex. In particular, as shown in Fig. 6a, in the presence of NPs the enzyme retains about 70% of its activity.

Ca^{2+}/CaM1 also has a clear impact on the spectral properties of Gad1. The UV-Vis spectrum of Gad1 displays characteristic absorption bands with maxima at 415 and 338 nm, which are attributed to the ketoenamine and enolimine forms of the Schiff base, respectively,[31] and whose relative intensities depend on pH: the 338 nm band increases with increasing pH,

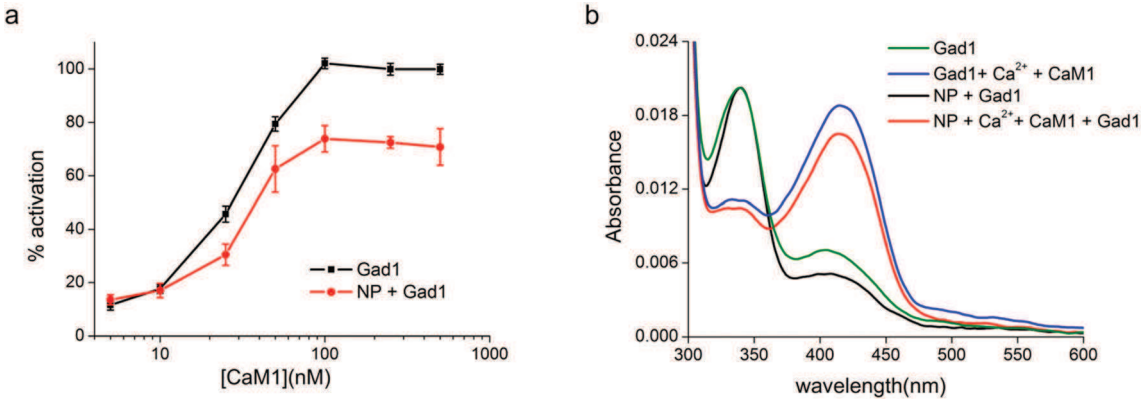

Fig. 6 Effects of CaF_2 NPs on the Gad1–Ca^{2+}/CaM1 complex activity and spectral properties. (a) GABA formation as a function of CaM1 concentrations in the presence and absence of CaF_2 NPs. Gad1 activity assays were performed in a solution containing 25 mM MES, 25 mM MOPS, 150 mM NaCl, and 2 mM $CaCl_2$ at pH 7.5 in the absence (black squares) and presence (red circles) of 0.13 mg mL^{-1} CaF_2 NPs. 100 mM L-glutamate, 0.6 μg of Gad1, and the indicated concentration of CaM1 were used for each assay. (b) Absorbance spectra were recorded in 25 mM MES, 25 mM MOPS, 150 mM NaCl, and 2 mM $CaCl_2$ at pH 7.5 for Gad1 and Gad1–Ca^{2+}/CaM1 complex in the presence and absence of 1.4 mg mL^{-1} NPs.

while the 415 nm band decreases. Ca^{2+}/CaM1-binding essentially abolishes the pH-dependence in the UV-Vis spectrum: the 338 nm species is strongly reduced, while the protonated Schiff base (415 nm) is enhanced compared to unbound Gad1. In order to determine the impact of NPs on the spectral properties of Gad1, we monitored the spectral behavior of the enzyme after NPs-CaM1 binding. After subtraction of the contribution of CaF_2 NPs, which show a modest absorption band around 330 nm, Gad1 spectra in the presence of Ca^{2+}/CaM1 are still characterized by a lack of interconversion of the two tautomers, indicating that CaM1 after interaction with NPs is able to move into solution, bind Gad1 at its CaM binding domain, and affect the tautomeric equilibrium of the internal aldimine, as in the absence of NPs (Fig. 6b).

Conclusions

Taken together, our data revealed that, upon NPs interaction, CaM1 retains an almost complete functionality, being able to both bind the peptide encompassing the putative C-terminal CBD of Gad1 and to activate the Gad1 protein. Thus, the capability of the protein to work as a Ca^{2+} sensor, recognizing and activating its biological target, is fully preserved in the presence of CaF_2 NPs, which seem to represent suitable surface carriers for this protein, likely due to the high structural plasticity of CaM1. The apparent protein affinity towards nanoparticle surfaces ($K_d \sim 2$ μM) is lower compared to the value of the dissociation constant of the Gad1–CaM1 complex ($K_d \sim 0.1$ μM) previously reported,[31] pointing to a very tight binding of the three CaM molecules to the Gad1 hexamer. Thus, after interaction with NPs, it is reasonable to conclude that CaM1 is able to dissociate, move into solution and activate the Gad1 enzyme. Furthermore, the fact that both interactions (NPs–CaM1 and CaM1–Gad1) are characterized by affinity constants with physiological relevance makes the system of great interest for different biotechnological and biomedical applications.

Experimental

Protein preparation and peptide synthesis

CaM1 from *Arabidopsis thaliana* was expressed and purified as described previously[31] with some modifications elucidated in the ESI.†

The recombinant mutant carrying various E to Q substitutions was generated based on the sequence alignment of CaM1 with human, bovine and other plant CaMs. The EE105-141QQ mutant form of CaM1 was made from the wt construct pET12b-AtCaM1 using the QuikChange® site-directed mutagenesis kit (Agilent Technologies) following the manufacturer's protocols. The kit employs double-stranded DNA as a template, two complementary oligonucleotide primers containing the desired mutation, and *Dpn*I endonuclease to digest the parental DNA template. The coding region of the mutated plasmid was verified by DNA sequencing. *E. coli* strain BL21 (DE3) cells were transformed and used for expression. The conditions for expression and purification of the mutant were as described for the wt protein.[31] Purified CaM1 EE105-141QQ mutant was at least 95% pure with an estimated molecular mass of 17 kDa based on SDS-PAGE analysis.

Purified wt and mutant proteins were dialyzed against decalcified NH_4HCO_3 buffer, lyophilized, and stored at −80 °C until use.

The 32 amino acid polypeptide encompassing the putative C-terminal CaM-binding domain of Gad1 (CBD) was chemically synthesized by GenScript Corporation. The sequence was as follows: VTVKKSDIDKQRDIITGWKKFVADRKKTSGIC. The peptide was 93.6% pure as determined by high pressure liquid chromatography. The concentration of the peptide was determined from the calculated molar extinction coefficient (ε_{280} = 5500 M^{-1} cm^{-1}, http://web.expasy.org/protparam/).

Building a homology model of CaM1 from *A. thaliana*

The homology model of the Ca^{2+}-bound CaM1 from *A. thaliana* was built using the SWISS-MODEL Homology Modeling server

(swissmodel.expasy.org).[37,38] The best template chosen for the modeling was CaM from potato (PCM6, PDB entry: 1rfj; resolution: 2.0 Å[39]), sharing a ~96% sequence identity with CaM1 from *A. thaliana* and likewise harboring a tyrosine residue at position 138. The Global Model Quality Estimation (GMQE) index was 0.97, indicating a high reliability for the homology model, also confirmed by the satisfactory values of the four structural descriptors (torsion angles, all atom and C-beta interactions, solvation potential) making up the QMEAN potential scoring function.

Nanoparticle synthesis and decalcification

The synthesis of CaF_2 NPs was performed as previously described.[17,18] The suspension of NPs in the working buffer (5 mM Tris-HCl, pH 7.5, 150 mM KCl) was highly monodisperse with 24.9 ± 0.4 nm average diameter for the NPs, as probed by dynamic light scattering as described previously.[17] A 15 mg mL^{-1} stock NPs solution was prepared in decalcified water. The complete decalcification of NPs was achieved by stirring the solution overnight in the presence of a dialysis membrane tube containing the chelating ion exchange resin Chelex®100 (BioRad).

Estimate of size-dependent protein coverage of the NP surface and concentration adjustments

The evaluation of the maximum number of CaM1 bound to CaF_2 NPs was done as previously reported by our group.[17] In the presence of NPs with a diameter of 25 nm, the theoretical maximum number of bound CaM1 is ~144. Details are provided in the ESI.†

Dynamic light scattering experiments

DLS measurements were performed as reported in the ESI.†

Isothermal titration calorimetry

Calorimetric measurements were performed using a TA isothermal titration microcalorimeter (TA Instruments). CaM1 was titrated into suspended NPs at 25 °C. For a typical NP–CaM1 titration, 0.24 μM NPs were placed in the reaction cell (200 μL). The protein was dissolved to 190 μM, corresponding to 3.2 mg mL^{-1}, in decalcified 5 mM Tris-HCl, pH 7.5, 150 mM KCl. This protein concentration was chosen because in CaM1 solutions above 4 mg mL^{-1}, CaM1 exists as dimers due to the formation of inter-chain disulfide bonds involving a cysteine residue at position 27. For titration experiments, 1.5 μL of CaM1 solution was injected into the reaction cell at 300 s intervals, with a total number of 34 injections, which were found to be sufficient to obtain complete binding curves. The pH of the protein solution was adjusted to match the pH of the particle solution (pH 7.5). Particle and protein solutions were equilibrated to 25 °C and degassed prior to each titration. The reference cell was filled with water during all titration experiments and the NP suspension in the sample cell was constantly stirred at 250 rpm. Calorimetric curves provide a correlation between thermal flow involved in each injection and time. Positive peaks stand for endothermic reactions and negative peaks stand for exothermic reactions. From the known concentrations of the protein and particles, the stoichiometry, affinity, and enthalpy changes upon binding were derived by fitting the data to a one-site binding model using the software NanoAnalyze (TA Instruments). In order to determine the heat of dilution, CaM1 at the same concentration as in the particle-binding experiments was titrated into the buffer.

Spectroscopic measurements

Absorption spectra were obtained with a Jasco-V560 UV-Vis spectrophotometer using 4 μM Gad1 in 25 mM MES, 25 mM MOPS, 150 mM NaCl, 2 mM $CaCl_2$ without CaM1 or with 12 μM CaM1 in the presence and absence of 1.4 mg mL^{-1} NPs.

CD measurements were obtained using a Jasco J-710 spectropolarimeter at 25 °C in a buffer solution containing 5 mM Tris-HCl, pH 7.5, and 150 mM KCl. Both near-UV (250–320 nm) and far-UV spectra (200–250 nm) were recorded at a scan rate of 50 nm min^{-1}, a bandwidth of 1 nm, and an integration time of 4 s. Five spectra accumulations were averaged for each sample, and the spectrum of the buffer (with or without NPs) was considered as blank and subtracted. For far-UV spectra, the protein concentration was 12 μM in 0.1 cm cuvettes, while for near-UV spectra it was 60–65 μM in 1 cm cuvettes.

CD spectra of the CaM1–peptide complex were obtained using a protein : peptide ratio of 1 : 2. In particular, for far-UV spectra 12 μM CaM1 and 24 μM peptide were used, while for near-UV spectra 60 μM CaM1 and 120 μM peptide were mixed in 5 mM Tris-HCl, pH 7.5, containing 150 mM KCl.

Thermal denaturation experiments were carried out as reported in ESI.†

Gad1 activity assay

Enzyme activity assays were done as described previously[40] with slight modifications. Briefly, Gad1 reactions were performed at 30 °C using 100 mM L-glutamate as a substrate in 25 mM MES, 25 mM MOPS, 150 mM NaCl, 2 mM $CaCl_2$ without CaM1 or with various concentrations of CaM1 (from 5 nM to 1 μM) in the absence and presence of NPs, at pH 7.5. GABA produced by the Gad1 reaction was estimated using a GABASE (Sigma) coupled reaction, which produces NADPH. The NADPH concentration was calculated from the absorbance at 340 nm, using a molar extinction coefficient ε_{NADPH} = 6220 M^{-1} cm^{-1}. The GABASE reaction mix contains 1 mM α-ketoglutarate, 1 mM NADP, 1 mM DTT, and 0.6 U GABASE in 0.1 M Hepes buffer, pH 8.6.

References

1 M. J. Berridge, P. Lipp and M. D. Bootman, The Versatility and Universality of Calcium Signalling, *Nat. Rev. Mol. Cell Biol.*, 2000, **1**(1), 11–21.

2 E. A. Permyakov and R. H. Kretsinger, Color Plates, in *Calcium Binding Proteins*, John Wiley & Sons, Inc., 2010, pp. c1–c12.
3 E. Carafoli, Calcium Signaling: A Tale for All Seasons, *Proc. Natl. Acad. Sci. U. S. A.*, 2002, **99**(3), 1115–1122.
4 D. Chin and A. R. Means, Calmodulin: A Prototypical Calcium Sensor, *Trends Cell Biol.*, 2000, **10**(8), 322–328.
5 Y. S. Babu, C. E. Bugg and W. J. Cook, Structure of Calmodulin Refined at 2.2 a Resolution, *J. Mol. Biol.*, 1988, **204**(1), 191–204.
6 M. Piazza, V. Taiakina, S. R. Guillemette, J. G. Guillemette and T. Dieckmann, Solution Structure of Calmodulin Bound to the Target Peptide of Endothelial Nitric Oxide Synthase Phosphorylated at Thr495, *Biochemistry*, 2014, **53**(8), 1241–1249.
7 S. Linse, A. Helmersson and S. Forsen, Calcium Binding to Calmodulin and Its Globular Domains, *J. Biol. Chem.*, 1991, **266**(13), 8050–8054.
8 W. S. VanScyoc, B. R. Sorensen, E. Rusinova, W. R. Laws, J. B. Ross and M. A. Shea, Calcium Binding to Calmodulin Mutants Monitored by Domain-Specific Intrinsic Phenylalanine and Tyrosine Fluorescence, *Biophys. J.*, 2002, **83**(5), 2767–2780.
9 H. Kuboniwa, N. Tjandra, S. Grzesiek, H. Ren, C. B. Klee and A. Bax, Solution Structure of Calcium-Free Calmodulin, *Nat. Struct. Biol.*, 1995, **2**(9), 768–776.
10 M. Zhang, T. Tanaka and M. Ikura, Calcium-Induced Conformational Transition Revealed by the Solution Structure of Apo Calmodulin, *Nat. Struct. Biol.*, 1995, **2**(9), 758–767.
11 M. Zhang, C. Abrams, L. Wang, A. Gizzi, L. He, R. Lin, Y. Chen, P. J. Loll, J. M. Pascal and J. F. Zhang, Structural Basis for Calmodulin as a Dynamic Calcium Sensor, *Structure*, 2012, **20**(5), 911–923.
12 A. Villarroel, M. Taglialatela, G. Bernardo-Seisdedos, A. Alaimo, J. Agirre, A. Alberdi, C. Gomis-Perez, M. V. Soldovieri, P. Ambrosino, C. Malo and P. Areso, The Ever Changing Moods of Calmodulin: How Structural Plasticity Entails Transductional Adaptability, *J. Mol. Biol.*, 2014, **426**, 2717–2735.
13 M. W. Berchtold and A. Villalobo, The Many Faces of Calmodulin in Cell Proliferation, Programmed Cell Death, Autophagy, and Cancer, *Biochim. Biophys. Acta, –Mol. Cell Res.*, 2014, **1843**(2), 398–435.
14 L. Crotti, C. N. Johnson, E. Graf, G. M. De Ferrari, B. F. Cuneo, M. Ovadia, J. Papagiannis, M. D. Feldkamp, S. G. Rathi, J. D. Kunic, M. Pedrazzini, T. Wieland, P. Lichtner, B. M. Beckmann, T. Clark, C. Shaffer, D. W. Benson, S. Kaab, T. Meitinger, T. M. Strom, W. J. Chazin, P. J. Schwartz and A. L. George Jr., Calmodulin Mutations Associated with Recurrent Cardiac Arrest in Infants, *Circulation*, 2013, **127**(9), 1009–1017.
15 N. Esteras, C. Alquezar, A. de la Encarnacion, A. Villarejo, F. Bermejo-Pareja and A. Martin-Requero, Calmodulin Levels in Blood Cells as a Potential Biomarker of Alzheimer's Disease, *Alzheimer's Res. Ther.*, 2013, **5**(6), 55.
16 V. L. Colvin, The Potential Environmental Impact of Engineered Nanomaterials, *Nat. Biotechnol.*, 2003, **21**(10), 1166–1170.
17 V. Marino, A. Astegno, M. Pedroni, F. Piccinelli and D. Dell'Orco, Nanodevice-Induced Conformational and Functional Changes in a Prototypical Calcium Sensor Protein, *Nanoscale*, 2014, **6**(1), 412–423.
18 N. N. Dong, M. Pedroni, F. Piccinelli, G. Conti, A. Sbarbati, J. E. Ramirez-Hernandez, L. M. Maestro, M. C. Iglesias-de la Cruz, F. Sanz-Rodriguez, A. Juarranz, F. Chen, F. Vetrone, J. A. Capobianco, J. G. Sole, M. Bettinelli, D. Jaque and A. Speghini, Nir-to-Nir Two-Photon Excited Caf2:Tm3+, Yb3+ Nanoparticles: Multifunctional Nanoprobes for Highly Penetrating Fluorescence Bio-Imaging, *ACS Nano*, 2011, **5**(11), 8665–8671.
19 D. N. Batchelder and R. O. Simmons, Lattice Constants and Thermal Expansivities of Silicon and of Calcium Fluoride between 6° and 322°K, *J. Chem. Phys.*, 1964, **41**(8), 2324–2329.
20 S. R. Martin and P. M. Bayley, The Effects of Ca2+ and Cd2+ on the Secondary and Tertiary Structure of Bovine Testis Calmodulin. A Circular-Dichroism Study, *Biochem. J.*, 1986, **238**(2), 485–490.
21 T. H. Crouch and C. B. Klee, Positive Cooperative Binding of Calcium to Bovine Brain Calmodulin, *Biochemistry*, 1980, **19**(16), 3692–3698.
22 I. Protasevich, B. Ranjbar, V. Lobachov, A. Makarov, R. Gilli, C. Briand, D. Lafitte and J. Haiech, Conformation and Thermal Denaturation of Apocalmodulin: Role of Electrostatic Mutations, *Biochemistry*, 1997, **36**(8), 2017–2024.
23 D. Dell'Orco, P. Behnen, S. Linse and K. W. Koch, Calcium Binding, Structural Stability and Guanylate Cyclase Activation in Gcap1 Variants Associated with Human Cone Dystrophy, *Cell. Mol. Life Sci.*, 2010, **67**(6), 973–984.
24 S. Sulmann, D. Dell'Orco, V. Marino, P. Behnen and K. W. Koch, Conformational Changes in Calcium-Sensor Proteins under Molecular Crowding Conditions, *Chemistry*, 2014, **20**(22), 6756–6762.
25 J. P. Browne, M. Strom, S. R. Martin and P. M. Bayley, The Role of Beta-Sheet Interactions in Domain Stability, Folding, and Target Recognition Reactions of Calmodulin, *Biochemistry*, 1997, **36**(31), 9550–9561.
26 J. F. Maune, K. Beckingham, S. R. Martin and P. M. Bayley, Circular Dichroism Studies on Calcium Binding to Two Series of Ca2+ Binding Site Mutants of Drosophila Melanogaster Calmodulin, *Biochemistry*, 1992, **31**(34), 7779–7786.
27 J. A. Cox, C. Ferraz, J. G. Demaille, R. O. Perez, D. van Tuinen and D. Marme, Calmodulin from Neurospora Crassa. General Properties and Conformational Changes, *J. Biol. Chem.*, 1982, **257**(18), 10694–10700.
28 T. J. Lukas, D. B. Iverson, M. Schleicher and D. M. Watterson, Structural Characterization of a Higher Plant Calmodulin: Spinacia Oleracea, *Plant Physiol.*, 1984, **75**(3), 788–795.

29 P. Dieter, J. A. Cox and D. Marme, Calcium-Binding and Its Effect on Circular Dichroism of Plant Calmodulin, *Planta*, 1985, **166**(2), 216–218.
30 J. Gariepy and R. S. Hodges, Primary Sequence Analysis and Folding Behavior of Ef Hands in Relation to the Mechanism of Action of Troponin C and Calmodulin, *FEBS Lett.*, 1983, **160**(1–2), 1–6.
31 H. Gut, P. Dominici, S. Pilati, A. Astegno, M. V. Petoukhov, D. I. Svergun, M. G. Grutter and G. Capitani, A Common Structural Basis for Ph- and Calmodulin-Mediated Regulation in Plant Glutamate Decarboxylase, *J. Mol. Biol.*, 2009, **392**(2), 334–351.
32 M. Ikura, G. M. Clore, A. M. Gronenborn, G. Zhu, C. B. Klee and A. Bax, Solution Structure of a Calmodulin-Target Peptide Complex by Multidimensional NMR, *Science*, 1992, **256**(5057), 632–638.
33 W. E. Meador, A. R. Means and F. A. Quiocho, Target Enzyme Recognition by Calmodulin: 2.4 a Structure of a Calmodulin-Peptide Complex, *Science*, 1992, **257**(5074), 1251–1255.
34 S. M. Roth, D. M. Schneider, L. A. Strobel, M. F. Van Berkum, A. R. Means and A. J. Wand, Characterization of the Secondary Structure of Calmodulin in Complex with a Calmodulin-Binding Domain Peptide, *Biochemistry*, 1992, **31**(5), 1443–1451.
35 N. Choy, V. Raussens and V. Narayanaswami, Inter-Molecular Coiled-Coil Formation in Human Apolipoprotein E C-Terminal Domain, *J. Mol. Biol.*, 2003, **334**(3), 527–539.
36 V. Raussens, J. Drury, T. M. Forte, N. Choy, E. Goormaghtigh, J. M. Ruysschaert and V. Narayanaswami, Orientation and Mode of Lipid-Binding Interaction of Human Apolipoprotein E C-Terminal Domain, *Biochem. J.*, 2005, **387**(Pt 3), 747–754.
37 K. Arnold, L. Bordoli, J. Kopp and T. Schwede, The Swiss-Model Workspace: A Web-Based Environment for Protein Structure Homology Modelling, *Bioinformatics*, 2006, **22**(2), 195–201.
38 P. Benkert, M. Biasini and T. Schwede, Toward the Estimation of the Absolute Quality of Individual Protein Structure Models, *Bioinformatics*, 2011, **27**(3), 343–350.
39 C. H. Yun, J. Bai, D. Y. Sun, D. F. Cui, W. R. Chang and D. C. Liang, Structure of Potato Calmodulin Pcm6: The First Report of the Three-Dimensional Structure of a Plant Calmodulin, *Acta Crystallogr., Sect. D: Biol. Crystallogr.*, 2004, **60**(Pt 7), 1214–1219.
40 D. De Biase, A. Tramonti, R. A. John and F. Bossa, Isolation, Overexpression, and Biochemical Characterization of the Two Isoforms of Glutamic Acid Decarboxylase from *Escherichia coli*, *Protein Expression Purif.*, 1996, **8**(4), 430–438.

ChemPubSoc Europe

DOI: 10.1002/chem.201402146

CHEMISTRY A European Journal Full Paper

Sensors

Conformational Changes in Calcium-Sensor Proteins under Molecular Crowding Conditions

Stefan Sulmann,[a] Daniele Dell'Orco,[b] Valerio Marino,[b] Petra Behnen,[c] and Karl-Wilhelm Koch*[a]

Abstract: Fundamental components of signaling pathways are switch modes in key proteins that control start, duration, and ending of diverse signal transduction events. A large group of switch proteins are Ca^{2+} sensors, which undergo conformational changes in response to oscillating intracellular Ca^{2+} concentrations. Here we use dynamic light scattering and a recently developed approach based on surface plasmon resonance to compare the protein dynamics of a diverse set of prototypical Ca^{2+}-binding proteins including calmodulin, troponin C, recoverin, and guanylate cyclase-activating protein. Surface plasmon resonance biosensor technology allows monitoring conformational changes under molecular crowding conditions, yielding for each Ca^{2+}-sensor protein a fingerprint profile that reflects different hydrodynamic properties under changing Ca^{2+} conditions and is extremely sensitive to even fine alterations induced by point mutations. We see, for example, a correlation between surface plasmon resonance, dynamic light scattering, and size-exclusion chromatography data. Thus, changes in protein conformation correlate not only with the hydrodynamic size, but also with a rearrangement of the protein hydration shell and a change of the dielectric constant of water or of the protein–water interface. Our study provides insight into how rather small signaling proteins that have very similar three-dimensional folding patterns differ in their Ca^{2+}-occupied functional state under crowding conditions.

Introduction

Conformational transitions in proteins control the on and off modes of cellular responses in a very precise manner. These conformational changes can be induced, for example, by small organic ligands, protein–protein interactions, or second messengers like Ca^{2+}. The versatile action of Ca^{2+} is based on the operation of hundreds of different Ca^{2+}-sensor proteins that detect changes in intracellular Ca^{2+}, thereby switching into a mode of controlling the function of a target protein.[1] Often, one Ca^{2+}-sensor protein can regulate different targets, among which the most prominent example is probably calmodulin (CaM), a member of the superfamily of EF-hand Ca^{2+}-binding proteins. CaM exhibits a kind of conformational plasticity, meaning it is able to control different target protein function by adopting a fitting conformation for a specific target structure.[2,3] A similar task is probably performed by neuronal Ca^{2+}-sensor (NCS) proteins, a subgroup of the EF-hand superfamily.[4,5] However, despite their rather similar three-dimensional folding, each member of this group may regulate only a few or just one target out of a large diversity of different proteins. For example, rod and cone cells of the vertebrate retina specifically express Ca^{2+}-sensors like recoverin[5] and guanylate cyclase-activating protein 1 (GCAP1),[6–8] of which the latter regulates the activity of sensory membrane guanylate cyclases. Considering the conformational variety of one small Ca^{2+} sensor like CaM[2,3] on the one hand and the similar general folding of NCS proteins[4,5] on the other poses the following questions. Which conformational changes control the on and off states of a particular Ca^{2+} sensor? How do these states differ in proteins of the same subgroup or between mutants and the corresponding wild type?

Fluorescence, circular dichroism, and NMR spectroscopy have been widely employed among other methods to detect conformational changes in proteins. A more recent rather innovative approach was to use the surface plasmon resonance (SPR) phenomenon for the detection of conformational transitions. Two different experimental procedures have mainly been tested so far. Localized SPR (LSPR)[9,10] employs silver or gold nanoparticles coated with the protein under study. Commercial SPR sensors use dextran-coated gold surfaces with covalently and non-covalently attached proteins. By using the latter approach conformational changes have been detected in enzymes, redox proteins, and Ca^{2+}-binding proteins.[11–17] Furthermore, coupled plasmon-waveguide resonance spectroscopy,

[a] S. Sulmann, Prof. Dr. K.-W. Koch
Department of Neurosciences, Biochemistry Group
University of Oldenburg, 26111 Oldenburg (Germany)
E-mail: karl.w.koch@uni-oldenburg.de

[b] Dr. D. Dell'Orco, V. Marino
Department of Life Sciences and Reproduction
Section of Biological Chemistry and Center for BioMedical Computing (CBMC)
University of Verona, Verona (Italy)

[c] Dr. P. Behnen
Department of Biomedical Sciences
University of Modena, Modena (Italy)

Supporting information for this article is available on the WWW under http://dx.doi.org/10.1002/chem.201402146.

a technique related to SPR, has been employed to study conformational changes in G protein-coupled receptors.[18,19] It has been argued that the rather long (ca. 200 nm) decay length of the electromagnetic field in commercially available SPR sensor chips, such as CM5 supplied by Biacore, dramatically reduces the sensitivity to small refractive index changes occurring close to the sensor surface,[10] thus making the much shorter (ca. 5 nm) decay length in LSPR systems more appropriate for detecting a conformational change of an adsorbed protein on its surface. However, SPR responses obtained with proteins immobilized on dextran-coated sensor chips have been clearly correlated with conformational changes using appropriate controls.[11–19] Artefact signals were excluded in a recent study that compares Ca^{2+}-induced conformational changes in the neuronal Ca^{2+}-sensor protein recoverin with a specifically designed recoverin mutant, which does not undergo a Ca^{2+}-triggered conformational change.[16] We noticed that increasing the Ca^{2+} concentration ($[Ca^{2+}]$) into the millimolar range leads to dextran matrix effects on the sensor chip surface independent of the immobilized protein.[16] This study was more recently extended by comparing different Ca^{2+}-sensor proteins under experimental conditions, in which the influence of ionic strength, divalent cations, and different sensor chip surfaces was tested.[17] This SPR-based approach allows us to investigate Ca^{2+}-induced conformational changes in a working range of physiologically relevant free $[Ca^{2+}]$, thereby distinguishing non-specific matrix effects from protein-derived signals in a setting of precisely defined parameters. A further advantage of our method is that it uses a commercial SPR device and a sensor chip, which provides four flow cells to immobilize and investigate up to three proteins and one control surface under identical buffer flow and sample injections.[16,17]

It has been suggested that the solvent around the immobilized protein rearranges during a conformational transition, especially when a significant variation in the hydrophobicity of the solvent-exposed protein surface occurs, thus leading to changes in the dielectric milieu of the whole flow cell of the sensor chip.[11,13,14,16,17]

Based on previous and present observations we sought to discriminate different forms of conformational changes in a set of Ca^{2+}-sensor proteins. For this purpose we determined the Ca^{2+}-dependent changes in the hydrodynamic properties of Ca^{2+}-sensor proteins and compared them with Ca^{2+}-induced SPR responses. Our results confirm that the SPR-based approach is extremely sensitive to even fine alterations induced by mutations in the conformational switch of Ca^{2+}-sensor proteins. The signal depends not only on the change in hydrodynamic protein size upon Ca^{2+}-binding, but likely reflects a different hydration structure, which can be significantly affected in the crowding conditions occurring on the sensor chip.

Results

Ca^{2+}-induced changes in hydrodynamic volume

First, we investigated Ca^{2+}-dependent changes in the hydrodynamic radius of Ca^{2+}-sensor proteins that are known to differ significantly in their conformational transitions. For this purpose we determined the hydrodynamic diameter (d in nm) of several Ca^{2+}-sensor proteins by dynamic light scattering (DLS) in the presence and absence of Ca^{2+}, of which representative results are displayed in Figure 1 for CaM^{S17C}, a mutant of myristoylated recoverin ($mRec^{2-190}$),[20,21] myristoylated GCAP1 (mGCAP1) and troponin C (TnC). These measurements showed a size distribution of light scattering intensity resulting in one peak of high intensity (peak 1) and one of lower intensity (peak 2). However, one exception was observed in the case of TnC, for which the intensity of peak 2 was higher (see also further below). Determination of hydrodynamic diameters revealed for Ca^{2+}-free proteins the following d values (Table 1): 4.97 (CaM^{S17C}), 5.53 ($mRec^{2-190}$), 7.5 (mGCAP1), and 7.88 nm (TnC). Adding saturating Ca^{2+} caused a shift of peak 1 to either higher (CaM^{S17C}, $mRec^{2-190}$) or lower d values (mGCAP1, TnC) indicating a Ca^{2+}-induced change of the hydrodynamic volume. The same set of measurements was performed with wild type myristoylated (m) and nonmyristoylated (nm) recoverin, and with several point mutants of GCAP1 known to cause retinal cone-rod dystrophies[22–24] (Table 1).

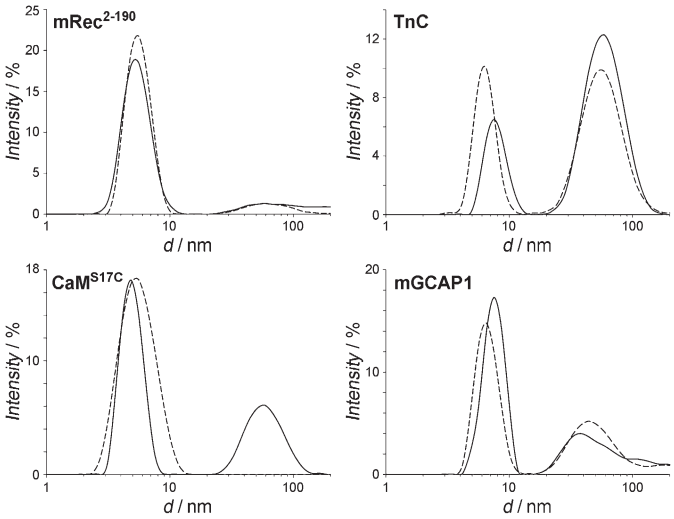

Figure 1. Determination of hydrodynamic diameters of Ca^{2+}-sensor proteins by dynamic light scattering. All measurements were performed at $T = 25\,^{\circ}C$ in 5 mM Tris/HCl pH 7.5, 150 mM KCl buffer. Black solid lines refer to measurements in the presence of saturating EGTA, while dashed lines to saturating Ca^{2+} conditions. Size distributions of: 26 μM $mRec^{2-190}$ in the presence of 240 μM EGTA and 260 μM Ca^{2+} (upper left); 55 μM TnC in the presence of equal amounts (1.5 mM) of saturating EGTA or Ca^{2+} (upper right); 187 μM CaM^{S17C} in the presence of 4 mM EGTA and 5 mM Ca^{2+} (lower left); 60 μM mGCAP1 in the presence of equal amounts (1.5 mM) of saturating EGTA or Ca^{2+}. Data obtained by DLS measurements reporting the intensity of scattered light as % of the total area.

In order to compare the changes in d among all tested Ca^{2+}-sensor proteins in relative and not in absolute terms, we evaluated our data by calculating the relative change $\Delta d/d_{EGTA}$ (Δd is defined as the diameter in the presence of Ca^{2+} minus that in the presence of EGTA ($d_{Ca^{2+}}$-d_{EGTA})). Values for $\Delta d/d_{EGTA}$ of 5.7 and 14.7% were found for recoverin and CaM, respectively

Table 1. Dynamic light scattering measurements of Ca^{2+}-sensor proteins. Determination of the hydrodynamic diameter d from peaks 1 and 2 ($\pm$standard error $=\sigma/N^{1/2}$; N is the number of repetitions; d was determined in the presence or absence of Ca^{2+}. Δd [nm] is the difference $d_{Ca}-d_{EGTA}$ ($\pm$propagation of errors $=(\sigma_1^2+\sigma_2^2)^{1/2}$. CaM was the S17C-mutant.[17]. Wild type recoverin is abbreviated Rec.

Protein [nm]	d (peak 1) [nm]	d (peak 2) [nm]	N	Δd [nm]	$\Delta d/d_{EGTA}$ [%]
TnC (EGTA)	7.88±0.11	61.78±2.80	21	−1.44±0.30	−18.3
TnC (Ca^{2+})	6.44±0.06	60.22±4.20	21		
CaM (EGTA)	4.97±0.01	62.14±5.50	25	+0.73±0.03	+14.7
CaM (Ca^{2+})	5.70±0.03		25		
$mRec^{2-190}$ (EGTA)	5.53±0.05		23	+0.13±0.06	+2.3
$mRec^{2-190}$ (Ca^{2+})	5.66±0.02		26		
mRec (EGTA)	5.22±0.02	79.91±11.10	20	+0.30±0.03	+5.7
mRec (Ca^{2+})	5.52±0.02	78.60±5.20	19		
nmRec (EGTA)	5.57±0.06	37.43±1.57	12	−0.23±0.10	−4
nmRec (Ca^{2+})	5.34±0.08	36.18±1.50	13		
mGCAP1 (EGTA)	7.5±0.2		20	−0.8±0.2	−10.3
mGCAP1 (Ca^{2+})	6.69±0.04		26		
D100E (EGTA)	7.82±0.12		21	−1.08±0.14	−13.8
D100E (Ca^{2+})	6.74±0.07	29.48±3.34	18		
L151F (EGTA)	7.50±0.11	26.82±4.60	27	−0.42±0.19	−5.6
L151F (Ca^{2+})	7.08±0.15	26.65±6.50	20		
E89K (EGTA)	8.30±0.09	44±17	21	−0.6±0.1	−7.2
E89K (Ca^{2+})	7.70±0.09	40.40±13.38	25		
nmGCAP1 (EGTA)	6.25±0.05		23	+0.51±0.09	+8.2
nmGCAP1 (Ca^{2+})	6.76±0.07		26		

(Table 1). Deletion of twelve amino acids at the C-terminus of recoverin in the mutant Rec^{2-190} diminished the Ca^{2+}-dependent change in d yielding a $\Delta d/d_{EGTA}=2.3\%$, which is consistent with previous reports identifying this region as Ca^{2+}-sensitive control module.[20,21] Changes in TnC were also large, but with an inverted sign of $\Delta d/d_{EGTA}$ (−18.3%).

GCAP1 is an NCS protein like recoverin, but does not show a large rearrangement of its myristoyl group.[25] Interestingly, it also displayed a pronounced change in d ($\Delta d/d_{EGTA}=-10.3\%$). Wild type (WT) GCAP1 was further compared with several of its single-point mutants known to cause retinal cone-rod dystrophies.[22–24] Ca^{2+}-saturated GCAP1 mutants had a d value of around 7 nm, which is not much different to that of WT. However, the relative changes $\Delta d/d_{EGTA}$ showed a larger variation yielding −5.6% for L151F, −7.2% for E89 K and −13.8% for D100E (Table 1).

Intensity peaks corresponding to higher order oligomers were detected for each protein, and they were particular apparent for TnC. Their effective weight on the photon correlation signal is, however, modest due to the $1/d^6$ scaling of scattered light intensity. Monitoring number and volume distributions of the same molecular species in fact confirmed that monomers were the most populated species in each case.

DLS measurements confirmed that all tested Ca^{2+}-sensor proteins undergo significant Ca^{2+}-induced changes in their hydrodynamic volume. However, the relative changes expressed in $\Delta d/d_{EGTA}$ are rather different among the proteins and even became visible among myristoylated and nonmyristoylated protein forms. Ca^{2+}-induced changes in WT recoverin and WT GCAP1 led to significant Δd and $\Delta d/d_{EGTA}$ values, but sign inversion occurred when a myristoyl group was posttranslational attached to the protein (Table 1).

Detection of Ca^{2+}-switch modes by an SPR biosensor

An alternative approach to detect differences in Ca^{2+}-induced protein dynamics had previously been reported for recoverin, CaM, GCAP1, and GCAP2 using SPR.[16,17] Therefore, we hypothesized that the diverse switch modes of Ca^{2+}-sensor proteins, which we observed by dynamic light scattering, can also be detected using the SPR approach and we included in the present study Ca^{2+} titrations with TnC, $mRec^{2-190}$ and the GCAP1 mutants E89K, D100E, L151F, and G159V (Figure 2). TnC on the chip surface reacted to increasing [Ca^{2+}] with responses of increasing amplitudes reaching saturation at $>30\ \mu M$ Ca^{2+} (Figure 2, upper panel). A similar Ca^{2+} sensitivity was observed with the recoverin mutant Rec^{2-190} (Figure 2, lower panel), which was almost identical to previously determined values of the wild type (Table 2). However, the maximal amplitudes that were reached at the end of the titrations were

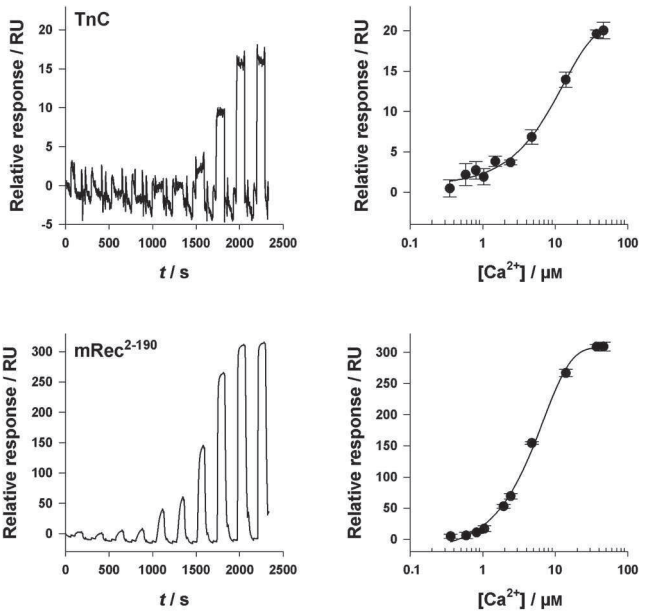

Figure 2. SPR responses of Ca^{2+}-sensor proteins at increasing free [Ca^{2+}]. Examples of sensorgrams obtained upon Ca^{2+} titrations (left panel). The response amplitude at the end of each Ca^{2+} injection is plotted as a function of Ca^{2+} (right panel; the error bars represent the SD). Sensorgrams were obtained for TnC and the myristoylated recoverin mutant Rec^{2-190}. Data fitting by a Hill sigmoidal curve resulted in $K_{1/2}^{SPR}=11.5\pm0.3\ \mu M$ for TnC ($n=5$) and a $K_{1/2}^{SPR}=4.90\pm0.02\ \mu M$ ($n=8$) for Rec^{2-190}.

Table 2. SPR-based detection of conformational changes expressed in half-maximal values of response amplitudes and normalized RU_{max} values. CaM was the S17C-mutant.[17]

Protein	Divalent cations	$K_{1/2}^{SPR}$ [μM]	Normalized RU_{max}
TnC	Ca^{2+}	11.5 ± 0.3	10.2 ± 0.5
$mRec^{2-190}$	Ca^{2+}	4.90 ± 0.02	39.9 ± 0.9
mGCAP1[a]	Ca^{2+}	19.7 ± 0.8	2.3 ± 0.1
	$Ca^{2+} + Mg^{2+}$	25.4 ± 1.2	1.0 ± 0.1
mE89K	Ca^{2+}	30.8 ± 1.4	1.8 ± 0.1
	$Ca^{2+} + Mg^{2+}$	59.9 ± 0.7	1.5 ± 0.1
mD100E	Ca^{2+}	20.9 ± 0.3	2.6 ± 0.1
	$Ca^{2+} + Mg^{2+}$	45.8 ± 0.7	1.5 ± 0.1
mL151F	Ca^{2+}	31.6 ± 0.6	1.9 ± 0.1
	$Ca^{2+} + Mg^{2+}$	52.4 ± 1.4	1.1 ± 0.1
mG159V	Ca^{2+}	24.0 ± 1.1	2.0 ± 0.1
	$Ca^{2+} + Mg^{2+}$	79.4 ± 2.3	1.1 ± 0.1
CaM[a]	Ca^{2+}	5.70 ± 0.03	11.7 ± 0.1
	$Ca^{2+} + Mg^{2+}$	17.2 ± 0.4	6.6 ± 0.1
mGCAP2[a]	Ca^{2+}	24.9 ± 0.2	3.6 ± 0.3
	$Ca^{2+} + Mg^{2+}$	37.7 ± 0.5	2.0 ± 0.1
mRec[a]	Ca^{2+}	5.0 ± 0.2	36.3 ± 0.3
	$Ca^{2+} + Mg^{2+}$	5.2 ± 0.1	19.5 ± 0.1

[a] See reference [17].

dramatically different between TnC and Rec^{2-190} (Table 2). This was partly due to differences in immobilization density, which was in all tests much lower for TnC than for all recoverin forms (see the Experimental Section and below). Additionally, differences in the structure and dynamics of the protein hydration shell contribute to the observed effects (see also the Discussion section). Mutants of GCAP1 also showed a characteristic response pattern (Figure 3) allowing the determination of the $[Ca^{2+}]$ at which the increase in response amplitude is half maximal ($K_{1/2}^{SPR}$ in Table 2). The $K_{1/2}^{SPR}$ of the GCAP1 mutants was shifted to higher $[Ca^{2+}]$, indicating a decrease in Ca^{2+}-binding affinity, which is in agreement with previous results that these cone-rod dystrophy related mutations cause a change in Ca^{2+} sensitivity.[23,24] The experiments were also performed in the presence of physiological levels of free magnesium. The presence of 1 mM Mg^{2+} during the Ca^{2+}-titrations had mainly two effects; it decreased the response amplitudes and increased the $K_{1/2}^{SPR}$ of both WT and mutant GCAP1 (Figure 3 and Table 2). Thus, the Ca^{2+} titrations displayed two main features that were characteristic for each protein: the $K_{1/2}^{SPR}$ and different amplitudes that were reached at saturating $[Ca^{2+}]$ (Figures 2 and 3).

The response amplitudes of the titration series at saturating Ca^{2+} were normalized to the amount of immobilized protein and were defined as normalized RU_{max} (Table 2). It became clear that response amplitudes were highly dependent on the type of protein as well as on the immobilization technique. However, a different chemistry of coupling does not significantly affect the $K_{1/2}^{SPR}$, instead it results in important variation of response amplitudes reached at the end of each analyte injection.[16] Therefore we compared quantitatively the results from the three techniques employed in this work on a series of GCAP1 mutants, which were all immobilized by means of amine coupling at similar amounts on the sensor chip surface. We point out that detecting subtle variations in the conformational properties of proteins differing from one another only by a single-point mutation represents a proof of the sensitivity of the approach. Figure 4 reports the results of quantitative comparisons. The SPR signal clearly correlates with the change

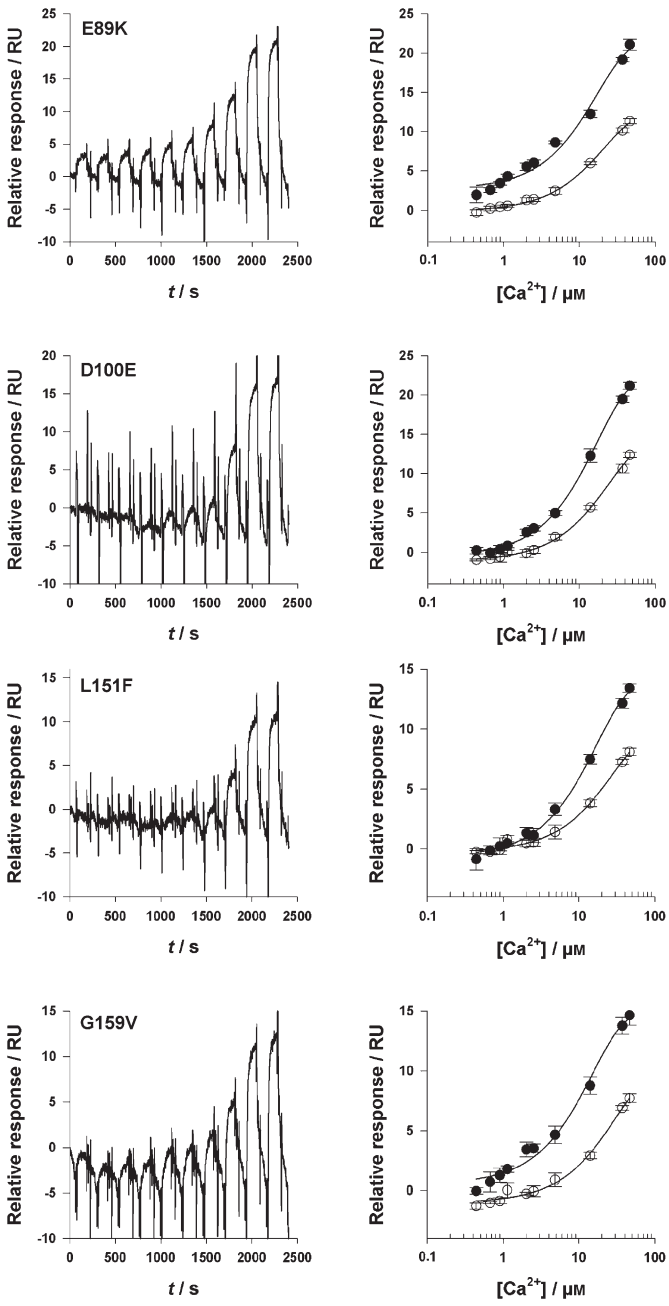

Figure 3. Sensorgrams obtained for myristoylated GCAP1 mutants E89K, D100E, L151F and G159V. Sensorgrams are on the left panel, evaluation of data without Mg^{2+} (●) and in the presence of 1 mM free Mg^{2+} (○) is shown on the right panel. Data fitting by a Hill sigmoidal curve resulted in the following values of $K_{1/2}^{SPR}$ (in brackets): E89K (30.8 ± 1.4 μM; $n = 4$); D100E (20.9 ± 0.3 μM, $n = 3$), L151F (31.6 ± 0.6 μM, $n = 4$), G159V (24. ± 1.1 μM, $n = 3$). Values of $K_{1/2}^{SPR}$ in the presence of 1 mM Mg^{2+} were: E89K (59.9 ± 0.7 μM; $n = 6$); D100E (45.8 ± 0.7 μM, $n = 5$), L151F (52.4 ± 1.4 μM, $n = 6$), G159V (79.4 ± 2.3 μM, $n = 4$). Error bars represent the standard deviation.

in hydrodynamic radius as detected both by size exclusion chromatography (SEC) ($R^2 = 0.83$) and DLS ($R^2 = 0.88$), thus confirming that the signal originates from changes in hydrodynamic properties of the protein upon Ca^{2+} binding.

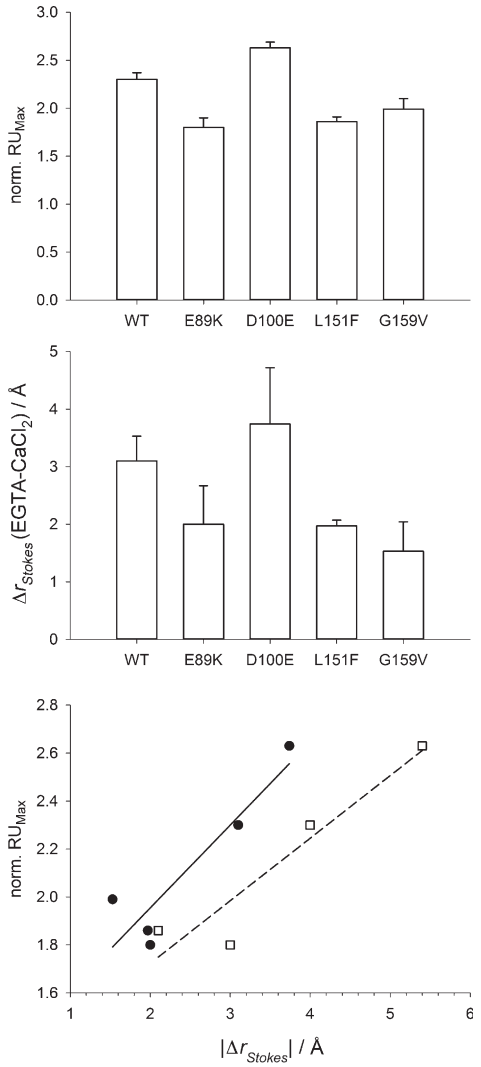

Figure 4. Comparison of normalized RU_{max} values and differences in Stokes radii ($|\Delta r_{Stokes}| = |r_{Stokes}^{EGTA} - r_{Stokes}^{Ca^{2+}}|$) for the series of mGCAP1 variants. The upper panel shows the normalized values of RU_{max} obtained from Ca^{2+} titration series as seen in Figure 2 for myristoylated GCAP1 WT and the mutants E89K, D100E, L151F, and G159V. Differences in Stokes radii were obtained both from analytical size exclusion chromatography (mid panel) and dynamic light scattering (see Table 1), and the absolute value of the variation linearly correlates with RU_{max} in both cases (lower panel: ●:SEC data set ($R^2 = 0.83$); □: DLS data set ($R^2 = 0.88$)).

Discussion

Ca^{2+}-sensor proteins like recoverin and CaM undergo extensive changes in their three-dimensional structure upon Ca^{2+} binding[2,3,5] and thereby switch between on and off modes. Multifunctional Ca^{2+} sensors like CaM, however, can operate in more complex ways by, for example, controlling target function in Ca^{2+}-bound and Ca^{2+}-free states.[1–3] In the present work, we investigated how protein parameters like size and hydrodynamic volume change, when a Ca^{2+} sensor is switching between Ca^{2+}-bound and Ca^{2+}-free states. Large structural changes in recoverin and CaM were mirrored in significant changes of their hydrodynamic diameters (Table 1). Further, we employed classical techniques like DLS and SEC, which provided us with a data set that for each protein gave a fingerprint profile reflecting different hydrodynamic properties. For example, CaM and TnC showed among all tested Ca^{2+}-sensor proteins the largest differences in size (Ca^{2+}-free versus Ca^{2+}-bound), and SPR confirmed these important variations. However, a clear mismatch was observed for recoverin and its truncated mutant Rec^{2-190}, for which relative changes in size determined by DLS differed significantly from each other, and were less prominent compared to CaM and TnC, (Table 1), at odds with determinations by SPR (Figure 2, Table 2). On the other hand, when the same set of GCAP1 mutant was similarly compared, DLS, SEC, and SPR showed consistent results (Figure 4). Where does this discrepancy originate from? We previously analyzed[16] the available structural data on recoverin and postulated that the significant increase in hydrophobicity upon Ca^{2+} binding would reflect on the structure of the hydration shell, and consequently on the refractive index of the protein–water dielectric milieu, which is the physical signal detected by SPR instruments. It is in fact known that, owing to the lack of hydrogen bonds, water molecules near hydrophobic surfaces behave different from bulk water.[26] The different properties of hydration water in terms of local density reflect in a different dielectric constant and eventually refractive index, which is its square root. This is, however, true for both proteins in solution, like in SEC and DLS experiments, and those immobilized on the SPR sensor chip. What is significantly different in the two situations is the molecular crowding, which is definitely higher in the SPR conditions and might affect differently the structure and dynamics of the hydration shell.[26]

Physiological protein solutions in a cellular environment are highly concentrated (up to 400 $g\,L^{-1}$) filling 5–40% of the total cell volume.[27] As we have pointed out in a recent publication the SPR approach for detecting conformational changes relies on a high amount of immobilized protein in a dextran-like mesh.[17] Therefore, it differs from the "canonical" use of the SPR technology (particularly the Biacore system), in which low immobilization levels on the sensor chip surface should be achieved in order to obtain reliable kinetic constants.[28] However, it was not the aim of the present study to extract kinetic constants from the sensorgrams. Instead we have a high density of proteins covalently attached to a 100 nm dextran layer mimicking crowding effects, for which inert synthetic polymers including dextran are often used.[29,30]

The Ca^{2+}-dependent changes of CaM in the presence of crowding reagents differ significantly from those of the diluted protein solution.[31] Our results here indicate that this conclusion might be true for a variety of different sensor proteins pointing to a more general principle. However, the parameter $K_{1/2}^{SPR}$ that we determined here is different from apparent K_D values for direct Ca^{2+} binding to recoverin[16,20,21] and GCAP1 forms[24,32] or values that describe the [Ca^{2+}], at which a biologi-

cal regulatory effect is halfmaximal (IC_{50}, EC_{50}).[4–8,20–23,25] In our previous work[17] we related apparent K_D values of Ca^{2+} binding to $K_{1/2}^{SPR}$ by the equation $K_D^{app} = K_{cc} \times K_{1/2}^{SPR}$, in which K_{cc} is a unitless quantity defined as conformational change contribution. Thus, the empirical parameter $K_{1/2}^{SPR}$ is a useful tool to describe a concerted binding-conformational switch, either among different, but related, proteins or under conditions that influence conformational transitions.[17]

Then, how can SPR signals of increasing amplitudes at increasing [Ca^{2+}] be interpreted? SPR signals originate from changes in the refractive index close to the sensor surface and the refractive index equals the square root of the dielectric constant of the medium and of the soluble compounds. Although the dextran–protein compartment on the surface of the sensor chip is in an aqueous environment the relative dielectric constant of water in a crowded protein environment is lower than $\varepsilon = 80$, the value in bulk solution. In our SPR experiments the volume fraction of the immobilized protein is around 0.2 (Supporting Information) and under these conditions the ε of water decreases to about 60.[26] The maximal amplitudes that we observed in different Ca^{2+}-sensor proteins are between 10 and 300 RU, which correspond to a relative change[33] in bulk refractive index of 10^{-5} to 3×10^{-4}. The relative change $\Delta\varepsilon_r$ in dielectric constant of the aqueous protein–dextran compartment corresponds to 3.2×10^{-3} and 1.7×10^{-2}, respectively. Thus, the Ca^{2+}-induced conformational changes for proteins like recoverin as detected by SPR are accompanied by an approximately fivefold higher change in dielectric constant compared to GCAP1 variants, higher than the relative change attributed to water when passing from bulk to a highly crowded environment. We therefore conclude that the changes in protein conformation correlate with a rearrangement of both the hydration shell and the hydrodynamic protein properties (see above). We further conclude that the positive SPR amplitudes during a Ca^{2+} titration originate from an increase of the dielectric constant of water or of the protein–water interface. Thus, it would reflect a less "crowded" state in the dextran matrix, when Ca^{2+} is bound to Ca^{2+}-sensor proteins like recoverin, GCAPs, and CaM. If this hypothesis is true, one should find conditions under which Ca^{2+} titrations result in negative SPR amplitudes. In fact, we observed in a previous paper[17] that the nonmyristoylated forms of recoverin and GCAP1 exhibited negative amplitudes indicating a kind of reverse process with a lowering of ε (water). This observation would also be consistent with our dynamic light scattering measurements, during which changes in hydrodynamic diameter and $\Delta d/d_{EGTA}$ occurred with sign inversion. Indeed, when taken as absolute values, changes in hydrodynamic radii as detected by SEC and DLS significantly correlate with changes in SPR signals (Figure 4).

Conclusion

We determined physicochemical properties for a set of Ca^{2+}-sensor proteins that regulate the activity of various target proteins like kinases, cyclases, and ion channels. They operate by performing Ca^{2+}-induced switches between on and off states that are triggered by incremental changes of Ca^{2+}, which are significant for cellular processes. We here show that these Ca^{2+} sensors exhibit different responses to changing [Ca^{2+}] in combination with the surrounding water shell. In particular, we were able to correlate data from the SPR biosensor approach, dynamic light scattering, and size exclusion chromatography experiments. Thereby, we obtained characteristic fingerprint profiles relevant for the proteins under conditions of molecular crowding.

Experimental Section

Preparation of protein samples, buffers and calcium stocks

Wild type and mutant forms of recoverin and GCAP1 were heterologously expressed in *E. coli* and purified to homogeneity as described previously.[20–24] The recoverin mutant $mRec^{2-190}$ was a variant of myristoylated recoverin that lacks 12 residues at the C-terminus.[20,21] Preparation and use of CaM^{S17C} in SPR experiments containing a Cys at position 17 have been described previously.[17] Samples used in this work were a kind gift of Prof. Sara Linse (University of Lund, Sweden). Troponin C (TnC) was commercially obtained from Apollo Scientific Ltd., Stockport, UK.

For SPR experiments, we used the SPR running buffer consisting of 5 mM Tris/HCl pH 7.5, 150 mM KCl. For removing Ca^{2+} contaminants the buffer was applied on a Chelex 100 resin column (Biorad) with a flow rate of 3 mL min^{-1}. Treatment of the Chelex resin before use was exactly as described previously.[16,17] The remaining concentration of Ca^{2+} in the buffer after decalcification was measured by withdrawing a small volume and by performing a BAPTA absorption assay as described.[17] It was found to range between 0.11 and 0.20 μM. For the Ca^{2+} titration experiments we used $CaCl_2$ of the highest grade available, dissolved it in the decalcified buffer to a final concentration of 46 mM. This Ca^{2+} stock solution was used to obtain Ca^{2+} stocks of lower concentration by subsequent dilutions to the following final concentrations used in SPR experiments (injections in Figure 2): 0.4, 0.7, 0.9, 1.1, 1.6, 2.5, 4.8, 14, 37, 46.2 μM. All buffers were filtered (0.22 μm) and degassed for at least 1 h before use. For SPR runs Tween20 was added at a final concentration of 0.005 % (v/v).

Dynamic light scattering

DLS measurements were performed with a Zetasizer Nano-S (Malvern Instruments) using a polystyrene, low-volume, disposable, sizing cuvette (ZEN0112). Viscosity and refractive index were set to 0.8872 cP and 1.330 (default values for water), temperature was set to 25 °C with 2 min equilibration time. The measurement angle was 173° backscatter and the analysis model was set to multiple narrow modes. For each measurement a minimum of 12 determinations were performed, each consisting of 13–15 repetitions. Buffers (5 mM Tris-HCl, 150 mM KCl, pH 7.5, adjusted with saturating levels of $CaCl_2$ or EGTA), were filtered through a Jet Biofilm 0.22 μm membrane, while protein-only solutions were filtered through an Anotop 10 filter (Whatman, 0.02 μm).

SPR experiments and data analysis

A Biacore2000 surface plasmon resonance instrument (GE Healthcare) was employed for detecting conformational changes in Ca^{2+}-sensor proteins upon injections of Ca^{2+}. Proteins were immobilized at high surface densities on commercial CM5 sensor chips (GE

Healthcare, Uppsala, Sweden). Changes in resonance units (RU) after immobilization are at 2000–9000 RU (1000 RU correspond to 1 ng protein per mm^2).[33] Typical immobilization densities were 2 ng×mm^{-2} (TnC), 7 ng×mm^{-2} (GCAP1 forms), 8 ng×mm^{-2} (CaM^{S17C}) and 9 ng×mm^{-2} (recoverin forms). CaM^{S17C} and recoverin forms were immobilized by means of thiol coupling, GCAP1 forms by means of amine coupling. Details about general performance of SPR experiments, of Ca^{2+} titrations, and data evaluation have been described,[16,17] but a brief summary is given in the following. Ca^{2+} solutions of increasing free [Ca^{2+}] were injected for 2 min into SPR running buffer (see above). Control injections over a blank surface were done in parallel and were subtracted from sensorgrams obtained with protein coated surfaces. The response amplitude of each Ca^{2+} injection was determined by measuring the difference between RU at start and end of the corresponding Ca^{2+} injection yielding Ca^{2+} titration series. Plotting the response amplitude as a function of Ca^{2+} yields the [Ca^{2+}], at which the response amplitude is half maximal ($K_{1/2}^{SPR}$) as described in detail before.[17] Maximal amplitudes of Ca^{2+} titration series were divided by the amount of immobilized protein yielding normalized RU_{max} values.

Analytical size exclusion chromatography

Ca^{2+}-sensor proteins were analyzed by size exclusion chromatography using a Bio-Sept SEC2000 column (250×4 mm, Phenomenex, Aschaffenburg, Germany). Standard proteins for calibration were bovine serum albumin (66 kDa, Stokes radius 35.5 Å), ovalbumin (43 kDa, Stokes radius 30.5 Å), carboanhydrase (30 kDa, Stokes radius 23.6 Å), myoglobin (17.8 kDa, Stokes radius 20.2 Å), and ribonuclease (13.7 kDa, Stokes radius 16.4 Å). Buffer used in chromatography was the SPR running buffer (s. above) with either 1 mM $CaCl_2$ or 1 mM EGTA added. The protein (50 to 150 μg) was applied on the column and the elution profile was recorded at 280 nm. Elution volumes V_e of Ca^{2+}-sensor proteins were determined at high and low [Ca^{2+}] and the distribution coefficient K_{AV} was calculated according to $K_{AV}=(V_e-V_0)/(V_t-V_0)$, in which V_t is the total column volume and V_0 is the void volume. Stokes radii were determined from a calibration plot of log Stokes radius versus K_{AV} from 4–9 different chromatography runs.

Acknowledgements

This work was supported by the Deutsche Forschungsgemeinschaft (DFG) to K.-W.K. (KO948/10–1) and by funds from the Italian Ministry for Research and Education via departmental funds to D.D.O..

Keywords: calcium sensor · conformational change · protein crowding · protein folding · surface plasmon resonance

[1] M. J. Berridge, M. D. Bootman, H. L. Roderick, *Nat. Rev. Mol. Cell Biol.* **2003**, *4*, 517–529.
[2] S. W. Vetter, E. Leclerc, *Eur. J. Biochem.* **2003**, *270*, 404–414.
[3] M. Ikura, J. B. Ames, *Proc. Natl. Acad. Sci. USA* **2006**, *103*, 1159–1164.
[4] R. D. Burgoyne, *Nat. Rev. Neurosci.* **2007**, *8*, 182–193.
[5] P. P. Philippov, K.-W. Koch, *Neuronal Calcium Sensor Proteins*, Nova Publishers, Hauppauge, NY, **2006**.
[6] K. Palczewski, I. Subbaraya, W. A. Gorczyca, B. S. Helekar, C. C. Ruiz, H. Ohguro, J. Huang, X. Zhao, J. W. Crabb, R. S. Johnson, W. Baehr, *Neuron* **1994**, *13*, 395–404.
[7] S. Frins, W. Bönigk, F. Müller, R. Kellner, K.-W. Koch, *J. Biol. Chem.* **1996**, *271*, 8022–8027.
[8] I. V. Peshenko, A. M. Dizhoor, *J. Biol. Chem.* **2006**, *281*, 23830–23841.
[9] W. Paige Hall, J. N. Anker, Y. Lin, J. Modica, M. Mrksich, R. P. Van Duyne, *J. Am. Chem. Soc.* **2008**, *130*, 5836–5837.
[10] W. Paige Hall, J. Modica, J. N. Anker, Y. Lin, M. Mrksich, R. P. Van Duyne, *Nano Lett.* **2011**, *11*, 1098–1105.
[11] H. Sota, Y. Hasegawa, *Anal. Chem.* **1998**, *70*, 2019–2024.
[12] S. Boussaad, J. Pean, N. J. Tao, *Anal. Chem.* **2000**, *72*, 222–226.
[13] J. E. Gestwicki, H. V. Hsieh, J. B. Pitner, *Anal. Chem.* **2001**, *73*, 5732–5737.
[14] T. Mannen, S. Yamaguchi, J. Honda, S. Sugimoto, A. Kitayama, T. Nagamune, *Anal. Biochem.* **2001**, *293*, 185–193.
[15] T. Christopeit, T. Gossas, U. H. Danielson, *Anal. Biochem.* **2009**, *391*, 39–44.
[16] D. Dell'Orco, M. Müller, K.-W. Koch, *Chem. Commun.* **2010**, *46*, 7316–7318.
[17] D. Dell'Orco, S. Sulmann, S. Linse, K.-W. Koch, *Anal. Chem.* **2012**, *84*, 2982–2989.
[18] Z. Salamon, Y. Wang, M. F. Brown, H. A. MacLeod, G. Tollin, *Biochemistry* **1994**, *33*, 13706–13711.
[19] Z. Salamon, S. Cowell, E. Varga, H. I. Yamagura, V. J. Hruby, G. Tollin, *Biophys. J.* **2000**, *79*, 2463–2474.
[20] O. Weiergräber, I. I. Senin, E. Y. Zernii, V. A. Churumova, N. A. Kovaleva, A. A. Nazipova, S. E. Permyakov, E. A. Permyakov, P. P. Philippov, J. Granzin, K.-W. Koch, *J. Biol. Chem.* **2006**, *281*, 37594–37602.
[21] E. Zernii, K. Komolov, S. Permyakov, T. Kolpakova, D. Dell'Orco, A. Poetzsch, E. Knyazeva, I. Grigoriev, E. Permyakov, I. Senin, P. P. Philippov, K.-W. Koch, *Biochem. J.* **2011**, *435*, 441–450.
[22] V. B. D. Kitiratschky, P. Behnen, U. Kellner, J. R. Heckenlively, E. Zrenner, H. Jägle, S. Kohl, B. Wissinger, K.-W. Koch, *Hum. Mutat.* **2009**, *30*, E782–796.
[23] D. Dell'Orco, P. Behnen, S. Linse, K.-W. Koch, *Cell. Mol. Life Sci.* **2010**, *67*, 973–984.
[24] L. Jiang, T. Z. Li, S. E. Boye, W. W. Hauswirth, J. M. Frederick, W. Baehr, *PLoS One* **2013**, *8*, e57676.
[25] R. Stephen, G. Bereta, M. Golczak, K. Palczewski, M. C. Sousa, *Structure* **2007**, *15*, 1392–1402.
[26] R. Harada, Y. Sugita, M. Feig, *J. Am. Chem. Soc.* **2012**, *134*, 4842–4849.
[27] R. J. Ellis, A. P. Minton, *Nature* **2003**, *425*, 27.
[28] D. Myszka, *J. Mol. Recognit.* **1999**, *12*, 279–284.
[29] S. B. Zimmerman, A. P. Minton, *Annu. Rev. Biophys. Biomol. Struct.* **1993**, *22*, 27–65.
[30] D. J. Winzor, P. R. Wills, *Biophys. Chem.* **2006**, *119*, 186–195.
[31] D. Homouz, H. Sanabria, M. N. Waxham, M. S. Cheung, *J. Mol. Biol.* **2009**, *391*, 933–943.
[32] S. Lim, I. Peshenko, A. Dizhoor, J. B. Ames, *Biochemistry* **2009**, *48*, 850–862.
[33] *Biacore 2000 Instrument Handbook*, Biacore AB **2001**.

Received: February 12, 2014
Published online on March 27, 2014

Biochimica et Biophysica Acta 1853 (2015) 2055–2065

Contents lists available at ScienceDirect

Biochimica et Biophysica Acta

journal homepage: www.elsevier.com/locate/bbamcr

Structural effects of Mg^{2+} on the regulatory states of three neuronal calcium sensors operating in vertebrate phototransduction☆

Valerio Marino [a], Stefan Sulmann [b], Karl-Wilhelm Koch [b], Daniele Dell'Orco [a,c,*]

[a] Department of Life Sciences and Reproduction, Section of Biological Chemistry, University of Verona, Italy
[b] Department of Neurosciences, Biochemistry Group, University of Oldenburg, Germany
[c] Center for BioMedical Computing (CBMC), University of Verona, Italy

ARTICLE INFO

Article history:
Received 5 September 2014
Received in revised form 25 October 2014
Accepted 28 October 2014
Available online 4 November 2014

Keywords:
Phototransduction
Neuronal calcium sensor
Conformational switch
Guanylate cyclase-activating protein
Magnesium
Molecular dynamics

ABSTRACT

The effects of physiological concentration of magnesium on the switch states of the neuronal calcium sensor proteins recoverin, GCAP1 and GCAP2 were investigated. Isothermal titration calorimetry was applied for binding studies. Circular dichroism spectroscopy was used to characterize protein thermal stability, secondary and tertiary structure in conditions of high and low [Ca^{2+}], mimicking respectively the dark-adapted and light-exposed photoreceptor states during the phototransduction cascade. Further, molecular dynamics (MD) simulations were run to investigate the dynamical structural properties of GCAP1 in its activator, inhibitor and putative transitory states.

Our results confirmed that Mg^{2+} is unable to trigger the typical Ca^{2+}-induced conformational change of recoverin (myristoyl switch) while it decreases its thermal stability. Interestingly, Mg^{2+} seems to affect the conformation of GCAP2 both at high and low [Ca^{2+}], however the variations are more substantial for myristoylated GCAP2 in the absence of Ca^{2+}. GCAP1 is responsive to Mg^{2+} only in its low [Ca^{2+}] state and Mg^{2+}-GCAP1 tertiary structure slightly differs from both apo and Ca^{2+}-bound states. Finally, MD simulations suggest that the GCAP1 state harboring one Mg^{2+} ion bound to EF2 acquires structural characteristics that are thought to be relevant for the activation of the guanylate cyclase. Moreover, all the putative Mg^{2+}-bound states of myristoylated GCAP1 are structurally less flexible than Ca^{2+}-bound states. GCAP1 acquires a more compact tertiary structure that is less accessible to the solvent, thereby inducing a different conformation to the myristoyl moiety, which might be crucial for the activation of the guanylate cyclase. This article is part of a Special Issue entitled: 13th European Symposium on Calcium.

1. Introduction

Calcium (Ca^{2+}) plays a crucial role as a second messenger in rod and cone photoreceptor cells where, depending on the species, its concentration drops from ~250–800 nM to ~20–100 nM during the activation of the phototransduction cascade [1,2]. Being directly involved in negative feedback mechanisms, Ca^{2+} permits the regulation of light-sensitivity in photoreceptors and allows the typical adaption mechanisms observed under different light regimes [3–6]. Subtle changes in [Ca^{2+}] are detected by neuronal calcium sensor (NCS) proteins belonging to the EF-hand superfamily, which precisely regulate the enzymatic activity of their targets [7,8], by adopting specific conformations in response to Ca^{2+}-binding. Among NCS proteins, recoverin (Rec) exerts its regulatory properties on the activity of rhodopsin kinase by exploiting a mechanism known as myristoyl switch. Recoverin triggers from a "tense" (T), compact conformation in which, at low [Ca^{2+}] the post-translationally-bound myristoyl group is buried in a hydrophobic pocket to a more "relaxed" (R), extended conformation in which, at high [Ca^{2+}] the myristic moiety is solvent-exposed and more likely anchored to disk membranes [9,10]. Unlike Rec, the NCS guanylate cyclase-activating proteins 1 and 2 (GCAP1, GCAP2) do not undergo a myristoyl switch mechanism, but operate in a calcium-relay system [3] to make gradual responses to small changes in [Ca^{2+}], which results in a fine-tuned control of the activities of photoreceptor specific sensory membrane bound guanylate cyclases (which for reasons of simplicity we will refer in the text to a singular GC), specifically inhibiting the enzyme responsible for the synthesis of cyclic GMP (cGMP) at high [Ca^{2+}], and stimulating it at low [Ca^{2+}] [4,11].

While it is well established that Ca^{2+} plays a major role in many biochemical processes underlying the phototransduction cascade, the role of magnesium (Mg^{2+}), another divalent cation present at much

Abbreviations: Rec, recoverin; GCAP1, guanylate cyclase-activating protein 1; GCAP2, guanylate cyclase-activating protein 2; GC, membrane bound guanylate cyclase; MD, molecular dynamics; CD, circular dichroism; SASA, solvent accessible surface area; RMSD, root-mean square deviation; RMSF, root-mean square fluctuation

☆ This article is part of a Special Issue entitled: 13th European Symposium on Calcium.

* Corresponding author at: Strada le Grazie 8, 37134 Verona, Italy. Tel.: +39 045 802 7637.
E-mail address: daniele.dellorco@univr.it (D. Dell'Orco).

http://dx.doi.org/10.1016/j.bbamcr.2014.10.026
0167-4889/

higher concentration in both rod and cone outer and inner segments is less well understood. Mg^{2+} is an important cofactor for the fundamental nucleosides triphosphate ATP and GTP and a large number of enzymes appear to be regulated by Mg^{2+} in conditions that match the large physiological concentrations observed in tissues and cells [12]. In photoreceptor cells, [Mg^{2+}] stabilizes at relatively high values (~1 mM), independent of significant variations of pH, Ca^{2+} and Na^{+}, leading to the conclusion that unlike Ca^{2+} it does not participate in the dynamic regulation of phototransduction [13]. It is however known that EF-hand motifs that bind Ca^{2+} via an ideal pentagonal bipyramid geometry consisting of six oxygen atoms from carboxyl and carbonyl groups of the protein and an oxygen atom from a water molecule, may also bind Mg^{2+} in the same binding sites, though via an octahedral geometry [14]. The lack of a bidentate coordination usually provided by a Glu residue in the case of Ca^{2+} binding results in a monodentate coordination, overall leading to six rather than seven oxygen ligands in the case of Mg^{2+}. Depending on their specific affinity for Ca^{2+}, which may vary from 10^{-9} M to 10^{-6} M, Ca^{2+}-binding sites usually bind Mg^{2+} ions four to five orders of magnitude less strongly, thus making it particularly difficult to measure the dissociation constants [15]. Moreover, the radius of a hydrated Mg^{2+} ion is ~400-fold larger compared to the dehydrated one, while that of Ca^{2+} increases ~25-fold upon hydration. As a consequence, Mg^{2+} cannot be easily stripped of its hydration shell, and despite the similar chemical reactivity and charge the two cations show often very different biochemical behaviors [16]. Establishing general principles to quantify Mg^{2+} competition for Ca^{2+}-binding sites is therefore not trivial, as each binding site, and eventually each protein may behave differently, depending on the relative affinity for the cations and their local concentrations.

In the last years a number of exhaustive biochemical and biophysical investigations have revealed that free Mg^{2+} is important for the activation of GC by GCAP1. Mg^{2+} seems to bind to apo-GCAP1 with moderate affinity [17,18] and the apo form of GCAP1 seems not to exist physiologically, nor to be able to activate GC or colocalize with it in experiments with cells [19]. Previous studies on Rec suggest that Mg^{2+} does not influence the known myristoyl switch mechanism [20], but no dedicated structural study was performed so far. Finally, while a Ca^{2+}/Mg^{2+} exchange mechanism of general validity for GCAP-mediated activation of GC was proposed [21] based on the evidence that GCAP2 is also functionally affected by Mg^{2+} [17,22], to our knowledge the structural effects of Mg^{2+} on GCAP2 have never been experimentally studied so far, nor has the affinity for binding been estimated.

In this work we present a comparative analysis of the structural effects of Mg^{2+} on the regulatory states of Rec, GCAP1 and GCAP2 by focusing on conditions of high and very low Ca^{2+}, thus mimicking dark-adapted and illuminated photoreceptor cells. We measured variations of secondary and tertiary structure in different conditions, including the presence and absence of the post-translational myristoylation of the NCS proteins at the N-terminal. For myristoylated GCAP1 (mGCAP1), we performed comparative molecular dynamics simulations of the activating, inhibitory and putative transitory states, highlighting important dynamical features, which might be critical for switching between different regulatory states.

2. Material and methods

2.1. Protein expression and purification

Proteins were heterologously expressed in *Escherichia coli* and purified by hydrophobic interaction chromatography (myristoylated and non-myristoylated Rec (m/nmRec); see Refs. [23,24] for details) or by size exclusion chromatography and anion-exchange chromatography (m/nmGCAP1; see ref. [25] for details; m/nmGCAP2 see [26] for details). Protein sample purity was verified by SDS-PAGE. Protein buffer was exchanged with decalcified NH_4HCO_3, and samples were then concentrated, lyophilized and stored at −80 °C until use.

2.2. Circular dichroism spectroscopy and thermal denaturation studies

Circular dichroism (CD) spectroscopy studies were performed with a Jasco V-710 spectropolarimeter equipped with a Peltier type thermostated cell holder, using quartz cuvettes with path length of 1 cm for near UV spectra (250–320 nm) and 0.1 cm for far UV spectra (200–250 nm). Both near UV and far UV spectra were recorded at 37 °C at a scan rate of 50 nm min^{-1}, with a bandwidth of 1 nm and an integration time of 4 s. For each spectrum five accumulations were averaged and the spectrum of the buffer was recorded before each set of measurements and subtracted. For far UV spectra protein concentration was 8–10 μM for Rec, 17–20 μM for GCAP2 and 8–13 μM for GCAP1, while for near UV spectra it was respectively 15–20 μM, 40–42 μM and 26–52 μM. All experiments were performed in 5 mM Tris–HCl pH 7.5, 150 mM KCl, and 2 mM DTT.

Both far UV and near UV spectra were recorded: i) in the presence of 10-fold excess EGTA with respect to protein concentration; ii) after the addition of 1 mM $MgCl_2$ or 2-fold excess $CaCl_2$ with respect to the concentration of EGTA; and iii) after the addition of the other salt not added in the previous step. Thermal denaturation of all proteins was monitored between 20 °C and 96 °C in the same conditions as for far UV spectra, as far as protein, EGTA, $CaCl_2$ and $MgCl_2$ concentrations are concerned. The ellipticity signal at 208 nm (θ_{208}) was recorded at a scan rate of 1 °C min^{-1} and a response time of 4 s. The thermal denaturation analysis was performed assuming a two-state transition process, where the θ_{208} signal recorded as a function of temperature represents the fraction of folded and partly unfolded protein. When possible, thermal denaturation curves were fitted to a 4-parameter Hill sigmoid and a value for the melting temperature was estimated, otherwise a minimum value of transition temperature evaluation was estimated. The equation for the fitting curve was:

$$y = b_n + \frac{|b_n - b_u| T^H}{T_m^H + T^H}$$

where b_n is the baseline value (θ_{208}) of the native protein, b_u is the baseline value of the partly unfolded protein, T is the temperature, H is the Hill coefficient and T_m is the melting temperature.

2.3. Mg^{2+}-GCAP2 titrations monitored by intrinsic fluorescence spectroscopy

Protein samples were excited at 290 nm wavelength, while emission fluorescence spectra were recorded between 300 and 380 nm at 25 °C in 1 cm quartz cuvette using a Jasco FP-750 spectrofluorimeter, where the scan rate was set to 60 nm min^{-1} and excitation and emission bandwidth was set to 5 nm. Mg^{2+} buffers used for fluorescence titration experiments were prepared using 5 mM Tris–HCl pH 7.5, 150 mM KCl, 100 mM EGTA and $MgCl_2$ at variable concentrations, everything was dissolved in or diluted with the aforementioned Tris–HCl buffer. Free Mg^{2+} concentration for each titration point was calculated according to the Ca-Mg-ATP-EGTA Calculator software using NIST database (http://maxchelator.stanford.edu/CaMgATPEGTA-NIST.htm) by fixing T = 25 °C, pH = 7.5, and ionic strength = 0.15 M. By mixing these solutions, the final free Mg^{2+} concentration was varied in the 9.8 μM–29.9 mM range. Protein concentration was ~0.8 μM for each titration point. After recording three accumulations of the spectrum in the presence of 100 μM EGTA, only the intensity at the wavelength corresponding to the maximum intensity of fluorescence emission of the apo spectrum was monitored for the other titration points, which was expected to change according to Mg^{2+}-binding.

2.4. Isothermal titration calorimetry

Mg^{2+} binding to apo-GCAP2 was monitored by isothermal titration calorimetry (ITC) as described earlier [27]. In brief we used an VP-ITC instrument from Microcal (Northampton, MA, USA) at T = 25 °C, and the decalcified GCAP2 form was present in the recording cell at 3.6–14 μM concentration in the same decalcified Tris buffer (5 mM Tris–HCl pH = 7.5, 150 mM KCl) used for the CD studies. The titration was performed by subsequential injections of 3–5 μL 10 mM $MgCl_2$ into the recording cell. Remaining Ca^{2+} impurities in the decalcified Tris buffer were determined by a BAPTA absorption assay and ranged from 10 to 13 nM.

Best fitting results of the ITC data were obtained by a sequential two site binding model implemented in the Origin 7 software package (Microcal), providing apparent dissociation constants (K_D) and enthalpy changes (ΔH) upon magnesium binding.

2.5. Molecular dynamics simulations

A homology model of human mGCAP1 was built using the three-dimensional structure of chicken mGCAP1 in its Ca^{2+}-bound form as template [28], according to a procedure elucidated in a previous work [29]. All simulation states were modeled either by removing Ca^{2+} ions from each respective EF-hand binding site or by substitution with a Mg^{2+} ion, thus obtaining the states shown in Fig. 5. In particular, we prepared starting structures corresponding to: i) two GC-activating states (one Mg^{2+} ion bound to EF2, the other EF-hands accommodating no ion; indicated from now on as $EF2^{Mg^{2+}}$; another one accommodating two Mg^{2+} ions, $EF2^{Mg^{2+}}$ $EF3^{Mg^{2+}}$); ii) two possible transitory states ($EF2^{Mg^{2+}}$ $EF3^{Ca^{2+}}$ and $EF2^{Ca^{2+}}$ $EF3^{Ca^{2+}}$); iii) the GC inhibiting state ($EF2^{Ca^{2+}}$ $EF3^{Ca^{2+}}$ $EF4^{Ca^{2+}}$); and iv) two hypothetical, presumably non physiological states (apo protein and $EF2^{Mg^{2+}}$ $EF3^{Mg^{2+}}$ $EF4^{Mg^{2+}}$).

MD simulations of all seven systems were performed using GROMACS 4.6.3 simulation package [30], with the CHARMM27 all-atom force field [31,32]. CHARMM27 parameters for describing the post-translational myristoylation were generated manually, and are available upon request for academic use. Periodic Boundary Conditions (PBC) were applied using a dodecahedral box as the cell unit and choosing 12 Å as minimum distance between the protein and the box boundaries. Water model TIP3P was used to describe the solvent. Depending on the number of cations bound to the protein, a variable number of Mg^{2+} ions was added in the solvation box in order to set the concentration of Mg^{2+} ions to 1 mM and to neutralize the system, together with 29 K^+ and 29 Cl^- ions, which were added to adjust the salt concentration to 150 mM while keeping the system neutral. In detail, the systems included: 32,610 total atoms for the apo form (9853 water molecules, 6 Mg^{2+} counterions), 32,619 total atoms for $EF2^{Mg^{2+}}$ (9856 water molecules, 5 Mg^{2+} counterions), 32,622 total atoms for $EF2^{Mg^{2+}}$ $EF3^{Mg^{2+}}$ (9857 water molecules, 4 Mg^{2+} counterions), 32,622 total atoms for $EF2^{Mg^{2+}}$ $EF3^{Ca^{2+}}$ (9857 water molecules, 4 Mg^{2+} counterions), 32,628 total atoms for $EF2^{Mg^{2+}}$ $EF3^{Mg^{2+}}$ $EF4^{Mg^{2+}}$ (9859 water molecules, 3 Mg^{2+} counterions), 32,622 total atoms for $EF2^{Ca^{2+}}$ $EF3^{Ca^{2+}}$ (9857 water molecules, 4 Mg^{2+} counterions) and 32,628 total atoms for $EF2^{Ca^{2+}}$ $EF3^{Ca^{2+}}$ $EF4^{Ca^{2+}}$ (9859 water molecules, 3 Mg^{2+} counterions).

All structures were subjected to energy minimization, first with the steepest descent (F_{max} = 1000 kJ mol^{-1} nm^{-1}) and then with the conjugate gradients algorithm (F_{max} = 500 kJ mol^{-1} nm^{-1}), keeping the position of the backbone atoms and cations bound to the protein restricted in both cases. The system was then equilibrated at 310 K for 2 ns of backbone position-restrained MD simulations and then at 310 K for 2 ns of unrestricted MD simulations. V-rescale thermostat [33] was used to keep the system temperature fixed at 310 K, by using a coupling constant τ_t of 0.1 ps. The Particle Mesh Ewald (PME) [34] method was employed to calculate electrostatic interactions. Short range attractive and repulsive interactions were computed using a Lennard-Jones potential with a cutoff of 12 Å. LINCS algorithm [35] was used to constrain all but water molecules bond length, allowing for an integration time step of 2 fs by the leap-frog algorithm. After equilibration the system underwent 200 ns unrestrained isothermal-isobaric (NPT ensemble; T = 310 K, P = 1 atm) MD simulation. System pressure was set to 1 atm using the Berendsen weak coupling algorithm [36] with a coupling constant τ_p of 1 ps.

2.6. Analysis of MD trajectories

Generated MD trajectories were subjected to different analyses. The surface accessible surface area (SASA) and the root-mean square deviation (RMSD) were calculated over the 200 ns trajectory, the latter being referred to each structure after the 4 ns equilibration. The intrinsic flexibility of the system was evaluated by computing the root mean squared fluctuation (RMSF) for each amino acid, in the time frame of the simulation, defined as time averaged-RMSD:

$$\mathrm{RMSF}_i = \sqrt{\frac{1}{T}\sum_{t_j=1}^{T}\left|r_i\left(t_j\right) - r_i^{ref}\right|^2}$$

where T is the 200 ns MD time frame and r_i (t_j) and r_i^{ref} represent the coordinates of the C_α atom of residue i at the time t_j and after 4 ns equilibration, respectively.

RMSD and RMSF analyses were applied only on alpha carbons, while the SASA was calculated on the entire protein.

All analyses were performed using Wordom software [37,38].

Smoothing of the RMSD and SASA plots as a function of time was performed with the smoothing function within the SigmaPlot 12 package, by using the running average module with 10,000 intervals averaging 2000 points each, corresponding to one tenth of the points in the original dataset. Raw data for RMSD and SASA are reported without smoothing in Supplementary Figs. S2 and S3, respectively.

Table 1
Structural and biophysical properties of Rec, GCAP1 and GCAP2 in different conditions.

Protein	Apo		Mg^{2+}		Mg^{2+} + Ca^{2+}		Ca^{2+}		Ca^{2+} + Mg^{2+}	
	$\theta_{222}/\theta_{208}$	T_m	$\theta_{222}/\theta_{208}$	T_m	$\theta_{222}/\theta_{208}$	T_m	$\theta_{222}/\theta_{208}$	T_m	$\theta_{222}/\theta_{208}$	T_m
mRec	0.77	73.1[a]	0.76	68.8	0.87	76.5	0.86	78.8[a]	0.88	76.5
nmRec	0.85	73.8[a]	0.86	68.8	0.90	86.0	0.90	79.4[a]	0.90	86.0
mGCAP1	0.88	50.1[b]	0.90	51.5	0.91	ND[c]	0.91	>70[b]	0.92	ND[c]
nmGCAP1	0.88	42.7[b]	0.91	54.5	0.92	ND[c]	0.93	>60[b]	0.91	ND[c]
mGCAP2	0.89	ND[c]	0.87	ND[c]	0.90	ND[c]	0.89	ND[c]	0.89	ND[c]
nmGCAP2	0.90	92.1	0.90	>96	0.88	ND[c]	0.86	ND[c]	0.87	ND[c]

[a] Data from ref. [39].
[b] Data from ref. [29].
[c] Fit not possible.

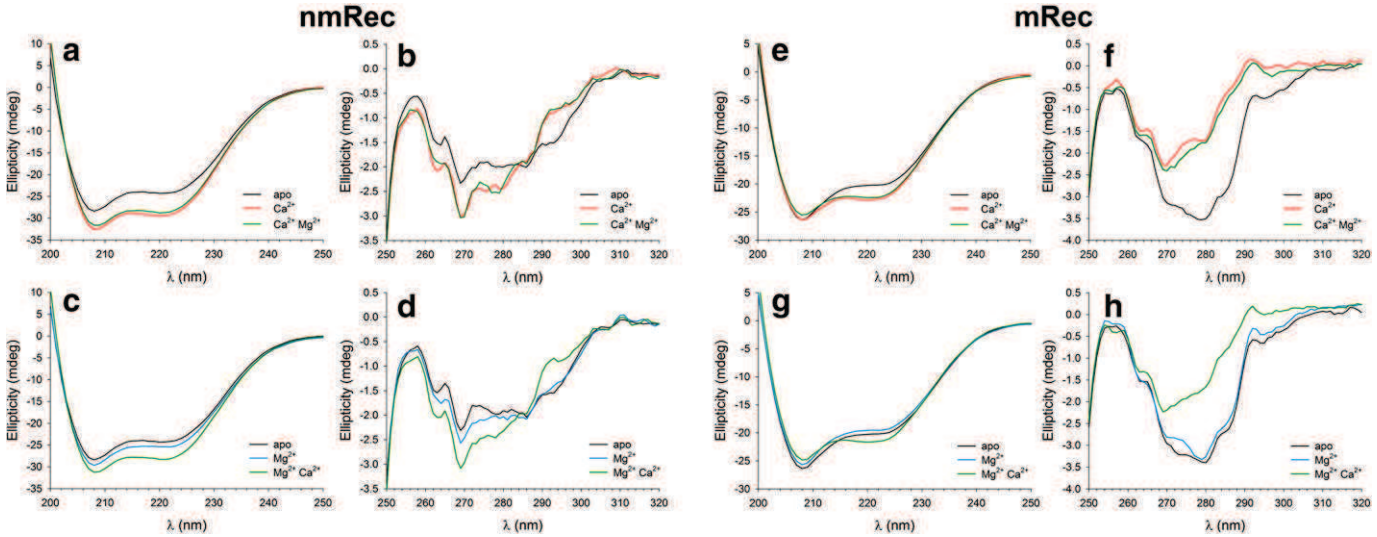

Fig. 1. Structural changes occurring in recoverin upon binding of Ca^{2+} and Mg^{2+}. All measurements were performed at T = 37 °C in 5 mM Tris–HCl pH 7.5, 150 mM KCl, 2 mM DTT buffer. (a) Far UV CD spectra of 9.8 μM nmRec in the presence of 200 μM EGTA (black), 200 μM free Ca^{2+} (red) and after addition of 1 mM Mg^{2+} (green). (b) Near UV CD spectra of 20.4 μM nmRec in the presence of 250 μM EGTA (black), 250 μM free Ca^{2+} (red) and after addition of 1 mM Mg^{2+} (green). (c) Far UV CD spectra of 9.8 μM nmRec in the presence of 200 μM EGTA (black), 1 mM Mg^{2+} (blue) and after addition of 200 μM free Ca^{2+} (green). (d) Near UV CD spectra of 20.4 μM nmRec in the presence of 250 μM EGTA (black), 1 mM Mg^{2+} (blue) and after addition of 250 μM free Ca^{2+} (green). (e) Far UV CD spectra of 8.1 μM mRec in the presence of 200 μM EGTA (black), 200 μM free Ca^{2+} (red) and after addition of 1 mM Mg^{2+} (green). (f) Near UV CD spectra of 17.2 μM mRec in the presence of 250 μM EGTA (black), 250 μM free Ca^{2+} (red) and after addition of 1 mM Mg^{2+} (green). (g) Far UV CD spectra of 8.1 μM mRec in the presence of 200 μM EGTA (black), 1 mM Mg^{2+} (blue) and after addition of 200 μM free Ca^{2+} (green). (h) Near UV CD spectra of 17.2 μM mRec in the presence of 250 μM EGTA (black), 1 mM Mg^{2+} (blue) and after addition of 250 μM free Ca^{2+} (green).

3. Results and discussion

3.1. Comparative analysis of the structural effects of Mg^{2+} on the neuronal calcium sensor proteins

In order to test whether the sequence of binding events of the different cations (Ca^{2+} and/or Mg^{2+}) matters for achieving the specific protein structures, for all three NCS proteins analyzed and both for their myristoylated and non-myristoylated forms we recorded CD spectra in the far and in the near UV after each of the following steps: i) starting from the apo protein (saturating [EGTA]); ii) addition of either 1 mM Mg^{2+} or saturating Ca^{2+}; and iii) inverting the order of the cation additions described in the previous point. Results are reported in the following figures, while a summary of the results obtained for far UV spectroscopy and thermal stability is reported in Table 1.

3.2. Effects of Mg^{2+} on the secondary and tertiary structure of Rec and on its thermal stability

The addition of saturating Ca^{2+} to apo-nmRec caused a typical increase in ellipticity (more negative signal, Fig. 1a), which was observed in earlier studies [39]. When Mg^{2+} was added to nmRec after Ca^{2+} saturation, a slight decrease in ellipticity was observed in the far UV (Fig. 1a), but no significant change was observed in protein tertiary structure, as demonstrated by the substantially overlapped spectra in the near UV region (compare green and red curves in Fig. 1b), which describe the local asymmetric environment of aromatic residues known to be especially sensitive to protein tertiary structure.

Interestingly, when $Mg^{2+}$was added to apo-nmRec, a significant increase in ellipticity was observed both in the far (Fig. 1c) and in the near UV spectra (Fig. 1d), especially in the dichroic bands of Phe and Tyr residues, suggesting that the protein might bind Mg^{2+} in these conditions. However, when Ca^{2+} was added on the top (Mg^{2+}+Ca^{2+}), the spectra became undistinguishable from the ones obtained in the reverse order (compare green lines in Fig. 1b and d).

Thermal denaturation studies showed that the Mg^{2+}-bound form of nmRec in the absence of Ca^{2+} is less stable than the apo form (T_m^{apo} = 73.8 °C; $T_m^{Mg^{2+}}$ = 68.8 °C; see Fig. S1 and Table 1). However, when Ca^{2+} was added at a saturating level after previous incubation with Mg^{2+}, we observed an increase in stability with respect to the one in the presence of saturating Ca^{2+} only ($T_m^{Mg^{2+}/Ca2+}$ = 86.0 °C, $T_m^{Ca^{2+}}$ = 79.4 °C, Table 1). Therefore, the structural effect of Mg^{2+} on nmRec is mostly a mild destabilization of the apo form but a major stabilization of the Ca^{2+}-bound form.

We observed some similar behavior for the myristoylated form of Rec (mRec) (Fig. 1, Table 1). Indeed, the spectral properties of mRec appeared to be only slightly affected by Mg^{2+}, both when starting from the apo and the Ca^{2+}-saturated form. Fig. 1e and g shows that the overall effect of Mg^{2+} is dampening the intensity of both the apo and Ca^{2+}-bound CD spectra in the far UV, but no significant perturbation of the spectral shape was observed either in the far or near UV (Table 1), indicative of an overall good preservation of both the secondary and the tertiary structure. In line with these structural findings, Mg^{2+} destabilized both apo and Ca^{2+}-bound mRec, with a more prominent effect on the apo form (T_m^{apo} = 73.1 °C; $T_m^{Mg^{2+}}$ = 68.8 °C; $T_m^{Ca^{2+}}$ = 78.8 °C; $T_m^{Mg^{2+}/Ca2+}$ = 76.5 °C, see Table 1).

In conclusion, these observations are in line with previous work [20] showing that Mg^{2+} may bind Rec, but it does not trigger the conformational switch, probably because the monodentate, six-coordinate structure of Mg^{2+}-bound EF-hands in the protein does not allow the myristic moiety to move out of the hydrophobic cleft where it is buried.

3.3. Effects of Mg^{2+} on the secondary and tertiary structure of GCAP1 and on its thermal stability

While the main effect of Mg^{2+} on the far UV CD spectra of Ca^{2+}-bound nmGCAP1 was a mild dampening in the intensity of the spectrum (Fig. 2a), apo-nmGCAP1 far UV spectra showed appreciable changes upon Mg^{2+} binding (Fig. 2c and Table 1), consistent with slight changes in the secondary structure or protein compactness. The molar ratio $\theta_{222}/\theta_{208}$, which describes quantitatively the spectral shape of all-α helix proteins, indeed increased from 0.88 to 0.91 (Table 1). Interestingly, while the $\theta_{222}/\theta_{208}$ ratio in the presence of both Mg^{2+} and Ca^{2+} substantially did not depend on the order by which the incubation was performed, the Ca^{2+}-bound form in the absence of Mg^{2+} showed a ratio (0.93) slightly higher than all other cases (Table 1). Near UV

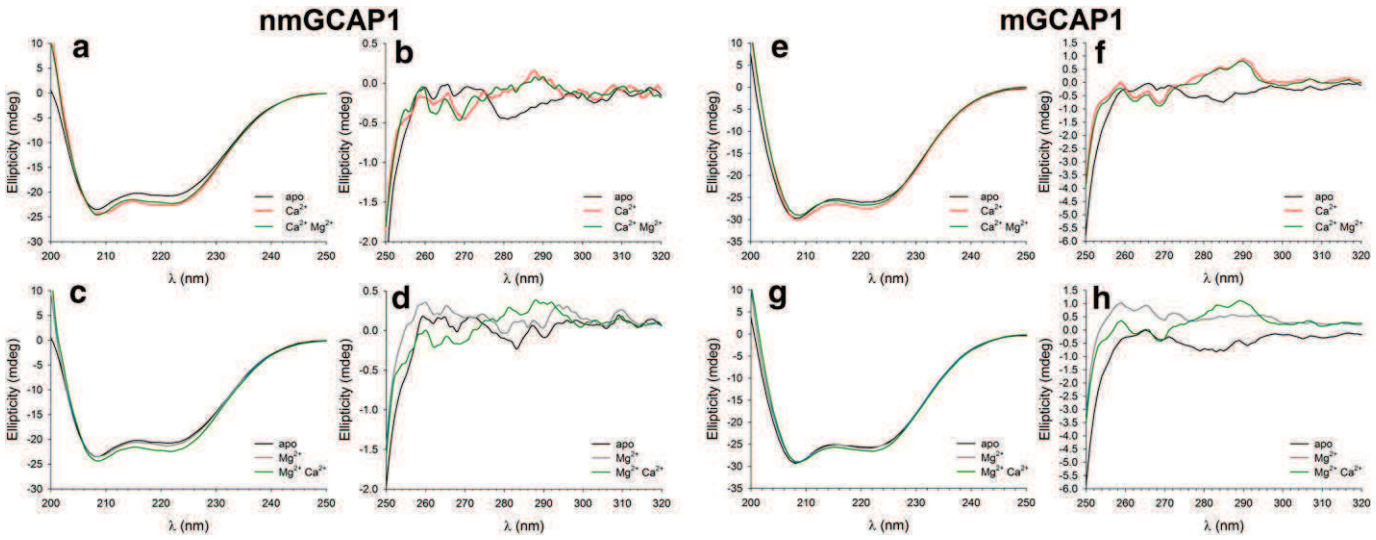

Fig. 2. Structural changes occurring in GCAP1 upon binding of Ca^{2+} and Mg^{2+}. All measurements were performed at T = 37 °C in 5 mM Tris–HCl pH 7.5, 150 mM KCl, 2 mM DTT buffer. (a) Far UV CD spectra of 13 μM nmGCAP1 in the presence of 200 μM EGTA (black), 400 μM free Ca^{2+} (red) and after addition of 1 mM Mg^{2+} (green). (b) Near UV CD spectra of 52 μM nmGCAP1 in the presence of 625 μM EGTA (black), 1.35 mM free Ca^{2+} (red) and after addition of 1 mM Mg^{2+} (green). (c) Far UV CD spectra of 13 μM nmGCAP1 in the presence of 200 μM EGTA (black), 1 mM Mg^{2+} (blue) and after addition of 400 μM free Ca^{2+} (green). (d) Near UV CD spectra of 52 μM nmGCAP1 in the presence of 625 μM EGTA (black), 1 mM Mg^{2+} (blue) and after addition of 1.35 mM free Ca^{2+} (green). (e) Far UV CD spectra of 13 μM mGCAP1 in the presence of 200 μM EGTA (black), 200 μM free Ca^{2+} (red) and after addition of 1 mM Mg^{2+} (green). (f) Near UV CD spectra of 26 μM mGCAP1 in the presence of 400 μM EGTA (black), 400 μM free Ca^{2+} (red) and after addition of 1 mM Mg^{2+} (green). (g) Far UV CD spectra of 13 μM mGCAP1 in the presence of 200 μM EGTA (black), 1 mM Mg^{2+} (blue) and after addition of 200 μM free Ca^{2+} (green). (h) Near UV CD spectra of 26 μM mGCAP1 in the presence of 400 μM EGTA (black), 1 mM Mg^{2+} (blue) and after addition of 400 μM free Ca^{2+} (green).

spectra of Ca^{2+}-bound nmGCAP1 showed only very minor variations upon the addition of Mg^{2+} (Fig. 2b), in particular in the fine structure of the Phe region, which could however be attributed to instabilities of the signal due to protein flexibility.

Interestingly, in line with what we observed for the secondary structure, binding of Mg^{2+} to apo-nmGCAP1 caused more pronounced alterations of the near UV CD spectra, extending from the Phe to the Trp bands (Fig. 2d). Upon the addition of saturating Ca^{2+} however, the spectrum became almost undistinguishable from the one obtained the other way around (adding Mg^{2+} first and then saturating with Ca^{2+}; compare green curves in Fig. 2b and d). In conclusion, in the apo form of nmGCAP1 or at conditions of very low Ca^{2+}, Mg^{2+} affects both the secondary and the tertiary structure, but it has substantially no effect on the Ca^{2+}-bound form. This also reflects on the increased thermal stability of the Mg^{2+}-bound form of nmGCAP1 versus the apo form ($T_m^{apo} = 42.7$, $T_m^{Mg^{2+}} = 54.5$, Table 1), substantially in line with what was determined by Lim et al. with differential scanning calorimetry [18]. No estimate of $T_m^{Mg^{2+}/Ca2+}$ was possible from the thermal denaturation curves (see Fig. S1), as the denaturation profile was apparently monotonic up to ~90 °C.

A slightly different situation was observed for mGCAP1. The addition of 1 mM Mg^{2+} to Ca^{2+}-saturated mGCAP1 resulted in a significant

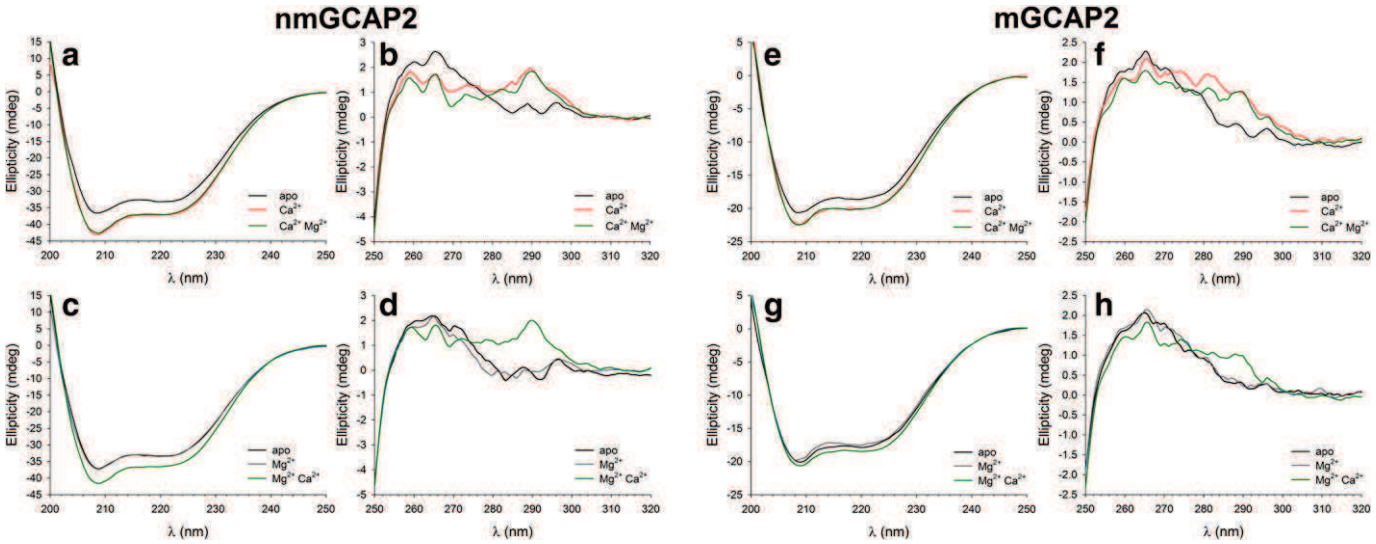

Fig. 3. Structural changes occurring in GCAP2 upon binding of Ca^{2+} and Mg^{2+}. All measurements were performed at T = 37 °C in 5 mM Tris–HCl pH 7.5, 150 mM KCl, 2 mM DTT buffer. (a) Far UV CD spectra of 19 μM nmGCAP2 in the presence of 300 μM EGTA (black), 300 μM free Ca^{2+} (red) and after addition of 1 mM Mg^{2+} (green). (b) Near UV CD spectra of 42 μM nmGCAP2 in the presence of 600 μM EGTA (black), 1.4 mM free Ca^{2+} (red) and after addition of 1 mM Mg^{2+} (green). (c) Far UV CD spectra of 19 μM nmGCAP2 in the presence of 300 μM EGTA (black), 1 mM Mg^{2+} (blue) and after addition of 300 μM free Ca^{2+} (green). (d) Near UV CD spectra of 42 μM nmGCAP2 in the presence of 600 μM EGTA (black), 1 mM Mg^{2+} (blue) and after addition of 1.4 mM free Ca^{2+} (green). (e) Far UV CD spectra of 19 μM mGCAP2 in the presence of 300 μM EGTA (black), 300 μM free Ca^{2+} (red) and after addition of 1 mM Mg^{2+} (green). (f) Near UV CD spectra of 42 μM mGCAP2 in the presence of 600 μM EGTA (black), 1.4 mM free Ca^{2+} (red) and after addition of 1 mM Mg^{2+} (green). (g) Far UV CD spectra of 19 μM mGCAP2 in the presence of 300 μM EGTA (black), 1 mM Mg^{2+} (blue) and after addition of 300 μM free Ca^{2+} (green). (h) Near UV CD spectra of 42 μM mGCAP2 in the presence of 600 μM EGTA (black), 1 mM Mg^{2+} (blue) and after addition of 1.4 mM free Ca^{2+} (green).

dampening of the far UV CD spectra (Fig. 1e), but the spectral shape did not change significantly ($\theta_{222}/\theta_{208} = 0.91$ versus 0.92, Table 1). In line with this observation, in the near UV range the addition of Mg^{2+} did not affect at all the spectral properties of Ca^{2+}-saturated mGCAP1 in any of the typical aromatic bands (Fig. 1f).

When Mg^{2+} was added to apo-mGCAP1, the intensity of the spectrum did not significantly change, although the shape changed in a similar manner compared to the non-myristoylated form (Table 1). Spectral alterations were observed also in the near UV range (Fig. 1h), especially in the Tyr and partially in the Trp band. However, also for mGCAP1 the spectra obtained by adding first Ca^{2+} and then Mg^{2+}, or the other way around were substantially indistinguishable from one another (compare green curves in Fig. 2f and h). Thus, at high Ca^{2+} the presence of Mg^{2+} does not influence the structural properties of either the myristoylated and non-myristoylated forms of GCAP1.

The presence of Mg^{2+} slightly stabilized mGCAP1 secondary structure ($T_m^{apo} = 50.1$ °C, $T_m^{Mg^{2+}} = 51.5$ °C, Table 1), but no conclusion could be drawn as to the comparison between the Ca^{2+}-bound form and the same in the presence of Mg^{2+}, since both transitions were not complete at 95 °C (Fig. S1, Table 1: $T_m^{Ca^{2+}} > 70$, $T_m^{Mg^{2+}/Ca^{2+}} > 70$ °C).

3.4. Effects of Mg^{2+} on the secondary and tertiary structure of GCAP2 and on its thermal stability

The structural behavior of nmGCAP2 in the presence of physiological Mg^{2+} significantly differed from that observed with GCAP1. No difference was detected in intensity and shape of the far UV CD spectra when Mg^{2+} was added to the apo-nmGCAP2 (Fig. 3c) or to the Ca^{2+}-saturated form (Fig. 3a), which is reflected by the identical $\theta_{222}/\theta_{208}$ ratios in the two cases (0.90 and 0.86, respectively; see Table 1). This might suggest that no Mg^{2+}-binding occurs. However, the presence of Mg^{2+} slightly influenced the environment of aromatic residues, both with or without Ca^{2+}-saturating levels (Fig. 3b and d), as proven by small but significant alterations of the near UV fine spectra. Surprisingly, the effect was more apparent when Mg^{2+} was added after Ca^{2+}-saturating levels (Fig. 3b), where differences could be appreciated in the Phe and Tyr bands.

From the analysis of thermal denaturation curves it was not possible to assess a value for the melting temperature for any of the tested case, since no transition apparently occurred at T < 96 °C (Fig. S1).

Similar to what we observed for the non-myristoylated form, addition of Mg^{2+} to the Ca^{2+}-saturated mGCAP2 did not perturb its secondary structure, as demonstrated by the overlapped far UV CD spectra (Fig. 3e, compare green and red curves), which was quantitatively confirmed by the identical (0.89) $\theta_{222}/\theta_{208}$ ratios (Table 1). Also in this case however, the tertiary structure appeared to be somewhat sensitive to Mg^{2+}, even after saturation with Ca^{2+} (Fig. 3f), as indicated by spectral changes and a decrease in intensity of the dichroic bands of Phe and Tyr residues. Interestingly and at odds with the non-myristoylated form, Mg^{2+} slightly perturbed the far UV CD spectrum of apo-mGCAP2 (Fig. 3g), with the $\theta_{222}/\theta_{208}$ ratios shifting from 0.89 to 0.87 (Table 1), but adding saturating Ca^{2+} restored the original spectral shape and intensity (Fig. 3g and Table 1; compare green curves in Fig. 3e and g). However, the tertiary structure resulted to be far less affected by Mg^{2+} when starting from the apo form of mGCAP2 (Fig. 3h), and saturating with Ca^{2+} restored a similar $Ca^{2+} + Mg^{2+}$ spectrum (see Fig. 3f for comparison). Also for mGCAP2, no clear conclusion as to the role of Mg^{2+} in stabilizing each structural state could be drawn from the analysis of thermal denaturation profiles because no transition was visible in any case (Fig. S1). The only appreciable difference was the thermal denaturation profile of mGCAP2 in the sole presence of Mg^{2+}, which compared to the non-myristoylated form, seems to start a transition earlier, thus suggesting a lower thermal stability (Fig. S1).

In conclusion, results from CD spectroscopy for m/nmGCAP2 significantly differ from those for GCAP1 and suggest that Mg^{2+} might bind to GCAP2 with different affinity and/or dynamics than it does to GCAP1. The binding might however be specific for different activation states of the calcium sensor. In particular, we could observe the following: i) for nmGCAP2, if the binding occurred, it would affect only the local environment of its aromatic residues, mostly and surprisingly at high [Ca^{2+}]; ii) for mGCAP2, results from far UV CD suggest that the binding might occur in the condition of low Ca^{2+}, however this would leave the tertiary structure substantially unperturbed; and iii) for mGCAP2, results from near UV CD suggest that the local environment of its aromatic residues is influenced by physiological Mg^{2+} even after saturation with Ca^{2+}.

While the conclusions from our CD spectroscopy analysis of GCAP1 are substantially in line with what is known as to the role of Mg^{2+} interacting with the NCS, and are compatible with defined structural consequences of a pure binding process, results for GCAP2 seem intrinsically hard to interpret, and somewhat contradictory. Overall, the data are not feasible for an interpretation based on a pure binding process, and in fact they raise some questions. Is GCAP2 binding Mg^{2+} depending on the presence of the myristoyl moiety? Does the putative binding occur even in the presence of saturating Ca^{2+}, thus presumably in other binding sites than those highly specific for Ca^{2+}? We tried to answer some of these questions by further focusing on the putative interaction of GCAP2 with Mg^{2+}.

3.5. Biophysical studies of the interaction between myristoylated/non-myristoylated GCAP2 and Mg^{2+}

In order to quantitatively investigate the binding of Mg^{2+} to GCAP2, we performed ITC experiments starting from conditions of carefully decalcified proteins and buffers. While for nmGCAP2 the pattern of heat pulses observed in all the titration experiments was incompatible with a binding process (results not shown), only in 4 out of 15 experiments performed with mGCAP2 the observed pattern was

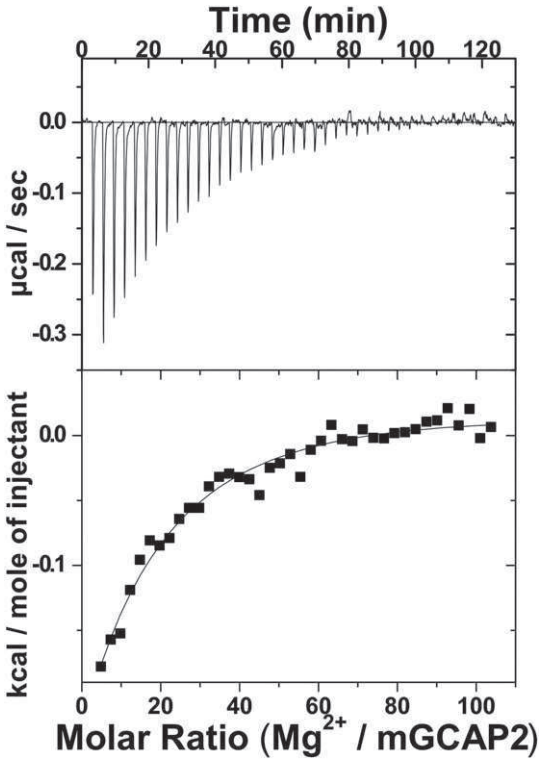

Fig. 4. Example of Mg^{2+}-mGCAP2 binding curve monitored by ITC. The upper part shows the heat pulse obtained by the injection 5 µL 10 mM $MgCl_2$ in 14 µM mGCAP2 in decalcified Tris buffer. The lower part displays the resulting enthalpy change as a function of the molar ratio of Mg^{2+} and mGCAP2 and the fitting curve.

Table 2
Thermodynamic parameters for Mg^{2+} binding to mGCAP2.

K_D^1/mM	K_D^2/mM	ΔH^1/kcal mol^{-1}	ΔH^2/kcal mol^{-1}
0.32 ± 0.20	4.4 ± 2.3	−4.6 ± 3.5	−2.7 ± 35.6

ascribable to a binding process. An example of successful titration is reported in Fig. 4, and a summary of the obtained thermodynamic parameters is shown in Table 2. Fitting the data to a sequential two-site binding model led to a physiologically relevant affinity (320 μM) for the first binding site and a non-physiological (4.4 mM) affinity for the second, lowest affinity binding site, similarly to what has been previously obtained by Lim et al. [18] for GCAP1. While the four successful titrations were per se reproducible and compatible with an exothermic process, we stress that in the majority of the other cases and in spite of the same experimental conditions and protein samples used in repeated experiments, no specific binding pattern could be obtained, thus pointing to a phenomenon that might be intrinsically poorly reproducible. Indeed, when we tried an alternative approach to detect Mg^{2+} binding to GCAP2 by performing titration experiments using the intrinsic Trp fluorescence of the protein with the same setup previously used for GCAP1 [17], we could neither observe a reproducible pattern for mGCAP2 nor for nmGCAP2 (results not shown).

Overall, our results clearly showed that the structural effects of Mg^{2+} on GCAP2 and the binding mode significantly differ from what has been so far observed for GCAP1. In particular, under the tested conditions it has been especially difficult to measure binding constants for Mg^{2+}, as some other process not occurring for GCAP1 seems to interfere with the putative binding of Mg^{2+}. One possibility to explain our data is that GCAP2 may be dimeric independent of the Ca^{2+} levels [40]. In particular, the observation that in the apo form GCAP2 is more flexible [40] may explain, at least partly, why the observed changes in far UV CD spectra (Fig. 3g) could be ascribed to the binding of Mg^{2+}. However, it could well be that even slight changes in the amount of cations as well as in protein concentration lead to different populations of monomers vs. dimers, which would complicate the interpretation of ITC and fluorescence data. Another possible phenomenon interfering with our titration experiments could be the different behavior of the myristoyl moiety in mGCAP2. Like in GCAP1, the acylic group does not extrude totally in a myristoyl switch fashion [41], however and at odds with GCAP1 it seems to be rather exposed to the solvent in both apo and Ca^{2+} states [42] and more sensitive to the external environment, as seen in experiments with membranes and micelles [43]. This could also partially contribute to the complex behavior observed in our experiments.

3.6. Molecular dynamics simulations of different regulatory states of myristoylated GCAP1

3.6.1. Diverse GC activating and inhibitory states of mGCAP1

While it is generally established that the fully Ca^{2+}-loaded state of GCAP1 is responsible for the maximal inhibition of the GC target, several recent lines of evidence showed that, when Ca^{2+} concentration drops to lower values (20–50 nM) as a consequence of photoreceptor illumination, it is a specific Mg^{2+}-bound form of GCAP1 rather than its apo state, that triggers the activation of GC [17,19,21]. In different studies, Peshenko et al. measured by fluorescence spectroscopy a moderate affinity of GCAP1 for Mg^{2+} (~0.25 mM), which was shown not to depend significantly on the presence of myristoylation [17,44]. The binding was also confirmed by ITC experiments performed by the same authors, although the detected affinity for the only physiologically relevant binding constant was lower (~0.7 mM) [18]. These quantitative data confer reliability to the hypothesis that, at least one EF-hand in GCAP1 may be occupied by Mg^{2+}, when [Ca^{2+}] is significantly low. By means of exhaustive mutational analysis and functional assays the same group demonstrated that the metal-free state of EF3, supposedly

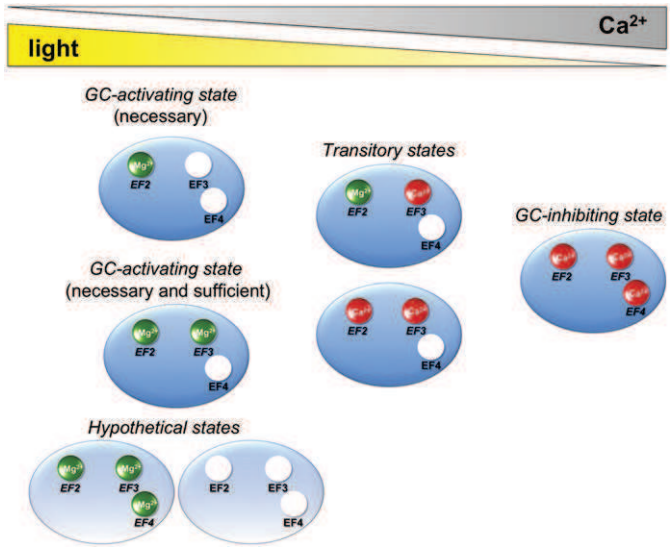

Fig. 5. Regulatory states of mGCAP1 simulated in 200 ns molecular dynamics simulations. Each of the cation-binding EF-hand is indicated. Writing in italics refers to a binding site occupied by either a Ca^{2+} (red sphere) or Mg^{2+} (green sphere) ion. The schematic positioning of each state refers to the light conditions and the relative intracellular levels of Ca^{2+}, represented at the top of the figure.

the lower affinity binding site for Mg^{2+}, reduced the efficiency of GC binding and activation, thus leading to the conclusion that the binding of a cation to EF3 seems necessary for reaching the proper functional state of the target enzyme [19,45].

By making use of the knowledge arising from these previous studies we set up 200 ns MD simulations of mGCAP1 in seven different states, reported in Fig. 5. We simulated the states corresponding to low [Ca^{2+}] and light-exposed conditions, where EF2 is necessarily occupied by Mg^{2+}, which was predicted to be bound to EF3 as well in order to activate the GC efficiently [21]. We also simulated the dark-adapted state that inhibits GC, in which EF2, EF3 and EF4 are all occupied by Ca^{2+} [21] and built models for intermediate, transitory states, in which Ca^{2+} has dissociated from the lowest affinity site EF4, and EF2 is either still occupied by a Ca^{2+} or a Mg^{2+} ion. Finally, for the sake of comparison of structure dynamics, we simulated two putative states: one in which no EF-hand is occupied by any cation (apo), and the other one where all three EF-hands are ideally occupied by Mg^{2+} ions. Neither of these states is likely to be physiologically relevant, as in the first case it was demonstrated by comprehensive mutagenesis experiments that GCAP1 mutants that do not bind Ca^{2+} and Mg^{2+} are incapable of activating GC [46]; on the other hand, the rather low affinity of GCAP1 for Mg^{2+} compared to the ~1 mM intracellular concentration together with the competition for Ca^{2+} makes it rather unlikely that more than two binding sites are ever occupied by Mg^{2+} even in the total absence of Ca^{2+}.

In the following paragraphs, we shall present the results of MD simulations of diverse GCAP1 states by first comparing the structure of each state after 4 ns equilibration with that of the apo form, in which no EF-hand is occupied by any cation, and then describing the structural features observed in the 200 ns MD production phase.

3.6.2. General structural properties of mGCAP1 states after equilibration

The comparison of seven mGCAP1 states before the production phase of MD simulations confirmed that important structural differences that distinguish specific states with respect to the putative apo form already manifest in the equilibration phase. As a clarifying example, Fig. 6 reports on the comparison between the equilibrated structures (after 4 ns) of apo-mGCAP1 and the fully Ca^{2+}-loaded state $EF2^{Ca2+}$ $EF3^{Ca2+}$ $EF4^{Ca2+}$ (holo). In apo-mGCAP1 all EF-hands were in an "open" conformation, resulting in an overall higher accessibility to

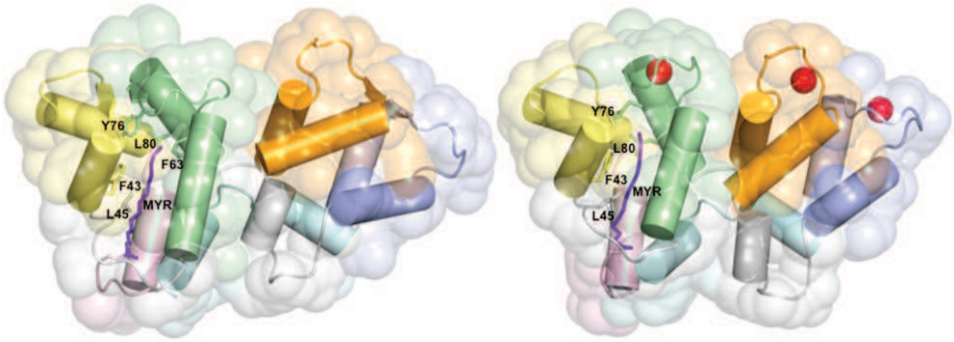

Fig. 6. Cartoon structural model of mGCAP1 in the apo form (left), and in the fully Ca^{2+}-loaded form (right) after 4 ns equilibration in all-atom MD simulations. The EF1 motive is yellow, EF2 green, EF3 orange and EF4 violet blue. Loops interconnecting EF-hand motifs are colored gray, while the N-term and the C-term are colored pale pink and pale cyan, respectively. The myristoyl moiety is represented by purple sticks. The main residues interacting with myristoyl are also represented by sticks, labeled and colored according to the structural elements they belong to. The SASA, shown in transparency, is 10,606 Å^2 for the apo form and 10,043 Å^2 for the Ca^{2+}-bound form.

the solvent as compared to the holo-mGCAP1. The fully Ca^{2+}-loaded state appeared indeed more compact already at the beginning of the MD production phase. After the equilibration phase, the myristoyl group in apo-mGCAP1 was bent at C5, to tighten the interaction with key hydrophobic residues, among which Phe 43, Leu 45, Phe 63 and Leu 80, and marginally Tyr 76. A similar bent conformation was observed for the myristic group in holo-mGCAP1, although the motion of the N-terminal loop toward the protein interior in the holo form significantly reduced the interaction with Phe 63, while maintaining the other hydrophobic interactions substantially unaltered (Fig. 6).

3.6.3. Structural dynamics of putative GC-activating states over 200 ns simulations

The 119–132 loop interconnecting EF3 with EF4 (represented in gray in Fig. 6) was generally highly flexible in the tested states, as reflected by the high RMSF values found for this structural region over 200 ns (Fig. 7b). Moreover, in some of the tested states the 120–125 strand of this loop acquired a local α-helix conformation, which showed a transient behavior. In contrast to other states however, in the apo-mGCAP1 the loop was found to be rather stable and the local helix conformation persisted over the 200 ns simulation. Another peculiar feature of the apo state was a conserved pair of H-bonds between the backbone groups NH of Ile 107 and C═O of Leu 151 and NH of Leu 153 and C═O of Gly 105, which created a short antiparallel β-sheet stable during the 200 ns simulation, which contributed to maintain EF3 and EF4 in an open conformation. Interestingly, both residues Ile 107 and Leu 151 have been found to be mutated respectively in Thr and Phe in patients suffering from cone dystrophy [47,48]. Another similarly short β-sheet was observed between EF1 and EF2, which however was not stable during the production phase. The hydrophobic interactions stabilizing the myristoyl moiety were generally conserved. When all the EF-hands were virtually occupied by a Mg^{2+} ion ($EF2^{Mg^{2+}}$ $EF3^{Mg^{2+}}$ $EF4^{Mg^{2+}}$) the C_α-RMSD calculated with respect to the apo form after the 4 ns equilibration was 3.4 Å, the highest in the whole series of GCAP1 simulated states. An apparent difference was the kink of the myristoyl group at C10, due to the hydrophobic interaction with Leu 80, but structural differences were generally spread over the whole tertiary structure, especially at the EF3 motif and 119–132 loop. Overall the $EF2^{Mg^{2+}}$ $EF3^{Mg^{2+}}$ $EF4^{Mg^{2+}}$ form was the most dynamically compact one in the series, as clearly shown by the lowest SASA profile (Fig. 7 and Fig. S3). After the first 50 ns dynamics production the structure was significantly stable, and even the highly dynamic 119–132 loop showed only minor rearrangement as compared to other cases. With respect to the equilibrated structure, main differences concerned only the EF3 loop and the conformation of the myristoyl moiety, likely due to an outward rigid displacement of the C-terminal helix.

3.6.4. Structural dynamics of more realistic GC-activating states over 200 ns simulations

The structure of mGCAP1 with one Mg^{2+} bound to EF2 ($EF2^{Mg^{2+}}$) after equilibration was significantly different from the apo form, with a C_α-RMSD of 2.8 Å. The EF2 loop (64–76), which was in an open conformation in the apo form, became now properly closed to bind a Mg^{2+} cation. The myristoyl group was still involved in interactions with Phe 43 and Leu 45 with the same orientation as in the apo form, while Phe 63 acquired a different conformation, resulting in a weaker interaction, similar to what was observed for the holo form. New stabilizing interactions involved Val 83 and Leu 176. The main structural difference with apo-mGCAP1 in the N-term domain was a different inclination and orientation of the entering helix (helix E) in the EF2 motif. Significant variations were observed also in the C-term domain, where helices had generally undergone rigid motions and the 119–132 loop showed a significantly different conformation.

During the course of the 200 ns simulation the structure of $EF2^{Mg^{2+}}$ mGCAP1 was overall fairly stable when compared to all other GCAP1 states, which is reflected by the stable and lowest C_α-RMSD profile (Fig. 7a). Even the 119–132 region was rather stable, as shown in Fig. 7b. The most flexible region was the 142–148 stretch (Fig. 7b), which corresponds to the E-helix and the loop of EF4. The formation of the transient helix in the 119–132 loop connecting EF3 and EF4 was also observed. Interestingly, due to the fact that residues 2–8 (N-terminus) tend to close toward the protein core, in line with the decrease in the overall SASA (Fig. 7c) the myristic moiety became kinked at the level of C4, acquiring a novel L-shaped conformation that was fairly stable in the simulated time course. Overall, the SASA profile confirmed that after approximately 40 ns the $EF2^{Mg^{2+}}$ mGCAP1 structure, like all the other Mg^{2+}-only-bound cases, acquired an overall conformation less solvent-exposed compared to the tested Ca^{2+}-bound forms (Fig. 7c).

The other mGCAP1 state hypothesized to be relevant for GC activation, in which two Mg^{2+} ions are bound respectively to EF2 and EF3 ($EF2^{Mg^{2+}}$ $EF3^{Mg^{2+}}$) showed a 3.2 Å C_α-RMSD compared to apo mGCAP1, which became 1.9 Å when compared to $EF2^{Mg^{2+}}$. Comparison with the $EF2^{Mg^{2+}}$ state highlighted, as the main difference, a higher flexibility of the 119–132 region in the time course of the 200 ns-simulation (Fig. 7b), otherwise a rather similar conformation was observed. In line with what was observed in the $EF2^{Mg^{2+}}$ form, the SASA stabilized after ~80 ns to an average value that was lower compared to the Ca^{2+}-bound forms. The acyl chain of the myristoyl group in some of the frames kinked around C7 and was stabilized by interactions with Phe 63, Trp 21 and Val 83. Moreover, the simulation showed a rotation of the myristoyl group around C1 leading to an L-shaped conformation, which was however significantly less stable than the one observed for $EF2^{Mg^{2+}}$.

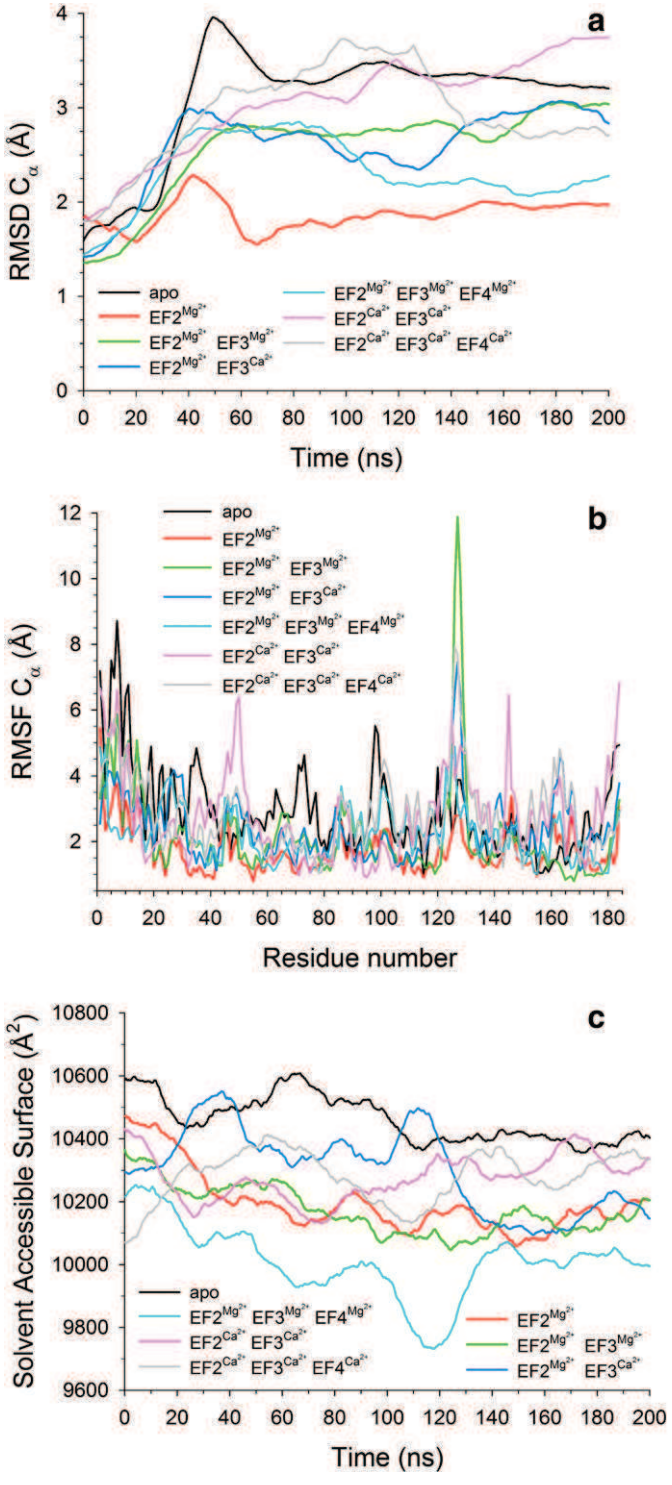

Fig. 7. Structural descriptors of mGCAP1 dynamical features calculated on the trajectories obtained by 200 ns all-atom molecular dynamics simulations. All figures have the same legend: apo black, $EF2^{Mg^{2+}}$ red, $EF2^{Mg^{2+}}$ $EF3^{Mg^{2+}}$ green, $EF2^{Mg^{2+}}$ $EF3^{Ca^{2+}}$ blue, $EF2^{Mg^{2+}}$ $EF3^{Mg^{2+}}$ $EF4^{Mg^{2+}}$ cyan, $EF2^{Ca^{2+}}$ $EF3^{Ca^{2+}}$ pink, $EF2^{Ca^{2+}}$ $EF3^{Ca^{2+}}$ $EF4^{Ca^{2+}}$ gray. (a) Smoothed curves describing the time evolution over 200 ns of the C_α-RMSD calculated with respect to the relative equilibrated structure (for raw data see Fig. S2). (b) RMSF of C_α atoms for each amino acid calculated with respect to the equilibrated structure. (c) Smoothed curves describing the time evolution over 200 ns of the SASA for each mGCAP1 state (for raw data see Fig. S3).

Overall, the conformation of EF2 and EF3 was in a closed form, very similar to that of $EF2^{Mg^{2+}}$, even though the latter had no Mg^{2+} bound to EF3. This seems to support the idea that binding of Mg^{2+} to EF3 is not essential to properly structure the EF3 loop and make GCAP1 switch to its GC activating state, although the ion occupancy of EF3 seems to be a functional requirement [19,45].

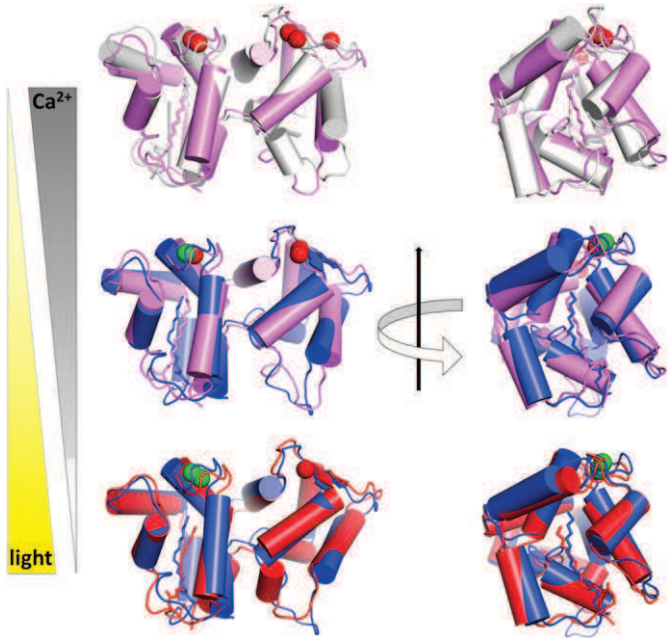

Fig. 8. Structural representation of the transition from inhibitor to activator state of mGCAP1. Left: front view, right: side view, rotated π/2 counter-clockwise. $EF2^{Ca^{2+}}$ $EF3^{Ca^{2+}}$ $EF4^{Ca^{2+}}$ inhibitor state is colored in gray, $EF2^{Ca^{2+}}$ $EF3^{Ca^{2+}}$ transition state is pink, $EF2^{Mg^{2+}}$ $EF3^{Ca^{2+}}$ transition state is blue and $EF2^{Mg^{2+}}$ activator state is red. α-Helices are represented as cylinders, β-sheets are represented by arrows, the myristoyl group is represented by sticks and Mg^{2+} and Ca^{2+} ions are represented by green and red spheres, respectively. Each structure represents the final frame after 200 ns MD simulations. C_α-RMSD values for the overlapped structures are respectively 2.8 Å (top), 2.1 Å (middle) and 2.3 Å (bottom).

3.6.5. Structural dynamics of putative GCAP1 transitory states over 200 ns simulations

The mGCAP1 state with one Mg^{2+} ion bound to EF2 and one Ca^{2+} ion bound to EF3 ($EF2^{Mg^{2+}}$ $EF3^{Ca^{2+}}$) showed a significant C_α-RMSD (2.8 Å) compared to the apo state already after equilibration. The myristoyl moiety was kinked at C4 and C8, overall inducing an S-shape in the acylic chain after equilibration. During the 200 ns MD production the myristoyl moiety was rather flexible, with kinks maintained at C7/C8, and some extended conformations observed in some frames. The 119–132 loop was quite flexible over the simulated time frame, while peculiar features of this state were: i) the short helix at the C-terminus, which closed up toward the protein interior right after the equilibration phase, and stabilized there for the whole MD production; ii) the appearance of another flexible region, namely the loop 142–149 associated to EF4; and iii) helix E in EF1 was observed to oscillate in a rigid fashion around a rather stable average position. These structural features resulted in a 2.3 Å RMSD value after the 200 ns MD production as compared to the GC activating state $EF2^{Mg^{2+}}$ (Fig. 8).

Rather different structural features characterized the other putative state of mGCAP1, namely that with two Ca^{2+} ions bound to EF2 and EF3 ($EF2^{Ca^{2+}}$ $EF3^{Ca^{2+}}$). The first difference appeared clearly after equilibration, as the C_α-RMSD (3.5 Å) compared to apo form was significantly higher than that calculated with respect to $EF2^{Mg^{2+}}$ $EF3^{Ca^{2+}}$ (2.3 Å), which maintained rather similar even at the end of 200 ns simulations (2.1 Å; Fig. 8). Binding of Ca^{2+} to both EF-hands constrained the conformation of the relative loops and made the two EF-hands interact more tightly with one another, with far reaching effects on the whole tertiary structure. Indeed, the time course of the C_α-RMSD increased monotonically (Fig. 7a), and reached the highest values in the whole set of tested

states, suggesting that this state of mGCAP1 is indeed rather unstable, and may precede $EF2^{Mg^{2+}}$ $EF3^{Ca^{2+}}$ in the time course of GCAP1 switch from GC inhibitory to activating states.

Peculiar features in the binding pocket of the myristoyl moiety were observed. The myristoyl group did not interact anymore with Leu 176 but was stabilized by interactions with Leu 80 and Tyr 76 which, compared to other cases, showed here a stronger interaction with the acylic chain. Interestingly, the C_α-RMSD calculated with respect to the $EF2^{Mg^{2+}}$ $EF3^{Mg^{2+}}$ form was 2.1 Å after equilibration, and the structures were indeed rather similar, except for the highly flexible interconnecting region 119–132 and the conformation of EF-4 at the level of the 142–148 region (E-helix and loop). Nonetheless, the $EF2^{Ca^{2+}}$ $EF3^{Ca^{2+}}$ form showed overall high local flexibilities compared to the all other forms in several structural regions, as clearly shown by the RMSF plots (Fig. 7b). This is presumably due to the fact that this transitory state serves indeed to induce to the GC the transition from inhibitor to activator states, therefore an overall flexibility may be necessary. Among the most prominent collective motions occurring during the course of the 200 ns dynamics, a slight outward tilt of helix E in EF3 was observed, as well as a rotation of the ψ angle between the peptide bond involving the myristoyl moiety and that of Gly 2, a feature already observed after equilibration. The SASA profile (Fig. 7c) highlighted already after 80 ns a higher exposition to the solvent compared to all other forms with only Mg^{2+} ions bound.

3.6.6. Structural dynamics of the GC inhibiting state over 200 ns simulations

The structure of the Ca^{2+}-saturated, holo-mGCAP1, corresponding to the GC-inhibitory state ($EF2^{Ca^{2+}}$ $EF3^{Ca^{2+}}$ $EF4^{Ca^{2+}}$) showed a C_α-RMSD of 2.7 Å with respect to the apo form after equilibration. Major differences concerned the structure of all three EF-hand calcium-binding loops, as already described in Section 3.6.2 (see Fig. 6). The C_α-RMSD with respect to the $EF2^{Ca^{2+}}$ $EF3^{Ca^{2+}}$ state after 4 ns equilibration was 2.3 Å, mostly ascribable to differences in the flexible interconnecting loop 119–132 and EF4, as expected considering that EF4 is the binding site with the lowest affinity for Ca^{2+} [18,29]. However, the structural difference increased in the time course of MD simulations, resulting in a 2.8 Å RMSD after the production phase (Fig. 8).

Analysis of MD simulations over the 200 ns showed significant variations in the N-terminal part, especially in the 2–8 strand, which caused significant changes in the amplitude of the O═C–C1–C2 dihedral angle in the myristoyl moiety, which remained stable in the 50–200 ns time frame.

Interestingly, despite the C_α-RMSD increased monotonically up to ~100 ns, reaching values among the higher ones within the tested set of mGCAP1 states (Fig. 7a), it then stabilized to values lower than those of the apo, $EF2^{Ca^{2+}}$ $EF3^{Ca^{2+}}$, $EF2^{Mg^{2+}}$ $EF3^{Mg^{2+}}$ and $EF2^{Mg^{2+}}$ $EF3^{Ca^{2+}}$ states although the SASA (Fig. 7c) was higher than the respective values for these states, except for $EF2^{Ca^{2+}}$ $EF3^{Ca^{2+}}$.

3.6.7. General conclusions from MD simulations: essential structural features for switching between different mGCAP1 regulatory states

Results from our MD simulations provide a structural interpretation that is missing so far. For instance, it provides an explanation why at least one Mg^{2+} ion has to be bound to mGCAP1 in order to switch to its activating state. Indeed, when Mg^{2+} is bound to EF2, structures are characterized by a more compact conformation, with reduced SASA compared to the inhibitory state (see Fig. 7c). The analysis also suggests another reason for apo-mGCAP1 not to exist physiologically, namely that it is characterized by high solvent accessibility (Fig. 7c) and too many regions of high flexibility (Fig. 7b). Such a state would very likely interfere with the stable and site-directed targeting to the GC. The final conformation of the myristoyl moiety is similar in both Mg^{2+}-bound activating states ($EF2^{Mg^{2+}}$ and $EF2^{Mg^{2+}}$ $EF3^{Mg^{2+}}$), and significantly differs from that of the transitory and inhibitory states.

Exchanging Mg^{2+} for Ca^{2+} in EF2 seems also a crucial step in defining the transitory state, in order to drive mGCAP1 toward its fully activating state. It is in fact apparent from MD simulations that the transitory state with two Ca^{2+} ions bound is structurally far less stable and compact than the one with one Mg^{2+} and one Ca^{2+} ion bound (Fig. 7). While our data are in agreement with Mg^{2+} being bound to EF2 in order to achieve structural features allowing the activation of the GC [21], results from MD simulations suggest that the binding of Mg^{2+} also to EF3 would cause an extreme flexibility of the 119–132 loop, and a general higher flexibility compared to the case in which the EF3 site is empty (Fig. 7a and b). On the other hand, it has been previously demonstrated that binding of a cation to EF2 is crucial for GCAP1 attachment to GC, and that in EF3 it is in fact less critical, although it enhances the efficiency of the GCAP1 docking on the target enzyme [19] and its maximal stimulation [45]. The overall moderate affinity of GCAP1 for Mg^{2+} would still allow an occupancy of EF2 by Mg^{2+} of about 55% and of EF3 of about 33% in the absence of competition with Ca^{2+} (see Supplementary Information). Moreover, the binding of GCAP1 to the GC target might stabilize its structure and reduce the intrinsic flexibility, therefore the results from our MD simulations appear substantially in line with the current model of Mg^{2+}/Ca^{2+} exchange in the regulation of GC by GCAP1 [21].

Finally, it is worth noting that besides the intrinsic differences in structural features typical of each GCAP1 regulatory state, no occurrence of dramatic conformational changes was observed in our MD simulations, the overall C_α-RMSD never exceeding 4 Å (Fig. 7). This finding is in line with a very recent work by Lim et al. [49], in which a mutant of GCAP1 lacking Ca^{2+} binding in EF4 and thus mimicking the transition to the activating state was found to have similar NMR backbone chemical shifts compared to wild type Ca^{2+}-saturated GCAP1, thus suggesting the absence of dramatic conformational changes.

A graphical summary of the dynamical features of mGCAP1 switching from the GC inhibitory state to the GC activating form is reported in Fig. 8. The figure shows a snapshot of the regulatory states after 200 ns MD simulations, in their transition toward the activating state, upon release of Ca^{2+} ions from the three EF-hands, and replacement with a Mg^{2+} ion in EF2.

4. Conclusions

By using different biophysical techniques we demonstrated that the structural effects of physiological Mg^{2+} on the regulatory state strongly depend on the specific neuronal calcium sensor. While Rec in its myristoylated form constituting the physiological condition is only slightly affected by Mg^{2+} in terms of protein structure and stability, GCAP1 and GCAP2 are both significantly affected. In particular, our results confirm that the GC activating state of GCAP1 requires the presence of at least a Mg^{2+} ion bound to the EF2 motif, a result consistent with previous biochemical investigations [45]. MD simulations further suggest a sequence of dynamical events that accompany the switch of mGCAP1 from its GC inhibitory to its activator state, which include: i) the release of a Ca^{2+} ion bound to EF4; ii) the Mg^{2+}/Ca^{2+} ion exchange in EF2; iii) and the release of a Ca^{2+} ion bound to EF3. These events accompany the structural transition toward a rather compact state, in which the myristoyl moiety shows a certain flexibility, and is eventually stabilized in a conformation that differs significantly from that of the holo, inhibitory state. It will be interesting to further investigate, whether the transition does strengthen and/or stabilize the interaction with the target GC.

The structural behavior of nm/mGCAP2 in the presence of Mg^{2+} appears significantly different from that of GCAP1, and overall rather complex. While our data clearly show that Mg^{2+} does exert an effect on the structure of both GC-activating and inhibitory states, it likely affects specific oligomeric states of GCAP2, perhaps influencing the environment of the myristic moiety in ways yet to be clarified in future studies.

Acknowledgements

We would like to thank Dr. Francesco Raimondi for his valuable technical support. This work was supported by funds from the Italian Ministry for Research and Education via Departmental funds (FUR2013) and via support from CINECA through the Italian Super Computing Resource Allocation project (ISCRA Grant: HP10CB736X to DDO) and by a grant from the Deutsche Forschungsgemeinschaft (DFG) supporting the Research Training Group GRK1885 in Oldenburg.

Appendix A. Supplementary data

Supplementary data to this article can be found online at http://dx.doi.org/10.1016/j.bbamcr.2014.10.026.

References

[1] K. Nakatani, C. Chen, K.W. Yau, Y. Koutalos, Calcium and phototransduction, Adv. Exp. Med. Biol. 514 (2002) 1–20.
[2] M.L. Woodruff, A.P. Sampath, H.R. Matthews, N.V. Krasnoperova, J. Lem, G.L. Fain, Measurement of cytoplasmic calcium concentration in the rods of wild-type and transducin knock-out mice, J. Physiol. 542 (2002) 843–854.
[3] K.W. Koch, D. Dell'Orco, A calcium-relay mechanism in vertebrate phototransduction, ACS Chem. Neurosci. 4 (2013) 909–917.
[4] K.W. Koch, T. Duda, R.K. Sharma, Ca(2+)-modulated vision-linked ROS-GC guanylate cyclase transduction machinery, Mol. Cell. Biochem. 334 (2010) 105–115.
[5] E.N. Pugh Jr., T.D. Lamb, Phototransduction in Vertebrate Rods and Cones: Molecular Mechanisms of Amplification, Recovery and Light Adaptation, Elsevier Science B.V, 2000.
[6] R. Stephen, S. Filipek, K. Palczewski, M.C. Sousa, Ca^{2+}-dependent regulation of phototransduction, Photochem. Photobiol. 84 (2008) 903–910.
[7] R.D. Burgoyne, Neuronal calcium sensor proteins: generating diversity in neuronal Ca^{2+} signalling, Nat. Rev. Neurosci. 8 (2007) 182–193.
[8] P. Philippov, K.-W. Koch, Neuronal Calcium Sensor Proteins, Nova Science Publishers, New York, 2006.
[9] J.B. Ames, R. Ishima, T. Tanaka, J.I. Gordon, L. Stryer, M. Ikura, Molecular mechanics of calcium–myristoyl switches, Nature 389 (1997) 198–202.
[10] T. Tanaka, J.B. Ames, T.S. Harvey, L. Stryer, M. Ikura, Sequestration of the membrane-targeting myristoyl group of recoverin in the calcium-free state, Nature 376 (1995) 444–447.
[11] M.E. Burns, A. Mendez, J. Chen, D.A. Baylor, Dynamics of cyclic GMP synthesis in retinal rods, Neuron 36 (2002) 81–91.
[12] A.M. Romani, A. Scarpa, Regulation of cellular magnesium, Front. Biosci. 5 (2000) D720–D734.
[13] C. Chen, K. Nakatani, Y. Koutalos, Free magnesium concentration in salamander photoreceptor outer segments, J. Physiol. 553 (2003) 125–135.
[14] W. Yang, H.W. Lee, H. Hellinga, J.J. Yang, Structural analysis, identification, and design of calcium-binding sites in proteins, Proteins 47 (2002) 344–356.
[15] E.A. Permyakov, R.H. Kretsinger, Calcium Binding Proteins, John Wiley & Sons, Hobok, New Jersey, 2011.
[16] M.E. Maguire, J.A. Cowan, Magnesium chemistry and biochemistry, Biometals 15 (2002) 203–210.
[17] I.V. Peshenko, A.M. Dizhoor, Guanylyl cyclase-activating proteins (GCAPs) are Ca^{2+}/Mg^{2+} sensors: implications for photoreceptor guanylyl cyclase (RetGC) regulation in mammalian photoreceptors, J. Biol. Chem. 279 (2004) 16903–16906.
[18] S. Lim, I. Peshenko, A. Dizhoor, J.B. Ames, Effects of Ca^{2+}, Mg^{2+}, and myristoylation on guanylyl cyclase activating protein 1 structure and stability, Biochemistry 48 (2009) 850–862.
[19] I.V. Peshenko, E.V. Olshevskaya, A.M. Dizhoor, Binding of guanylyl cyclase activating protein 1 (GCAP1) to retinal guanylyl cyclase (RetGC1). The role of individual EF-hands, J. Biol. Chem. 283 (2008) 21747–21757.
[20] T. Ozawa, M. Fukuda, M. Nara, A. Nakamura, Y. Komine, K. Kohama, Y. Umezawa, How can Ca^{2+} selectively activate recoverin in the presence of Mg^{2+}? Surface plasmon resonance and FT-IR spectroscopic studies, Biochemistry 39 (2000) 14495–14503.
[21] A.M. Dizhoor, E.V. Olshevskaya, I.V. Peshenko, Mg^{2+}/Ca^{2+} cation binding cycle of guanylyl cyclase activating proteins (GCAPs): role in regulation of photoreceptor guanylyl cyclase, Mol. Cell. Biochem. 334 (2010) 117–124.
[22] I.V. Peshenko, G.P. Moiseyev, E.V. Olshevskaya, A.M. Dizhoor, Factors that determine Ca^{2+} sensitivity of photoreceptor guanylyl cyclase. Kinetic analysis of the interaction between the Ca^{2+}-bound and the Ca^{2+}-free guanylyl cyclase activating proteins (GCAPs) and recombinant photoreceptor guanylyl cyclase 1 (RetGC-1, Biochemistry 43 (2004) 13796–13804.
[23] T. Senin II, K.E. Fischer, D.V. Komolov, P.P. Zinchenko, K.W. Philippov, Koch, Ca^{2+}-myristoyl switch in the neuronal calcium sensor recoverin requires different functions of Ca^{2+}-binding sites, J. Biol. Chem. 277 (2002) 50365–50372.
[24] K.W. Senin II, M. Koch, P.P. Akhtar, Philippov, Ca^{2+}-dependent control of rhodopsin phosphorylation: recoverin and rhodopsin kinase, Adv. Exp. Med. Biol. 514 (2002) 69–99.
[25] A. Helten, W. Saftel, K.W. Koch, Expression level and activity profile of membrane bound guanylate cyclase type 2 in rod outer segments, J. Neurochem. 103 (2007) 1439–1446.
[26] A. Helten, K.W. Koch, Calcium-dependent conformational changes in guanylate cyclase-activating protein 2 monitored by cysteine accessibility, Biochem. Biophys. Res. Commun. 356 (2007) 687–692.
[27] D. Dell'Orco, S. Sulmann, P. Zägel, V. Marino, K.-W. Koch, Impact of cone dystrophy-related mutations in GCAP1 on a kinetic model of phototransduction, Cell. Mol. Life Sci. 71 (19) (2014) 3829–3840.
[28] R. Stephen, G. Bereta, M. Golczak, K. Palczewski, M.C. Sousa, Stabilizing function for myristoyl group revealed by the crystal structure of a neuronal calcium sensor, guanylate cyclase-activating protein 1, Structure 15 (2007) 1392–1402.
[29] D. Dell'Orco, P. Behnen, S. Linse, K.W. Koch, Calcium binding, structural stability and guanylate cyclase activation in GCAP1 variants associated with human cone dystrophy, Cell. Mol. Life Sci. 67 (2010) 973–984.
[30] B. Hess, C. Kutzner, D. Van Der Spoel, E. Lindahl, GROMACS 4: algorithms for highly efficient, load-balanced, and scalable molecular simulation, J. Chem. Theory Comput. 4 (2008) 435–447.
[31] P. Bjelkmar, P. Larsson, M.A. Cuendet, B. Bess, E. Lindahl, Implementation of the CHARMM force field in GROMACS: analysis of protein stability effects from correction maps, virtual interaction sites, and water models, J. Chem. Theory Comput. 6 (2010) 459–466.
[32] A.D. Mackerell Jr., M. Feig, C.L. Brooks III, Extending the treatment of backbone energetics in protein force fields: limitations of gas-phase quantum mechanics in reproducing protein conformational distributions in molecular dynamics simulations, J. Comput. Chem. 25 (2004) 1400–1415.
[33] G. Bussi, D. Donadio, M. Parrinello, Canonical sampling through velocity rescaling, J. Chem. Phys. 126 (2007) 014101.
[34] U. Essmann, L. Perera, M.L. Berkowitz, T. Darden, H. Lee, L.G. Pedersen, A smooth particle mesh Ewald method, J. Chem. Phys. 103 (1995) 8577.
[35] B. Hess, H. Bekker, H.J.C. Berendsen, J.G.E.M. Fraaije, LINCS: a linear constraint solver for molecular simulations, J. Comput. Chem. 18 (1997) 1463–1472.
[36] H.J.C. Berendsen, J.P.M. Postma, W.F. Vangunsteren, A. Dinola, J.R. Haak, Molecular-dynamics with coupling to an external bath, J. Chem. Phys. 81 (1984) 3684–3690.
[37] M. Seeber, A. Felline, F. Raimondi, S. Muff, R. Friedman, F. Rao, A. Caflisch, F. Fanelli, Wordom: a user-friendly program for the analysis of molecular structures, trajectories, and free energy surfaces, J. Comput. Chem. 32 (2011) 1183–1194.
[38] M. Seeber, M. Cecchini, F. Rao, G. Settanni, A. Caflisch, Wordom: a program for efficient analysis of molecular dynamics simulations, Bioinformatics 23 (2007) 2625–2627.
[39] V. Marino, A. Astegno, M. Pedroni, F. Piccinelli, D. Dell'Orco, Nanodevice-induced conformational and functional changes in a prototypical calcium sensor protein, Nanoscale 6 (2014) 412–423.
[40] J. Pettelkau, I. Thondorf, S. Theisgen, H. Lilie, T. Schroder, C. Arlt, C.H. Ihling, A. Sinz, Structural analysis of guanylyl cyclase-activating protein-2 (GCAP-2) homodimer by stable isotope-labeling, chemical cross-linking, and mass spectrometry, J. Am. Soc. Mass Spectrom. 24 (2013) 1969–1979.
[41] J.Y. Hwang, K.W. Koch, The myristoylation of the neuronal Ca^{2+}-sensors guanylate cyclase-activating protein 1 and 2, Biochim. Biophys. Acta 1600 (2002) 111–117.
[42] R.E. Hughes, P.S. Brzovic, A.M. Dizhoor, R.E. Klevit, J.B. Hurley, Ca^{2+}-dependent conformational changes in bovine GCAP-2, Protein Sci. 7 (1998) 2675–2680.
[43] S. Theisgen, L. Thomas, T. Schroder, C. Lange, M. Kovermann, J. Balbach, D. Huster, The presence of membranes or micelles induces structural changes of the myristoylated guanylate-cyclase activating protein-2, Eur. Biophys. J. 40 (2011) 565–576.
[44] I.V. Peshenko, E.V. Olshevskaya, S. Lim, J.B. Ames, A.M. Dizhoor, Calcium-myristoyl Tug is a new mechanism for intramolecular tuning of calcium sensitivity and target enzyme interaction for guanylyl cyclase-activating protein 1: dynamic connection between N-fatty acyl group and EF-hand controls calcium sensitivity, J. Biol. Chem. 287 (2012) 13972–13984.
[45] I.V. Peshenko, A.M. Dizhoor, Activation and inhibition of photoreceptor guanylyl cyclase by guanylyl cyclase activating protein 1 (GCAP-1): the functional role of Mg^{2+}/Ca^{2+} exchange in EF-hand domains, J. Biol. Chem. 282 (2007) 21645–21652.
[46] I.V. Peshenko, A.M. Dizhoor, Ca^{2+} and Mg^{2+} binding properties of GCAP-1. Evidence that Mg^{2+}-bound form is the physiological activator of photoreceptor guanylyl cyclase, J. Biol. Chem. 281 (2006) 23830–23841.
[47] P. Behnen, D. Dell'Orco, K.W. Koch, Involvement of the calcium sensor GCAP1 in hereditary cone dystrophies, Biol. Chem. 391 (2010) 631–637.
[48] K. Kamenarova, M. Corton, B. Garcia-Sandoval, P. Fernandez-San Jose, V. Panchev, A. Avila-Fernandez, M.I. Lopez-Molina, C. Chakarova, C. Ayuso, S.S. Bhattacharya, Novel GUCA1A mutations suggesting possible mechanisms of pathogenesis in cone, cone-rod, and macular dystrophy patients, Biomed. Res. Int. 2013 (2013) 517570.
[49] S. Lim, I.V. Peshenko, A.M. Dizhoor, J.B. Ames, Structural insights for activation of retinal guanylate cyclase by GCAP1, PLoS One 8 (2013) e81822.

ACS chemical biology

Articles

pubs.acs.org/acschemicalbiology

Differential Nanosecond Protein Dynamics in Homologous Calcium Sensors

Jörg Robin,[†,‡] Jens Brauer,[†,‡] Stefan Sulmann,[§] Valerio Marino,[∥] Daniele Dell'Orco,[∥,⊥] Christoph Lienau,[†,‡] and Karl-Wilhelm Koch*[,‡,§]

[†]Ultrafast Nano-Optics, Institute of Physics, Faculty V, University of Oldenburg, D-26111 Oldenburg, Germany

[‡]Center of Interface Science, University of Oldenburg, D-26111 Oldenburg, Germany

[§]Biochemistry, Department of Neurosciences, Faculty VI, University of Oldenburg, D-26111 Oldenburg, Germany

[∥]Department of Life Sciences and Reproduction, Section of Biological Chemistry, University of Verona, Verona, Italy

[⊥]Center for BioMedical Computing (CBMC), University of Verona, Verona, Italy

Supporting Information

ABSTRACT: Shaping the temporal response of photoreceptors is facilitated by a well-balanced second messenger cascade, in which two neuronal Ca^{2+}-sensor proteins operate in a sequential relay mechanism. Although they share structurally similar sensing units, they differentially activate the same target protein. Here, as a prototypical case in Ca^{2+}-mediated signal processing, we investigate differential cellular responsiveness in protein conformational dynamics on a nanosecond time scale. For this, we have site-specifically labeled cysteine residues in guanylate cyclase-activating protein GCAP1 by the fluorescent dye Alexa647 and probed its local environment via time-resolved fluorescence spectroscopy. Fluorescence lifetime and rotational anisotropy measurements reveal a distinct structural movement of the polypeptide chain around position 106 upon release of Ca^{2+}. This is supported by analyzing the diffusional dye motion in a wobbling-in-a-cone model and by molecular dynamics simulations. We conclude that GCAP1 and its cellular cognate GCAP2 operate by distinctly different switching mechanisms despite their high structural homology.

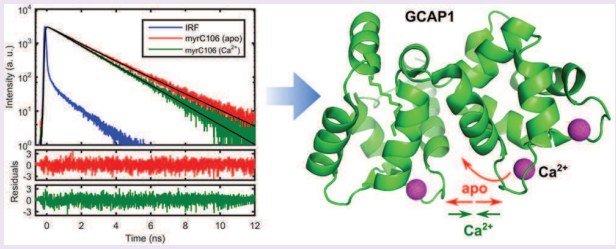

Spatial and temporal variations in intracellular Ca^{2+} signals are key phenomena in physiological processes like, for example, fertilization, apoptosis, muscle contraction, and sensory perception.[1−3] A general open question in Ca^{2+}-mediated signal processing is how physiological specificity is achieved by unique forms of target interaction and activation. For example, the ubiquitous Ca^{2+} sensor calmodulin can adopt different three-dimensional structures depending on target binding,[2] whereas members of the neuronal Ca^{2+} sensor (NCS) protein family share common structural features like EF-hand Ca^{2+}-binding sites but are more specific in target regulation.[3] However, all these signaling pathways have in common that a Ca^{2+}-induced conformational change in the specific Ca^{2+} sensor triggers subsequent protein−protein interaction modes and different target regulatory features.

Photoreceptor cells are remarkable single photon detectors, in which Ca^{2+} transport and Ca^{2+}-sensor systems fulfill key functions for temporally precise responses. Utilizing the second messengers cGMP and Ca^{2+}, these cells respond to changing light conditions on a millisecond time scale.[4] Negative feedback loops further control and shape photoreceptor responses, thereby involving NCS proteins like guanylate cyclase-activating proteins (GCAP) that target membrane guanylate cyclases.[5−7] GCAPs harbor three functional EF-hands and operate in a Ca^{2+}-relay mode fashion in photoreceptor cells,[8−10] which is evident by differences in Ca^{2+}-sensing and catalytic efficiency of target regulation,[8−16] electrophysiological recordings,[9,17] and computational modeling.[18]

The response to fluctuating Ca^{2+}-concentrations by GCAPs is assumed to be mediated by conformational changes.[11−16] For GCAP2, this conformational change was found, in an earlier time-resolved fluorescence study, to reflect a piston-like movement[19] of the α-helix situated between positions C111 and C131. This raises the interesting question of whether the structurally related GCAP1 protein undergoes a similar or even identical conformational transition, even though it differs significantly in its Ca^{2+}-signaling properties. Specifically, one may ask whether these functional differences are already manifesting in early stages of Ca^{2+}-controlled protein dynamics. Previous studies of GCAP1 did not yet conclusively address those questions. Static studies of tryptophan fluorescence quantum yield and Ca^{2+}-induced modifications of cysteines showed conformational transitions without, however, providing insight into structural dynamics.[14,23,24] An amide hydrogen−

Received: April 17, 2015
Accepted: July 23, 2015
Published: July 23, 2015

DOI: 10.1021/acschembio.5b00278
ACS Chem. Biol. 2015, 10, 2344−2352

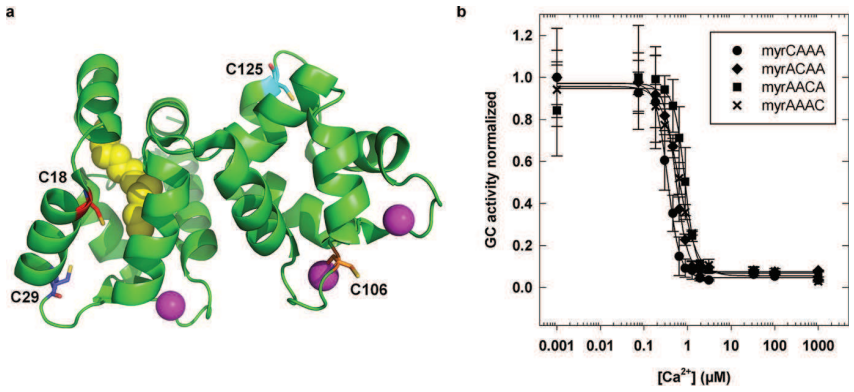

Figure 1. (a) Three-dimensional structural model of GCAP1. The position of each cysteine is highlighted. The myristoyl group (yellow) is layered in a hydrophobic crevice, and the three functional EF-hand motifs have each a bound Ca^{2+} (magenta). (b) Ca^{2+}-sensitive activation of ROS-GC1 by myristoylated GCAP1 mutants as indicated. The IC_{50} values are the following (three to four data sets): 336 nM (Alexa647-labeled CAAA), 529 nM (Alexa647-labeled ACAA), 832 nM (Alexa647-labeled AACA), and 659 nM (Alexa647-labeled AAAC).

deuterium exchange study indicated movements of the *N*-terminal and *C*-terminal fragment upon Ca^{2+}-dissociation.[25] Employing a GCAP1 mutant with an inactive EF-hand 4 in an NMR spectroscopy approach suggested a remote control mechanism, in which EF-hand 4 influences EF-hand 1 for switching the protein form the activator to the inhibitor state.[26,27]

Here, we study the conformational dynamics of GCAP1 by time-resolved fluorescence spectroscopy. Mutants of GCAP1 were expressed with all but one of its four cysteine residues replaced, checked for functionality, and then site-specifically labeled with the fluorescent dye Alexa647. The local environment of the dye was probed by time-resolved fluorescence spectroscopy in the apo-state and with either Ca^{2+} or Mg^{2+} bound to the protein. A major conformation rearrangement of the polypeptide chain around amino acid position 106 is revealed upon release of Ca^{2+}. These results are supported by a wobbling-in-a-cone model analysis and by molecular dynamics simulations, which overall suggest distinctly different switching mechanisms for GCAP1 and GCAP2 upon Ca^{2+} release.

RESULTS AND DISCUSSION

Biochemical Properties of Labeled GCAP1 Mutants. Native GCAP1 contains four cysteine residues at positions C18, C29, C125, and C106 (Figure 1a). In previous work we constructed and thoroughly analyzed the biochemical properties of isolated cysteine mutants of nonmyristoylated (nmyr) GCAP1 revealing that all mutants are functional.[22] In the present work, nmyr and myristoylated (myr) mutants with one C left were expressed in *E. coli*, purified, and biochemically analyzed. The remaining cysteine in mutants annotated CAAA (C18), ACAA (C29), AACA (C106), and AAAC (C125) allowed site-specific labeling with the fluorescent dye Alexa647 (see Table 1). Degree of myristoylation was high for all mutants as routinely observed for wildtype GCAP1 (88 to 95%). Labeling with Alexa647 was also successful for all mutants yielding (84 to 95%), except for nmyrC125 and myrC125, where 78% and 63% were obtained, respectively. Attachment of Alexa647 did not impair the Ca^{2+}-sensitive activating properties of GCAP1, since all labeled GCAP1 forms activated native rod outer segment guanylate cyclase 1 (ROS-GC1) with similar IC_{50} values, i.e. defining the free Ca^{2+} concentration of half-maximum guanylate cyclase activation (Figure 1b). In addition, we labeled nmyrGCAP1 variants and determined their Ca^{2+}-sensitive activation profiles. All curves were similar but shifted to slightly higher free Ca^{2+}-concentrations (Supporting Information Figure S1). This difference between the myristoylated and nonmyristoylated form is a characteristic feature of wildtype GCAP1[7,27] and demonstrates that mutants labeled with Alexa647 undergo the critical Ca^{2+}-dependent conformational changes in a nearly identical manner as the nonlabeled wildtype protein and, therefore, are well suited for subsequent fluorescence studies.

Table 1. Labelling of Myristoylated and Non-myristoylated GCAP Mutants with Alexa647-C2-maleimide[a]

	myr GCAP		nonmyr GCAP
	degree of myristoylation (%)	degree of labeling (%)	degree of labeling (%)
CAAA	91.4	90.2	84.5
ACAA	91.0	88.5	89.8
AACA	87.8	95.2	94.9
AAAC	95.1	78.5	63.5

[a]The degree of myistoylation for the D6S mutants was determined by rp-HPLC.

Fluorescence Lifetime. For each mutant, the fluorescence lifetime was measured for the Ca^{2+}-bound, the Mg^{2+}-bound, a mixed Ca^{2+}/Mg^{2+} bound, and the apo-state of the protein. A representative fluorescence decay curve is displayed in Figure 2a showing fluorescence decay of myrC106 in the presence of Ca^{2+} (green curve) or EGTA (red curve) and the instrument response function (blue curve). A biexponential fit results in equally distributed residuals, indicating a good agreement with the experimental data.

Such an acceptable biexponential modeling was observed for all mutants when assuming a fast component ranging from 0.6 to 1.2 ns and a slow component ranging from 1.3 to 2.0 ns. Typically, the amplitude of the slow component exceeded that of the fast component by a factor of 3. Therefore, a summary of deduced lifetimes for the dominating slow component τ_1 is given in Figure 2b, exhibiting similar features for both myristoylated and nonmyristoylated mutants. Specifically, fluorescence lifetimes differed significantly among cysteine positions. The longest fluorescent lifetimes were observed for the dye at positions C18 and C29 located in the interior of the protein. In contrast, the fluorescence lifetime was shortest for

DOI: 10.1021/acschembio.5b00278
ACS Chem. Biol. 2015, 10, 2344−2352

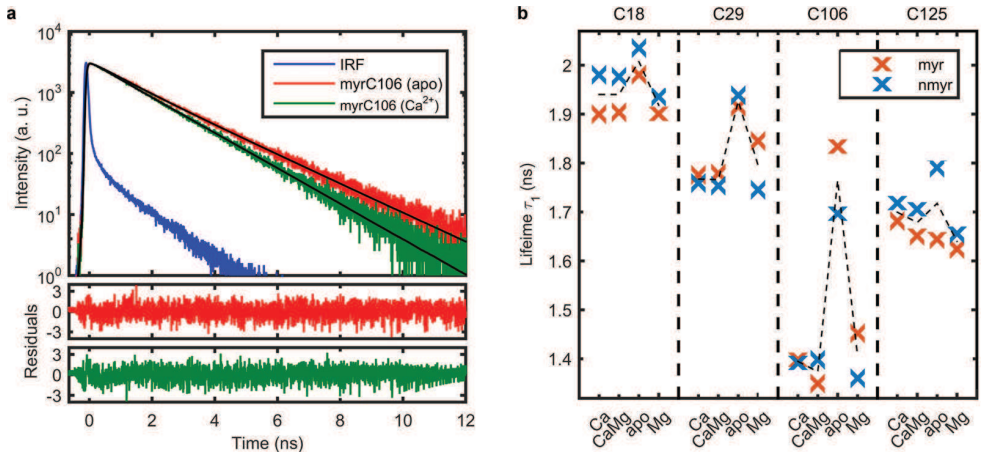

Figure 2. (a) Representative fluorescence decay curves of the mutant myrC106 in the apo (red) and Ca^{2+} bound (green) state and corresponding residuals for biexponentially fitted curves (black). The instrument response function (IRF) is shown in blue. (b) Summary of the high amplitude lifetime component for all mutants. Each section corresponds to one mutant, either myristoylated (red) or nonmyristoylated (blue), in all cation configurations. Each data point corresponds to the weighted average of 10 measurements with a weighted fitting error <5 ps. Error bars are smaller than the data point symbols.

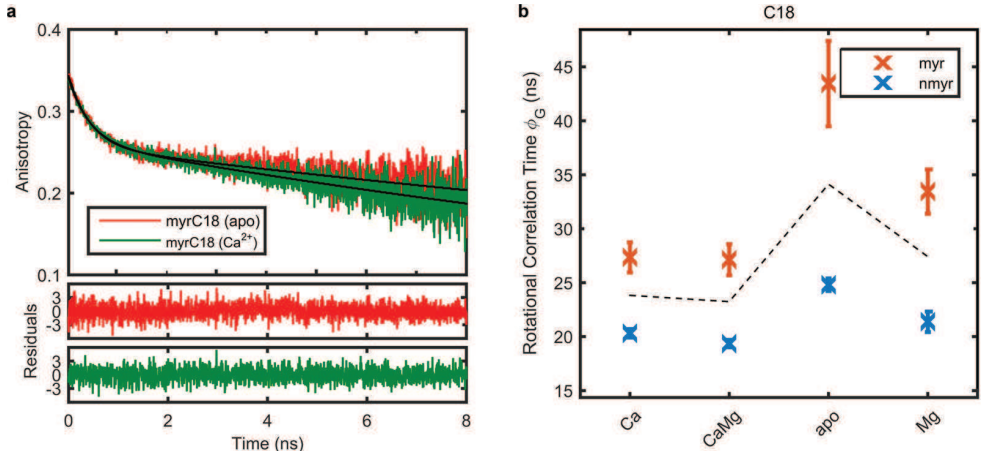

Figure 3. (a) Representative anisotropy decay curves of mutant myrC18 in the apo (red) and Ca^{2+} bound (green) state and corresponding residuals for biexponentially fitted curves (black). (b) Summary of the slow rotational correlation time component for the mutant C18, either myristoylated (red) or nonmyristoylated (blue), in all cation configurations. Each data point corresponds to the weighted average of 10 measurements with weighted fitting errors ranging from 0.33 to 4.0 ns, depending on excess of rotational correlation time over fluorescence lifetime.

the positions C106 and C125 corresponding to regions exposed to the solvent.

Most prominently, binding of either Ca^{2+}, Mg^{2+}, or a mixture thereof did hardly affect the fluorescence lifetimes. In stark contrast, in the apo-state, i.e. in the presence of the chelating agent EGTA, the fluorescence lifetime of the dye increased significantly at each of the dye positions. This increase in fluorescence lifetime is most pronounced for dye labeling at C106. Here, lifetime increases by more than 30% from 1.4 ns with either Ca^{2+} or Mg^{2+} bound to 1.8 ns in the apo-state of the myristoylated protein.

Fluorescence Anisotropy. Similarly, the fluorescence anisotropy was measured for each of the eight mutants in each of the four cation configurations. A representative anisotropy decay curve is shown in Figure 3a for myrC18 in the presence of Ca^{2+} (green curve) or for the apo-state (red curve). Again, a biexponential model gives a statistical distribution of residuals indicating a good agreement with the experimental data for the fluorescence anisotropy of the protein−dye complex. Therefore, we can identify two distinct two rotational correlation times, which can be distinguished into a fast component ranging from 0.43 to 0.82 ns for all mutants and a slow component ranging from 19 to 43 ns for the mutants C18 and C29 with the dye located in the interior of the protein−dye complex. For the mutants C106 and C125 with the dye facing the exterior of the protein, the rotational correlation times of the protein−dye complex greatly exceeded the fluorescence lifetime and only lower limits of several hundreds of nanoseconds could be estimated (results not shown).

For the mutant C18, the slow component is shown in Figure 3b for all cation configurations. In the myristoylated protein, we find similar rotational correlation times from 27 to 33 ns in the case of Ca^{2+} or Mg^{2+} binding and a slight increase to 43 ns in the apo-state. Under all conditions, the rotational correlation time of the nonmyristoylated protein is significantly faster than in the myristoylated case, and again the correlation time in the

DOI: 10.1021/acschembio.5b00278
ACS Chem. Biol. 2015, 10, 2344−2352

apo-state is slightly longer than in the case of Ca^{2+} or Mg^{2+} binding.

Change in Local Environment of the Dye. The fluorescence lifetime τ of a dye is related to the local viscosity η of its environment via $\tau \propto \eta^{\beta}$, where β is a positive number.[28] In the interior of the protein, the diffusive rotational motion of the dye is constrained, and the local viscosity of the environment therefore is large. This gives rise to a comparatively long fluorescence lifetime. In contrast, an exposure of the dye to the solvent buffer will reduce the local viscosity and hence fluorescence lifetime. The observed pronounced increase in fluorescence lifetime of the dye in the apo-state therefore necessarily reflects a tighter confinement of the dye in the interior of the protein than in the Ca^{2+}- or Mg^{2+}-bound state and thus indicates that the loop region around position C106 moves toward the interior of the protein, when GCAP1 releases its Ca^{2+}.

Motional Restriction by Wobbling-in-a-Cone. This local movement at position C106 is further supported by analyzing the diffusional dye motion in a phenomenological wobbling-in-a-cone model (see Figure 4).[19,29−31] This model

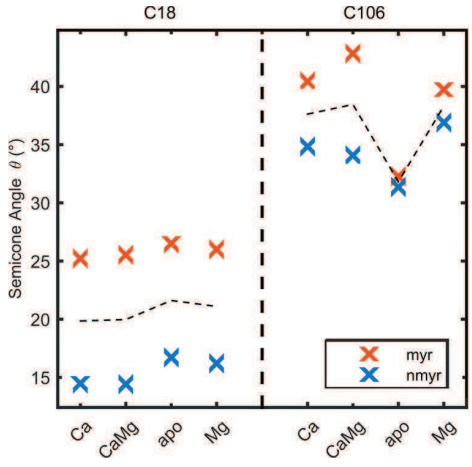

Figure 4. Semicone angle obtained from a wobbling-in-a-cone model for mutants C18 and C106, either myristoylated (red) or non-myristoylated (blue), in all cation configurations. Each data point corresponds to the weighted average of 10 evaluations with weighted errors ranging from 0.15° to 0.57°. Error bars are smaller than the data point symbols.

separates a rapid diffusive rotational motion of the dye within its local environment from the much slower global rotational motion of the protein−dye complex and hence naturally accounts for the two distinct decay times in the experimentally measured anisotropy curves. The geometric constraint of the dye motion due to the surface of the protein is taken into account by restricting the dye rotation to the interior of a cone with semicone angle

$$\theta = \cos^{-1}\left(\sqrt{2\left(\frac{r_D}{r_G}+1\right)^{-1/2}+\frac{1}{4}}-\frac{1}{2}\right)$$

Here, the amplitudes of the fast and slow components, r_D and r_G, are the amplitudes of the fast and slow components of the anisotropy decay.

An analysis of our experimental data within the framework of this model suggests that at dye position C106 this semicone angle decreases markedly from 41° in the Ca^{2+}-bound state to 32° in the apo-state of the myristoylated protein. Clearly, a dye closer to the interior of the protein should be more restricted in its motion than a dye more exposed to the solvent. Therefore, the analysis of both our fluorescence and anisotropy measurements strongly indicates a movement of the loop region around position C106 toward the interior of the protein, when GCAP1 releases its Ca^{2+}. Rebinding of Ca^{2+} or Mg^{2+} reverses this movement. This is consistent with the notion that the binding of cations to an EF hand loop, where C106 is located, results in a structural transition from an open conformation in the apo-state to a more closed conformation in the case of cation binding. When switching from open to closed conformation, a covalently bound dye molecule would therefore necessarily move outward with respect to the protein interior.

In contrast, the diffusional dye motion is similar in all cation configurations of the mutant C18 but differs strongly between the myristoylated and nonmyristoylated form. The distance between the cysteine sulfur in C18 and the end-standing carbon of the myristoyl group is ∼1.03 nm and is located at the end of the hydrophobic crevice harboring the fatty acyl chain. One would expect a larger semicone angle due to larger spatial freedom, if the myristoyl group is missing. However, we deduce a reduction in the semicone angle from 26° in the myristoylated protein to 15° in the nonmyristoylated protein, which is accompanied by an increase in lifetime by ∼0.1 ns (Figure 2b). This indicates a movement of the region around C18 into the hydrophobic pocket, thereby constraining its circular movement.

Global Rotation of the Protein−Dye Complex. Our anisotropy measurements further indicate that the local conformational change upon release of Ca^{2+} or Mg^{2+} at position C106 results in an increase in the slow, global rotational correlation time ϕ_G, which is directly related to the hydrodynamic radius r_{st} of the protein by the Stokes−Einstein−Debye equation

$$\phi_G = \frac{4\pi\eta r_{st}^3}{3k_BT}$$

Here, k_BT is the Boltzmann factor and η = 1 mNs/m^2 is the viscosity of water at a temperature T = 293.15 K. In our measurements, we necessarily probe the rotational motion of the protein−dye complex. To extract information on the rotational correlation time of the unlabeled protein, the presence of the dye molecule must not enlarge the hydrodynamics radius of the protein. This requirement is met for a dye located in the interior of the protein, i.e. for a motionally restricted dye showing the longest fluorescence lifetimes. From our fluorescence lifetime measurements, the most suitable mutant to probe the rotational correlation time of GCAP1 is C18. The increase in rotational correlation time from 27 ns (Ca^{2+}-bound) to 43 ns (apo) therefore corresponds to an increase in hydrodynamic radius from r_{st} = 2.98 ± 0.05 nm (Ca^{2+}-bound) to r_{st} = 3.48 ± 0.10 nm (apo). This global enlargement of the mutated protein upon release of Ca^{2+} agrees with dynamic light scattering measurements on myristoylated, wild type GCAP1,[32] in which the hydrodynamic radius was determined as r_{st} = 3.35 ± 0.02 nm for the Ca^{2+}-bound state and r_{st} = 3.75 ± 0.10 nm for the apo-state.

Molecular Dynamics Simulations. To gain further structural insights into the local movement at position C106, as compared to the global enlargement of the protein observed

DOI: 10.1021/acschembio.5b00278
ACS Chem. Biol. 2015, 10, 2344−2352

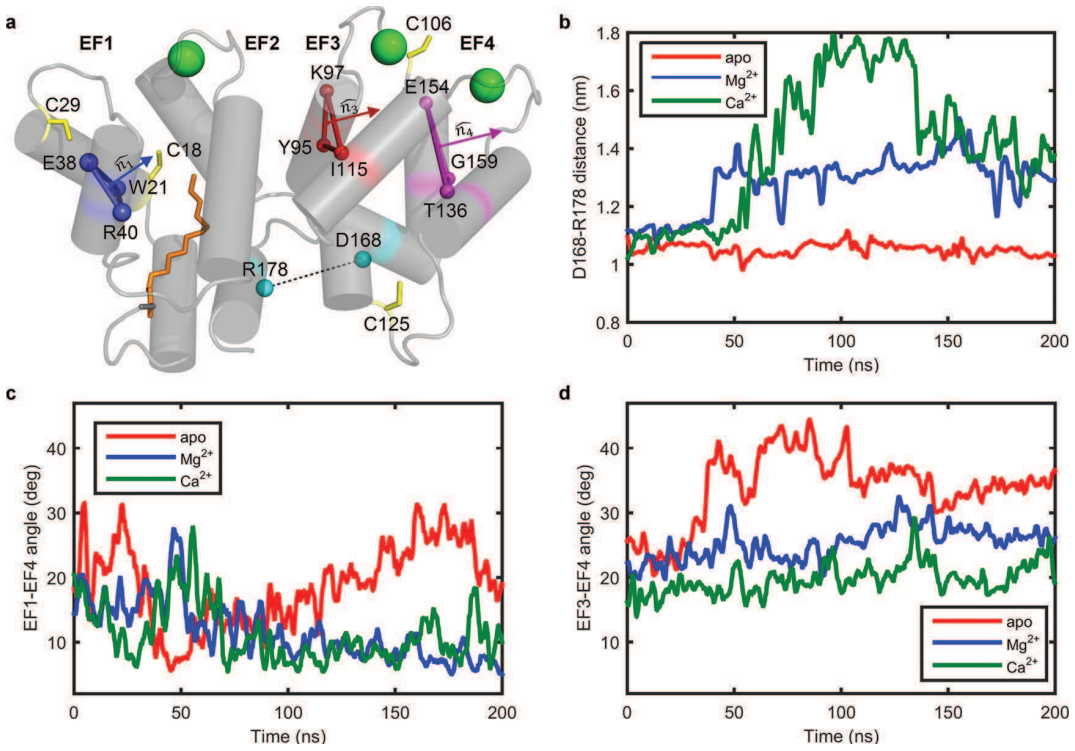

Figure 5. Structural descriptors of myrGCAP1 dynamical features calculated on the trajectories obtained by carrying out 200 ns all-atom molecular dynamics simulations. (a) Cartoon structural model of myrGCAP1 in the Ca^{2+}-bound form with the myristoyl moiety (orange), cysteine side chains (yellow), Ca^{2+} ions (green), as well as C_α atoms of key residues belonging to EF1 (blue), EF3 (red), EF4 (purple), and defining the distance between the *N*- and *C*-terminal domains (cyan). (b) Evolution of the distance between C_α of D168 and R178: apo (red), Mg^{2+}-EF2 (blue), Ca^{2+}-loaded (green). (c) Evolution of the angle between EF1 and EF4: apo (red), Mg^{2+}-EF2 (blue), Ca^{2+}-loaded (green). (d) Evolution of the angle between EF3 and EF4: apo (red), Mg^{2+}-EF2 (blue), Ca^{2+}-loaded (green).

upon Ca^{2+} and/or Mg^{2+} release, we analyzed the results from a previous 200 ns molecular dynamics (MD) study[33] of myristoylated GCAP1 in the light of the time-resolved fluorescence measurements presented here (Figure 5). Although the dye was not explicitly included in MD simulations, the biochemical assays performed in this study (Figure 1b) suggest that the dye exerts only minimal perturbations to the GCAP1 structure/function.

The analysis of MD trajectories focused on selected regions representative for those structural elements, in which the dye was experimentally bound as a probe for the structural dynamics. At the same time, it allowed us to assess global dynamical properties of the GCAP1 tertiary structure, which is characterized by two lobes, each consisting of two EF-hand regions (EF1−EF2 and EF3−EF4).[20]

The distance between these lobes is well represented by the distance between the Cα atoms of D168 and R178, which are both located in the *C*-terminal region, but in the two different lobes. As D168 and R178 form a salt bridge, this distance remains nearly constant at 1.03 ± 0.02 nm in the apo-state (Figure 5b) but is dynamically disturbed upon Ca^{2+} (~32% salt bridge presence) or Mg^{2+} binding (~72% salt bridge presence) increasing the distance to 1.38 ± 0.07 nm and 1.31 ± 0.04 nm, respectively. In consequence, formation of the salt bridge in the apo-state enables the protein to open up near the Ca^{2+}-binding sites, which should be accompanied by an increased separation between the EF-hands.

To elucidate this feature the EF-hand motifs are conveniently represented by planes, which stand at an angle with respect to each other. For example, EF1 and EF4 are nearly parallel in the Ca^{2+} and Mg^{2+} bound state (6.8 ± 0.9°) but are significantly tilted (19.5 ± 1.8°) against each other in the apo-state. Similarly, the angle between EF3 and EF4 increases from 23.3 ± 1.7° in the Ca^{2+} bound state to 34.8 ± 0.8° in the apo-state (Figure 5c,d).

Therefore, molecular dynamics simulations point to two main reorganizing movements in the GCAP1 structure during the transition from the cation-bound to the apo-state: decreasing the distance between the two lobes by forming a salt bridge and a concomitant slight but significant expulsion of the EF4 region with respect to other regions (EF1 and EF3). These parallel movements lead to a slight increase in the radius of gyration of the protein in the apo-state (1.711 ± 0.009 nm) as compared to the Ca^{2+}-bound state (1.68 ± 0.01 nm) and to an overall more important increase in the hydrodynamic volume of GCAP1, which is in agreement with previous theoretical[33] and experimental[32] observations. Additionally, the increased angles between the EF-hand motifs upon release of Ca^{2+} open a cavity for the loop region around position C106 to move toward the interior of GCAP1. Pictorially, this dynamic process can be illustrated as a "twisted accordion"-like movement.

The large-scale motions described above are in fact in line with principal component analysis (PCA) performed on the whole 200 ns MD trajectory. Analysis of the first two principal components (PCs) describing the large-scale movements indeed shows that, in the apo-state, EF1, EF2, EF3, and *C*- and *N*-termini move in a concerted fashion along the direction

DOI: 10.1021/acschembio.5b00278
ACS Chem. Biol. 2015, 10, 2344−2352

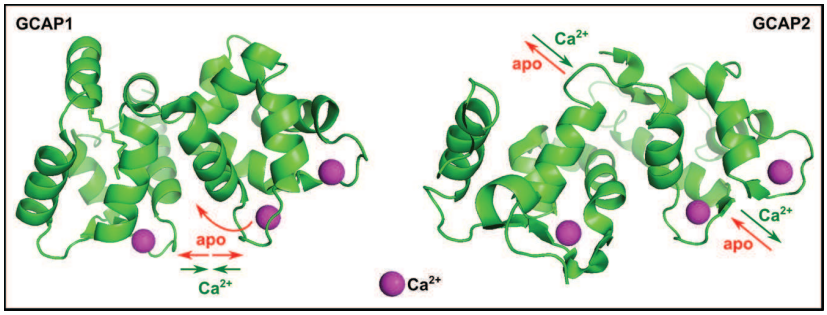

Figure 6. Comparison of the three-dimensional structures of GCAP1 and GCAP2 showing distinctly different switching mechanisms upon Ca^{2+} release. Structural model of GCAP2 is based on the NMR structure (PDB ID: 1JBA).[21]

of the first PC (Supporting Information Figure S2). Projection of the concerted trajectories over the second PC of the apo-state suggests that the loop connecting EF1 and EF2 as well as the highly flexible 121−133 region and the loops of EF-hands 2, 3, and 4 are collectively moving along the same direction, orthogonal to that defined by the first PC, which is substantially in line with the "twisted accordion" model described above. On the other hand, the first two PCs describing large scale motions of the Ca^{2+}-bound state of GCAP1 show a concerted motion of the *C*- and *N*-termini and of the highly flexible 121−133 loop, while the movement along the longitudinal axis of the "accordion" is much less pronounced.

Summary and Conclusions. In conclusion, our model of a twisted accordion-like movement for GCAP1 upon a changing Ca^{2+} concentration distinctly contrasts the piston-like movement deduced from a previous time-resolved fluorescence study on its structurally similar cognate GCAP2 (see Figure 6 for a comparison).[18] Recently, another pair of related NCS proteins, NCS-1 and calneuron-1, was found to differentially modulate by selective Ca^{2+} sensing a signaling pathway involving the heterodimeric adenosine/dopamine receptor.[34] Thus, our results constitute an example of a more general concept beyond retina specific Ca^{2+} sensors. Previously, the variability of target recognition and regulation by NCS proteins despite their structural similarities has been related in the past to differences in the number and location of Ca^{2+}-binding sites, in surface charge distribution, and in Ca^{2+}-sensitive dimerization.[2,8−11,32,35] Here, we present a new concept, in which differential cellular responsiveness mediated by two structurally similar proteins is directly mirrored by a difference in protein conformational dynamics, which tunes their physiological specificity.

METHODS

Cloning of GCAP1 Cysteine Mutants. The cloning of the single cysteine mutants of bovine GCAP1, in which three cysteine residues are replaced by alanine, namely C18AAA, AC29AA, AAC106A, and AAAC125, was described in detail before.[22] To facilitate myristoylation of GCAP1 variants at the *N*-terminus, an additional point mutation at position 6 (D6S) is necessary for creating a consensus sequence for the yeast *N*-myristoyltransferase (NMT). It was shown earlier that this point mutation has virtually no effect on the biochemical and biophysical properties of wildtype GCAP1.[36] Accordingly, we prepared the D6S mutants employing the following primers 5′-AAACAT-ATGGGGAACATTATGTCCGGTAAGTCG-3′ and 3′-TTTGAA-TTCTCAGCCGTCGGCCTCCGC-5′ and used the respective cysteine mutant as a template. The amplified PCR product was cut with *NdeI* and *NheI* and ligated in an analogous treated template clone. All sequences were verified by DNA sequencing (LGC Genomics).

Expression and Purification of GCAP1, Wild-Type, and Cysteine Mutants. GCAP1 mutants were overexpressed in BL21 *E. coli* cells as described before.[8,15,22] In order to myristoylate GCAP1, mutants cells were cotransformed with the plasmid pBB131 containing a gene for the yeast (*S. cerevisiae*) NMT. After cell lysis, the myristoylated and nonmyristoylated GCAP1 mutants were isolated from the insoluble fraction.[8,15,22] Briefly, the insoluble material was homogenized in 6 M guanidinium hydrochloride and afterward dialyzed against Tris-buffer (20 mM Tris-HCl, 150 mM NaCl, 1 mM DTT pH 7.5). Prior to chromatographic steps, the volume of the protein solution was reduced by ammonium sulfate precipitation. Subsequently, the protein was resolved and applied onto a size exclusion column (Superdex 75, GE Healthcare) equilibrated in Tris-buffer. Fractions containing the respective GCAP form were further purified with an anion exchange column (HiLoad 26/10 Q Sepharose; GE Healthcare) equilibrated in Tris-buffer with 2 mM EGTA. Chromatography was performed with a gradient of 200−550 mM NaCl in 40 mL.

The purity of the obtained GCAP forms was verified by sodium dodecyl-sulfate polyacrylamide gel electrophoresis. The myristoylation degree of the D6S mutants was determined by a reversed phase HPLC on a silica based C-18 column (Luna 5 μm C18, Phenomenex).[37]

Labeling with the Fluorescent Dye Alexa647 and Validation of Protein Function. GCAP1 mutants with one reactive cysteine were labeled with the fluorescent dye Alexa647-C2-maleimide (Life Technologies) using the following protocol: the respective lyophilized GCAP1 form was dissolved in 10 mM Hepes-KOH pH 7.0 to a final concentration of 30 μM. The Alexa647 dye was added in 5-fold molar excess in a final volume of 0.5 mL. The reaction mixture was incubated for 1−3 h in a light-protected vial at room temperature, before the reaction was terminated by adding 2 mM DTT.

Removal of the excessive dye was done by passing the reaction mixture over a NAP5 column (GE Healthcare) equilibrated in fluorescence buffer (125 mM NaCl, 25 mM Tris-HCl pH 7.4). If excessive dye was still present, it was removed by dialysis against the same buffer.

For the calculation of the labeling efficiency, the concentration of the bound dye was determined by UV−VIS spectrophotometry at 650 nm (ε = 265 000 M^{-1} cm^{-1}) and the protein concentration by the Coomassie Blue assay.

A critical point for further use of fluorescence labeled mutants was the ability to regulate the target guanylate cyclase ROS-GC1. For this purpose, we isolated membranes from bovine rod outer segments,[7,8] providing us with a native ROS-GC1 source. The cyclase activity was determined as a function of free [Ca^{2+}] exactly as described before.

Fluorescence Lifetime Measurement. Fluorescence lifetime measurements were performed by time-correlated single photon counting (TCSPC). A pulsed diode laser (PicoQuant, LDH 8−1−060 with PDL 800) operating at a repetition rate of 6 MHz provided 50 ps pulses centered at 656 nm and at an average power < 5 μW. Vertically polarized laser pulses were weakly focused into a microcuvette. Emitted fluorescence light was collected and focused by a glass objective (Nikon, NA = 0.7) onto an avalanche photodiode (ID Quantique 100).

DOI: 10.1021/acschembio.5b00278
ACS Chem. Biol. 2015, 10, 2344−2352

To avoid anisotropy effects, all lifetime measurements were performed under magic angle conditions (54.7°). Fluorescence decay curves $I(t)$ were collected with a timing resolution of 4 ps (PicoQuant, PicoHarp 300) and fitted with the software FluoFit (PicoQuant) to an exponential decay model by reconvolution:

$$I(t) = \int_{-\infty}^{t} \mathrm{IRF}(t') \sum_{i=1}^{n} A_i \, e^{-(t-t')/\tau_i} \, dt'$$

Here, A_i denotes the amplitude of the decay component with fluorescence lifetime τ_i.

The instrument response function (IRF) was recorded with excitation light scattered from diluted milk and found to have a full width at half-maximum (fwhm) of about 100 ps.

Our setup yielded a monoexponential decay for free oxazine 1. However, a biexponential decay was observed for free Alexa647, which we attribute to a low but nonzero probability for the dye to take an alternative configuration due to its chemical structure. Reference measurements of free Alexa647 in the presence of Ca^{2+}, Mg^{2+}, or the chelating agent EGTA used for the apo-state measurements yielded no change in fluorescence lifetime.

For each of the four mutants, either myristoylated or non-myristoylated, and in each of the four cation configurations, we carried out 10 measurements and calculated the weighted mean $\bar{x} = (\Sigma w_i x_i)/(\Sigma w_i)$ with $w_i = 1/(\Delta x_i)^2$ and the overall error as $\Delta x = [1/(\Sigma w_i)]^{1/2}$.

Fluorescence Anisotropy Measurement. For fluorescence anisotropy measurements, the intensity of fluorescence emission with a polarization component parallel, $I_{\parallel}(t)$, and perpendicular, $I_{\perp}(t)$, to the vertically polarized excitation light was measured. The fluorescence anisotropy $r(t)$ is then defined as

$$r(t) = \frac{I_{\parallel}(t) - G \cdot I_{\perp}(t)}{I_{\parallel}(t) + 2G \cdot I_{\perp}(t)}$$

Here, an instrument parameter G corrects for biased polarization detection efficiency and was found to be $G = (\int I_{HV}(t)\,dt / \int I_{HH}(t)\,dt) = 0.95$ for our setup.

Anisotropy decay curves were fitted with the software FluoFit (PicoQuant) to an exponential decay model

$$r_{\mathrm{fit}}(t) = r_{\infty} + \sum_{i=1}^{n} r_i \, e^{-t/\phi_i}$$

Here, r_i denotes the amplitude of the decay component with rotational correlation time ϕ_i and r_{∞} is the steady state anisotropy.

Similar to the lifetime measurements, we carried out 10 measurements for both $I_{\parallel}(t)$ and $I_{\perp}(t)$, for all mutants and in all configurations, and calculated the weighted mean accordingly.

Molecular Dynamics Simulations. Molecular dynamics simulations were set up as previously described[33] using as a starting structure the homology model of human mGCAP1 built using Ca^{2+}-bound chicken mGCAP1[20] as a template (PDB ID: 2R2I), according to a procedure previously elucidated.[12] Simulated states were modeled either by removing Ca^{2+} ions from all three EF-hand binding sites (apo) or by removing Ca^{2+} ions from EF3 and EF4 and substitution with a Mg^{2+} ion in EF2 (Mg^{2+}-EF2).

MD simulations were performed using the GROMACS 4.6.3 simulation package,[38] with the CHARMM27 all-atom force field.[39,40] Structures were subjected to energy minimization, 4 ns equilibration, and 200 ns MD production with an integration time step of 2 fs. See ref 33 for details. Values reported for distances and angles are mean values ± standard deviations calculated over the last 10 ns of MD production.

Analysis of MD Trajectories. MD trajectories generated in Marino et al.[33] were subjected to different analyses. The distance between the centers of mass of C_α of D168 (belonging to the EF3–EF4 lobe) and R178 (belonging to the EF1–EF2 lobe) was calculated over the 200 ns MD time frame with the *g_dist* function implemented in the GROMACS simulation package. The angles between the versors orthogonal to the planes cutting EF1 (represented by C_α Ca^{2+}'s of W21, E38 and R40), EF3 (represented by C_α's of Y95, K97 and I115), and EF4 (represented by C_α's of T136, E154 and G159) were calculated over the 200 ns MD time frame with the *g_sgangle* function implemented in the GROMACS simulation package, which is based on the equation $\cos \widehat{EF1EF4} = \hat{n}_1 \cdot \hat{n}_4$ and $\cos \widehat{EF3EF4} = \hat{n}_3 \cdot \hat{n}_4$.

Smoothing of distance and angle data plots was performed with the smoothing function within the SigmaPlot 12 package, by using the running average module with 10 000 intervals averaging 200 points each, corresponding to one-hundredth of the points in the original data set (2 ns frequency).

Principal component analysis was performed using the pca module of the Wordom software[41] by computing progressive comparisons every 10 ns. Radius of gyration measurement calculated on all protein atoms was performed using the rgyr module of the Wordom software.

■ ASSOCIATED CONTENT

Supporting Information

The Supporting Information is available free of charge on the ACS Publications website at DOI: 10.1021/acschembio.5b00278.

Two additional figures are supplied. Figure S1: Ca^{2+}-sensitive activation of ROS-GC1 by nonmyristoylated GCAP1 mutants. Figure S2: Analysis of the first two principal components describing 200 ns all-atom molecular dynamics simulations of apo and Ca^{2+}-bound myristoylated GCAP1 (PDF)

■ AUTHOR INFORMATION

Corresponding Author

*E-mail: karl.w.koch@uni-oldenburg.de.

Author Contributions

J.R., C.L., and K.W.K. developed the concept. J.R., J.B., and S.S. designed experiments. V.M and DDO performed molecular dynamics simulations. J.R., J.B., and S.S. carried out experiments. All authors analyzed data. J.R. and K.W.K. wrote the first draft of the manuscript. All authors corrected and completed the manuscript.

Notes

The authors declare no competing financial interest.

■ ACKNOWLEDGMENTS

This work was supported by a grant from the Deutsche Forschungsgemeinschaft (GRK 1885/1) and by funds from the Italian Ministry for Research and Education via Departmental funds (FUR2013) and via support from CINECA through the Italian Super Computing Resource Allocation project (ISCRA Grant: HP10CB736X to DDO). Part of this work resulted from a Fellowship at the Hanse-Wissenschaftskolleg Delmenhorst (Germany) to DDO.

■ REFERENCES

(1) Berridge, M. J., Lipp, P., and Bootman, M. D. (2000) The versatility and universality of calcium signalling. *Nat. Rev. Mol. Cell Biol. 1*, 11–21.

(2) Ikura, M., and Ames, J. B. (2006) Genetic polymorphism an dprotein conformational plasticity in the calmodulin superfamily: Two ways to promote multifunctionality. *Proc. Natl. Acad. Sci. U. S. A. 103*, 1159–1164.

(3) Burgoyne, R. D., Haynes, L. P. (2014) Sense and specificity in neuronal calcium signalling. *Biochim. Biophys. Acta, Mol. Cell Res.* DOI: 10.1016/j.bbamcr.2014.10.029.

DOI: 10.1021/acschembio.5b00278
ACS Chem. Biol. 2015, 10, 2344–2352

(4) Pugh, E. N., Jr., and Lamb, T. D. (2000) Phototransduction in Vertebrate Rods and Cones: Molecular Mechanisms of Amplification, Recovery and Light Adaptation. *Handb. Biol. Phys. 3*, 183−255.
(5) Palczewski, K., Subbaraya, I., Gorczyca, W. A., Helekar, B. S., Ruiz, C. C., Ohguro, H., Huang, J., Zhao, X., Crabb, J. W., Johnson, R. S., Walsh, K. A., Gray-Keller, M. P., Detwiler, P. B., and Baehr, W. (1994) Molecular cloning and characterization of retinal photoreceptor guanylyl cyclase-activating protein. *Neuron 13*, 395−404.
(6) Dizhoor, A. M., Olshevskaya, E. V., Henzel, W. J., Wong, S. C., Stults, J. I., Ankoudinova, I., and Hurley, J. B. (1995) Cloning,sequencing, and expression of a 24-kDa Ca2+-binding protein activating photoreceptor guanylyl cyclase. *J. Biol. Chem. 270*, 25200−25206.
(7) Bönigk, W., Müller, F., Kellner, R., Koch, K.-W., and Frins, S. (1996) Functional characterization of a guanylyl cyclase-activating protein from vertebrate rods. *J. Biol. Chem. 271*, 8022−8027.
(8) Hwang, J. Y., Lange, C., Helten, A., Höppner-Heitmann, D., Duda, T., Sharma, R. K., and Koch, K.-W. (2003) Regulatory modes of rod outer segment membrane guanylate cyclase differ in catalytic efficiency and Ca^{2+}-sensitivity. *Eur. J. Biochem. 270*, 3814−3821.
(9) Makino, C. L., Wen, X.-H., Olshevskaya, E. V., peshenko, I. V., Savchenko, A. B., and Dizhoor, A. M. (2012) Enzymatic relay mechanism stimulates cyclic GMP synthesis in rod photoresponse: biochemical and physiological study in guanyly cyclase activating protein 1 knockout mice. *PLoS One 7*, e47637.
(10) Koch, K.-W., and Dell'Orco, D. A. (2013) Calcium relay mechanism in vertebrate phototransduction. *ACS Chem. Neurosci. 4*, 909−917.
(11) Lim, S., Peshenko, I., Dizhoor, A., and Ames, J. B. (2009) Effects of Ca^{2+}, Mg^{2+}, and myristoylation on guanylyl cyclase activating protein 1 structure and stability. *Biochemistry 48*, 850−862.
(12) Dell'Orco, D., Behnen, P., Linse, S., and Koch, K.-W. (2010) Calcium binding, structural stability and guanylate cyclase activation in GCAP1 variants associated with human cone dystrophy. *Cell. Mol. Life Sci. 67*, 973−984.
(13) Otto-Bruc, A., Buczylko, J., Surgucheva, I., Subbaraya, I., Rudnicka-Nawrot, M., Crabb, J. W., Arendt, A., Hargrave, P. A., Baehr, W., and Palczewski, K. (1997) Functional reconstitution of photoreceptor guanylate cyclase with native and mutant forms of guanylate cyclase-activating protein 1. *Biochemistry 36*, 4295−4302.
(14) Sokal, I., Li, N., Klug, C. S., Filipek, S., Hubbell, W. L., Baehr, W., and Palczewski, K. (2001) Calcium-sensitive regions of GCAP1 as observed by chemical modifications, fluorescence, and EPR spectroscopies. *J. Biol. Chem. 276*, 43361−43373.
(15) Hwang, J.-Y., Schlesinger, R., and Koch, K.-W. (2004) Irregular dimerization of guanylate cyclase-activating protein 1 mutants causes loss of target activation. *Eur. J. Biochem. 271*, 3785−3793.
(16) Peshenko, I. V., Olshevskaya, E. V., and Dizhoor, A. M. (2008) Binding of guanylyl cyclase activating protein 1 (GCAP1) to retinal guanylyl cyclase (RetGC1). The role of individual EF-hands. *J. Biol. Chem. 283*, 21747−21757.
(17) Makino, C. L., Peshenko, I. V., Wen, X. H., Olshevskaya, E. V., Barrett, R., and Dizhoor, A. M. (2008) A role for GCAP2 in regulating the photoresponse. Guanylyl cyclase activation and rod electrophysiology in GUCA1B knock-out mice. *J. Biol. Chem. 283*, 29135−29143.
(18) Dell'Orco, D., Sulmann, S., Zägel, P., Marino, V., and Koch, K.-W. (2014) Impact of cone dystrophy-related mutations in GCAP1 on a kinetic model of phototransduction. *Cell. Mol. Life Sci. 71*, 3829−3840.
(19) Kollmann, H., Becker, S. F., Shirdel, J., Scholten, A., Ostendorp, A., Lienau, C., and Koch, K.-W. (2012) Probing the Ca^{2+} switch of the neuronal Ca^{2+} sensor GCAP2 by time-resolved fluorescence spectroscopy. *ACS Chem. Biol. 7*, 1006−1014.
(20) Stephen, R., Bereta, G., Golczak, M., Palczewski, K., and Sousa, M. C. (2007) Stabilizing function for myristoyl group revealed by the crystal structure of a neuronal calcium sensor, guanylate cyclase-activating protein 1. *Structure 15*, 1392−1402.
(21) Ames, J. B., Dizhoor, A. M., Ikura, M., Palczewski, K., and Stryer, L. (1999) Three-dimensional structure of guanylyl cyclase activating protein-2, a calcium-sensitive modulator of photoreceptor guanylyl cyclase. *J. Biol. Chem. 274*, 19329−19337.
(22) Hwang, J.-Y., Schlesinger, R., and Koch, K.-W. (2001) Calcium-dependent cystein reactivities in the neuronal calcium sensor guanylate cyclase-activating protein 1. *FEBS Lett. 508*, 355−359.
(23) Sokal, I., Otto-Bruc, A. E., Surgucheva, I., Verlinde, C. L. M. J., Wang, C.-K., Baehr, W., and Palczewski, K. (1999) Conformational changes in guanylyl cyclase-activating protein 1 (GCAP1) and its tryptophan mutants as a function of calcium concentration. *J. Biol. Chem. 274*, 19829−19837.
(24) Peshenko, I. V., and Dizhoor, A. M. (2006) Ca^{2+} and Mg^{2+} binding properties of GCAP-1. Evidence that Mg^{2+}-bound form is the physiological activator of photoreceptor guanylyl cyclase. *J. Biol. Chem. 281*, 23830−23841.
(25) Orban, T., Bereta, G., Miyagi, M., Wang, B., Chance, M. R., Sousa, M. C., and Palczewski, K. (2010) Conformation changes in guanylate cyclase-activating protein 1 induced by Ca^{2+} and N-terminal fatty acid acylation. *Structure 18*, 116−126.
(26) Lim, S., Peshenko, I. V., Dizhoor, A. M., and Ames, J. B. (2013) Structural insights for activation of retinal guanylate cyclase by GCAP1. *PLoS One 8* (11), e81822.
(27) Peshenko, I. V., Olshevskaya, E. V., Lim, S., Ames, J. B., and Dizhoor, A. M. (2012) Calcium-myristoyl tug is a new mechanisms for intramolecular tuning of calcium sensitivity and tarbet enzyme interaction for guanylyl cyclase-activating protein 1. *J. Biol. Chem. 287*, 13972−13984.
(28) Sundström, V., and Gillbro, T. (1981) Viscosity dependent radiationless relaxation rate of cyanine dyes. A picosecond laser spectroscopy study. *Chem. Phys. 61*, 257−269.
(29) Hovius, R., Vallotton, P., Wohland, T., and Vogel, H. (2000) Fluorescence techniques: shedding light on ligand-receptor interactions. *Trends Pharmacol. Sci. 21*, 266−273.
(30) Kinosita, K., Kawato, S., and Ikegami, A. (1977) A theory of fluorescence polarization decay in membranes. *Biophys. J. 20*, 289−305.
(31) Schröder, G. F., Alexiev, U., and Grubmüller, H. (2005) Simulation of Fluorescence Anisotropy Experiments: Probing Protein Dynamics. *Biophys. J. 89*, 3757−3770.
(32) Sulmann, S., Dell'Orco, D., Marino, V., Behnen, P., and Koch, K.-W. (2014) Conformational changes in calcium-sensor proteins under molecular crowding conditions. *Chem. - Eur. J. 20*, 6756−6762.
(33) Marino, V., Sulmann, S., Koch, K.-W., and Dell'Orco, D. (2014) Structural effects of Mg^{2+} on the regulatory states of three neuronal calcium sensors operating in vertebrate phototransduction. *Biochim. Biophys. Acta, Mol. Cell Res. 1853*, 2055−2065.
(34) Navarro, G., Aguinaga, D., Moreno, E., Hradsky, J., Reddy, P. P., Cortés, A., Mallol, J., Casadó, V., Mikhaylova, M., Kreutz, M. R., Lluís, C., Canela, E. I., McCormick, P. J., and Ferré, S. (2014) Intracellular calcium levels determine differential modulation of allosteric interactions within G protein-coupled receptor heteromers. *Chem. Biol. 21*, 1546−1556.
(35) Ames, J. B., and Lim, S. (2012) Molecular structure and target recognition of neuronal calcium sensor proteins. *Biochim. Biophys. Acta, Gen. Subj. 1820*, 1205−1213.
(36) Krylov, D. M., Niemi, G. A., Dizhoor, A. M., and Hurley, J. B. (1999) Mapping sites in guanylyl cyclase activating protein-1 required for regulation of photoreceptor membrane guanylyl cyclases. *J. Biol. Chem. 274*, 10833−10839.
(37) Hwang, J.-Y., and Koch, K.-W. (2002) The myristoylation of the neuronal Ca^{2+}-sensors guanylate cyclase-activating protein 1 and 2. *Biochim. Biophys. Acta, Proteins Proteomics 1600*, 111−117.
(38) Hess, B., Kutzner, C., Van Der Spoel, D., and Lindahl, E. (2008) GROMACS 4: Algorithms for Highly Efficient, Load-Balanced, and Scalable Molecular Simulation. *J. Chem. Theory Comput. 4*, 435−447.
(39) Bjelkmar, P., Larsson, P., Cuendet, M. A., Hess, B., and Lindahl, E. (2010) Implementation of the CHARMM force field in GROMACS: Analysis of protein stability effects from correction maps, virtual interaction sites, and water models. *J. Chem. Theory Comput. 6*, 459−466.

DOI: 10.1021/acschembio.5b00278
ACS Chem. Biol. 2015, 10, 2344−2352

(40) Mackerell, A. D., Jr., Feig, M., and Brooks, C. L., 3rd. (2004) Extending the treatment of backbone energetics in protein force fields: limitations of gas-phase quantum mechanics in reproducing protein conformational distributions in molecular dynamics simulations. *J. Comput. Chem. 25*, 1400−1415.
(41) Seeber, M., Felline, A., Raimondi, F., Muff, S., Friedman, R., Rao, F., Caflisch, A., and Fanelli, F. (2011) Wordom: a user-friendly program for the analysis of molecular structures, trajectories, and free energy surfaces. *J. Comput. Chem. 32*, 1183−94.

DOI: 10.1021/acschembio.5b00278
ACS Chem. Biol. 2015, 10, 2344−2352

Impact of cone dystrophy-related mutations in GCAP1 on a kinetic model of phototransduction

Daniele Dell'Orco, Stefan Sulmann, Patrick Zägel, Valerio Marino & Karl-Wilhelm Koch

Cellular and Molecular Life Sciences

ISSN 1420-682X
Volume 71
Number 19

Cell. Mol. Life Sci. (2014) 71:3829-3840
DOI 10.1007/s00018-014-1593-4

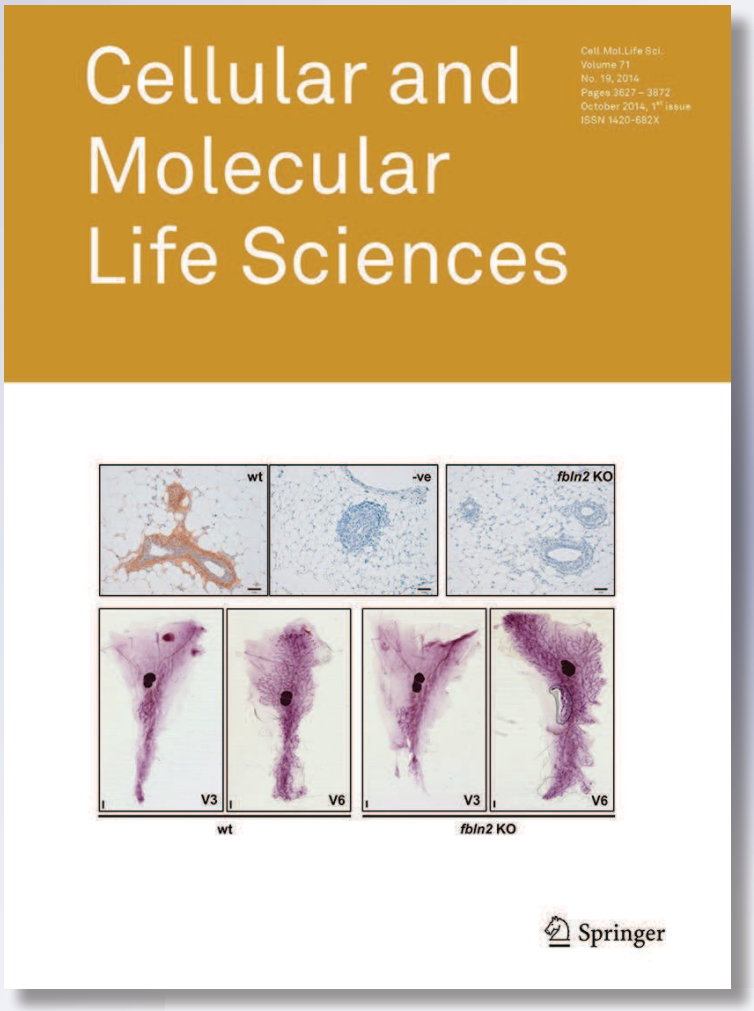

Springer

Cell. Mol. Life Sci. (2014) 71:3829–3840
DOI 10.1007/s00018-014-1593-4

Cellular and Molecular Life Sciences

RESEARCH ARTICLE

Impact of cone dystrophy-related mutations in GCAP1 on a kinetic model of phototransduction

Daniele Dell'Orco · Stefan Sulmann · Patrick Zägel · Valerio Marino · Karl-Wilhelm Koch

Received: 12 December 2013 / Revised: 13 February 2014 / Accepted: 14 February 2014 / Published online: 25 February 2014

Abstract Cone dystrophy-related mutations in guanylate cyclase-activating protein 1 (GCAP1) are known to cause severe disturbance of their Ca^{2+}-sensing properties affecting also their regulatory modes. However, crucial biochemical properties of mutant GCAP1 forms have not been fully elucidated and regulatory parameters of GCAP1 mutants have not been considered within the context of a comprehensive description of the phototransduction cascade kinetics. We investigated therefore the structure–function relationships of four dystrophy-relevant point mutations in GCAP1 harboring the following amino acid substitutions: E89K, D100E, L151F, and G159V. All mutations decrease the catalytic efficiency in regulating the target guanylate cyclase and decrease the affinity of Ca^{2+}-binding in at least one, but in most cases two EF-hand Ca^{2+}-binding sites. Although the wild type and mutants of GCAP1 displayed large differences in Ca^{2+}-binding and regulation, circular dichroism (CD) spectroscopy revealed that all proteins preserved an intact secondary and tertiary structure with a significant rearrangement of the aromatic residues upon binding of Ca^{2+}. To gain insight into the dynamic changes of cyclic GMP levels in a photoreceptor cell, we incorporated parameters describing the regulation of target guanylate cyclase by GCAP1 mutants into a comprehensive kinetic model of phototransduction. Modeling led us to conclude that the contribution of GCAP1 to the dynamic synthesis of cyclic GMP in rod cells would depend on the expression level of the wild-type form. Although the synthesis rate controlled by GCAP1 remains at a constant level, in the case of high expression levels of cone-dystrophy GCAP1 mutants it would not contribute at all to shaping the cGMP rate, which becomes dynamically regulated solely by the other present Ca^{2+}-sensor GCAP2.

Keywords Guanylate cyclase · GCAP · Retinal dystrophy · Phototransduction · Kinetic modeling

Introduction

Inherited retinal dystrophies are very often caused by an imbalance of Ca^{2+}- and cGMP homeostasis. These two second messengers operate in rod and cone photoreceptor cells to control their excitation by light and their adaptation to different light intensities [1, 2]. While the phototransduction cascade in rod and cone cells leads to the light-induced hydrolysis of cGMP, closure of cyclic nucleotide-gated (CNG) channels and hyperpolarization of the cell, the cytoplasmic concentration of Ca^{2+} ($[Ca^{2+}]$) is indirectly controlled by light: Ca^{2+} flows into the cell by open CNG channels, and is extruded via a Na^+/Ca^{2+}, K^+-exchanger. Light-triggered closure of CNG channels stops the influx of Ca^{2+}, but extrusion via the exchanger leads to a decrease in $[Ca^{2+}]$. By these two mechanisms, $[Ca^{2+}]$ is

Electronic supplementary material The online version of this article (doi:10.1007/s00018-014-1593-4) contains supplementary material, which is available to authorized users.

D. Dell'Orco · V. Marino
Section of Biological Chemistry, Department of Life Sciences and Reproduction, University of Verona, 37134 Verona, Italy

D. Dell'Orco (✉)
Center for BioMedical Computing (CBMC), University of Verona, 37134 Verona, Italy
e-mail: daniele.dellorco@univr.it

S. Sulmann · P. Zägel · K.-W. Koch (✉)
Biochemistry Group, Department of Neurosciences, University of Oldenburg, 26111 Oldenburg, Germany
e-mail: karl.w.koch@uni-oldenburg.de

strictly controlled over a rather narrow range being several hundred nanomolar Ca^{2+} in the dark and going down to below 100 nM in the light [1, 2]. Ca^{2+}-sensor proteins like calmodulin, recoverin, and the guanylate cyclase-activating proteins (GCAPs) detect in photoreceptors these changes in $[Ca^{2+}]$ and respond by controlling the activity of target proteins involving the CNG channel, rhodopsin kinase GRK1, and membrane-bound guanylate cyclases, respectively [3–5].

Mutations in the guanylate cyclase signaling complex correlate for example with retinal diseases like Leber congenital amaurosis and cone-rod dystrophies and are linked to mutations in the genes GUCY2D and GUCA1A coding for photoreceptor guanylate cyclase 1 (ROS-GC1) and GCAP1, respectively [6, 7]. GCAPs can respond to incremental changes in $[Ca^{2+}]$ and work in a relay mode fashion [8–11]. Most GCAP1 mutations found in patients suffering from retinal dystrophies exhibit a more or less severe disturbance in their Ca^{2+}-sensing properties, resulting in constitutively active GCAP1 forms under physiological conditions [12–16]. Thus, they maintain the cyclase constitutively active over the range of $[Ca^{2+}]$, in which they normally switch between activating and inhibiting regulatory modes. We have recently investigated in more detail the structural and functional properties of four mutants (E89K, D100E, L151F, G159F) that have some common properties that are shared by other mutant GCAP1 forms. For example, they are located in the domains consisting of the Ca^{2+}-binding motifs EF-hand 3 and 4 (for a structural model see figures in Refs. [7] and [16]), have a decreased thermal stability and display a significantly large shift in the IC_{50}-value, the $[Ca^{2+}]$, at which the activation of the target ROS-GC is half maximal [15, 16]. Experimental work on transgenic mice further supports the notion that GCAP1 mutations that are linked to retinal dystrophies cause photoreceptor degeneration, probably by apoptotic processes [17, 18]. However, so far, the biochemical properties of mutant GCAP1 forms have not been considered in the context of the whole cascade, since they have not yet been integrated into a computational kinetic model of the phototransduction cascade [19–22].

Wild-type (WT) GCAPs are known to influence and regulate catalytic parameters like k_{cat}/K_m of the target ROS-GCs [8]. In the present work, we determined therefore, how cone-dystrophy related mutants of GCAP1 influence parameters like k_{cat}/K_m. Further, using isothermal titration calorimetry (ITC) we determined thermodynamic parameters and constants for Ca^{2+}-binding to GCAPs and relate them to the changes observed in the near UV circular dichroism (CD) spectra upon Ca^{2+}-binding, which show tertiary structure rearrangement in each GCAP1 variant. Finally, the experimentally determined parameters describing the regulation of ROS-GC1 by GCAP1 at different $[Ca^{2+}]$ were incorporated into a comprehensive kinetic model of phototransduction [20–22], allowing the assessment of how individual point mutations affect the signaling pathway and the Ca^{2+}-dependent GCAP relay system [23] as well as the overall cell photoresponse. Our results suggest that GCAP1 mutants perturb the shape of photoresponse, prolonging its duration, and increase its amplitude in each tested illumination condition. Interestingly, the dysfunction of GCAP1 pathogenic forms is predicted to be partly compensated by the action of native GCAP2, which becomes dominant in shaping the dynamics of cGMP synthesis upon light stimulation.

Materials and methods

Protein expression and purification

WT and mutants of GCAP1 were overexpressed in BL21 *E. coli* cells as described previously and subsequently purified to homogeneity as outlined elsewhere [8, 15, 16]. Briefly, GCAP1-forms were extracted from inclusion bodies by homogenization in 6 M guanidinium hydrochloride and dialyzed against 3 l of Tris buffer (20 mM Tris–HCl, 150 mM NaCl, 1 mM DTT pH 7.5). After one buffer change, any remaining insoluble fractions were removed by centrifugation (100,000 × *g* for 30 min). GCAP variants in the resulting supernatant were purified in the presence of 1 mM EDTA or 2 mM EGTA by a combination of size exclusion and ion-exchange chromatography using a Superdex 75 column and a HiLoad 26/10 Q Sepharose, respectively (GE Healthcare, Germany).

Guanylate cyclase assay and kinetic analysis

For guanylate cyclase activity assays, we used washed bovine rod outer segment (ROS) membranes that were prepared from frozen bovine retinae as described [24]. These membranes are a source of intact and active outer-segment guanylate cyclase type 1 (ROS-GC1 or RetGC1, GC-E). Membranes (corresponding to a content of 70 µg rhodopsin) were reconstituted with 10 µM of purified WT or mutant GCAP1. Guanylate cyclase activity was assayed at 2 mM EGTA (≤10 nM free $[Ca^{2+}]$) as a function of the substrate Mg^{2+}-GTP at a free $[Mg^{2+}]$ of 1 mM. Analysis of data was performed with SIGMA plot 10.0 software. A direct plot of activity versus $[Mg^{2+}$-GTP] resulted in a sigmoidal curve as observed previously [8], which indicates cooperative substrate binding. We analyzed the data further by linearizing a corresponding Lineweaver–Burk plot [8] using a Hill coefficient n from a fit of the direct plot. Values of V_{max} and K_m were then determined from a plot of $1/V$ (reciprocal of guanylate cyclase activity) versus 1/

$[S]^n$ (reciprocal of the substrate concentration raised to the power of n).

Isothermal titration calorimetry (ITC)

For ITC experiments, we used a VP-ITC instrument from MicroCal (Northampton, MA, USA) at $T = 25$ °C. Purified GCAP1 forms were present in the recording cell in titration buffer (5 mM Tris/HCl, pH = 7.5; 150 mM KCl) at 10–30 μM and titrated with increasing $CaCl_2$ concentrations. All buffers were decalcified using a Chelex 100 resin column (Bio-Rad, Hercules, CA, USA) with a flow rate of 3 ml/min as described [16]. $CaCl_2$ was of the highest grade available and dissolved in the decalcified titration buffer to a final 1 M concentration and Ca^{2+} stocks were prepared by subsequent dilutions to final concentrations 0.5–2 mM. All buffers were filtered (0.22 μm) and degassed for at least 1 h before use.

$CaCl_2$ in the titration buffer was placed in the microsyringe chamber at 0.5–1 mM. Ca^{2+} titration was performed by subsequent injections of 5 μl Ca^{2+} solution into the recording cell keeping a time interval of 180 s between injections and an initial delay of 600 s after temperature equilibration. Control injections of Ca^{2+} into the decalcified buffer without protein were also performed, but did not result in specific heat changes. The baselines of the raw data were automatically adjusted by Origin (MicroCal) and the same software was employed for data analysis and fitting. Optimal fitting results were obtained with a model assuming three binding sites for Ca^{2+} providing an estimate for K_D^{app} and molar enthalpy (ΔH) changes at the given temperature.

Circular dichroism (CD) spectroscopy and thermal denaturation studies

Circular dichroism spectroscopy studies were performed with a Jasco V-710 spectropolarimeter equipped with a Peltier-type thermostated cell holder. Near-UV (250–320 nm) spectra were recorded at 25 °C at a scan rate of 50 nm/min, a bandwidth of 1 nm, and an integration time of 4 s. Protein concentration was in the 0.5–0.7 mg/ml range (22–35 μM) as measured by Bradford assay [25]. Spectra were recorded in a 1-cm cuvette at final 1 mM concentration of Ca^{2+} or EGTA. Five spectra accumulations were averaged for each sample, and the spectrum of the buffer was subtracted. Far-UV CD spectra were recorded for the myristoylated E89K variant between 200 and 250 nm, in the same conditions as those described in [16]. Protein concentration was 21 μM in 0.1-cm cuvette, and spectra were recorded in the presence of either 200 μM EDTA or Ca^{2+}. Spectra were recorded both at 25 and 37 °C, to directly compare the results with those of other mutants [15, 16]. Thermal denaturation studies of the E89K variant in the presence of Ca^{2+} or EDTA were performed in the 4–96 °C range. The ellipticity signal at 222 nm (θ_{222}) was recorded at a scan rate of 1 °C/min and a response time of 16 s, using a 0.1-cm quartz cuvette. Thermally denatured samples were cooled down to 25 and 4 °C and, after 5–15 min, a far-UV CD spectrum was recorded to check for residual structures. The analysis of thermal denaturation curves was performed for each sample assuming a two-state transition process, as previously described [16].

Computational kinetic model of cGMP synthesis and simulation of photoresponses

A previously developed mathematical model of phototransduction in rod cells accounting for the comprehensive biochemical mechanisms [19–22] was employed to simulate rod responses to flashes leading from 1.5 to 1,100 rhodopsin photoisomerizations. The model used in this work was originally developed for quantitative simulations of photoresponses from amphibian rod cells [19, 20] but it has been widely demonstrated that the model proved also able to predict with great accuracy the qualitative dynamics observed in mouse photoreceptors [20–22].

The synthesis of cGMP by ROS-GC1 was modeled according to the recently developed Ca^{2+}-relay implementation [23]. In the current implementation, the cGMP synthesis was specifically modeled as follows:

$$a_b \frac{\mathrm{d}[\mathrm{cGMP}]_{\mathrm{synth}}}{\mathrm{d}t} = 0.5 \times \frac{a_{\max 1}}{1 + \left(\frac{\mathrm{Ca}^{2+}_{\mathrm{free}}}{\mathrm{IC}_{50}^{\mathrm{GCAP1}}}\right)^{h1}} + 0.5 \times \frac{a_{\max 1}^{\mathrm{mut}}}{1 + \left(\frac{\mathrm{Ca}^{2+}_{\mathrm{free}}}{\mathrm{IC}_{50}^{\mathrm{GCAP1mut}}}\right)^{h1^{mut}}} + \frac{a_{\max 2}}{1 + \left(\frac{\mathrm{Ca}^{2+}_{\mathrm{free}}}{\mathrm{IC}_{50}^{\mathrm{GCAP2}}}\right)^{h2}} \quad (1)$$

in which the first two terms represent the regulation by GCAP1 in its wild-type (first term) and mutated (second term) form, and the third one that by GCAP2. In order to simulate the autosomal dominant form of the disease, the expression of mutated GCAP1 was considered to be approximately half of the total protein expression. We further simulated a hypothetical (recessive) form (Online Resource 1), the first term in (1) was omitted and the weight of the second term was set to unity. In each term, the numerator is defined as the maximal activation of ROS-GC1:

$$a_{\max} = \beta_{\mathrm{dark}} \mathrm{cGMP}_{\mathrm{dark}} \left(1 + \left(\frac{\mathrm{Ca}^{2+}_{\mathrm{dark}}}{\mathrm{IC}_{50}}\right)\right)^{h} \quad (2)$$

in which β_{dark}, the dark rate of cGMP synthesis, was set to 1.2 s^{-1}, $\mathrm{cGMP}_{\mathrm{dark}} = 4$ μM is the cGMP concentration in the dark, $\mathrm{Ca}^{2+}_{\mathrm{dark}} = 0.6$ μM is the concentration of free

Table 1 Catalytic parameters of the activated state of native ROS-GC1

GCAP1 form	V_{max} (nmol × min^{-1} per mg rhodopsin)	K_m (mM)	k_{cat} (s^{-1})	k_{cat}/K_m (10^3 M^{-1} s^{-1})	n	IC_{50} (μM)	h
WT	8.2 ± 1.7	0.14 ± 0.03	2.86 ± 0.58	20.42 ± 5.95	2.8	0.8	1.80
E89K	6.5 ± 0.3	0.52 ± 0.03	2.27 ± 0.12	4.37 ± 0.33	2.3	4.7	1.17
D100E	5.2 ± 0.2	0.61 ± 0.02	1.81 ± 0.07	2.97 ± 0.17	2.2	21.9	4.91
L151F	11.5 ± 0.4	0.60 ± 0.02	3.99 ± 0.14	6.65 ± 0.32	2.4	39.0	1.88
G159V	16.9 ± 1.1	0.82 ± 0.05	5.86 ± 0.38	7.15 ± 0.65	2	14.5	2.05

Assays were performed at constant concentrations of GCAP1 (10 μM) and free [Ca^{2+}] (10^{-8} M) at varying concentrations of the substrate Mg^{2+}-GTP. Values are the mean ± SD (three independent determinations). Two different Hill coefficients are listed, n was obtained from a sigmoidal plot of activity versus [Mg^{2+}-GTP], h represents the coefficient obtained from Ca^{2+}-dependent activation curves. Values for IC_{50} and h were taken from Refs. [16, 26]

calcium in the dark, IC_{50} is the calcium concentration at which the synthesis of cGMP is half maximal and h is the Hill coefficient for the action of calcium on the cyclase rate via each specific GCAP protein. If no mutations were present in GCAP1, then numerators would equal each other ($a_{max1} = a_{max2} = a_{max} = 60$ μM/s, see [23]), thus leading to the results discussed in the recent Ca-relay implementation model [23]. If, however, cone dystrophy-related mutations were present in GCAP1, a_{max1} would be affected, which is accounted for by a^{mut}_{max1}, as well as it would be the denominator of the first term in Eq. (1). Specifically, $IC_{50}^{GCAP1mut}$ and $h1^{mut}$ were set to their relative values (-fold variation) compared to the wild type, according to the data in [16, 26]. No changes were done to parameters determining the contribution to GC1 regulation by GCAP2. The model was implemented using SBTOOLBOX2 for MATLAB (http://www.sbtoolbox2.org website) [20] and all numerical simulations were carried out in this framework. Deterministic simulations were run from automatically generated and compiled C-code models, based on the CVODE integrator from SUNDIALS [27].

Results

Influence of GCAP1 mutants on enzyme catalysis

Mammalian GCAP1 and GCAP2 activate the target ROS-GCs by increasing their catalytic efficiencies expressed in k_{cat}/K_m [8, 28]. Previous biochemical characterization of dystrophy-related GCAP1 mutants was mainly focused on their Ca^{2+}-sensitive activation profiles and on Ca^{2+}-triggered changes in protein conformation, but these studies have not addressed questions concerning changes in catalytic efficiency. We determined the enzyme kinetics of ROS-GC1 in native bovine rod outer segments by varying the substrate Mg^{2+}-GTP, but keeping the concentration of GCAP1 at a constant value of 10 μM GCAP1. The free [Ca^{2+}] was set to 10^{-8} M. With WT GCAP1, we obtained a k_{cat}/K_m of 2×10^4 M^{-1} s^{-1} (Table 1) that was almost identical to our previously published value [8]. All four tested GCAP1 mutants decreased the catalytic efficiency, but to a different extent (Table 1). The largest effect was seen with D100E (~7-fold decrease) followed by E89K (~5-fold), L151F, and G159V (~3-fold). The decrease is mainly caused by an increase of K_m. Only E89K and D100E decreased slightly the k_{cat}, whereas L151F and G159V even increased the k_{cat} value. Binding of Mg^{2+}-GTP and synthesis of cGMP is known to occur in a cooperative fashion. The mutations in GCAP1 had only a modest effect (decrease) on the Hill coefficient (Table 1).

Thermodynamic characterization of Ca^{2+} binding to GCAP1 mutants

ITC measurements were used to determine thermodynamic parameters of Ca^{2+} binding to WT and mutant forms of GCAP1. Representative examples of ITC titrations are shown in Fig. 1a–e for WT and four GCAP1 mutants. A comprehensive overview of all data is presented in Table 2. A common feature of nearly all GCAP1 forms was that the binding processes were exothermic in most cases, which is typically seen on negatively spiking heat pulses in the original recording traces (Fig. 1, upper part of each panel). Only G159V displayed in all measurements small positive spikes at higher molar ratios of Ca^{2+} per protein indicating an endothermic binding process. Binding isotherms were obtained from the titration recordings by curve fitting using a sequential binding model with three different binding sites for Ca^{2+} (Fig. 1, lower part of each panel). WT GCAP1 is known to harbor three functional EF-hand Ca^{2+}-binding sites of high, medium, and low affinity, which we could confirm by the fit of the experimental data (K^1_D K^2_D K^3_D in Table 2). GCAP1 mutants differed, however, in several aspects from the WT. They displayed lower affinities for Ca^{2+} in particular for K^2_D and/or K^3_D while the high affinity site remained nearly unchanged in all GCAP1 forms showing a K^1_D below 100 nM. The relative decrease in Ca^{2+} affinity in the mutants was highest in D100E (difference

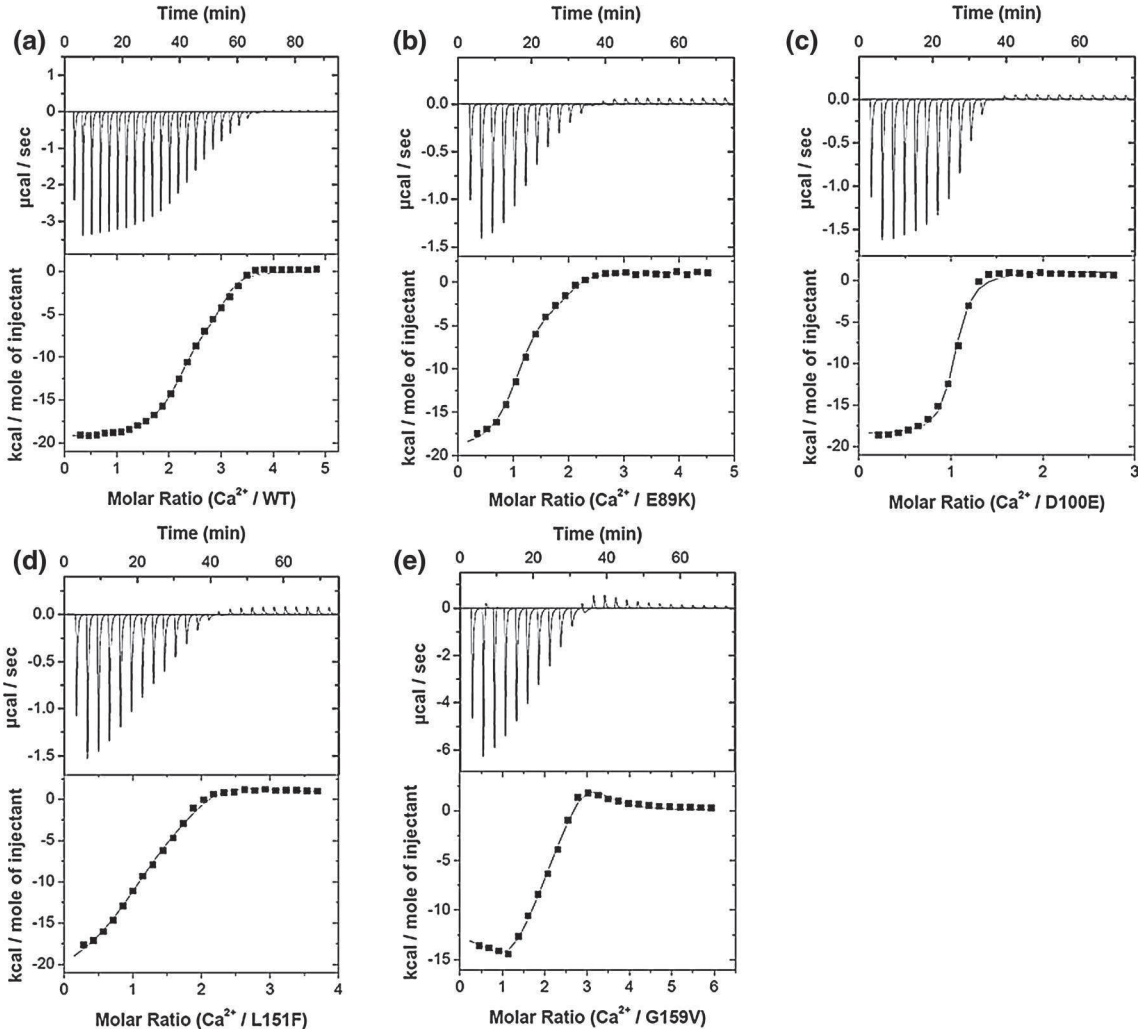

Fig. 1 Ca^{2+} binding to GCAP1 WT and mutants. Representative ITC measurements of Ca^{2+} titrations with 23 µM WT GCAP1 (**a**) in comparison to mutants: 10 µM E89K (**b**), 19 µM D100E (**c**), 22 µM L151F (**d**), and 30 µM G159V (**e**) as indicated. Data were obtained by repetitive injections of $CaCl_2$ into the protein solution. The *upper part* of each graphic shows the heat pulses obtained by injection of $CaCl_2$, and the *lower part* shows the corresponding changes in enthalpy (kcal/mol of injectants). Data analysis by curve fitting yielded K_D values of three binding sites and corresponding ΔH values, which are listed for several sets of experiments in Table 2

Table 2 Thermodynamics of Ca^{2+} binding to WT and mutant forms of GCAP1

GCAP1 form	Rep	Dissociation constants K_D (µM)			Enthalpy change ΔH (kcal/mol)		
		K_D^1	K_D^2	K_D^3	ΔH^1	ΔH^2	ΔH^3
WT	3	0.08 ± 0.007	0.29 ± 0.13	2.53 ± 0.19	−19.4 ± 0.2	−19.2 ± 0.4	−15.1 ± 0.4
E89K	4	0.085 ± 0.030	2.07 ± 1.18	25 ± 14	−18.7 ± 0.6	−10.7 ± 5.9	11.6 ± 6.5
D100E	2	0.031 ± 0.005	3.54 ± 0.60	144 ± 12	−18.7 ± 0.1	2.4 ± 0.4	3.4 ± 1.8
L151F	5	0.056 ± 0.024	0.40 ± 0.16	111 ± 67	−20.1 ± 0.5	0.4 ± 1.3	11.1 ± 3.7
G159V	3	0.098 ± 0.024	0.82 ± 0.11	2.19 ± 0.68	−14.4 ± 1.8	−19.3 ± 1.1	8.67 ± 1.04

Apparent dissociation constants K_D and enthalpy changes were obtained from curve fitting

Rep number of repetitions

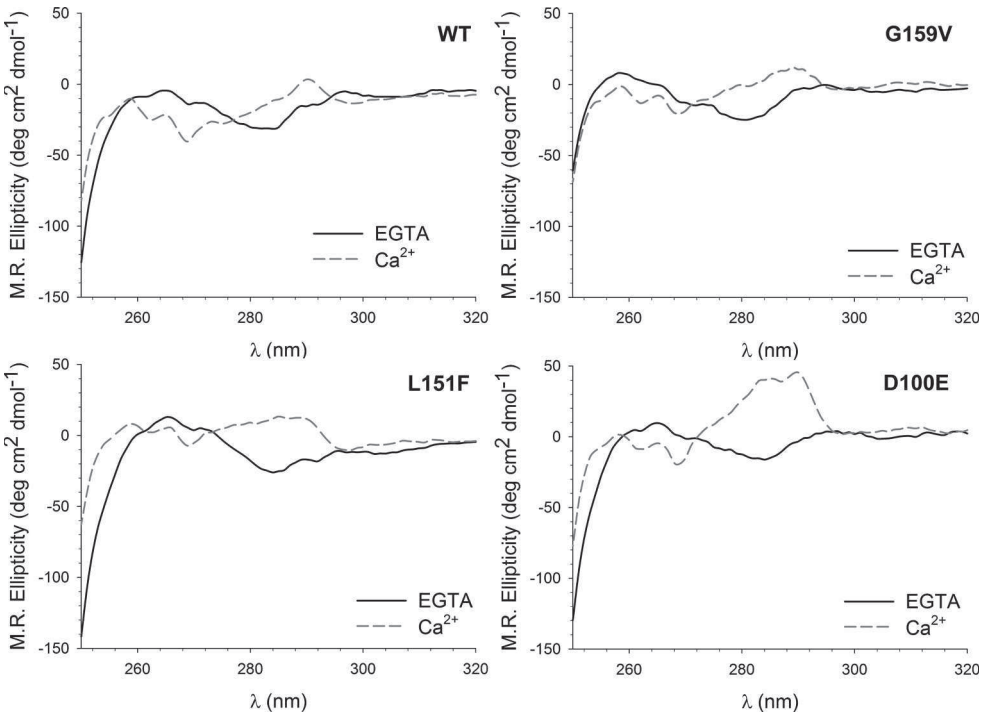

Fig. 2 Structural changes occurring in GCAP1 variants upon binding of Ca^{2+} at $T = 25$ °C, in 5 mM Tris/HCl pH 7.5, 150 mM KCl buffer. Near-UV CD spectra of 0.5–0.7 mg/ml GCAP1 were recorded in the presence of equal amounts (1 mM) of saturating EGTA or $CaCl_2$

of constants K_D^2 and K_D^3 to the corresponding WT value was 12- and 57-fold, respectively), while the mutant E89K showed a 7 to 10-fold decrease in affinities of these constants. In the mutant L151F only K_D^3 was affected (44-fold difference), whereas G159V displayed constants similar to the WT, only K_D^2 was 2.8-fold lower than the WT K_D.

Binding of Ca^{2+} to the high affinity binding site (K_D^1) was exothermic for all GCAP1 forms with values for ΔH between −14.4 kcal/mol (G159V) and −19.4 kcal/mol (WT). In contrast, the low affinity K_D^3 values of all mutants corresponded to positive enthalpy changes between 3.4 kcal/mol (D100E) and 11.6 kcal/mol (E89K). The medium affinity binding site was exothermic for WT, E89K, and G159V, but endothermic for D100E and L151F (Table 2).

Structural effects of Ca^{2+} binding to GCAP1 mutants

Near-UV CD spectroscopy was used to assess the effects of Ca^{2+} binding on the tertiary structure of each GCAP1 variant. For the wild-type GCAP1, the spectroscopic data showed a significant rearrangement of the aromatic residues upon binding of Ca^{2+}, especially in the Phe and Tyr bands (Fig. 2), with a less prominent involvement of the Trp region. Saturation with Ca^{2+} revealed a higher dichroism compared to the apo-form and a fine structure in the Phe band with characteristic minima at 261 and 264 nm, while the trend was reversed in the Tyr–Trp regions, with a local maximum at 285 nm. Interestingly, in the absence of Ca^{2+} all GCAP1 variants except E89K showed similar spectra compared to the wild type, suggesting that the tertiary structure of the apo-form is not significantly affected by the pathogenic mutations. However, the Ca^{2+}-bound forms showed major differences in the Tyr–Trp regions, with a similar pattern but lower dichroic intensity in the Phe region. The 278–288-nm band switched from mostly negative to fully positive ellipticity, an effect particularly visible for the L151F and D100E mutants, and rather modest for the G159V variant. Thus, tertiary structure rearrangements concern mostly the Ca^{2+}-bound forms of the mutants.

The E89K mutant showed a completely different near-UV CD spectrum (Fig. 3a), both in the presence and in the absence of Ca^{2+}. Strong positive ellipticity characterized both the EGTA and Ca^{2+}-bound forms, suggesting that, at odds with all other mutants, the tertiary structure might be significantly different from that of the wild type already in the apo-form. Since this mutant in its myristoylated form was not fully characterized in earlier studies [16], we asked whether the secondary structure and the thermal stability would also significantly differ compared to other mutants, therefore we repeated the same experiments performed earlier with the other GCAP1 forms [16]. Far-UV CD spectroscopy (Fig. 3b) showed that, like the E89K non-myristoylated form [16], the myristoylated variant also has a typical all-α helical fold, which upon Ca^{2+} binding increased the relative ellipticity at 222 nm by >22 %, thus showing full response to saturating Ca^{2+}. Thermal denaturation profiles (Fig. 3c) could be fitted by the same model used for other GCAP1 mutants, leading to a transition temperature of 37.3 °C in EDTA and approx 115 °C in the presence of saturating

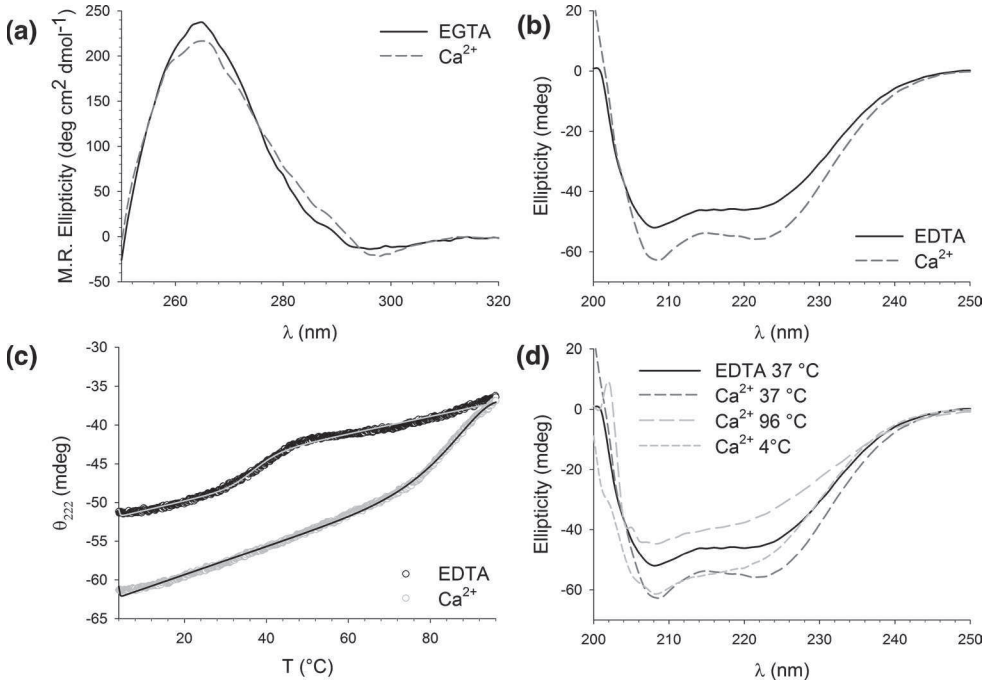

Fig. 3 Structural features of the E89K GCAP1 mutant. **a** Near-UV CD spectra recorded at 25 °C in 5 mM Tris/HCl pH 7.5, 150 mM KCl buffer, in the presence of equal amounts (1 mM) of saturating EGTA or Ca^{2+}. **b** Far-UV CD spectra measured at $T = 37$ °C with 21 μM protein in the presence of equal amounts (200 μM) of saturating EDTA or $CaCl_2$. **c** Thermal denaturation profile of 21 μM E89K-GCAP1 in the presence of equal amounts (200 μM) of EDTA or $CaCl_2$, followed by monitoring the change in ellipticity signal at 222 nm over the 20–96 °C temperature range. *Curves* obtained by fitting to a quantitative model for a two-state transition are superposed to experimental points. **d** Far-UV CD spectra measured in the presence of saturating (200 μM) $CaCl_2$ measured at $T = 96$ and 4 °C after thermal denaturation, as directly compared to spectra recorded at 37 °C

Ca^{2+}. Calcium-saturated spectra recorded at 96 °C after thermal denaturation (Fig. 3d) showed that a significant portion of the secondary structure was retained; however, the spectra demonstrated a loss of α-helical content when compared to the ones recorded at 37 °C. Cooling back to 4 °C led to further recovery of the signal, indicative of a partial recovery of secondary structure, but the spectral shape was still far from the native, purely α-helical one (Fig. 3d).

Effects of GCAP1 mutants on the kinetics of phototransduction

In order to explore the functional effects of cone dystrophy-related GCAP1 mutants on the whole phototransduction cascade, we used a recently developed comprehensive kinetic model of phototransduction in rod cells [20–22], in which the Ca^{2+}-relay mechanism was implemented allowing the separated contributions of GCAP1 and GCAP2 to the regulation of the ROS-GC1 activity to be monitored [23]. The functional effects of GCAP1 mutants on GC1 activity as assessed by in vitro assays were explicitly considered here by setting kinetic constraints related to the experimental IC_{50} and h values, which were implemented directly in the Ca^{2+}-relay model (see "Materials and methods").

Figure 4 shows the simulation of typical photocurrents obtained for an amphibian rod stimulated by flashes of increasing intensities, from dim light conditions to saturating ones. A common feature observed for each mutant is the slight perturbation of photoresponse shapes, at each tested light intensity. The difference in the photoresponse kinetics observed between wild-type rods and those expressing cone dystrophy-related GCAP1 forms is already apparent at dim light intensities leading to five photoisomerizations of rhodopsin. The superposition of simulated photocurrents (Fig. 4, last panel) highlights the most prominent effects, namely: (1) a higher response peak amplitude at each illumination intensity; (2) the prolongation of the response duration, with a delay in the recovery time; (3) the post-recovery stabilization at a lower current value, corresponding to an increased dark current. These effects are relatively small in the implemented model that mimics data from dominant mutations in human, in which wild-type GCAP1 accounts for ~50 % of the overall GCAP1 content. However, simulation of a hypothetical autosomal recessive form of the same mutants, thus leading to the complete absence of wild-type GCAP1 led to more significant effects (Online

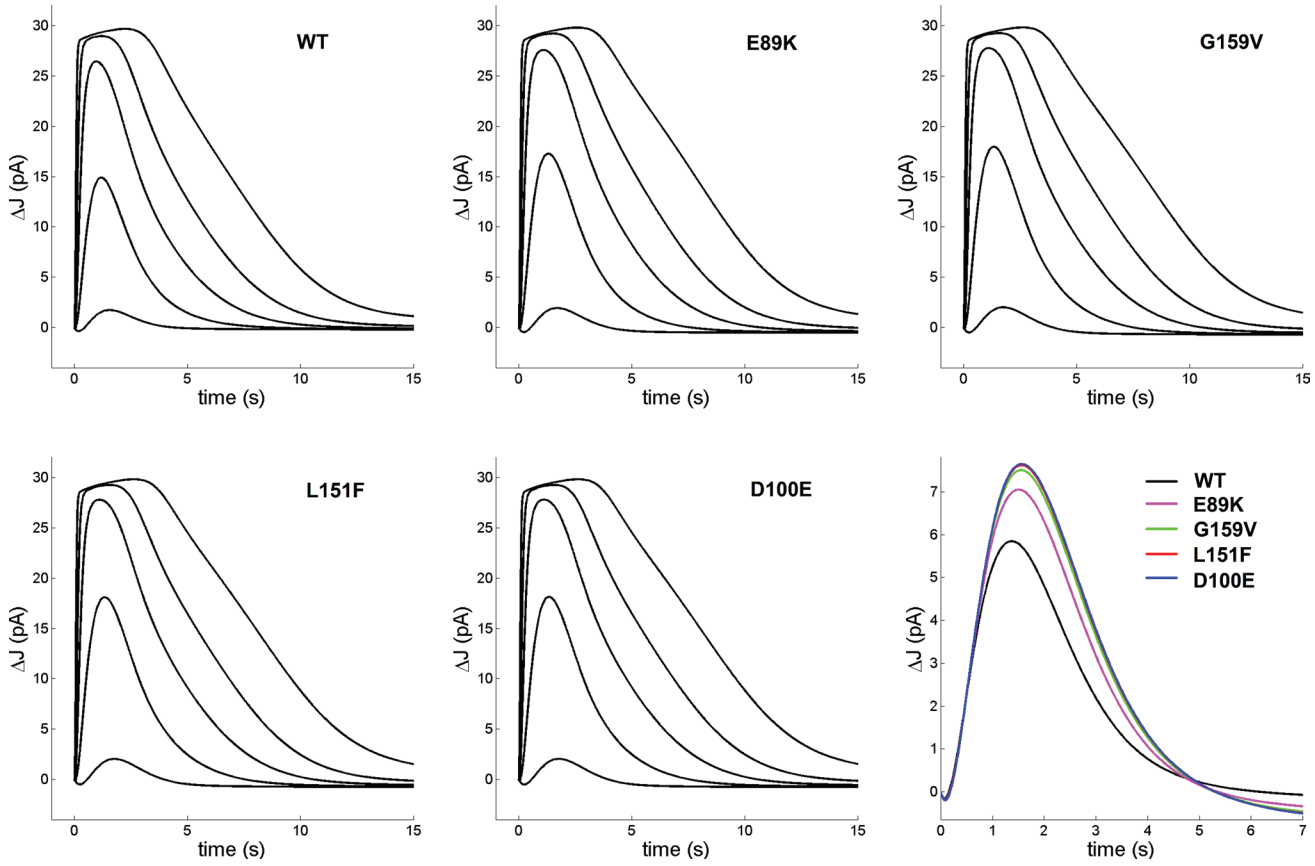

Fig. 4 Simulated photocurrents of a rod photoreceptor stimulated by light of increasing intensity in the presence of ~50 % wild-type and ~50 % cone dystrophy-related GCAP1 variants, and wild-type GCAP2. The duration of each flash is 24 ms, and each stimulus leads to 1.5, 18, 87, 280, and 1,100 photoisomerizations of rhodopsin. In the last panel, superposition of simulated photoresponses corresponding to wild-type and mutated GCAP1 variants to flashes leading to 5 photoisomerization of rhodopsin is shown. The mathematical model used for the simulation is that reported in [23], with the Ca^{2+}-relay model modified to include the parameters described in this work

Resource 1) with the onset of a "shoulder" at higher light intensities.

While present in each simulated GCAP1 mutant, these effects become more apparent for the variants in the following order: E89K, G159V, L151F, D100E. It is worth noticing that with respect to the nominal dark current initially set to 30.7 pA, the increase of dark current was similar for each mutant (+0.41 pA (E89K); +0.51 pA (G159V); +0.56 pA (L151F); +0.58 pA (D100E). However, in case of the sole expression of mutated GCAP1, e.g., in a hypothetical recessive form of disease (Online Resource 1), the increase would be significantly stronger and differential for each mutant: +1.29 pA (E89K); +2.45 pA (G159V); +3.15 pA (L151F); +3.38 pA (D100E).

Since the kinetic computational model allows monitoring individual reactions and molecular species within the simulated cascade, we sought to investigate the predicted dynamics for the rate of cGMP synthesis as determined by the sum of individual contributions by GCAP1, both in its wild-type and mutated forms, and GCAP2. Figure 5 shows the simulated curves for cGMP synthesis following a delivery of a light flash leading to 87 photoisomerizations.

While for wild-type GCAP1 both the absolute value and the shape of the cGMP rate are mostly determined by GCAP1, in the presence of ~50 % cone-dystrophy GCAP1 mutants the shape of cGMP synthesis dynamic variation is also significantly determined by GCAP2. The effect is particular apparent in simulations of a hypothetical recessive form of disease involving the same mutations (Online Resource 2). If no wild-type GCAP1 were present and the whole pool of GCAP1 were solely constituted by mutant proteins, in the cases of E89K and G159V mutants GCAP1 would still play a role in shaping the rate of cGMP synthesis, but by harboring the L151F or D100E mutation GCAP1 would not contribute at all to the dynamic synthesis of cGMP, although it is still the determinant factor for setting the entity of the cGMP rate. Instead, the shape of the rate would be dynamically regulated solely by GCAP2. Hence, for these GCAP1 mutants, the protein apparently does not switch between its normal regulatory states.

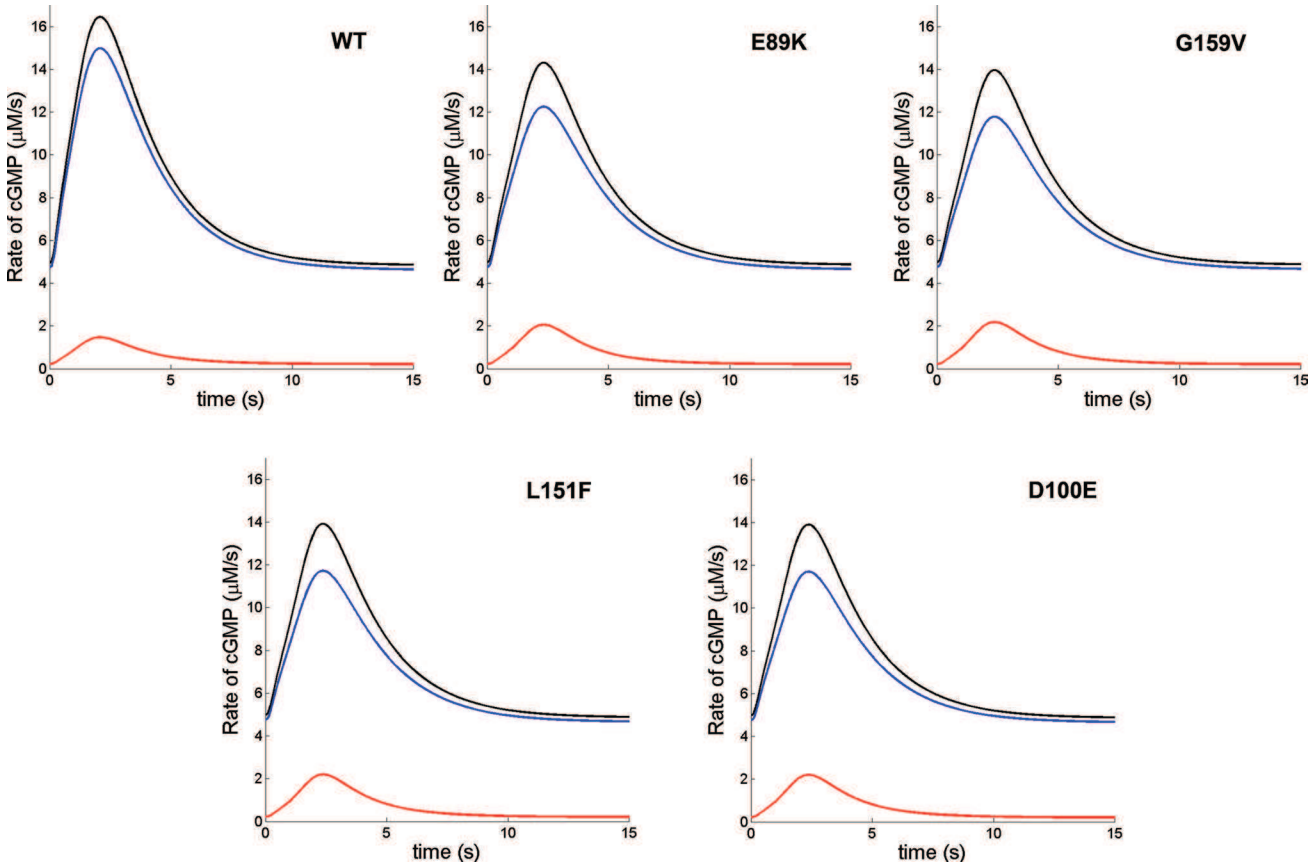

Fig. 5 Simulated time course of the synthesis of cGMP by GC in a rod cell under the Ca^{2+}-mediated regulation by ~50 % wild-type and ~50 % mutated GCAP1 and wild-type GCAP2 for a flash leading to 87 photoisomerization of rhodopsin. *Blue lines* report on the contribution of GCAP1 (both wild type and mutated) to the rate of cGMP synthesis, while *red lines* on that of GCAP2. The two contributions add up to form the overall rate (*black line*)

Discussion

A typical feature of GCAP1 mutations that are linked to cone-rod dystrophies is a change in the Ca^{2+}-sensitive control of the target guanylate cyclase ROS-GC1, namely a shift in the Ca^{2+}-dependent activation curve to higher Ca^{2+}-concentrations (for review see [7]). This then creates a situation under which the cyclase is under control of a constitutively active GCAP1 leading to a constant rate of cGMP synthesis, and an unperturbed GCAP2, which is known to adjust the operating range of rods to high light intensities [29]. GCAP1, like other GCAP isoforms, harbors three functional EF-hand Ca^{2+}-binding sites and the shift in Ca^{2+}-sensitive regulation of ROS-GC appears to originate from a change in affinity of Ca^{2+} for the individual EF-hands [30]. Lim et al. [31] assigned different affinities to the EF-hands in WT GCAP1 using ITC measurements. The apparent dissociation constants we observed for WT GCAP1 (Table 2) are in good agreement with their published data resulting in two high affinity binding sites (K_D^1 and K_D^2 corresponding to EF-hand 3 and 4, respectively) and one site of lower affinity (K_D^3 in EF-hand 2). Our data are also consistent with our previous determinations of macroscopic Ca^{2+}-binding constants using a competitive chromophoric Ca^{2+} chelator in a photometric assay, which, however, did not allow to assess potential contributions of the concerted conformational change upon Ca^{2+} binding [16]. Thus, the ITC measurements provided us with a reliable data set and showed that the high affinity site (K_D^1) remained nearly unchanged in comparison to the WT. More dramatic changes were observed for K_D^2 (in particular mutants E89K and D100E) and K_D^3 (particularly E89K, D100E, and L151F), which shifted to much higher values, indicating a decrease in affinity for Ca^{2+}. Interestingly, the decrease in Ca^{2+} affinity did not lead to a loss in activating properties, but merely shifted the switching mode from an activator to an inhibitor state.

It is worth noting that the GCAP1 mutants exhibited far-UV-CD spectra that showed the preservation of secondary structural features similar to the WT (Fig. 3 for E89K and Ref. [16]). Further, switching from Ca^{2+}-saturated to Ca^{2+}-free GCAP1 forms caused different changes in the near-UV

spectra of all mutants (Fig. 2), but these changes indicated more subtle rearrangements in the vicinities of aromatic amino acid side chains of D100E, L151F, and G159V. Only E89K seemed to be an exception, since the near-UV spectra showed a completely different profile, indicating a significant structural change from the WT form. We propose that the E89K mutation in both myristoylated and non-myristoylated GCAP1 leads to a misfolding of the protein, which could trigger photoreceptor cell death in ways not clarified yet.

Summarizing the results obtained with all other mutants, however, let us conclude that the main dystrophy-relevant aspect of the mutations does not originate from a structural instability or protein misfolding. Instead, it might be a direct consequence of the enzymatic and regulatory features.

This assumption was further confirmed by our studies on the catalytic efficiency. The two mammalian GCAPs (GCAP1 and 2) exhibit different regulatory properties including differences in catalytic efficiency (k_{cat}/K_m) [8, 28]. Since this effect was found in previous work to be more pronounced in GCAP1 than in GCAP2, we reasoned that GCAP1 mutations would affect k_{cat}/K_m in a previously unknown manner. Although the mutations led to lower catalytic efficiency, they did so by mixed effects having both consequences for K_m (increase) and in some cases also for k_{cat} (increase for L151F and G159V). It remains an open question, how these data on catalytic efficiency could contribute to the development of the retinal dystrophy, but since the decrease in k_{cat}/K_m is mainly governed by an increase in K_m, fluctuations in the substrate Mg^{2+}-GTP concentration could significantly disturb an efficient cGMP synthesis by the following scenario: because the target ROS-GC1 would be constitutively activated by GCAP1 mutants regardless of the cytoplasmic Ca^{2+}-concentration, the turnover of GTP is expected to increase leading to a GTP drain. This would cause an imbalance of constant GTP supply via metabolic routes, at least transiently, affecting negatively the catalytic efficiency. In turn, cGMP synthesis would decrease, but not in the precise time frame that is required for reliable photodetection.

In order to gain more insight into the cGMP synthesis rate, when a photoreceptor cell expresses one of the GCAP1 mutants (in the presence of approximately 50 % of WT GCAP1 and the whole pool of WT GCAP2), we integrated our experimental data on Ca^{2+}-dependent ROS-GC1 regulation by GCAP1 and GCAP2 into a kinetic model of phototransduction. Interestingly, the *dynamic changes* in cGMP synthesis rate became more pronounced the larger the changes of the biochemical properties of a particular GCAP1 mutant were, which is most significant for L151F and D100E (Figs. 4, 5). This effect seems to arise from the loss or reduction of any Ca^{2+}-sensitive regulation of the GC by mutant GCAP1 under normal physiological Ca^{2+}-concentrations, which by itself would lead to a constant synthesis rate. Under conditions of constant illumination, when the synthesis rate is high, but at the same time less dynamically regulated, the substrate GTP concentration might also decline due to exhaustion of the cellular GTP pool. These fluctuations would then have an effect on the catalytic performance of the ROS-GC/GCAP complex (see above).

It is interesting to note that the perturbations of the phototransduction kinetics observed in our simulations are in line with experimental data on transgenic mice expressing the Y99C mutation in GCAP1 also found in cone-dystrophy patients [17]. The Y99C variant showed similar biochemical features compared to the mutants analyzed here, and it constitutively activated the GC at physiological Ca^{2+}, thus leading to an increase of free cGMP. In their electrophysiological studies, Olshevskaya et al. [17] noticed an increase of dark current in the mutant mice, and a minor perturbation of the photocurrents over a broad range of light stimuli ranging from single photon to saturating responses. The extent of the perturbation (increased amplitude and time-to-peak for single photon response as well as the general prolongation of the light responses) was, however, found to depend on the expression level of mutant GCAP1 over a background of wild-type GCAP1. Our computational model fully reproduces this behavior. The effects of mutants expressed in the presence of ~50 % wild-type GCAP1 led to significantly lower perturbation of the photocurrents (Fig. 4) compared to the simulated case of total absence of wild-type GCAP1 and its complete replacement by mutant variants (Online Resource 1), which in fact completely exclude the switch between activating and inhibitory states. In the light of the Ca^{2+}-relay model formerly implemented [23], we can now propose a mechanistic explanation of the changes to the Ca^{2+}-dependent regulation of GC activity in the presence of GCAP1 mutants, which would block the cyclase in a constitutively active state, and the co-presence of wild-type GCAP2. Under the conditions where one of the two GCAP regulators are blocked into a state where the switch cannot occur, the lack of its regulatory capability can be partially compensated by the activity of the other GCAP that, with its different Ca^{2+} sensitivity, is expected to slightly perturb the dynamics of cGMP synthesis with respect to the case in which both GCAPs are fully active in normal conditions. In the conditions simulated here, as well as in the results reported on Y99C transgenic mice [17], both the presence of significant amount of normal GCAP1 and GCAP2 could compensate for the lack of GC regulation by mutated GCAP1 already at dimmer light intensities, thus contributing to the kinetics of cGMP synthesis at times (and Ca^{2+} levels) normally regulated mostly by normal GCAP1, in line with the need for a system that makes gradual responses to small changes

in Ca^{2+}, that is the Ca^{2+}-relay model. In cases where wild-type GCAP1 were totally absent and the cone dystrophy-related variants were solely expressed, the compensatory effect of GCAP2 would be even stronger (Figure S2 in Online Resource). The mechanism could hence partly explain the significant differences observed in autosomal dominant and hypothetical recessive forms of disease. This postulated mechanism of needed compensation would also explain why in GCAP2 knockout mice [29] the perturbation to the photoresponse kinetics were quantitatively very similar to those observed for Y99C-GCAP1 mice and in the present work.

In conclusion, our data suggest that the simultaneous presence of GCAP1 and GCAP2, acting in a synergic manner in vivo, produces a different regulation of the cyclase than each type alone, and in cases where a GCAP has been genetically altered, a compensatory effect may occur during the dynamics of the photoresponse that results in a less dramatic alteration of the photoresponses than what is expected by in vitro assays. However, even small alterations of the Ca^{2+} and cGMP homeostasis in resting conditions might be well sufficient to trigger the degenerative process in photoreceptors, thus being ultimately responsible for the onset of the disease.

Acknowledgments This work was supported by the Deutsche Forschungsgemeinschaft (DFG) to K-WK (KO 948/10-1) and by funds from the Italian Ministry for Research and Education via departmental funds (FUR2012) to DDO.

References

1. Pugh EN Jr, Lamb TD (2000) Phototransduction in vertebrate rods and cones: molecular mechanisms of amplification, recovery and light adaptation. In: Stavenga DG, DeGrip WJ, Pugh EN Jr (eds) Handbook of biological physics, vol 3. Elsevier Science BV, Amsterdam, pp 183–255
2. Korenbrot JI (2012) Speed, sensitivity, and stability of the light response in rod and cone photoreceptors: facts and models. Prog Retin Eye Res 31:442–466
3. Koch KW, Duda T, Sharma RK (2010) Ca^{2+}-modulated vision-linked ROS-GC guanylate cyclase transduction machinery. Mol Cell Biochem 334:105–115
4. Dizhoor AM, Olshevskaya EV, Peshenko IV (2010) Mg^{2+}/Ca^{2+} cation binding cycle of guanylyl cyclase activating proteins (GCAPs): role in regulation of photoreceptor guanylyl cyclase. Mol Cell Biochem 334:117–124
5. Senin II, Koch KW, Akhtar M, Philippov PP (2002) Ca^{2+}-dependent control of rhodopsin phosphorylation: recoverin and rhodopsin kinase. Adv Exp Med Biol 514:69–99
6. Kitiratschky VB, Wilke R, Renner AB, Kellner U, Vadalà M, Birch DG, Wissinger B, Zrenner E, Kohl S (2008) Mutation analysis identifies GUCY2D as the major gene responsible for autosomal dominant progressive cone degeneration. Invest Ophthalmol Vis Sci 49:5015–5023
7. Behnen P, Dell'Orco D, Koch KW (2010) Involvement of the calcium sensor GCAP1 in hereditary cone dystrophies. Biol Chem 391:631–637
8. Hwang JY, Lange C, Helten A, Höppner-Heitmann D, Duda T, Sharma RK, Koch KW (2003) Regulatory modes of rod outer segment membrane guanylate cyclase differ in catalytic efficiency and Ca^{2+}-sensitivity. Eur J Biochem 270:3814–3821
9. Scholten A, Koch KW (2011) Differential calcium signaling by cone-specific guanylate cyclase-activating proteins from the zebrafish retina. PLoS One 6:e23117
10. Mendez A, Burns ME, Sokal I, Dizhoor AM, Baehr W, Palczewski K, Baylor DA, Chen J (2001) Role of guanylate cyclase-activating proteins (GCAPs) in setting the flash sensitivity of rod photoreceptors. Proc Natl Acad Sci USA 98:9948–9953
11. Makino CL, Wen XH, Olshevskaya EV, Peshenko IV, Savchenko AB, Dizhoor AM (2012) Enzymatic relay mechanism stimulates cyclic GMP synthesis in rod photoresponse: biochemical and physiological study in guanylyl cyclase activating protein 1 knockout mice. PLoS One 7:e47637
12. Dizhoor AM, Boikov SG, Olshevskaya EV (1998) Constitutive activation of photoreceptor guanylate cyclase by Y99C mutant of GCAP-1. Possible role in causing human autosomal dominant cone degeneration. J Biol Chem 273:17311–17314
13. Sokal I, Li N, Surgucheva I, Warren MJ, Payne AM, Bhattacharya SS, Baehr W, Palczewski K (1998) GCAP1 (Y99C) mutant is constitutively active in autosomal dominant cone dystrophy. Mol Cell 2:129–133
14. Sokal I, Dupps WJ, Grassi MA, Brown J Jr, Affatigato LM, Roychowdhury N, Yang L, Filipek S, Palczewski K, Stone EM, Baehr W (2005) A novel GCAP1 missense mutation (L151F) in a large family with autosomal dominant cone-rod dystrophy (adCORD). Invest Ophthalmol Vis Sci 46:1124–1132
15. Kitiratschky VBD, Behnen P, Kellner U, Heckenlively JR, Zrenner E, Jägle H, Kohl S, Wissinger B, Koch KW (2009) Mutations in the GUCA1A gene involved in hereditary cone dystrophies impair calcium-mediated regulation of guanylate cyclase. Hum Mutat 30:E782–E796
16. Dell'Orco D, Behnen P, Linse S, Koch KW (2010) Calcium binding, structural stability and guanylate cyclase activation in GCAP1 variants associated with human cone dystrophy. Cell Mol Life Sci 67:973–984
17. Olshevskaya EV, Calvert PD, Woodruff ML, Savchenko AB, Makino CL, Ho YS, Fain GL, Dizhoor AM (2004) The Y99C mutation in guanylyl cyclase-activating protein 1 increases intracellular Ca^{2+} and causes photoreceptor degeneration in transgenic mice. J Neurosci 24:6078–6085
18. Olshevskaya EV, Peshenko IV, Savchenko AB, Dizhoor AM (2012) Retinal guanylyl cyclase isozyme 1 is the preferential in vivo target for constitutively active GCAP1 mutants causing congenital degeneration of photoreceptors. J Neurosci 32:7208–7217
19. Hamer RD, Nicholas SC, Tranchina D, Lamb TD, Jarvinen JLP (2005) Toward a unified model of vertebrate rod phototransduction. Vis Neurosci 22:417–436
20. Dell'Orco D, Schmidt H, Mariani S, Fanelli F (2009) Network-level analysis of light adaptation in rod cells under normal and altered conditions. Mol BioSyst 5:1232–1246
21. Dell'Orco D, Koch KW (2011) A dynamic scaffolding mechanism for rhodopsin and transducin interaction in vertebrate vision. Biochem J 440:263–271
22. Invergo BM, Montanucci L, Koch KW, Bertranpetit J, Dell'Orco D (2013) Exploring the rate-limiting steps in visual phototransduction recovery by bottom-up kinetic modeling. Cell Commun Signal 11:36
23. Koch KW, Dell'Orco D (2013) A calcium-relay mechanism in vertebrate phototransduction. ACS Chem Neurosci 4:909–917
24. Koch KW, Helten A (2008) Guanylate cyclase-based signaling in photoreceptors and retina. In: Fliesler SJ, Kisselev OG (eds) Signal transduction in the retina, chapter 6. Taylor and Francis/CRC Press, London, pp 121–143

25. Bradford M (1976) A rapid and sensitive method for the quantitation of microgram quantities of protein utilizing the principle of protein-dye binding. Anal Biochem 73:248–254
26. Behnen P (2010) Funktionelle Charakterisierung von GCAP1-Mutanten als Ursache erblicher Zapfen-Dystrophien. PhD Thesis. University of Oldenburg, Oldenburg, Germany
27. Hindmarsh A, Brown P, Grant K (2005) SUNDIALS: Suite of nonlinear and differential/algebraic equation solvers. ACM Trans Math Softw 31:363–396
28. Peshenko IV, Olshevskaya EV, Savchenko AB, Karan S, Palczewski K, Baehr W, Dizhoor W (2011) Enzymatic properties and regulation of the native isozymes of retinal membrane guanylyl cyclase (RetGC) from mouse photoreceptors. Biochemistry 50:5590–5600
29. Makino CL, Peshenko IV, Wen XH, Olshevskaya EV, Barrett R, Dizhoor AM (2008) A role for GCAP2 in regulating the photoresponse. Guanylyl cyclase activation and rod electrophysiology in GUCA1B knock-out mice. J Biol Chem 283:29135–29143
30. Peshenko IV, Olshevskaya E, Dizhoor AM (2008) Binding of guanylyl cyclase activating protein 1 (GCAP1) to retinal guanylyl cyclase (RetGC1). J Biol Chem 283:21747–21757
31. Lim S, Peshenko I, Dizhoor A, Ames JB (2009) Effects of Ca^{2+}, Mg^{2+}, and myristoylation on guanylyl cyclase activating protein 1 structure and stability. Biochemistry 48:850–862

OXFORD

Human Molecular Genetics, 2015, Vol. 24, No. 23 6653–6666

doi: 10.1093/hmg/ddv370
Advance Access Publication Date: 10 September 2015
Original Article

ORIGINAL ARTICLE

Two retinal dystrophy-associated missense mutations in *GUCA1A* with distinct molecular properties result in a similar aberrant regulation of the retinal guanylate cyclase

Valerio Marino[1], Alexander Scholten[3], Karl-Wilhelm Koch[3] and Daniele Dell'Orco[1,2,*]

[1]Department of Neurological, Biomedical and Movement Sciences, Section of Biological Chemistry, [2]Centre for BioMedical Computing (CBMC), University of Verona, 37134 Verona, Italy and [3]Department of Neurosciences, Biochemistry Group, University of Oldenburg, 26111 Oldenburg, Germany

*To whom correspondence should be addressed at: Department of Neurological, Biomedical and Movement Sciences, Section of Biological Chemistry, University of Verona, strada le Grazie 8, 37134, Verona, Italy. Tel: +39 045 802 7637; Fax: +39 045 802 7170; Email: daniele.dellorco@univr.it

Abstract

Two recently identified missense mutations (p. L84F and p. I107T) in *GUCA1A*, the gene coding for guanylate cyclase (GC)-activating protein 1 (GCAP1), lead to a phenotype ascribable to cone, cone-rod and macular dystrophies. Here, we present a thorough biochemical and biophysical characterization of the mutant proteins and their distinct molecular features. I107T-GCAP1 has nearly wild-type-like protein secondary and tertiary structures, and binds Ca^{2+} with a >10-fold lower affinity than the wild-type. On the contrary, L84F-GCAP1 displays altered tertiary structure in both GC-activating and inhibiting states, and a wild type-like apparent affinity for Ca^{2+}. The latter mutant also shows a significantly high affinity for Mg^{2+}, which might be important for stabilizing the GC-activating state and inducing a cooperative mechanism for the binding of Ca^{2+}, so far not been observed in other GCAP1 variants. Moreover, the thermal stability of L84F-GCAP1 is particularly high in the Ca^{2+}-bound, GC-inhibiting state. Molecular dynamics simulations suggest that such enhanced stability arises from a deeper burial of the myristoyl moiety within the EF1–EF2 domain. The simulations also support an allosteric mechanism connecting the myristoyl moiety to the highest-affinity Ca^{2+} binding site EF3. In spite of their remarkably distinct molecular features, both mutants cause constitutive activation of the target GC at physiological Ca^{2+}. We conclude that the similar aberrant regulation of the target enzyme results from a similar perturbation of the GCAP1–GC interaction, which may eventually cause dysregulation of both Ca^{2+} and cyclic GMP homeostasis and result in retinal degeneration.

Introduction

Autosomal-dominant cone (COD) and cone-rod (CORD) dystrophies constitute particularly severe forms of inherited visual diseases. The usually rapid clinical course leads to an initial decrease in visual acuity, abnormal color vision, photophobia and decreased sensitivity in the central visual field, later followed by progressive loss in peripheral vision and night blindness (1,2).

Most inherited retinal dystrophies are very often caused by an imbalance of the homeostasis of the second messengers operating in rod and cone photoreceptor cells, namely Ca^{2+} and cyclic GMP (cGMP). These important molecules control the kinetics of photoreceptor light response and play a crucial role in light adaptation (3,4). Indeed, photoactivation of the visual pigment in photoreceptors leads to the light-induced hydrolysis of cGMP,

Received: July 16, 2015. **Revised:** August 18, 2015. **Accepted:** September 4, 2015

thereby causing the closure of cyclic nucleotide-gated channels; these block the influx of cations including Ca^{2+}, and cause the hyperpolarization of the cell membrane. A second consequence of illumination is a decrease in intracellular Ca^{2+} due to the continuous extrusion of the cation via a Na^{+}/Ca^{2+}, K^{+}-exchanger.

Among other Ca^{2+}-sensor proteins, guanylate cyclase-activating proteins (GCAPs) detect changes in Ca^{2+} concentration and respond by adopting conformations that control the activity of their target protein, the membrane-bound guanylate cyclases (GC). At high [Ca^{2+}], GCAPs inhibit the GC activity, thus ensuring basal levels of cGMP; at low [Ca^{2+}], after light activation of the phototransduction cascade, they switch to a GC-activating state, which triggers the synthesis of cGMP and rapidly restores dark-adapted conditions (5,6). As a result of the delicate interplay between Ca^{2+} and cGMP homeostasis, the concentration of Ca^{2+} during the phototransduction cascade is strictly controlled, and ranges between several hundred nanomolar Ca^{2+} in the dark down to below 100 nM in the light (3,4).

GCAPs are sensor proteins able to bind up to three divalent metal ions in their EF-hand motifs, namely EF2, EF3 and EF4. They have been proven to be both Ca^{2+} and Mg^{2+} sensors, and the Mg^{2+}-bound form is implied in GC activation, while the Ca^{2+}-saturated form is necessary to fully inhibit the GC (5–9). The presence of various isoforms of GCAPs in photoreceptor cell types seems to be justified by the fact that GCAPs can respond to incremental changes in [Ca^{2+}] and work in a relay mode fashion (10–14).

To date, up to 12 missense mutations have been identified in *GUCA1A*, the gene coding GCAP1, in patients suffering from retinal disease, including COD, CORD and macular dystrophy (MACD) (15,16). Biochemical investigations revealed that most of such GCAP1 mutations exhibit a more or less severe disturbance in their Ca^{2+}-sensing properties, specifically, they maintain the GC constitutively active over the physiological range of [Ca^{2+}], in which they normally switch between activating and inhibiting regulatory modes (17–21). The final trigger of photoreceptor degeneration remains still unclear, although experiments performed on transgenic mice suggest apoptosis as a possible mechanism (22,23).

Among retinal dystrophy-related mutations in *GUCA1A*, two (c.250C>T and c.320T>C) were very recently discovered in unrelated Spanish families affected by autosomal-dominant retinal degeneration (16). The clinical phenotype was typically broad, showing features of COD, CORD and MACD (16). The missense mutations lead to amino acid substitutions that significantly modify the physico-chemical nature of the side chain, with possible consequent perturbation of the protein structure/function relationship. Indeed, the c.250C>T mutation leads to the Leu 84 to Phe substitution (L84F-GCAP1), while c.320T>C leads to Ile 107 to Thr substitution (I107T-GCAP1), in the expressed protein. The affected amino acid positions are in close vicinity at the level of the primary structure, but are located in significantly remote regions of the GCAP1 tertiary structure (Fig. 1A). L84 is located in the EF1–EF2 domain, at the end of the exiting helix (αF2) of the EF2 motif. The region includes several important hydrophobic residues that interact with the myristoyl moiety post-translationally bound at the N-terminal (Fig. 1B), and the neighbor residue K85 has been shown to be significantly involved in the binding interface with the GC (24,25). On the other hand, I107 is located in the EF3 Ca^{2+} binding loop, although the residue is not involved in direct Ca^{2+}-coordination. The EF3–EF4 domain has been defined a 'hot spot' for retinal dystrophies (15), in that many of the disease-associated mutations in *GUCA1A* codify for residues located in this structural region (Fig. 1A, blue sticks).

The particularly broad phenotypical variety of these two newly identified *GUCA1A* mutants includes MACD, which has so far only been associated with the Y99C (26,27) and P50L (28) substitutions. We therefore asked, whether L84F and I107T-GCAP1 share common molecular features with other retinal dystrophy variants of GCAP1, or rather exhibit novel properties. We performed a thorough biochemical and biophysical investigation of the two mutants and found that, surprisingly, very different molecular properties shown by the two mutants may result in a similarly aberrant regulation of the target enzyme.

Results

Ca^{2+}- and Mg^{2+}-dependent structural changes and protein thermal stability in I107T and L84F-GCAP1 monitored by circular dichroism spectroscopy

Circular dichroism (CD) spectroscopy was used to assess the potential effects of the point mutations on both the secondary and tertiary structure of I107T and L84F-GCAP1, in their GC-activating

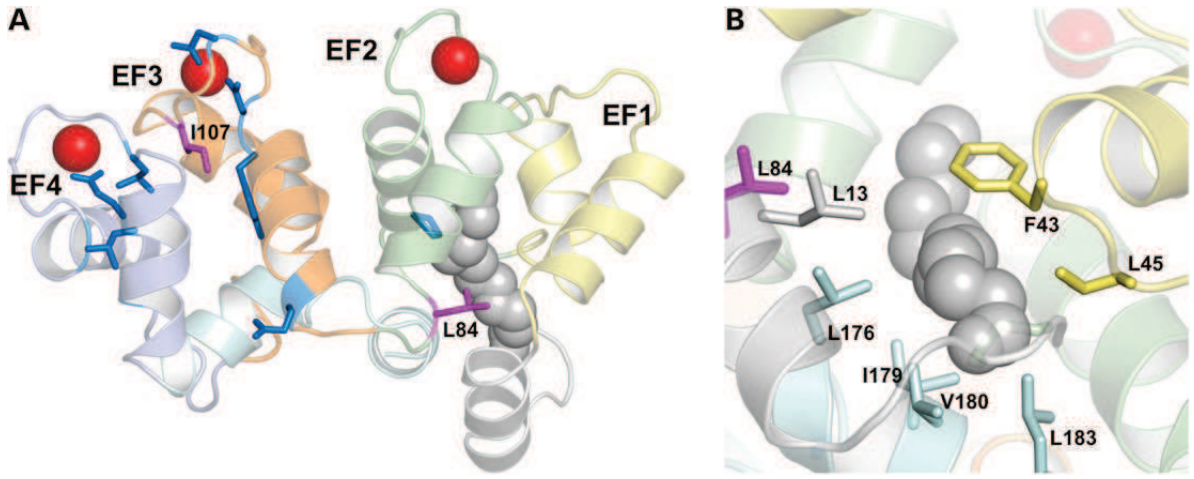

Figure 1. Three-dimensional homology model of human GCAP1. (**A**) Cartoon representation of the GCAP1 overall fold. EF1 is colored in yellow, EF2 in green, EF3 in orange and EF4 in light blue. N- and C-terminals are colored in pale grey and pale cyan, respectively, and the myristoyl group is represented by grey spheres. Calcium ions are represented by red spheres, while residue targets of cone dystrophy-associated mutations are shown by dark blue sticks. L84 and I107 are represented by magenta sticks. (**B**) Details of the region surrounding the myristoyl group. Hydrophobic residues showing persistent interactions with the myristoyl moiety are represented as sticks and labeled.

and inhibiting states, corresponding to the Mg^{2+}-bound and Ca^{2+}-bound conformations, respectively.

The apo form (EGTA) of I107T-GCAP1 (Fig. 2, upper left) showed a near-UV CD spectrum similar to that of the wild-type (7), though with a more pronounced negative dichroic band in the Tyr-Trp region. The addition of Mg^{2+} lowered the intensity of the spectrum and led to regions of positive dichroism (Fig. 2, upper left). Following saturation with Ca^{2+}, the spectrum yielded a typical shape already observed for wild-type GCAP1 (7) and for other COD-related mutants (29), with a mutant-specific variation in the amplitude of the positive Tyr band.

The binding of Ca^{2+} to apo I107T-GCAP1 caused significant variations in its tertiary structure, while the following addition of Mg^{2+} did not significantly perturb the near UV CD spectra (Fig. 2, upper right), substantially in line with what was observed for wild-type GCAP1 (7). The far UV CD spectra of I107T-GCAP1 (see Supplementary Material, Fig. S1, upper panels) showed the typical all α-helix pattern, with a dampening of the signal of the Mg^{2+}-bound form compared with the apo form, but no other alteration of the spectral shape as confirmed by the identical ratio between the ellipticity values at 208 and 222 nm ($\Theta_{222}/\Theta_{208} = 0.89$; Table 1). A major increase in the signal after addition of Ca^{2+} (see Supplementary Material, Fig. S1, upper left) and an increase in $\Theta_{222}/\Theta_{208}$ (0.91) was observed, indicative of changes in secondary structure and/or protein compactness (17). Ca^{2+}-bound I107T showed an increase in both the signal intensity (see Supplementary Material, Fig. S1, upper right) and in the $\Theta_{222}/\Theta_{208}$ ratio (0.91; Table 1) compared with the apo form, with no significant differences upon Mg^{2+} addition.

Interestingly, a significantly different tertiary structure was observed for L84F-GCAP1 already in the apo form (Fig. 2, lower left). Peculiar features were the positive dichroism in all the spectral regions and the onset of a maximum in the Phe band, at 255 nm, which was previously observed only in ion-bound

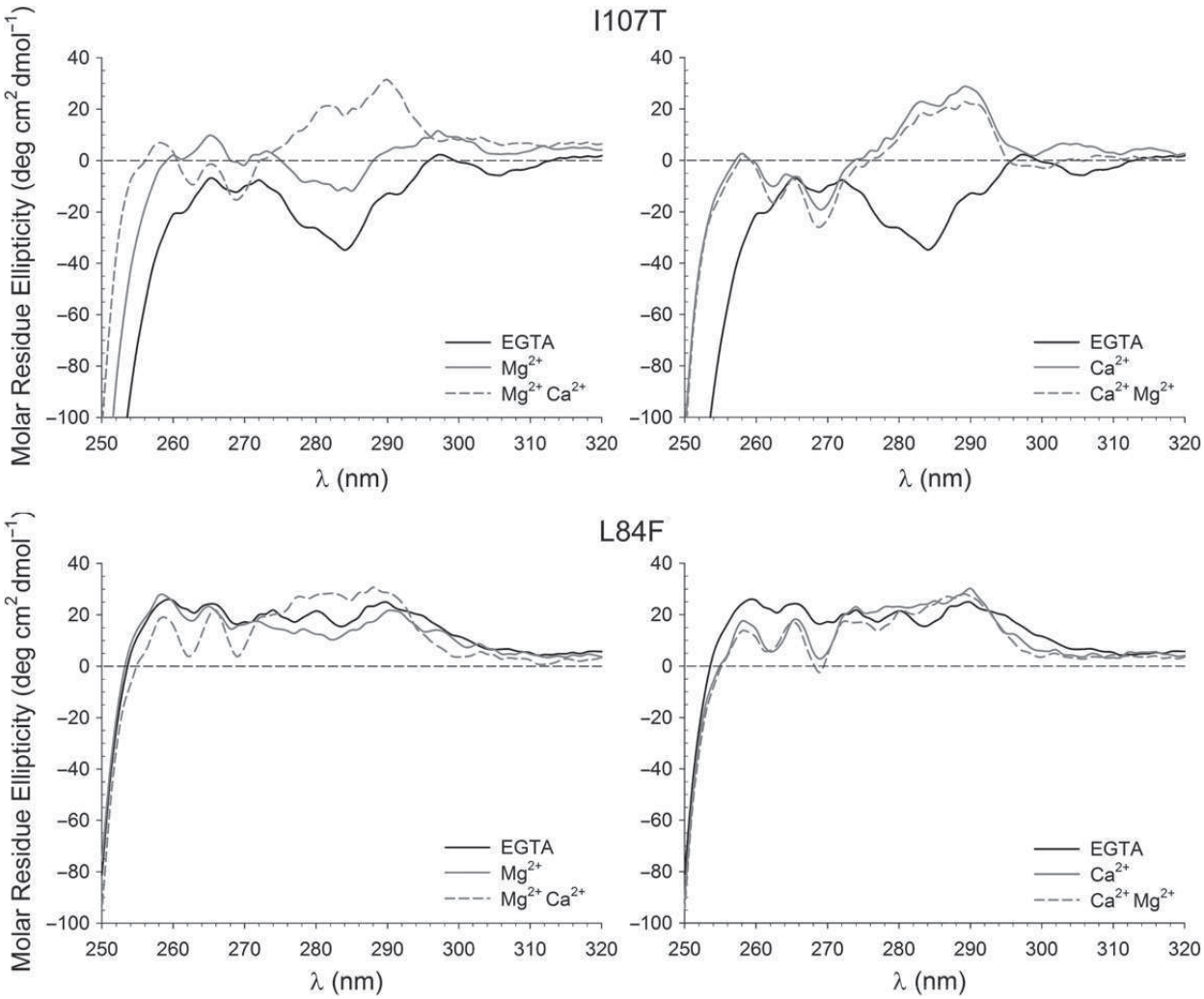

Figure 2. Structural changes occurring in I107T and L84F GCAP1 upon binding of Ca^{2+} and Mg^{2+} monitored by CD spectroscopy. Near UV spectra were recorded at $T = 37°C$ in 5 mM Tris–HCl pH 7.5, 150 mM KCl, 2 mM DTT buffer. Upper panel, left: 25.3 μM I107T-GCAP1 in the presence of 400 μM EGTA (black, solid line), 1 mM Mg^{2+} (gray, solid line) and after addition of 400 μM free Ca^{2+} (gray, dashed line); right: in the presence of 400 μM EGTA (black, solid line), 400 μM free Ca^{2+} (gray, solid line) and after addition of 1 mM Mg^{2+} (gray, dashed line). Lower panel, left: 26 μM L84F-GCAP1 in the presence of 400 μM EGTA (black, solid line), 1 mM Mg^{2+} (gray, solid line) and after addition of 400 μM free Ca^{2+} (gray, dashed line); right: in the presence of 400 μM EGTA (black, solid line), 400 μM free Ca^{2+} (gray, solid line) and after addition of 1 mM Mg^{2+} (gray, dashed line).

Table 1. Results from far UV CD spectroscopy, thermal denaturation and fluorescence spectroscopy

	$\Theta_{222}/\Theta_{208}$[a]	T_m[b] (°C)	λ_{max} fluo[c] (nm)
I107T			
EGTA	0.89	42.0–91.5	341
Mg^{2+}	0.89	43.4–91.8	341
Mg^{2+} Ca^{2+d}	0.91	79.3	344
Ca^{2+}	0.91	80.2	—
Ca^{2+} Mg^{2+d}	0.91	—	—
L84F			
EGTA	0.90	38.2 to >96	341
Mg^{2+}	0.94	42.2 to >96	341
Mg^{2+} Ca^{2+}	0.94	91.9	342
Ca^{2+}	0.92	92.6	—
Ca^{2+} Mg^{2+}	0.92	—	—

[a]Ratio between ellipticity signal at $\lambda = 222$ and $\lambda = 208$ nm.
[b]Melting temperature obtained by fitting the experimental curve to a four-parameter Hill sigmoid.
[c]Wavelength of maximal fluorescence emission upon excitation at $\lambda = 290$ nm.
[d]Lines labeled 'Mg^{2+} Ca^{2+}' refer to experiments where Ca^{2+} was added after saturating Mg^{2+}, whereas cations were added in the opposite order in the 'Ca^{2+} Mg^{2+}' cases.

wild-type GCAP1 (7). Mg^{2+}-binding caused a small but significant conformational change in the Tyr band, and further addition of Ca^{2+} changed the shape of the spectrum, particularly in the Phe and Tyr bands (Fig. 2, lower left). The same kind of changes were observed in Ca^{2+}-bound L84F-GCAP1 (Fig. 2, lower right) compared with the apo form, and the addition of Mg^{2+} after Ca^{2+} did not significantly alter the aromatic amino acid microenvironment. As for the far UV spectra, Mg^{2+}-binding slightly lowered the signal at 208 nm, as shown by the increase in $\Theta_{222}/\Theta_{208}$ from 0.90 to 0.94 (see Supplementary Material, Fig. S1, lower left; Table 1), while addition of Ca^{2+} increased the signal without altering the shape of the spectrum (Table 1). Ca^{2+}-binding to the apo protein caused instead an increase in both the intensity and the $\Theta_{222}/\Theta_{208}$ ratio to 0.92 (Table 1), while the addition of Mg^{2+} resulted only in a small dampening of the signal (see Supplementary Material, Fig. S1, lower right).

By taking advantage of the typical all-α architecture of both GCAP1 variants, demonstrated by the far UV CD spectra in all tested conditions, their thermal stability could be conveniently monitored by following the ellipticity signal at 208 nm. Differently from what observed for other COD/CORD-associated variants (17), apo I107T-GCAP1 showed a three-phase thermal denaturation profile (Fig. 3A) with two apparent transitions at 42.0 and 91.5°C (Table 1). The binding of Mg^{2+} had a very mild effect on the two transition temperatures (43.4 and 91.8°C, respectively) while keeping the same unfolding pattern as the apo form. This behavior also differs from wild-type GCAP1, which showed a typical two-phase transition pattern both in the apo and in the Mg^{2+}-bound forms, with melting temperatures of 50.1 and 51.5°C, respectively (7). Surprisingly, I107T-GCAP1 showed a higher thermal stability in the presence of Ca^{2+} compared with the wild-type (7) both in the absence (80.2 versus >70°C) and in the presence (79.3 versus >70°C) of Mg^{2+}, which slightly lowered the T_m (79.3 versus 80.2°C).

Thermal denaturation profiles for L84F-GCAP1 also showed the same three-phase transitions for apo and Mg^{2+}-bound forms (Fig. 3B), with a clear transition at 38.2 and 42.2°C (Table 1), respectively, and an only partly visible transition at >96°C. Ca^{2+} binding greatly increased the stability of L84F-GCAP1 both in the absence (92.6°C) and in the presence of Mg^{2+} (91.9°C).

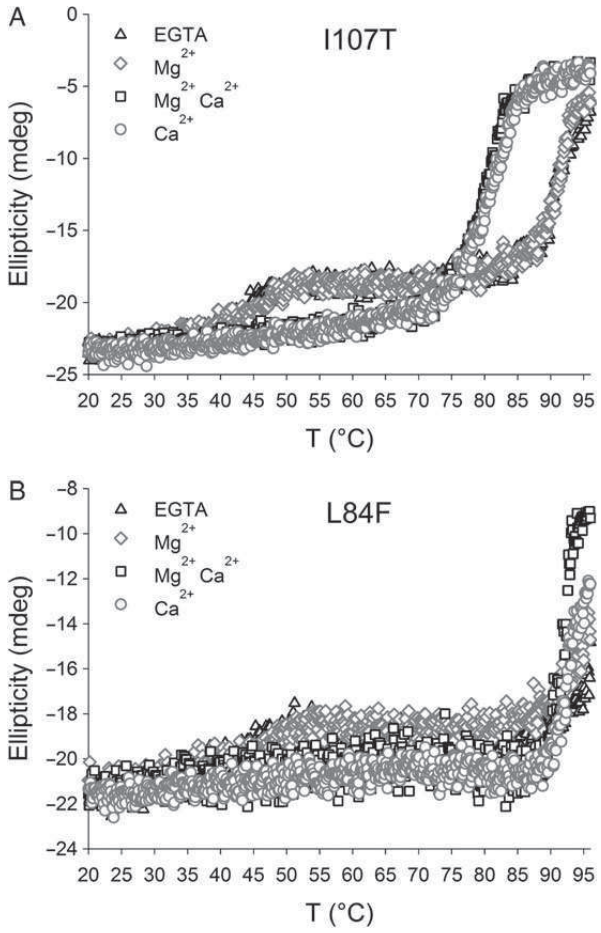

Figure 3. Thermal denaturation profiles of I107T and L84F GCAP1 mutants in the presence and in the absence of Ca^{2+} and Mg^{2+}. (**A**) Thermal denaturation profile of ~6 μM I107T-GCAP1 in the presence of 200 μM EGTA (black triangles), 1 mM Mg^{2+} (gray diamonds), 200 μM Ca^{2+} and 1 mM Mg^{2+} (black squares) and 200 μM Ca^{2+} (gray circles). (**B**) Thermal denaturation profile of ~6 μM L84F-GCAP1 in the presence of 200 μM EGTA (black triangles), 1 mM Mg^{2+} (gray diamonds), 200 μM Ca^{2+} and 1 mM Mg^{2+} (black squares) and 200 μM Ca^{2+} (gray circles). Thermal denaturation was followed by monitoring the ellipticity signal at 208 nm over the 20–96°C temperature range. Quantitative data obtained by fitting the experimental values to a four-parameter Hill sigmoidal function are reported in Table 1.

Intrinsic fluorescence properties of I107T and L84F-GCAP1

The fluorescence properties of the two retinal dystrophy-related GCAP1 mutants were compared with those of the wild-type in conditions mimicking dark-adapted (high [Ca^{2+}]) and illuminated (low [Ca^{2+}]) photoreceptors. Intrinsic fluorescence spectra of wild-type GCAP1 (Fig. 4A) showed a major decrease (~45%) of the intensity upon Mg^{2+} binding to the apo form, together with a small red shift in the wavelength of maximal intensity (342 versus 341 nm). Significant increases in fluorescence and red shift (344 nm) were observed upon saturation with Ca^{2+}. Apo I107-GCAP1 also showed (Fig. 4B) quenching of the intrinsic fluorescence upon Mg^{2+} binding, but to a lesser extent (~10%), without any shift in the maximum (341 nm, Table 1). Major quenching was instead observed upon Ca^{2+} addition (~50% with respect to the apo form), which shifted the maximum of fluorescence toward higher wavelength (344 nm).

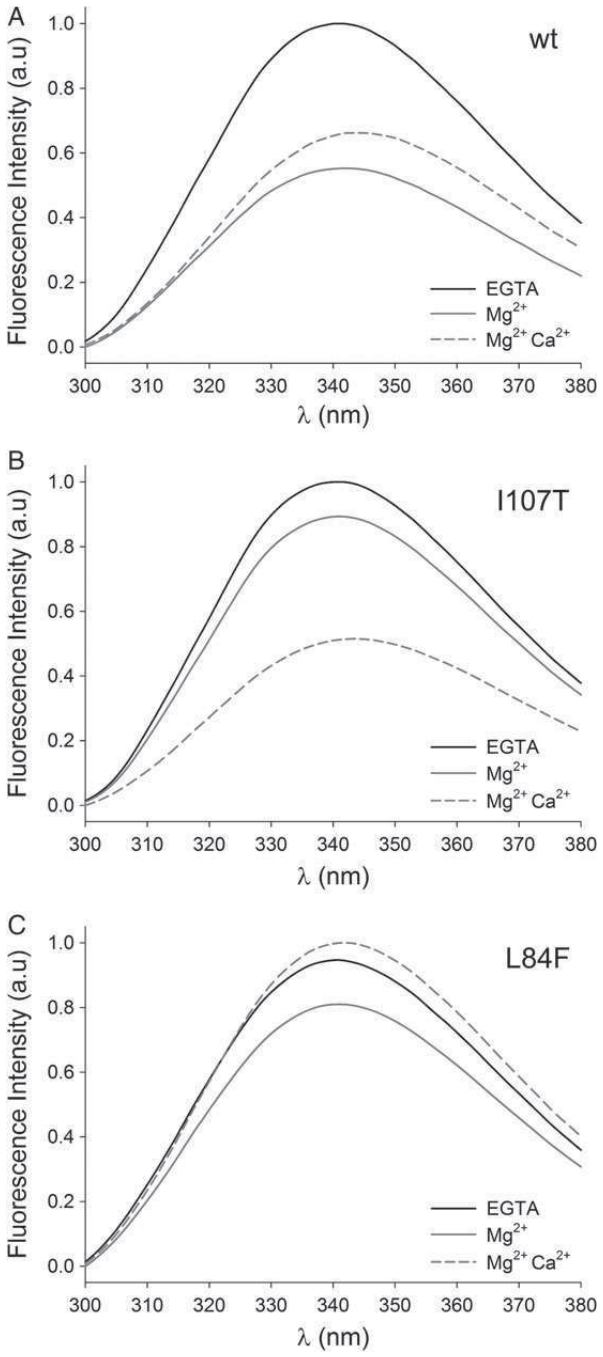

Figure 4. Fluorescence spectra of GCAP1 variants. Fluorescence emission spectra (λ_{ex} = 290 nm) were recorded at T = 25°C in 5 mM Tris–HCl pH 7.5, 150 mM KCl, 1 mM DTT buffer. (**A**) Intrinsic Trp fluorescence emission spectrum of ~8 μM wild-type GCAP1 in the presence of 1 mM EGTA (black, solid line), after addition of 1 mM Mg^{2+} (gray, solid line), after further addition of 1 mM free Ca^{2+} (gray, dashed line). (**B**) Intrinsic Trp fluorescence emission spectrum of ~8 μM I107T-GCAP1 in the presence of 1 mM EGTA (black, solid line), after addition of 1 mM Mg^{2+} (gray, solid line), after further addition of 1 mM free Ca^{2+} (gray, dashed line). (**C**) Intrinsic Trp fluorescence emission spectrum of ~8 μM L84F-GCAP1 in the presence of 1 mM EGTA (black, solid line), after addition of 1 mM Mg^{2+} (gray, solid line), after further addition of 1 mM free Ca^{2+} (gray, dashed line). The wavelengths of maximal emission are reported in Table 1.

L84F-GCAP1 exhibited a small quenching of fluorescence upon Mg^{2+} binding (~10%) (Fig. 4C) with no shift of the maximum (341 nm, Table 1), in a similar fashion to the I107T variant. Interestingly, after Ca^{2+} addition, this mutant showed a smaller red shift with respect to both wild-type and I107T-GCAP1 (342 nm), accompanied by an increase in fluorescence intensity.

Monitoring Ca^{2+} and Mg^{2+} binding to I107T and L84F-GCAP1

To investigate the origin of the distinct fluorescence properties observed for the two GCAP1 mutants in their different regulatory states, we monitored the binding of Ca^{2+} and Mg^{2+} to each variant by two titration experiments. In a first approach, Ca^{2+} titrations were studied by monitoring spectroscopically the competition with the 5,5′Br_2-BAPTA chelator, both in the absence and in the presence of physiological 1 mM Mg^{2+}. The working conditions under which Ca^{2+} titrations were performed ensured robust and reliable determinations in terms of protein stability and Ca^{2+} saturation. Examples of titration curves are reported in Figure 5A and B, and show very different patterns for I107T and L84F-GCAP1. Data could be nicely fitted by a two or three binding sites model and the macroscopic binding constants were hence determined (Table 2). Both variants bound Ca^{2+} with higher affinity with respect to the chelator (Fig. 5A and B) and the presence of Mg^{2+} slightly lowered the apparent affinity (Table 2). In detail, for the I107T-GCAP1 variant, which carries a mutation in the EF3 Ca^{2+} binding motif, only the higher affinity individual macroscopic binding constants K_1 and K_2 were reasonably detectable, being comparable to that of the chelator (log $K_{chelator}$ = 5.6, $K_{Dchelator}$ = 2.3 μM), while K_3 was below the experimental detection limit. Overall, this resulted in an apparent 2.5 μM affinity in the absence of Mg^{2+} and 2.8 μM in the presence of Mg^{2+}, thus more than 10-fold lower than that of the wild-type (31).

Surprisingly, L84F-GCAP1 showed a wild-type-like Ca^{2+} affinity in the absence of Mg^{2+} (K_D^{app} = 0.15 versus 0.16 μM) and an even higher affinity in the presence of 1 mM Mg^{2+} (K_D^{app} = 0.39 versus 0.50 μM). The shape of the titration curve in the presence of Mg^{2+} (Fig. 5B) showed a change in convexity typically observed in protein systems that bind Ca^{2+} with a positive cooperativity mechanism (30,32). Indeed, by assuming that one of the EF-hand binding motifs was occupied by a Mg^{2+} ion, fitting the experimental data to a two-binding site mechanism (Table 2) led to substantially unaltered values for the macroscopic association constants (logK_1 and logK_2) (Table 2), suggesting that the Ca^{2+} affinity for the second binding site increases as a consequence of the binding of a Ca^{2+} ion to the first binding site. It is worthwhile to notice that both wild-type and all other cone-dystrophy-related GCAP1 variants investigated to date with this method showed a sequential Ca^{2+} binding mechanism, without apparent cooperativity (17).

In a different titration experiment, we monitored the intrinsic Trp fluorescence of each variant upon titration with Ca^{2+} and Mg^{2+}. Ca^{2+} fluorescence titration measurements for L84F-GCAP1 (Fig. 5C) showed a wild-type-like biphasic behavior in the physiological range of Ca^{2+} (0.1–0.6 μM) and in the whole tested range, with a minimum around 100 nM, in line with a previous work (8). Moreover, consistent with the fluorescence spectra and at odds with the wild-type, L84F-GCAP1 showed an increase in fluorescence emission intensity in Ca^{2+}-saturating conditions with respect to the apo form. Interestingly, also I107T-GCAP1 showed an overall decrease in fluorescence intensity when switching between apo and Ca^{2+}-saturated forms and a biphasic conformational change, yet limited to the physiological range—a feature shown also by G159V-GCAP1 (19).

Mg^{2+} fluorescence titration for L84F-GCAP1 (Fig. 5D) showed an overall decreasing pattern, in line with fluorescence spectra,

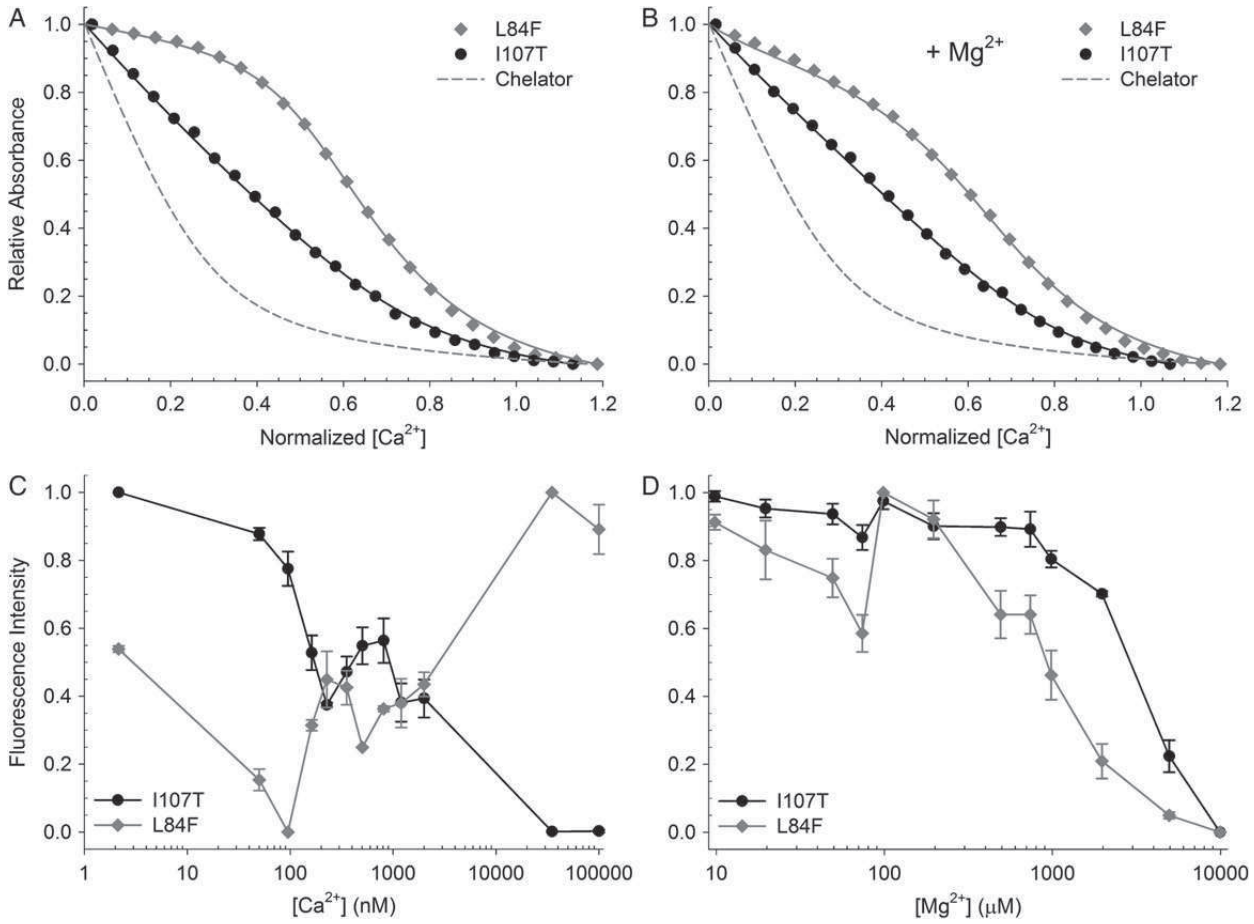

Figure 5. Ca^{2+} and Mg^{2+} titrations of I107T and L84F-GCAP1 mutants obtained by absorption and fluorescence spectroscopies. All experiments were performed at $T = 25°C$ in 5 mM Tris–HCl pH 7.5, 150 mM KCl, 1 mM DTT buffer. (**A**) Ca^{2+} titration curves obtained by absorption spectroscopy in the absence of Mg^{2+}. Experimental points for I107T-GCAP1 (black circles) and for L84F-GCAP1 (gray diamonds) are shown together with the optimal curve by computer fitting (black and gray solid lines, respectively) and the theoretical (simulated) curve for the titration in the sole presence of the chelator (gray dashed line). (**B**) Ca^{2+} titration curves obtained by absorption spectroscopy in the presence of 1 mM Mg^{2+}, experimental points for I107T-GCAP1 (black circles) and for L84F-GCAP1 (gray diamonds) are shown together with the optimal curve by computer fitting (black and gray solid lines, respectively) and the theoretical (simulated) curve for the titration in the sole presence of the chelator (gray dashed line). The curves include dilution effects upon titration. The axes have been normalized as elucidated in the Materials and Methods section. (**C**) Ca^{2+} titration monitored by fluorescence spectroscopy of ~0.7 μM I107T-GCAP1 (black line and circles) and of L84F-GCAP1 (gray line and diamonds) performed in the 2 nM–100 μM range. (**D**) Mg^{2+} titration monitored by fluorescence spectroscopy of ~0.7 μM I107T-GCAP1 (black line and circles) and of L84F-GCAP1 (gray line and diamonds) performed in the 9 μM–10 mM range. Titration experiments were performed by exciting Trp residues ($\lambda_{ex} = 290$ nm) and monitoring the intrinsic Trp fluorescence emission at $\lambda_{em} = 340$ nm. Three to four replicates were accumulated and results are shown as average ± standard deviation.

Table 2. Results of Ca^{2+} binding and guanylate cyclase assay experiments

	log K_1[a]	log K_2[a]	log K_3[a]	K_D^{app} (μM)[b]	IC_{50} (μM)[c]	EC_{50} (nM)[d]	X-fold[e]
Wt	7.1 ± 0.9[f]	6.5 ± 0.8[f]	6.1 ± 0.5[f]	0.16[f]	0.24 ± 0.01	61 ± 32	33x
Wt Mg^{2+}	6.7 ± 0.8[f]	5.9 ± 0.1[f]	6.1 ± 1.0[f]	0.50[f]	—	—	—
I107T	5.82 ± 0.14 (*5.79 ± 0.11*)	5.4 ± 0.3 (*5.4 ± 0.3*)	1.94 ± 1.91	2.5 (*2.6*)	7.5 ± 3.8	39 ± 26	17.5x
I107T Mg^{2+}	5.987 ± 0.002 (*5.98 ± 0.04*)	5.1 ± 0.5 (*5.2 ± 0.4*)	1.5 ± 1.1	2.8 (*2.7*)	—	—	—
L84F	6.98 ± 0.04	6.68 ± 0.14	4.72 ± 0.17	0.15	1.8 ± 0.5	49 ± 17	10.5x
L84F Mg^{2+}	6.24 ± 0.08 (*6.2 ± 0.3*)	6.58 ± 0.03 (*6.5 ± 0.3*)	4.90 ± 0.15	0.39 (*0.43*)	—	—	—

[a]Decimal logarithm of macroscopic binding constants for each Ca^{2+} binding site obtained by fitting experimental data to a model with three (or two, text in *italics*, in paraentheses) binding sites with the software CaLigator (30); errors represent standard deviation of at least three repetitions.
[b]Apparent affinity obtained by averaging the significant macroscopic binding constants, see the Materials and methods section.
[c]IC_{50} is the Ca^{2+} concentration at which the GC activity is half maximal; standard errors estimated from fitting.
[d]EC_{50} is the concentration of GCAP1 at which the GC activity is half maximal; standard errors estimated from fitting.
[e]X-fold activation is expressed as $GC_{max} - GC_{min}$ divided by GC_{min}.
[f]Data from (31).

but also a minimum at around 80 μM, which might possibly imply that a Mg^{2+} ion is bound to the protein with significant affinity in the absence of Ca^{2+}. I107T-GCAP1 exhibited a monophasic decreasing fluorescence behavior, in line with fluorescence spectra. Experimental points could also be fitted to a four-parameter Hill sigmoid, with estimated transition concentrations of 3.6 mM for I107T-GCAP1 and 1.1 mM for L84F-GCAP1.

Structural insights from molecular dynamics simulation

The biophysical data presented above could not completely clarify some important mechanistic aspects as to the specific structural features of I107T and L84F-GCAP1 variants, which confer distinct molecular hallmarks to each mutant. In particular, the following aspects remained somewhat unclear: (i) I107T-GCAP1 may bind only two, and not three, Ca^{2+} ions in physiological conditions corresponding to dark-adapted photoreceptors, i.e. high intracellular Ca^{2+}; (ii) Mg^{2+} could bind to L84F-GCAP1, presumably to EF2 and most likely to EF3 as well, with higher affinity compared with the wild-type. On the other hand, the data collected in this study indicate that the Mg^{2+}-EF2 form of I107T-GCAP1 ($EF2^{Mg2+}$ I107T-GCAP1) corresponding to the GC-activating state, as well as the Ca^{2+}-saturated form of L84F-GCAP1 ($EF2^{Ca2+}$ $EF3^{Ca2+}$ $EF4^{Ca2+}$ L84F-GCAP1), corresponding to its GC-inhibiting state, may indeed be of physiological relevance. We therefore ran 150 ns all-atom molecular dynamics (MD) simulations for each variant only in these latter states, and compared the results with those of the same states for the wild-type, investigated in a previous study (7).

$EF2^{Mg2+}$ I107T-GCAP1 was overall less structurally stable and more flexible than the wild-type, as clearly demonstrated by the higher α-carbon root mean-square deviation (RMSD) plot (see Supplementary Material, Fig. S2A) and root-mean square fluctuation (RMSF) per residue (see Supplementary Material, Fig. S2C). Significantly, higher flexibility was particularly apparent in the 95–105 and 115–135 regions, corresponding to the EF3 entering helix (αE3) and Ca^{2+} binding loop, and the linker region between EF3 and EF4, including portions of αF3 and αE4 (see Supplementary Material, Fig. S2C). On the contrary, the structure of $EF2^{Ca2+}$ $EF3^{Ca2+}$ $EF4^{Ca2+}$ L84F-GCAP1 was significantly more stable (see Supplementary Material, Fig. S2B) and less flexible (see Supplementary Material, Fig. S2D) than that of the wild-type in the same time frame, which is in line with the high thermal stability of this variant.

Interestingly, in the time course of 150 ns, the two GCAP1 mutants also showed distinct dynamical features in the structural region constituting the highest-affinity Ca^{2+} binding site EF3, fundamental for keeping the GC inhibiting state (9,33). Indeed, by monitoring for each mutant and for the wild-type, the RMSD of the EF3 Ca^{2+}-coordinating residues D100, N104 and E111 (see Supplementary Material, Fig. S3A, left panel), we found: (i) a significantly higher flexibility of the three residues for $EF2^{Mg2+}$ I107T-GCAP1 when compared with the $EF2^{Mg2+}$ wild-type (see Supplementary Material, Fig. S3B, left column); (ii) a significantly lower flexibility of the same residues for $EF2^{Ca2+}EF3^{Ca2+}EF4^{Ca2+}$ L84F-GCAP1 with respect to the Ca^{2+}-saturated wild type (see Supplementary Material, Fig. S3B, right column). While such effects were expected for the I107T mutation that is located in EF3, the decrease in flexibility of the Ca^{2+}-saturated L84F mutant came as a surprise and can be interpreted as long-range structural effects originating in EF3.

In order to get some further insight into the high stability of L84F-GCAP1, we analyzed the persistency of hydrophobic interactions with the myristoyl group by computing the percentage of frames along the 150 ns simulation, in which the distance between the centers of mass of hydrophobic residues and the myristoyl group was smaller than 5.5 Å (see Fig. 1B for a snapshot of such hydrophobic residues). Results for $EF2^{Ca2+}EF3^{Ca2+}EF4^{Ca2+}$ L84F-GCAP1 showed a significantly increased persistence of hydrophobic interactions with the myristoyl group (Fig. 6C) compared with the wild-type protein for most of the residues involved, namely L13, F43, L45, L176 and I179. M59 and L183 did not show significant variations and V180 was the only residue with decreased persistence of hydrophobic interactions. The significantly tighter packing of hydrophobic residues around the myristoyl group appears to be of particular importance for the sake of keeping the myristoyl moiety buried within the EF1–EF2 domain (see Supplementary Material, Movies S1 and S2). In particular, the interactions involving F43 (~80% of persistence) and L13 (~28% of persistence) became stronger as the two residues dynamically moved significantly closer to one another compared with the wild-type case (see Supplementary Material, Fig. S3A, right panel, representing the distance between the C_β of the 43 and 84 residues). Overall, this reflects a remarkable decrease in solvent accessible surface for the myristoyl group (Fig. 6D) compared with the wild-type case, along the whole simulated time frame.

At variance with this behavior, in $EF2^{Mg2+}$ I107T-GCAP1 (Fig. 6A), L13, L45, I179, V180 and L183 had considerably less persistent hydrophobic interactions with the myristoyl moiety compared with the wild-type, while F43, M59 and L176 had a more persistent interaction with the acyl group. A more loosely packed myristoyl group with respect to the wild-type case was also shown by a small increase in solvent accessibility (Fig. 6B) and high structural fluctuations (see Supplementary Material, Fig. S2C).

Hydrodynamic properties and oligomeric state of I107T and L84F-GCAP1

Dynamic light scattering (DLS) measurements were performed to assess the hydrodynamic properties of the two GCAP1 variants in their specific GC-activating and inhibiting states. I107T-GCAP1 (see Supplementary Material, Fig. S4A) showed a slight increase in the hydrodynamic diameter upon binding of Mg^{2+} [$d = (7.94 \pm 0.11)$ versus (7.65 ± 0.06) nm, see Supplementary Material, Table S1], while Ca^{2+} binding decreased the diameter to 6.79 ± 0.01 nm. No time-dependent aggregation was observed in all the investigated conditions as shown by the mean count rate stably ranging between 210 and 230 kcps. The reduction in the size of the mutant is in line with the behavior of the wild-type and of other COD-related GCAP1 mutants (34). Size exclusion chromatography (SEC) measurements for the same mutant (see Supplementary Material, Fig. S5) resulted in a hydrodynamic diameter of 6.6 nm for the apo form (see Supplementary Material, Table S1), which decreased to 6.0 nm upon Mg^{2+} binding and underwent a further shrinking upon Ca^{2+} binding to 5.8 nm, with a Ca^{2+}-dependent increase in dimerization from $2 \pm 1\%$ to $13 \pm 2\%$ with respect to the apo form (see Supplementary Material, Table S1).

DLS measurements of L84F-GCAP1 (see Supplementary Material, Fig. S4B) could not provide a definitive estimate for the hydrodynamic size in the absence of Ca^{2+} due to the presence of low-order oligomers, which affect the correlation signal. This GCAP1 variant exhibited, in the apo form, a clear time-dependent aggregation over the course of 350 min (see Supplementary Material, Fig. S4C), with an increasing count rate from 160 to 275 kcps. The aggregation propensity was somewhat impaired by Mg^{2+} binding, with a count rate between 160 and 180, and

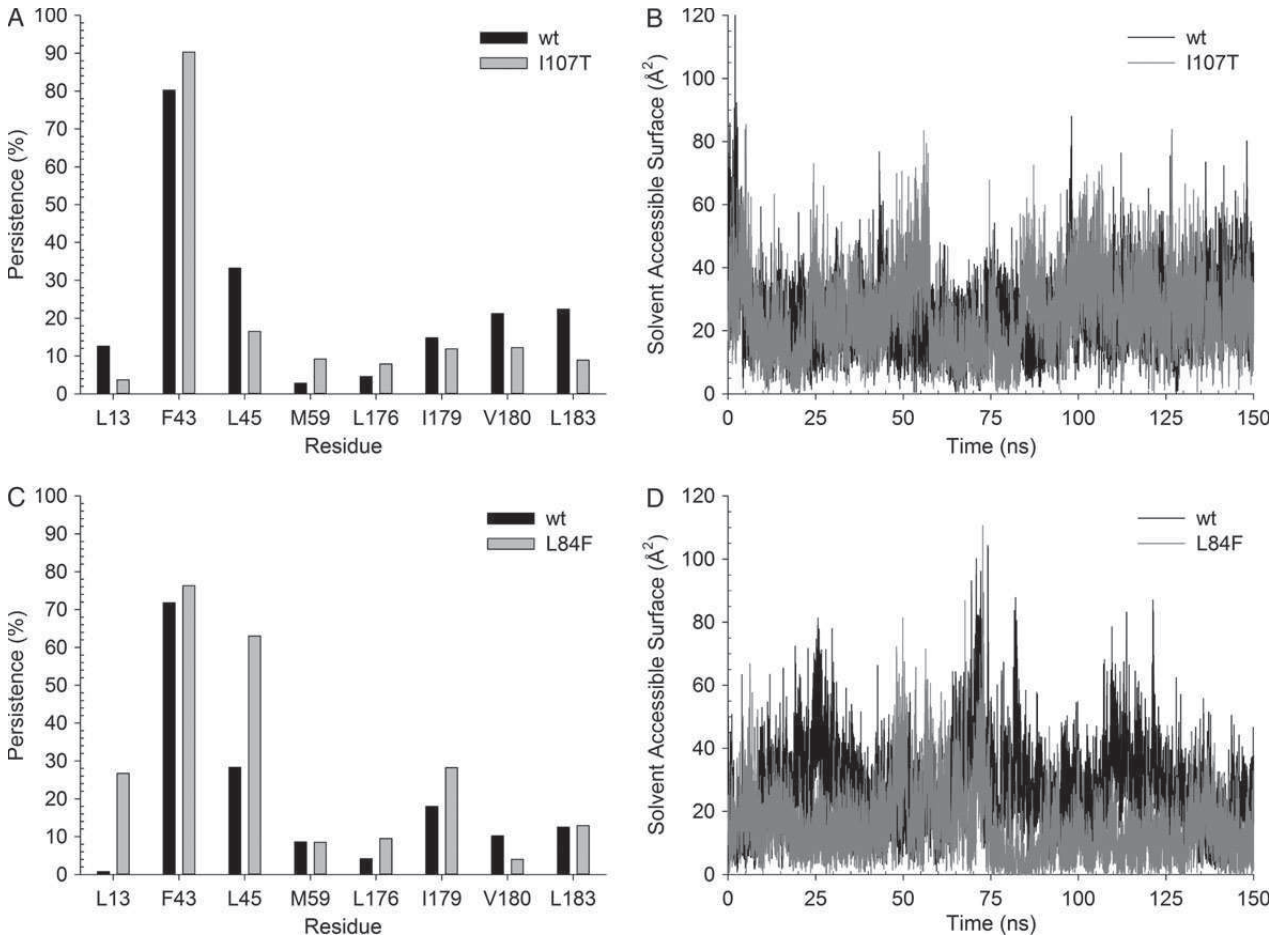

Figure 6. Intramolecular interactions and solvent accessibility of the myristoyl moiety monitored by MD simulations. (**A**) Histograms representing the persistence of intramolecular hydrophobic interactions with the myristoyl group for $EF2^{Mg2+}$ wild-type GCAP1 (black) and $EF2^{Mg2+}$ I107T-GCAP1 (gray) over the 150 ns simulation time frame. (**B**) Time evolution over 150 ns of the SASA for $EF2^{Mg2+}$ wild-type GCAP1 (black) and $EF2^{Mg2+}$ I107T-GCAP1 (gray). (**C**) Histograms representing the persistence of intramolecular hydrophobic interactions with the myristoyl group for $EF2^{Ca2+}EF3^{Ca2+}EF4^{Ca2+}$ wild-type GCAP1 (black) and $EF2^{Ca2+}EF3^{Ca2+}EF4^{Ca2+}$L84F-GCAP1 (gray). (**D**) Time evolution over 150 ns of the SASA for $EF2^{Ca2+}EF3^{Ca2+}EF4^{Ca2+}$ wild-type GCAP1 (black) and $EF2^{Ca2+}EF3^{Ca2+}EF4^{Ca2+}$ L84F-GCAP1 (gray). Persistence has been calculated as the percentage of frames, for which the distance between the center of mass of the myristoyl group and the hydrophobic side chains was lower than 5.5 Å.

even reversed by Ca^{2+} binding, which decreased the count rate from 160–200 to 95–100 kcps. The presence of Ca^{2+} allowed also a more realistic estimation of the L84F-GCAP1 monomer hydrodynamic diameter, which resulted 8.41 ± 0.04 nm when 1 mM Mg^{2+} was already present in solution, or 8.53 ± 0.04 nm when Mg^{2+} was added to Ca^{2+}-bound L84F-GCAP1. SEC measurements showed a different behavior for L84F-GCAP1 (see Supplementary Material, Fig. S5). Indeed, the estimated size for the monomer in the apo form was 6.4 nm (see Supplementary Material, Table S1), which decreased upon Mg^{2+} binding to 5.8 nm but increased again to 6.4 nm upon Ca^{2+} binding. All L84F samples though showed a higher percentage of aggregates (~14–19%) than I107T-GCAP1, and 6–7% dimers in solution, which may explain the partial discrepancy with the DLS determinations. In summary, both DLS and SEC experiments confirmed that in the physiologically relevant states (Mg^{2+}-bound and Ca^{2+}-bound), both mutants are essentially monomers.

Regulation of the guanylate cyclase activity by I107T and L84F-GCAP1

GCAP1 is the physiological Ca^{2+}-sensor regulating GC activity in mammalian rod and cone cells. Its regulating properties are characterized by two values: the EC_{50} is the concentration of GCAP1 at which the activation of the target GC is half-maximal; the IC_{50}-value is the free Ca^{2+}-concentration at which the GC activity is half-maximal in the presence of saturating GCAP1 concentration. We determined these values for the GCAP1 variants that were investigated in this study. The EC_{50}-values did not differ significantly among all tested GCAPs revealing 49 ± 17 nM for L84F, 39 ± 26 nM for I107T and 61 ± 32 nM for wild type (Fig. 7B and Table 2). These parameters indicate that the apparent affinity of GCAP1 for the target GC was not disturbed or changed by the point mutations. However, large differences were found for the IC_{50}-values (Fig. 7A; Table 2): while the wild-type activated GC with an IC_{50} of 0.24 μM (X-fold activation was 33-fold), activation by the mutants was shifted to higher free Ca^{2+} (IC_{50} = 1.8 μM for L84F and IC_{50} = 7.5 μM for I107T, Table 2). The X-fold activation was also lower, reaching only 10.5-fold for L84F and 17.5-fold for I107T.

Discussion

The analysis of biochemical and biophysical properties of COD- and CORD-related GCAP1 mutants previously performed by

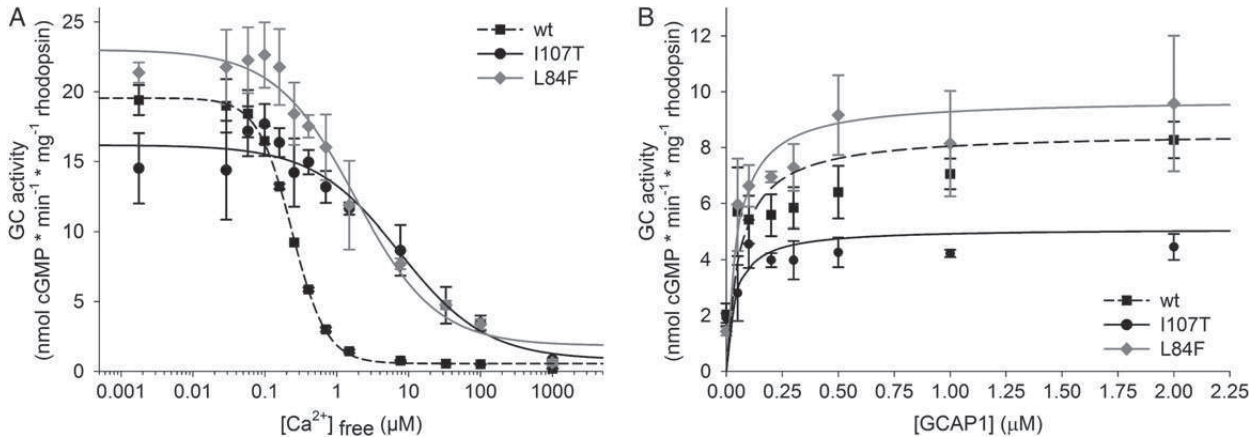

Figure 7. Photoreceptor guanylate cyclase 1 (ROS-GC1) regulation by wild-type and mutant GCAP1. (**A**) Washed bovine photoreceptor membranes containing ROS-GC1 were reconstituted with 5 μM GCAP1 wild-type or mutants between 0.0017 and 1000 μM free Ca^{2+}. Activation was half maximal (IC_{50}) at 0.24 μM (wt), 1.8 μM (L84F) or 7.5 μM (I107T) free Ca^{2+}. (**B**) ROS-GC1 activity as a function of the GCAP1 concentration at 0.0017 μM free Ca^{2+}. Activation was half maximal (EC_{50}) at 61 nM (wt), 49 nM (L84F) or 39 nM (I107T). In both cases, ROS-GC1 activity was estimated at 30°C in nmol cGMP min^{-1} mg^{-1} rhodopsin from the data obtained from at least three independent experiments. Error bars indicate the standard deviation.

some of us (17,19,29) highlighted common hallmarks, which allowed a clear distinction between the wild-type and the pathologic variants. These include minor structural changes (17,29), a generally lower thermal stability (17), significantly reduced affinity for Ca^{2+} (17,29), alteration in the hydrodynamic properties (34) and in fluorescence emission (19). From a functional viewpoint, significantly increased IC_{50} values leading to constitutive activation of the GC at physiological Ca^{2+} were observed for all the mutants investigated so far by us and by others, with less significant —if present at all—alterations in the EC_{50} values (15).

The study presented here extends the molecular characterization of disease-associated missense mutations found in *GUCA1A* to the biochemical and biophysical analysis of the proteins expressed by two gene mutations recently found in Spanish families (16). The newly identified L84F and I107T-GCAP1 variants showed a rather heterogeneous clinical phenotype (16) ascribable to COD, CORD and MACD, similar to those previously observed for Y99C and P50L-GCAP1 (26,28). We asked whether the expressed proteins showed molecular features in common with the previously characterized GCAP1 mutants. Surprisingly, we found that this is not the case for both the variants.

CD spectroscopy showed that, while both GCAP1 variants are clearly folded in a typical predominantly α-helix architecture (see Supplementary Material, Fig. S1), I107T-GCAP1 is characterized by a tertiary structure and a conformational transition pattern (Fig. 2) similar to that recently observed for D100E, L151F and G159V (29). Instead, L84F-GCAP1 showed slight but significant alterations in its tertiary structure in both the GC-inhibiting and activating states (Fig. 2). Moreover, the secondary structure and the protein compactness for L84F-GCAP1 appeared to be related to the sequence of cation binding events, as reflected by the different $\Theta_{222}/\Theta_{208}$ ratios obtained in the Mg^{2+} and Ca^{2+}-saturating conditions, depending on the order of cation saturation (Table 1 and see Supplementary Material, Fig. S1). A peculiar feature of the newly investigated mutants is that, while they both showed a 10–12°C lower thermal stability than the wild-type in the Mg^{2+} bound/GC-activating state (Fig. 3 and Table 1) (7,17), they displayed higher stability in the presence of saturating Ca^{2+} (GC-inhibiting state), a phenomenon that was particularly apparent for L84F, resulting in the most stable form of GCAP1 observed so far.

Distinct behaviors were also observed by analyzing the fluorescence emission of the two GCAP1 variants, which reflects different conformational and hydrophobicity properties following cation binding (Figs 4 and 5). Both forms showed a dynamically changing, Ca^{2+}-dependent emission pattern in the 100–600 nM physiological range of Ca^{2+}, indicating the operation as Ca^{2+} sensors. However, the two mutants showed opposite trends, resulting in a maximum for L84F and a minimum for I107T at ~200 nM Ca^{2+} (Fig. 5D). It is worth noticing that the Ca^{2+}-titration fluorescence pattern shown by I107T-GCAP1 lacked the typical biphasic behavior that is observed for the wild-type. However, this lack was observed earlier in other COD mutants (19), while L84F-GCAP1 displayed a unique and opposite trend, with enhanced intensity of fluorescence in conditions of saturating Ca^{2+}. Results from titrations with Mg^{2+} also significantly differed for the two mutants. While I107T-GCAP1 showed a pattern compatible with a wild-type like, relatively low affinity for Mg^{2+} (8,35), L84F-GCAP1 proved to switch its conformation in the physiological range of Mg^{2+} (1 mM), hence suggesting a more prominent role for this cation in regulating its function (Fig. 5D).

Ca^{2+}-titration experiments in competition with a chromophoric chelator also highlighted remarkable differences among the two mutants. I107T-GCAP1 showed, with respect to the wild-type (17,31), decreased macroscopic association constants for each EF-hand (Table 2), both in the presence and in the absence of physiological Mg^{2+}, consistent with a ~10-fold reduction in apparent affinity for Ca^{2+}. Data fitting to a two-site binding model further suggest that the binding of a Ca^{2+} ion might be compromised for this mutant. This trend is substantially in line with what was observed previously with the COD/CORD-associated mutants E89K, D100E, L151F and G159V (17). On the contrary, titrations for L84F-GCAP1 showed a very different pattern, with a wild-type-like distribution of macroscopic association constants, at least for the higher affinity binding sites, and an overall comparable apparent affinity for Ca^{2+} (Table 2). Interestingly, titration experiments performed in the presence of physiological Mg^{2+} resulted in a less prominent decrease in apparent affinity compared with the wild-type [see Table 2 and (31)]. Data fitting to a three-site binding model points to a positive cooperativity mechanism, in which the binding of a Ca^{2+} ion to a

first binding site increased the affinity for the second (Table 2). Notably, this proposed mechanism is consistent also with a two-site Ca^{2+}-binding model (Table 2), i.e. if one of the EF-hands were occupied by Mg^{2+} under physiological conditions, the binding of Ca^{2+} could still occur with positive cooperativity.

MD simulations were run to unveil mutant-specific structural features and helped explaining their distinct properties. For instance, they highlighted a significantly higher flexibility for I107T-GCAP1 when compared with the wild-type, in the $EF2^{Mg2+}$-bound form (see Supplementary Material, Fig. S2A and C), which is particularly apparent in the EF3–EF4 domain. On the contrary, in the Ca^{2+}-saturated state, L84F was significantly stable in all structural regions (see Supplementary Material, Fig. S2B and D) including the 120–135 region connecting EF3 and EF4, which has been shown to be highly dynamic in wild-type GCAP1 (7).

Structural differences between the two mutants in the vicinity of the myristoyl group became also visible by MD simulations. In the L84F mutant, the myristoyl moiety was found to be deeply buried in the cleft formed by the EF2 and EF3 motives (Fig. 6D), and most of the hydrophobic residues that interact with the acyl group, in particular, F43, L13 and L45 (Fig. 1B), were found to maintain significantly more persistent interactions compared with the wild-type, in the simulated time frame (Fig. 6C). This was not the case for the Mg^{2+}-bound I107T-GCAP1, in which the myristoyl moiety appeared more loosely packed than in the wild-type (Fig. 6B), as further demonstrated by the generally less persistent hydrophobic interactions (Fig. 6A).

Finally, MD simulations permitted us to explain possible functional consequence for the pathological mutants. The EF3 Ca^{2+}-coordinating residues D100, N104 and E111 were found to be more dynamical in the Mg^{2+}-bound I107T-GCAP1 than in the wild-type (see Supplementary Material, Fig. S3B, left column), which is not surprising considering the location of the substitution in the EF3 loop (Fig. 1A). However, the same residues were significantly less flexible in the L84F-GCAP1 variant than in the wild-type in the presence of saturating Ca^{2+} (see Supplementary Material, Fig. S3B, right column). The remote distance of L84F to the EF3 Ca^{2+}-binding loop implies an intra-molecular communication pathway that connects the region of the myristoyl group and the EF3 binding motif, which occurs via an allosteric mechanism. Such intra-molecular communication may be related to the one observed between the same region and EF4 in myristoylated wild-type GCAP1, and is involved in the recently proposed calcium-myristoyl 'tug'-mechanism for tuning Ca^{2+} sensitivity and interaction with the GC target (36).

In spite of their remarkably distinct biochemical and biophysical properties, I107T and L84F-GCAP1 showed rather similar functional properties, in terms of aberrant regulation of the GC target. They both led to constitutive activation of the target enzyme at physiological Ca^{2+} (Fig. 7 and Table 2), reflected by the 7.5-fold higher IC_{50} value for L84F and the ~31-fold higher IC_{50} for I107T. In line with other COD/CORD-associated GCAP1 mutants (17), no significant correlation exists between the apparent affinity for Ca^{2+} of the GCAP1 variant and the corresponding IC_{50} values (Table 2). This apparently surprising evidence might be explained by the fact that the IC_{50} values summarize a rather complex series of events, including the replacement of cations in the GC-bound GCAP1 and the concerted conformational change transferred to the target, as well as the rearrangement of the GC dimer interface. Interestingly, the concerted action of these sequential steps is mirrored in the extremely high cooperativity of GC activation (37), although Ca^{2+} binding to isolated GCAP1 *per se* occurs generally without cooperativity (17). Indeed, GCAP1 might display different Ca^{2+} affinities when GCAP1 is bound to the GC, pointing to a very complex regulation of the GC–GCAP1 complex. As proven recently by some of us (38), when GC variants carrying mutations in its dimerization domain are incubated with wild-type GCAP1, a significant shift in Ca^{2+}-sensitivity is observed. Although GC is *per se* not a Ca^{2+}-sensing unit, it seems to integrate and process information regarding Ca^{2+} sensing by GCAP1. Similar phenomena are observed in other Ca^{2+}-sensor systems, for example, for the ubiquitous protein calmodulin, which changes its affinity for Ca^{2+} when bound to the several physiological targets (39).

In terms of target functionality, both GCAP1 mutants showed remarkably decreased activation of the target GC (10.5× in the case of L84F, 17.5× in the case of I107T, versus 33× in the case of the wild-type). However, the EC_{50} values for the two mutants were relatively similar to those of the wild-type (Table 2), suggesting that the interaction between GCAP1 and GC may occur for the mutants with similar affinity as for the wild-type under physiological conditions.

A previous bioinformatic analysis (16) led to a proposal about the pathological mechanisms underlying the altered function of the two GCAP1 mutants. For I107T, perturbation of protein secondary (and eventually tertiary) structure was predicted, together with similar effects predicted for previously characterized COD/CORD-associated mutants (15). Since the same bioinformatic approach led to the prediction of no structural alteration for L84F, the authors hypothesized that the nucleotidic mutation c.250C>T may disrupt a splicing enhancer and/or create a splicing silencer (16), so that the final cause for disease would in that case be haploinsufficiency. Our data however suggest a different scenario. Indeed, the thorough biochemical and biophysical characterization performed here highlighted for I107T-GCAP1 very minor structural alterations with respect to the wild-type, in line with what we previously observed for the D100E, L151F and G159V COD/CORD-associated mutants (17,29,34). On the contrary, and at odds with the result of previous bioinformatic predictions (16), significant structural effects among retinal-disease-related GCAP1 mutants were indeed observed for L84F-GCAP1. Although our data cannot completely exclude the haploinsufficiency hypothesis, they rather strongly point to the autosomal-dominant nature of the disease for both of the expressed mutants. The observation that both I107T and L84F-GCAP1 lead to similar perturbation of target regulation, causing the constitutive activation of GC, suggests a similarly altered inter-molecular communication mechanism, which is described for nearly all the retinal-dystrophy GCAP1 mutants investigated so far (15). In light of the calcium-relay model (11), GCAPs that are unaffected by mutations, like GCAP2 in rods, may partly compensate for the dysfunction of the mutated GCAP1, thereby still allowing almost normal visual capabilities. In the long run, however, the photoreceptor would undergo a detrimental alteration of Ca^{2+} and cGMP homeostasis, thus triggering cell death. An important goal of future studies will be to understand in molecular detail, how remarkably distinct molecular features of GCAP1 variants exert a common regulatory effect on the target enzyme, thus leading to its aberrant regulation.

Materials and Methods

Materials

Tris (hydroxymethyl) aminomethane (Tris), 3-(*N*-morpholino) propanesulfonic acid (Mops), $CaCl_2$, $MgCl_2$, NaCl, KCl, EGTA and DTT were purchased from Sigma Aldrich or Carl Roth and were of the highest grade available.

Methods

Cloning of L84F and I107-GCAP1 mutants

The novel sequence variants c.320T>C (p.Ile107Thr) and c.250C>T (p.Leu84Phe) were introduced by PCR site-directed *in vitro* mutagenesis (primers available upon request). The amplified PCR product was cut with NdeI and NheI and ligated into the expression vector pET11-bGCAP1-D6S (40). All sequences were verified by DNA sequencing (LGC Genomics, Germany).

Expression and purification of I107T-GCAP1 and L84F-GCAP1

Wild-type, I107T and L84F-GCAP1 were overexpressed in BL21-CodonPlus *Escherichia coli* cells and subsequently purified to homogeneity as described before (10). In order to myristoylate GCAP1 variants, cells were co-transformed with the plasmid pBB131 containing a gene for the yeast (*Saccharomyces cerevisiae*) NMT. After cell lysis, GCAP1 wild-type and mutants were isolated from the insoluble fraction. Briefly, GCAP1 variants were extracted from inclusion bodies by homogenization in 6 M guanidinium hydrochloride and dialyzed against 3 l Tris-buffer (20 mM Tris–HCl, 150 mM NaCl, 1 mM DTT pH 7.5). Subsequently, the protein was applied onto a size exclusion column (Superdex 75, GE Healthcare, Germany) equilibrated in Tris-buffer with 2 mM EGTA. Fractions containing GCAP1 were further purified with an anion exchange column (HiLoad 26/10 Q Sepharose; GE Healthcare) equilibrated in Tris-buffer with 2 mM EGTA (40). Chromatography was performed with a gradient of 200–550 mM NaCl in 40 ml. The purity of the obtained GCAP1 forms was verified by sodium dodecyl sulfate–polyacrylamide gel electrophoresis. Proteins were decalcified, aliquoted and lyophilized until use.

CD spectroscopy and thermal denaturation profiles

CD spectroscopy studies were performed with a Jasco J-710 spectropolarimeter equipped with a Peltier type thermostated cell holder. Both near UV (250–320 nm) and far UV (200–250 nm) spectra were recorded at 37° C at a scan rate of 50 nm min^{-1}, a bandwidth of 1 nm and an integration time of 4 s. Five accumulations were averaged for each sample, the spectrum of the buffer (5 mM Tris–HCl pH 7.5, 150 mM KCl, 2 mM DTT) was recorded before each set of measurements and subtracted. Protein concentration for far UV spectra was ~6 μM in 0.1 cm cuvettes, while for near UV spectra, it was ~26 μM in 1.0 cm cuvettes. Both far UV and near UV spectra were recorded: (i) in the presence of >15-fold excess EGTA with respect to protein concentration; (ii) after addition of 1 mM $MgCl_2$ or 2-fold excess $CaCl_2$ with respect to the concentration of EGTA; and (iii) after the addition of the other salt, not added in the previous step. Thermal denaturation was monitored between 20°C and 96°C in the same conditions as for far UV spectra, as far as protein, EGTA, $MgCl_2$ and $CaCl_2$ concentrations are concerned. The ellipticity signal at λ = 208 nm (θ_{208}) was recorded at a scan rate of 1°C min^{-1} and a response time of 4 s. The thermal denaturation analysis was performed assuming a two-state transition process, where the θ_{208} signal recorded as a function of temperature represents the fraction of folded and unfolded protein. When possible, thermal denaturation curves were fitted to a four-parameter Hill sigmoid and a value for the melting temperature was estimated.

The equation for the fitting curve was:

$$y = b_n + \frac{|b_n - b_u|T^H}{T_m^H + T^H}$$

where b_n is the baseline value (θ_{208}) of the native protein, b_u the baseline value of the partly unfolded protein, T the temperature, H the Hill coefficient and T_m is the melting temperature.

DLS experiments

DLS measurements were performed with a Zetasizer Nano-S (Malvern Instruments) using a polystyrene low-volume disposable sizing cuvette (ZEN0112). Viscosity and refractive index of the aqueous solvent were set at 0.8872 cP and 1.330, refractive index of the protein was set to 1.45, protein absorption was set to 0.001 and the temperature was set to 25° C with 2 min equilibration time. The measurement angle was 173° backscatter and the analysis model was set to multiple narrow modes. For each measurement, a minimum of 24 determinations were performed, each consisting of at least 10 repetitions. All experiments were performed in 5 mM Tris–HCl, 150 mM KCl, pH = 7.5 buffer previously filtered through a Jet Biofilm 0.22 μm membrane; protein solutions were filtered through a 0.02 μm Anotop 10 filter (Whatman). The time evolution of the mean count rate over 350 min was monitored for L84F-GCAP1 in the same conditions as above, where each point was an accumulation of 10 measurements performed during 1 min time frame.

High performance liquid chromatography

Purified protein samples (100 μg) were analyzed for the presence of monomeric, dimeric and/or aggregated GCAP1 forms by employing SEC on a BioSep-SEC S2000 column (Phenomenex, Aschaffenburg, Germany). All experiments were performed in 30 mM Mops-KOH pH 7.2, 50 mM KCl, 4 mM NaCl, 1 mM DTT. One millimolar EGTA, 0.3 mM $CaCl_2$ and/or 3.5 mM $MgCl_2$ were added, respectively.

Fluorescence spectroscopy and Mg^{2+} and Ca^{2+} titrations

The emission fluorescence spectra after excitation at λ = 290 nm were recorded using a Jasco FP-750 spectrofluorimeter between 300 and 380 nm at 25°C, in 1 cm quartz cuvette and at a scan rate of 60 nm min^{-1}. The excitation and emission bandwidth were set to 5 nm. All experiments were performed in 5 mM Tris–HCl pH 7.5, 150 mM KCl, 1 mM DTT buffer. The collected data were obtained by subtracting the signal from the buffer to an average of three accumulations. The protein concentration for all fluorescence spectra measurements was ~8 μM in the presence of 1 mM EGTA, after addition of 1 mM $MgCl_2$ and after addition of 1 mM free $CaCl_2$.

Ca^{2+} buffers and Mg^{2+} buffers used for fluorescence titration experiments were prepared using 5 mM Tris–HCl pH 7.5, 150 mM KCl, 100 μM EGTA and $CaCl_2$ or $MgCl_2$ at variable concentrations, everything was dissolved in or diluted with the aforementioned buffer. Free Ca^{2+} and Mg^{2+} concentration for each titration point was calculated according to the Ca-Mg-ATP-EGTA Calculator software using NIST database (http://maxchelator.stanford.edu/CaMgATPEGTA-NIST.htm) by fixing T = 25°C, pH = 7.5 and ionic strength =0.15 M. By mixing these solutions, the final free Ca^{2+} concentration was varied in the 2 nM–100 μM range, while the free Mg^{2+} concentration was varied in the 9 μM–10 mM range. Protein concentration was ~0.7 μM for each titration point. After recording three accumulations of the spectrum in the presence of 100 μM EGTA, only the intensity at the wavelength corresponding to the maximum fluorescence emission intensity was monitored for the other titration points, which were expected to change according to Ca^{2+} or Mg^{2+} binding. For the data reported in Figure 6, Y-axis has been normalized in the following way: $Y = (F_{340} - F_{min})/(F_{max} - F_{min})$, where F_{340} is the fluorescence intensity of each titration point, F_{min} the minimal fluorescence intensity recorded and F_{max} the maximal fluorescence intensity recorded.

Guanylate cyclase assay

Guanylate cyclase activities were determined as described in (33,41) with buffer-washed ROS membranes as a source for native

ROS-GC1 [~96% of the total cyclase activity in the membranes from bovine ROS is provided by ROS-GC1 (41)] with the following modifications: for the determination of EC_{50}-values, the GCAP1 concentration was varied between 0.05 and 10 μM. Ca^{2+}-dependent GC activities were obtained by keeping GCAP1 concentrations fixed at 5 μM and varying the free [Ca^{2+}] using a K_2H_2EGTA/ CaH_2EGTA buffer system as described previously (33,42). The free Mg^{2+}-concentration was 1 mM. All incubation steps were performed under very dim red light; the reactions were stopped and further processed for analysis as described.

Determination of Ca^{2+}-binding constants using a chromophoric chelator

Calcium binding to GCAP1 variants was monitored by a precise titration method described previously (30,32) based on the competition for Ca^{2+} between the protein and a chromophoric chelator, 5,5′Br_2-BAPTA, whose absorbance changes upon Ca^{2+} concentration. Briefly, a Ca^{2+}-free solution of 5,5′Br_2-BAPTA was prepared by dissolving the chelator in the previously decalcified 5 mM Tris–HCl pH 7.5, 150 mM KCl buffer. Chelator concentration ranged between 17 and 26 μM, while initial Ca^{2+} concentration was 0.9–2.1 μM. For each titration experiment, Ca^{2+}-free lyophilized proteins were dissolved in the chelator solution, and the final concentration (13–16 μM) was measured with the Bradford assay (43). In each experiment, 0.8–1 ml of chelator-protein solution was inserted in 1.0 cm cuvette and the absorbance at 263 nm (λ_{max} for the Ca^{2+} free chelator) was monitored upon titration with fixed amounts (0.8–1 μl, respectively) of 3 mM $CaCl_2$. Titrations were performed until no significant change in absorbance was detected. Three or four replications of each titration experiment were performed, data (Fig. 5) were fitted using a Newton–Raphson direct least-square fitting procedure implemented in the CaLigator software (30) to obtain individual macroscopic binding constants (log K_A, Table 2), which were further used to determine apparent affinity values (K_D^{app}, Table 2) allowing for quantitative comparisons between the Ca^{2+} affinity of the wild-type and the mutants. With the same argument as in previous works (17,31), we defined the apparent affinity of each mutant from the average of the logarithms of the first two macroscopic binding constants [$K_D^{app} = 10^{-(\log K1 + \log K2)/2}$]. Given the much lower affinity for the third site, this apparent affinity is not affected by the poorly accurate information on the low affinity binding site (i.e. log K_3 for I107T-GCAP1, Table 2).

All Ca^{2+} titrations were performed at room temperature. Axes in Figure 5 were normalized as follows: $Y = (A_{263} - A_{Ca})/(A_0 - A_{Ca})$, where A_{263} is the absorbance at $\lambda = 263$ nm, A_{Ca} the absorbance at saturating [Ca^{2+}] and A_0 the absorbance at the lowest [Ca^{2+}]; $X = [Ca^{2+}]_{tot}/([Q]+3[P])$, where $[Ca^{2+}]_{tot}$ is the total Ca^{2+} concentration, [Q] the concentration of the chelator (μM), 3 is the maximum number of binding sites per protein and [P] the measured concentration of the protein (μM).

MD simulations and analyses

A homology model of human myristoylated GCAP1 was built using the three-dimensional structure of chicken GCAP1 in its Ca^{2+}-bound form as a template (44) according to a procedure elucidated in a previous work (17). Simulated states were modeled either by removing Ca^{2+} ions from each respective EF-hand binding site or by substitution with an Mg^{2+} ion as elucidated in (7). MD simulations of $EF2^{Mg2+}$ wild-type GCAP1 and of $EF2^{Ca2+}$ $EF3^{Ca2+}$ $EF4^{Ca2+}$ wild-type GCAP1 are the first 150 ns of the trajectories produced in (7). $EF2^{Mg2+}$ I107T-GCAP1 and $EF2^{Ca2+}EF3^{Ca2+}$ $EF4^{Ca2+}$ L84F-GCAP1 mutants were built using the structures of the states simulated in (7) as a template, by replacing the mutated residue with the highest-scored rotamer proposed by the 'Mutate Residue' function implemented in Maestro (Schrodinger) software.

MD simulations of the two mutants were performed using GROMACS 4.6.3 simulation package (45), with the CHARMM27 all-atom force field (46). CHARMM27 parameters for describing the post-translational myristoylation were generated manually, and are available upon request for academic use. All settings for MD simulations were the same as in (7), in which details are provided. The system was equilibrated at 310 K for 2 ns of backbone position-restrained MD simulations and then at 310 K for 2 ns of unrestricted MD simulations, and the resulting structure was used as a reference in RMSD and RMSF calculations. After equilibration, the system underwent 150 ns unrestrained isothermal–isobaric (NPT ensemble; $T = 310$ K, $P = 1$ atm) MD simulation.

Generated MD trajectories were subjected to different analyses. The solvent accessible surface area (SASA) and the α-carbon RMSD were calculated over the 150 ns trajectory, the latter being referred to each structure after the 4 ns equilibration. The intrinsic flexibility of the system was evaluated by computing the RMSF for each amino acid, in the time frame of the simulation, defined as time averaged-RMSD with respect to the reference structure:

$$\mathrm{RMSF}_i = \sqrt{\frac{1}{T}\sum_{t_j=1}^{T} |r_i(t_j) - r_i^{\mathrm{ref}}|^2}$$

where T is the 150 ns MD time frame and $r_i(t_j)$ and r_i^{ref} represent the coordinates of the C_α atom of each residue at the time t_j and after 4 ns equilibration, respectively.

RMSF analysis was applied only on all α-carbons, RMSD analysis was applied on α-carbons of both the entire protein and selected residues, while the SASA was calculated on the atoms forming up the myristoyl group. RMSD, RMSF and SASA analyses were performed using Wordom software (47,48).

Persistence over the 150 ns time frame of hydrophobic interactions involving the myristoyl group was calculated as the ratio of frames, in which hydrophobic interaction could be detected between hydrophobic residues and the myristoyl group, over the total number of frames. Hydrophobic interactions were present if the distance between the center of mass of the side chain of hydrophobic residues and the myristoyl group was smaller than 5.5 Å. This analysis was performed using the PyInteraph software (49).

Supplementary material

Supplementary Material is available at *HMG* online.

Acknowledgements

Invaluable technical assistance by Stefan Sulmann and Matteo Tiberti is gratefully acknowledged. Part of this work resulted from a Fellowship at the Hanse-Wissenschaftskolleg Delmenhorst (Germany) to D.D.O.

Conflict of Interest statement. None declared.

Funding

This work was supported by funding from the Italian Ministry for Research and Education (MIUR) via Departmental funding (FUR2013 to D.D.O.), from CINECA through the Italian Super

Computing Resource Allocation project (ISCRA Grant HP10CB7L79 to D.D.O.) and from the Deutsche Forschungsgemeinschaft (DFG grant KO948/10-2 to K.-W.K.). V.M. was the recipient of a travel grant provided by Consorzio Interuniversitario per le Biotecnologie (CIB).

References

1. Hamel, C.P. (2007) Cone rod dystrophies. *Orphanet J. Rare Dis.*, **2**, 7.
2. Michaelides, M., Hardcastle, A.J., Hunt, D.M. and Moore, A.T. (2006) Progressive cone and cone-rod dystrophies: phenotypes and underlying molecular genetic basis. *Surv. Ophthalmol.*, **51**, 232–258.
3. Korenbrot, J.I. (2012) Speed, sensitivity, and stability of the light response in rod and cone photoreceptors: facts and models. *Prog. Retin. Eye Res.*, **31**, 442–466.
4. Pugh, E.J. and Lamb, T. (2000) Phototransduction in Vertebrate Rods and Cones: Molecular Mechanisms of Amplification, Recovery and Light Adaptation. In: Stavenga, D., DeGrip, W. and Pugh, E.J. (eds.), *Handbook of Biological Physics*. Elsevier Science BV, North Holland, Vol. 3, pp. 183–255.
5. Koch, K.W., Duda, T. and Sharma, R.K. (2010) Ca(2+)-modulated vision-linked ROS-GC guanylate cyclase transduction machinery. *Mol. Cell. Biochem.*, **334**, 105–115.
6. Dizhoor, A.M., Olshevskaya, E.V. and Peshenko, I.V. (2010) Mg^{2+}/Ca^{2+} cation binding cycle of guanylyl cyclase activating proteins (GCAPs): role in regulation of photoreceptor guanylyl cyclase. *Mol. Cell. Biochem.*, **334**, 117–124.
7. Marino, V., Sulmann, S., Koch, K.W. and Dell'Orco, D. (2015) Structural effects of Mg^{2+} on the regulatory states of three neuronal calcium sensors operating in vertebrate phototransduction. *Biochim. Biophys. Acta*, **1853**, 2055–2065.
8. Peshenko, I.V. and Dizhoor, A.M. (2004) Guanylyl cyclase-activating proteins (GCAPs) are Ca^{2+}/Mg^{2+} sensors: implications for photoreceptor guanylyl cyclase (RetGC) regulation in mammalian photoreceptors. *J. Biol. Chem.*, **279**, 16903–16906.
9. Peshenko, I.V. and Dizhoor, A.M. (2006) Ca^{2+} and Mg^{2+} binding properties of GCAP-1. Evidence that Mg^{2+}-bound form is the physiological activator of photoreceptor guanylyl cyclase. *J. Biol. Chem.*, **281**, 23830–23841.
10. Hwang, J.Y., Lange, C., Helten, A., Hoppner-Heitmann, D., Duda, T., Sharma, R.K. and Koch, K.W. (2003) Regulatory modes of rod outer segment membrane guanylate cyclase differ in catalytic efficiency and Ca(2+)-sensitivity. *Eur. J. Biochem.*, **270**, 3814–3821.
11. Koch, K.W. and Dell'Orco, D. (2013) A calcium-relay mechanism in vertebrate phototransduction. *ACS Chem. Neurosci.*, **4**, 909–917.
12. Makino, C.L., Wen, X.H., Olshevskaya, E.V., Peshenko, I.V., Savchenko, A.B. and Dizhoor, A.M. (2012) Enzymatic relay mechanism stimulates cyclic GMP synthesis in rod photoresponse: biochemical and physiological study in guanylyl cyclase activating protein 1 knockout mice. *PLoS One*, **7**, e47637.
13. Mendez, A., Burns, M.E., Sokal, I., Dizhoor, A.M., Baehr, W., Palczewski, K., Baylor, D.A. and Chen, J. (2001) Role of guanylate cyclase-activating proteins (GCAPs) in setting the flash sensitivity of rod photoreceptors. *Proc. Natl Acad. Sci. USA*, **98**, 9948–9953.
14. Scholten, A. and Koch, K.W. (2011) Differential calcium signaling by cone specific guanylate cyclase-activating proteins from the zebrafish retina. *PLoS One*, **6**, e23117.
15. Behnen, P., Dell'Orco, D. and Koch, K.W. (2010) Involvement of the calcium sensor GCAP1 in hereditary cone dystrophies. *Biol. Chem.*, **391**, 631–637.
16. Kamenarova, K., Corton, M., Garcia-Sandoval, B., Fernandez-San Jose, P., Panchev, V., Avila-Fernandez, A., Lopez-Molina, M.I., Chakarova, C., Ayuso, C. and Bhattacharya, S.S. (2013) Novel GUCA1A mutations suggesting possible mechanisms of pathogenesis in cone, cone-rod, and macular dystrophy patients. *Biomed. Res. Int.*, **2013**, 517570.
17. Dell'Orco, D., Behnen, P., Linse, S. and Koch, K.W. (2010) Calcium binding, structural stability and guanylate cyclase activation in GCAP1 variants associated with human cone dystrophy. *Cell. Mol. Life Sci.*, **67**, 973–984.
18. Dizhoor, A.M., Boikov, S.G. and Olshevskaya, E.V. (1998) Constitutive activation of photoreceptor guanylate cyclase by Y99C mutant of GCAP-1. Possible role in causing human autosomal dominant cone degeneration. *J. Biol. Chem.*, **273**, 17311–17314.
19. Kitiratschky, V.B., Behnen, P., Kellner, U., Heckenlively, J.R., Zrenner, E., Jagle, H., Kohl, S., Wissinger, B. and Koch, K.W. (2009) Mutations in the GUCA1A gene involved in hereditary cone dystrophies impair calcium-mediated regulation of guanylate cyclase. *Hum. Mutat.*, **30**, E782–E796.
20. Sokal, I., Dupps, W.J., Grassi, M.A., Brown, J. Jr, Affatigato, L.M., Roychowdhury, N., Yang, L., Filipek, S., Palczewski, K., Stone, E.M. *et al.* (2005) A novel GCAP1 missense mutation (L151F) in a large family with autosomal dominant cone-rod dystrophy (adCORD). *Invest. Ophthalmol. Vis. Sci.*, **46**, 1124–1132.
21. Sokal, I., Li, N., Surgucheva, I., Warren, M.J., Payne, A.M., Bhattacharya, S.S., Baehr, W. and Palczewski, K. (1998) GCAP1 (Y99C) mutant is constitutively active in autosomal dominant cone dystrophy. *Mol. Cell.*, **2**, 129–133.
22. Olshevskaya, E.V., Calvert, P.D., Woodruff, M.L., Peshenko, I. V., Savchenko, A.B., Makino, C.L., Ho, Y.S., Fain, G.L. and Dizhoor, A.M. (2004) The Y99C mutation in guanylyl cyclase-activating protein 1 increases intracellular Ca^{2+} and causes photoreceptor degeneration in transgenic mice. *J. Neurosci.*, **24**, 6078–6085.
23. Olshevskaya, E.V., Peshenko, I.V., Savchenko, A.B. and Dizhoor, A.M. (2012) Retinal guanylyl cyclase isozyme 1 is the preferential in vivo target for constitutively active GCAP1 mutants causing congenital degeneration of photoreceptors. *J. Neurosci.*, **32**, 7208–7217.
24. Peshenko, I.V., Olshevskaya, E.V., Lim, S., Ames, J.B. and Dizhoor, A.M. (2014) Identification of target binding site in photoreceptor guanylyl cyclase-activating protein 1 (GCAP1). *J. Biol. Chem.*, **289**, 10140–10154.
25. Schrem, A., Lange, C., Beyermann, M. and Koch, K.W. (1999) Identification of a domain in guanylyl cyclase-activating protein 1 that interacts with a complex of guanylyl cyclase and tubulin in photoreceptors. *J. Biol. Chem.*, **274**, 6244–6249.
26. Michaelides, M., Wilkie, S.E., Jenkins, S., Holder, G.E., Hunt, D. M., Moore, A.T. and Webster, A.R. (2005) Mutation in the gene GUCA1A, encoding guanylate cyclase-activating protein 1, causes cone, cone-rod, and macular dystrophy. *Ophthalmology*, **112**, 1442–1447.
27. Payne, A.M., Downes, S.M., Bessant, D.A., Taylor, R., Holder, G. E., Warren, M.J., Bird, A.C. and Bhattacharya, S.S. (1998) A mutation in guanylate cyclase activator 1A (GUCA1A) in an autosomal dominant cone dystrophy pedigree mapping to a new locus on chromosome 6p21.1. *Hum. Mol. Genet.*, **7**, 273–277.
28. Downes, S.M., Holder, G.E., Fitzke, F.W., Payne, A.M., Warren, M.J., Bhattacharya, S.S. and Bird, A.C. (2001) Autosomal dominant cone and cone-rod dystrophy with mutations in the

guanylate cyclase activator 1A gene-encoding guanylate cyclase activating protein-1. *Arch. Ophthalmol.*, **119**, 96–105.
29. Dell'Orco, D., Sulmann, S., Zagel, P., Marino, V. and Koch, K.W. (2014) Impact of cone dystrophy-related mutations in GCAP1 on a kinetic model of phototransduction. *Cell. Mol. Life. Sci.*, **71**, 3829–3840.
30. Andre, I. and Linse, S. (2002) Measurement of Ca^{2+}-binding constants of proteins and presentation of the CaLigator software. *Anal. Biochem.*, **305**, 195–205.
31. Dell'Orco, D., Sulmann, S., Linse, S. and Koch, K.W. (2012) Dynamics of conformational Ca^{2+}-switches in signaling networks detected by a planar plasmonic device. *Anal. Chem.*, **84**, 2982–2989.
32. Linse, S. (2002) Calcium binding to proteins studied via competition with chromophoric chelators. *Methods Mol. Biol.*, **173**, 15–24.
33. Peshenko, I.V. and Dizhoor, A.M. (2007) Activation and inhibition of photoreceptor guanylyl cyclase by guanylyl cyclase activating protein 1 (GCAP-1): the functional role of Mg^{2+}/Ca^{2+} exchange in EF-hand domains. *J. Biol. Chem.*, **282**, 21645–21652.
34. Sulmann, S., Dell'Orco, D., Marino, V., Behnen, P. and Koch, K.W. (2014) Conformational changes in calcium-sensor proteins under molecular crowding conditions. *Chemistry*, **20**, 6756–6762.
35. Lim, S., Peshenko, I., Dizhoor, A. and Ames, J.B. (2009) Effects of Ca^{2+}, Mg^{2+}, and myristoylation on guanylyl cyclase activating protein 1 structure and stability. *Biochemistry*, **48**, 850–862.
36. Peshenko, I.V., Olshevskaya, E.V., Lim, S., Ames, J.B. and Dizhoor, A.M. (2012) Calcium-myristoyl Tug is a new mechanism for intramolecular tuning of calcium sensitivity and target enzyme interaction for guanylyl cyclase-activating protein 1: dynamic connection between N-fatty acyl group and EF-hand controls calcium sensitivity. *J. Biol. Chem.*, **287**, 13972–13984.
37. Koch, K.W. and Stryer, L. (1988) Highly cooperative feedback control of retinal rod guanylate cyclase by calcium ions. *Nature*, **334**, 64–66.
38. Zägel, P., Dell'Orco, D. and Koch, K.W. (2013) The dimerization domain in outer segment guanylate cyclase is a Ca^{2+}-sensitive control switch module. *Biochemistry*, **52**, 5065–5074.
39. Vetter, S.W. and Leclerc, E. (2003) Novel aspects of calmodulin target recognition and activation. *Eur J. Biochem.*, **270**, 404–414.
40. Hwang, J.Y. and Koch, K.W. (2002) Calcium- and myristoyl-dependent properties of guanylate cyclase-activating protein-1 and protein-2. *Biochemistry*, **41**, 13021–13028.
41. Helten, A., Saftel, W. and Koch, K.W. (2007) Expression level and activity profile of membrane bound guanylate cyclase type 2 in rod outer segments. *J. Neurochem.*, **103**, 1439–1446.
42. Behnen, P., Scholten, A., Ratscho, N. and Koch, K.W. (2009) The cone-specific calcium sensor guanylate cyclase activating protein 4 from the zebrafish retina. *J. Biol. Inorg. Chem.*, **14**, 89–99.
43. Bradford, M.M. (1976) A rapid and sensitive method for the quantitation of microgram quantities of protein utilizing the principle of protein-dye binding. *Anal. Biochem.*, **72**, 248–254.
44. Stephen, R., Bereta, G., Golczak, M., Palczewski, K. and Sousa, M.C. (2007) Stabilizing function for myristoyl group revealed by the crystal structure of a neuronal calcium sensor, guanylate cyclase-activating protein 1. *Structure*, **15**, 1392–1402.
45. Hess, B., Kutzner, C., Van Der Spoel, D. and Lindahl, E. (2008) GROMACS 4: algorithms for highly efficient, load-balanced, and scalable molecular simulation. *J. Chem. Theory Comput.*, **4**, 435–447.
46. Bjelkmar, P., Larsson, P., Cuendet, M.A., Bess, B. and Lindahl, E. (2010) Implementation of the CHARMM force field in GROMACS: analysis of protein stability effects from correction maps, virtual interaction sites, and water models. *J. Chem. Theory Comput.*, **6**, 459–466.
47. Seeber, M., Cecchini, M., Rao, F., Settanni, G. and Caflisch, A. (2007) Wordom: a program for efficient analysis of molecular dynamics simulations. *Bioinformatics*, **23**, 2625–2627.
48. Seeber, M., Felline, A., Raimondi, F., Muff, S., Friedman, R., Rao, F., Caflisch, A. and Fanelli, F. (2011) Wordom: a user-friendly program for the analysis of molecular structures, trajectories, and free energy surfaces. *J. Comput. Chem.*, **32**, 1183–1194.
49. Tiberti, M., Invernizzi, G., Lambrughi, M., Inbar, Y., Schreiber, G. and Papaleo, E. (2014) PyInteraph: a framework for the analysis of interaction networks in structural ensembles of proteins. *J. Chem. Inf. Model.*, **54**, 1537–1551.

OXFORD

Human Molecular Genetics, 2016, Vol. 0, No. 0 1–12

doi: 10.1093/hmg/ddw374
Advance Access Publication Date: 15 November 2016
Original Article

ORIGINAL ARTICLE

Dysfunction of cGMP signalling in photoreceptors by a macular dystrophy-related mutation in the calcium sensor GCAP1

Farina Vocke[1], Nicole Weisschuh[2], Valerio Marino[3], Silvia Malfatti[3], Samuel G. Jacobson[4], Charlotte M. Reiff[2,†], Daniele Dell'Orco[3] and Karl-Wilhelm Koch[1,*]

[1]Department of Neuroscience, Biochemistry Group, University of Oldenburg, Oldenburg, Germany, [2]Molecular Genetics Laboratory, Institute for Ophthalmic Research, University of Tübingen, Germany, [3]Department of Neurosciences, Biomedicine and Movement Sciences, Section of Biological Chemistry, University of Verona, Verona, Italy and [4]Scheie Eye Institute, Department of Ophthalmology, Perelman School of Medicine, University of Pennsylvania, Philadelphia, Pennsylvania, USA

*To whom correspondence should be addressed at: Karl-Wilhelm Koch, Department of Neuroscience, Biochemistry Group, University of Oldenburg, 26111 Oldenburg, Germany. Tel: +49 0441 798 3640; Fax: +49 0441 7983250; Email: karl.w.koch@uni-oldenburg.de

Abstract

Macular dystrophy leads to progressive loss of central vision and shows symptoms similar to age-related macular degeneration. Genetic screening of patients diagnosed with macular dystrophy disclosed a novel mutation in the *GUCA1A* gene, namely a c.526C > T substitution leading to the amino acid substitution p.L176F in the guanylate cyclase-activating protein 1 (GCAP1). The same variant was found in three families showing an autosomal dominant mode of inheritance. For a full functional characterization of the L176F mutant we expressed and purified the mutant protein and measured key parameters of its activating properties, its Ca^{2+}/Mg^{2+}-binding, and its Ca^{2+}-induced conformational changes in comparison to the wildtype protein. The mutant was less sensitive to changes in free Ca^{2+}, resulting in a constitutively active form under physiological Ca^{2+}-concentration, showed significantly higher activation rates than the wildtype (90-fold versus 20-fold) and interacted with an higher apparent affinity with its target guanylate cyclase. However, direct Ca^{2+}-binding of the mutant was nearly similar to the wildtype; binding of Mg^{2+} occurred with higher affinity. We performed molecular dynamics simulations for comparing the Ca^{2+}-saturated inhibiting state of GCAP1 with the Mg^{2+}-bound activating states. The L176F mutant exhibited significantly lower flexibility, when three Ca^{2+} or two Mg^{2+} were bound forming probably the structural basis for the modified GCAP1 function.

Introduction

Hereditary retinal disorders cause many different forms of retinal disease that can lead to severe visual impairment or blindness. Disease forms are often classified according to phenotype, for example, whether the peripheral retina is affected first or whether the cells in the macula are the early and most prominent site of degeneration.

Age-related macular degeneration (AMD) is a late-onset disease leading to progressive loss of central vision (1–4). AMD has been associated with genetic and non-genetic factors. The latter

†Present address: Klinik für Augenheilkunde, Killianstr. 5, 79106 Freiburg, Germany.
Received: September 2, 2016. **Revised:** October 24, 2016. **Accepted:** October 27, 2016

involve nutritional, lifestyle (smoking) or environmental factors, which in combination with aging lead to a higher risk of disease progression. Genetic and genomic studies have identified genetic risk loci and susceptibility genes that are expressed in the photoreceptor layer and its support system consisting of the retinal pigment epithelium (RPE) Bruch's membrane (BM) and the choroid. Phenotypic features of AMD can include the loss of large numbers of photoreceptors in the central macula and protein and lipid deposits in the BM or between BM and RPE (5).

Macular dystrophy (MD) presents similar symptoms but is linked to a different set of genetic mutations and, in contrast to AMD, is monogenic and not considered multifactorial (6). In addition, MD is a heterogeneous disease (caused by monoallelic or biallelic mutation/s in one out of many genes) with a variable age of onset (usually 5–50 years). One form of MD involves mutations in the *GUCA1A* gene (7), which encodes the guanylate cyclase-activating protein 1 (GCAP1) in rod and cone photoreceptor cells.

GCAP1 and its cognate GCAP2 regulate the activities of membrane bound guanylate cyclases (GC) in response to light-dependent changes of the cytoplasmic free Ca^{2+}-concentration ($[Ca^{2+}]$) and thereby are critical factors for Ca^{2+}-cGMP homeostasis in the outer segments of rods and cones (8). Function of GCAP1 and GCAP2 is not redundant as they operate in a Ca^{2+}-relay fashion (9,10), which is based on different molecular properties of GCAPs like, for example, differences in Ca^{2+}-binding, Ca^{2+}-sensitive operation, target regulation and conformational dynamics (10–14). The exact activation mechanism of GCAPs on the target GC at low free $[Ca^{2+}]$ and inhibition at high free $[Ca^{2+}]$ is unclear. Peshenko *et al.* (15) recently employed mutants of GCAP1 by inserting a phenylalanine (F) in critical amino acid positions around the 'myristoyl cavity' and found a major effect for the mutant L176F leading to a suggested 'Ca^{2+}-myristoyl tug mechanism' of GCAP1 action (15).

By genetic screening of patients diagnosed with MD we identified the novel variant c.526C > T (p.L176F) in the *GUCA1A* gene, which is identical to the mutant employed by Peshenko *et al.* (15) for investigating the intramolecular connections between the myristoyl group and Ca^{2+}-sensing. The aim of the present work was to understand which cellular and molecular events lead to the MD associated with L176F substitution. We present a characterization of the clinical phenotype and investigate key molecular properties of the expressed and purified mutant protein. Molecular dynamics simulations further provide us with insight into protein dysfunction with respect to its conformational dynamics.

Results

Genetic screening and clinical evaluation of patients

Sanger sequencing of the *GUCA1A* gene in family 1 revealed a novel variant c.526C > T (p.L176F) which is not reported in public sequence repositories (including the ExAC database, http://exac.broadinstitute.org). Mutations in other macular dystrophy-/cone dystrophy-related genes had been previously excluded in this family by ASPER chips and/or Sanger sequencing. The same variant was identified in family 2 upon a panel-based next-generation sequencing approach and in family 3 upon whole exome sequencing. All three families show an autosomal dominant mode of inheritance (Fig. 1). Detailed clinical characteristics of the patients are displayed in Table 1. Briefly, paracentral and central scotomas in the central visual field were present in all patients. Scotopic standard ganzfeld ERGs had normal

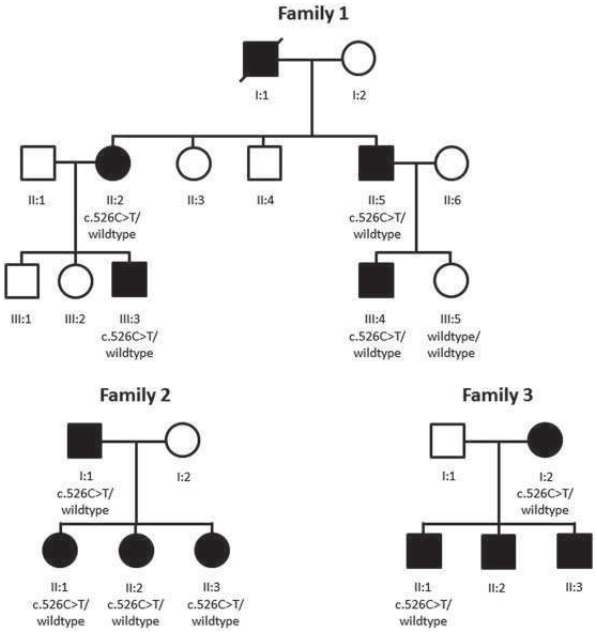

Figure 1. Segregation of the mutant allele harboring the c.526C > T transition in three families.

amplitudes and implicit times in all patients except in patient II:1 from family 3. Photopic ERGs were reduced only in families 2 and 3. Multifocal ERGs were performed in patients from families 2 and 3 only and showed diminished central responses, whereas the outer ring averages revealed reduced amplitudes and delayed implicit times only in patient II:1 from family 3. Fundus abnormalities were typically confined to the macula (Supplementary Material, Fig. S1). Optical coherence tomography in families 1 and 2 revealed a thinner photoreceptor layer in the foveal area.

Functional characterization of L176F-GCAP1, activation of target GC1

Regulatory properties of L176F GCAP1 were compared with those of WT GCAP1. For this purpose, the GCAP1 target human GC1 was heterologously expressed in HEK293 cells and HEK293 cell membranes were isolated and reconstituted with purified myristoylated (m) and non-myristoylated (nm) GCAP1 variants. Basic features of GCAP1 function were preserved in the WT and the mutant, namely activating the target GC1 at low free $[Ca^{2+}]$ and inhibiting it at increasing free $[Ca^{2+}]$ (Fig. 2A and B). However, characteristic differences were observed in the IC_{50} values ($[Ca^{2+}]$ at which activation is halfmaximal) of the activation profiles: these were at 0.41 ± 0.05 μM free $[Ca^{2+}]$ for mWT GCAP1 and shifted to 7.09 ± 1.4 μM $[Ca^{2+}]$ for mL176F-GCAP1 (Table 2). A different and less pronounced effect was seen with nmGCAP1 forms. Here, activation of human GC1 with WT GCAP1 was halfmaximal at an IC_{50} of 0.67 ± 0.18 μM $[Ca^{2+}]$; the L176F substitution in nmGCAP1 caused a slight shift to lower free $[Ca^{2+}]$ at of 0.55 ± 0.06 μM (Fig. 2 and Table 2). These results were broadly consistent with those reported by Peshenko *et al.* (15), although the shift in Ca^{2+}-sensitivity (IC_{50}-value), which we observed for the L176F mutant was more than 17-fold, whereas Peshenko *et al.* observed a shift of about 8-fold.

Table 1. Phenotype of patients with the *GUCA1A* mutation c.526C > T/p.L176F

Family	PatientID	Age at diagnosis/ examination	Diagnosis	BCVA OD; OS	Macular RPE changes	Reduction of foveal ONL thickness	Visual field	Ganzfeld ERG	mfERG	EOG	Comments
1	II:2	46	Macular dystrophy	0.4; 0.1	yes	yes	central dysfunction	Scotopic normal Photopic normal	NA	NA	No evidence of peripheral cone dysfunction
	II:5	44	Macular dystrophy	1.0; 0.8	yes	yes	small paracentral dysfunction	Scotopic normal Photopic normal	NA	NA	No evidence of peripheral cone dysfunction
	III:3	20	Macular dystrophy	1.0; 1.0	yes	yes	paracentral dysfunction	Scotopic normal Photopic normal	NA	NA	No evidence of peripheral cone dysfunction
	III:4	16	Macular dystrophy	1.0; 1.0	yes	yes	small paracentral dysfunction	Scotopic normal Photopic normal	NA	NA	No evidence of peripheral cone dysfunction
2	II:1	47	Macular dystrophy/Cone dystrophy	0.1; 0.1	yes	yes	central dysfunction	Scotopic normal Photopic reduced amplitudes	diminished central responses	normal	Slow progression from macular to peripheral cone dysfunction
	II:2	44	Macular dystrophy/ Cone dystrophy	NA	no	yes	central dysfunction	Scotopic normal Photopic reduced amplitudes and slightly prolonged implicit times	diminished central responses	normal	Slow progression from macular to peripheral cone dysfunction
3	I:2	40	Macular dystrophy	NA	NA	NA	central dysfunction	Scotopic normal Photopic normal	diminished central responses	normal	–
	II:1	49	Macular dystrophy	0.6; 0.6	yes	NA	paracentral dysfunction	OD: Scotopic and photopic normal OS: Scotopic and photopic reduced amplitudes	diminished central responses; slightly diminished peripheral responses	normal	Rod involvement in the left eye

BCVA, best corrected visual acuity; RPE, retinal pigment epithelium; ONL, outer nuclear layer; NA, not available.

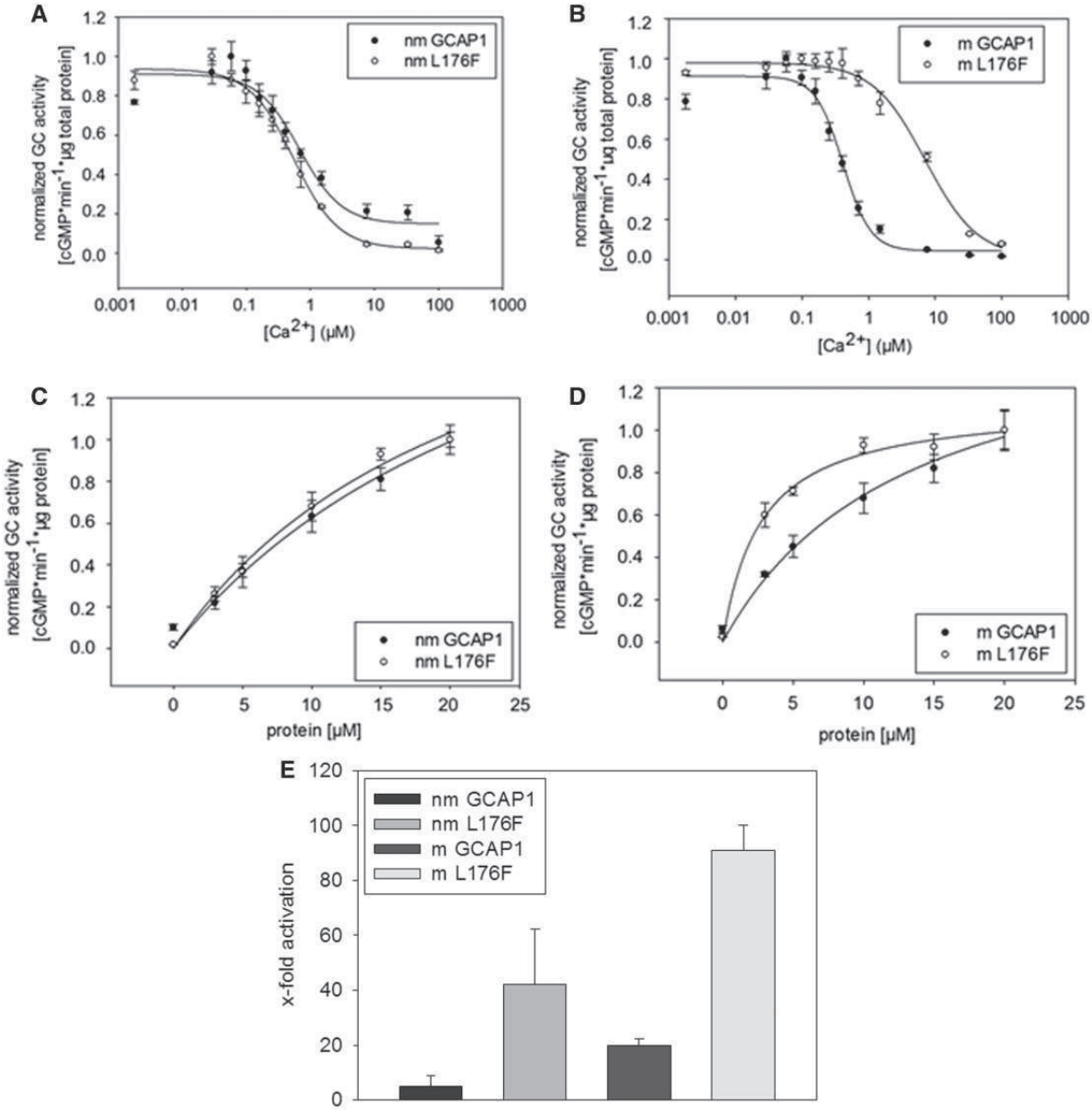

Figure 2. Functional analysis of the L176F GCAP1 mutant. Ca^{2+}-dependent regulation of human GC1 expressed in HEK293 cells was measured in the presence of non-myristoylated (**A**) and myristoylated (**B**) GCAP1 variants (WT and L176F). Corresponding IC_{50} are listed in Table 2. Nonmyristoylated (**C**) and myristoylated (**D**) GCAP1 variants activate human GC1 at low [Ca^{2+}] yielding values of apparent affinity, EC_{50} listed in Table 2. X-fold activation by GCAP1 variants is shown in panel (**E**).

A second feature concerning the activation properties of GCAP1 is the apparent affinity for the target GC1. An indirect way to measure apparent affinity values is GC1 activation as a function of the GCAP1 concentration resulting in EC_{50} values. The apparent affinity expressed in EC_{50} values was highest for mL176F and decreased in the following order: mL176F > nmL176 ≈ mWT > nmWT GCAP1 (Fig. 2C and D, Table 2).

A third profound alteration of GCAP1 function became apparent when we analysed the x-fold activation (expressed as GC_{max} - GC_{min} divided by GC_{min}). The mutants showed significantly higher x-fold activation rates than both WT GCAP1 forms. An x-fold activation of 91 for the mL176F mutants (Fig. 2E and Table 2) was the largest we have observed in disease-related GCAP1 mutants that we investigated in our laboratory in recent years (16–18). The x-fold activation of nmL176F was lower than mL176F, but still higher than mWT GCAP1.

Ca^{2+} binding to L176F in the presence/absence of Mg^{2+}

The distortion of Ca^{2+}-sensitive regulatory properties of GCAP1 could principally originate from changes in the Ca^{2+} and/or Mg^{2+}-binding properties (19). Therefore, we tested whether Ca^{2+}-binding constants were affected in the mutant protein employing a chromophoric chelator assay. Both mGCAP1 and nmGCAP1 variants were titrated with Ca^{2+} in the presence of the competing chelator/chromophore 5,5Br_2-BAPTA. In

Table 2. Ca^{2+}-binding and GC regulation of GCAP1 WT and the L176F mutant

	log K_1[a]	log K_2[a]	log K_3[a]	K_D^{app} (μM)[b]	IC_{50} (μM)[c]	EC_{50} (μM)[d]	X-fold[e]
nmWT	7.2±0.2	6.5±0.3	3.5±1.1	0.14	0.67±0.37	8.60±1.02	5.2±4.0
nmWT Mg^{2+}	6.83±0.06	6.57±0.12	5.63±0.12	0.2	–	–	–
mWT	6.9±0.4	6.9±0.4	4.1±0.7	0.13	0.41±0.01	4.10±0.94	20±2.2
mWTMg^{2+}	6.97±0.15	5.87±0.06	2.4±0.4	0.38	–	–	–
nmL176F	7.47±0.06	6.07±0.06	2.3±1.2	0.17	0.55±0.12	4.23±1.02	42±20.4
nmL176F Mg^{2+}	6.77±0.12	6.27±0.06	4.0±0.3	0.30	–	–	–
mL176F	7.52±0.13	6.2±0.2	–	0.13	7.09±2.78	2.13±0.23	91±9.1
mL176F Mg^{2+}	6.7±0.1	5.96±0.15	2.4±1.9	0.47	–	–	–

[a]Decimal logarithm of macroscopic binding constants for three Ca^{2+} binding sites; experimental data obtained from the chelator assay were fitted to a model with three binding sites; errors represent standard deviation of at least three repetitions.

[b]Apparent affinity obtained by averaging the significant macroscopic binding constants (see Materials and Methods for details).

[c]IC_{50} is the Ca^{2+} concentration at which the GC activity is half maximal.

[d]EC_{50} is the concentration of GCAP1 at which the GC activity at low [Ca^{2+}] is half maximal.

[e]X-fold activation is calculated according to GC_{max} - GC_{min} divided by GC_{min}.

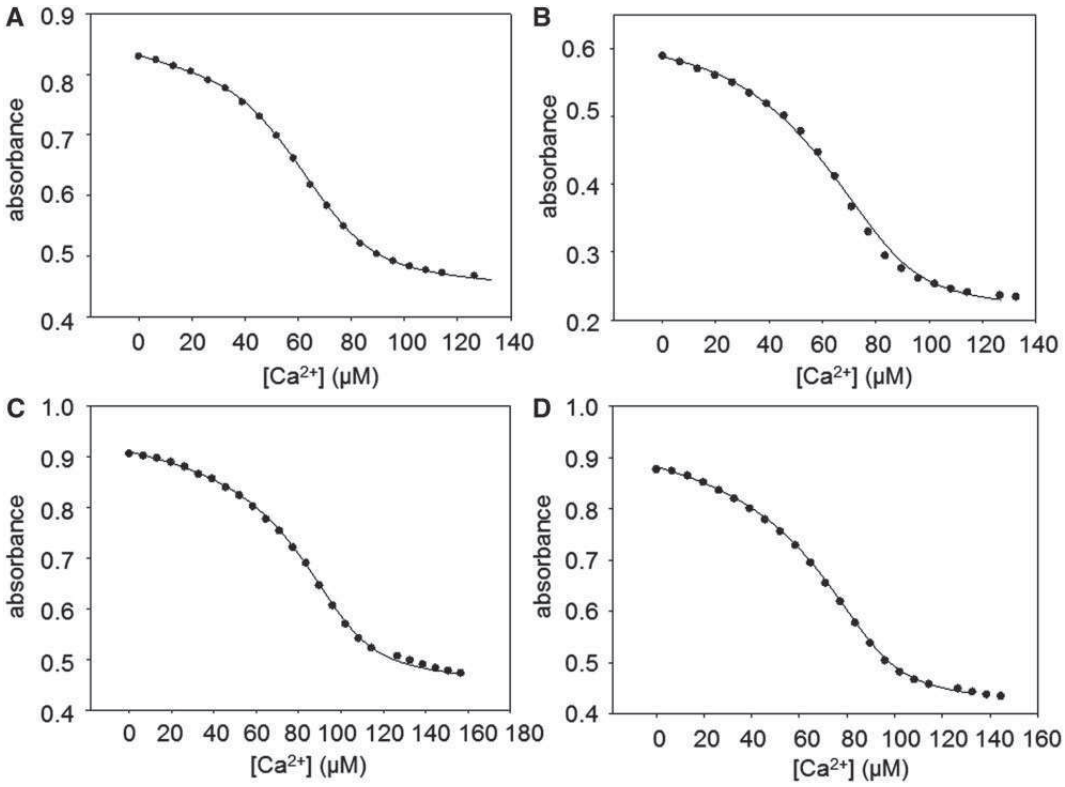

Figure 3. Determination of Ca^{2+}-binding to GCAP1 variants using the chelator assay. (A) nmWT; (B) mWT; (C) nmL176F; (D) mL176F. All data sets were fitted using a three-binding site model implemented in the Caligator software.

addition, we tested the influence of Mg^{2+} at physiological concentration in the buffer. Examples of chelator titrations are shown in Fig. 3; we employed a three binding sites model for fitting all data, which yielded macroscopic binding constants listed in Table 2. Two Ca^{2+}-binding sites in WT GCAP1 are of high to medium affinity and could easily be detected. Binding to the third binding site occurred with much lower affinity and values were intrinsically less robust due to the detection limit of the assay. We used the two macroscopic binding constants for calculating K_D^{app} as previously described (18) yielding a K_D^{app} of 0.14 μM and 0.13 μM for nmWT and mWT GCAP1, respectively. Adding Mg^{2+} shifted the K_D^{app} to slightly higher values (0.20 μM for nmWT and 0.38 μM for mWT). Titrations with WT GCAP1 served as a positive control and confirmed our previous results thus showing that the assay is suitable for testing the mutant. In the absence of Mg^{2+} affinities for Ca^{2+} were slightly lower for the nmL176F than for nmWT ($K_D^{app} = 0.17$ μM), but were not altered for mL176F ($K_D^{app} = 0.13$ μM). Presence of Mg^{2+} decreased the Ca^{2+}-affinity slightly for nmL176F ($K_D^{app} = 0.30$ μM), and for mL176F ($K_D^{app} = 0.47$ μM).

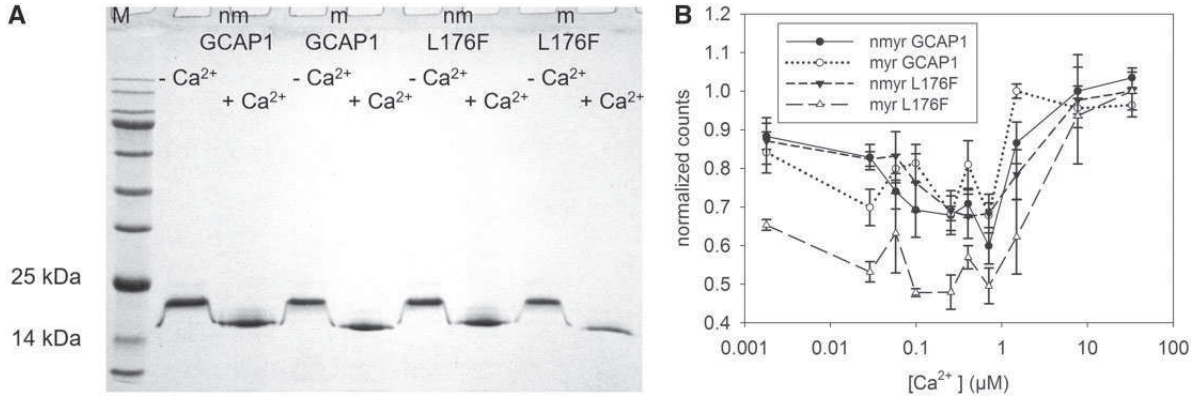

Figure 4. Ca^{2+}-induced conformational changes in L176F. (**A**) Ca^{2+}-dependent electrophoresis mobility shift in an SDS-polyacrylamide gel electrophoresis. (**B**) Ca^{2+}-titration of W fluorescence emission for GCAP1 variants as indicated. Emission was recorded at 336 nm (excitation at 280 nm).

Ca^{2+}-induced conformational changes and thermal stability of L176F

GCAPs undergo Ca^{2+}-induced conformational changes, which trigger a subsequent increase of target GC activities (15,18). Conformational changes in the GCAP1 structure can therefore serve as good indicators for dysfunctional features in a mutant (16,17,20). An electrophoretic Ca^{2+}-shift assay done with all GCAP1 variants showed that binding of Ca^{2+} caused a higher electrophoretic mobility for all tested variants (Fig. 4A) indicating that WT and mutant L176F undergo a similar conformational transition, which, however, might differ with respect to the exact Ca^{2+}-dependence. To better investigate this dependence, we monitored the intrinsic W fluorescence of GCAP1 variants as a function of the free Ca^{2+}. The fluorescence pattern of GCAP1 changed in a biphasic fashion, which is assigned to specific W positions (W21, W54 and W94; ref. 21). We observed that phase I at low free [Ca^{2+}] up to 1 μM was significantly diminished in mL176F and that fluorescence emission intensities were lower than those of the mWT (Fig. 4B) indicating that the environment of W21 or W54 is altered in the mutant. Phase II above 1 μM [Ca^{2+}] was very similar for all tested variants showing that exposure of W94 to a more hydrophobic environment is similar for WT and mutant. The emission patterns for nmWT and nmL176F were nearly identical. Presence of Mg^{2+} reduced the extent of phase I in mWT (21), but to a lesser degree in mL176F. The nonmyristoylated GCAP1 variants showed a nearly identical phase I (data not shown).

We further investigated the Mg^{2+}/Ca^{2+}-induced conformational transitions of both mL176F and nmL176F by circular dichroism (CD) spectroscopy in the far and in the near UV, to monitor respectively changes in the protein secondary and tertiary structure. Results are reported in Fig. 5 (mL176F) and in Supplementary Material, Fig. S2 (nmL176F). The overall fold of L176F is that of an all α-helix protein (Fig. 5A; Supplementary Material, Fig. S2), in line with all other GCAP1 mutants analysed so far in our group (17,18,22). Addition of 1 mM Mg^{2+} led to changes in far UV ellipticity only for nmL176F (compare Supplementary Material, Fig. S2A with Fig. 5A), while saturating Ca^{2+} led for both cases to an increased ellipticity that is a more negative signal. Quantitative far UV spectral properties observed for both variants in the three analysed states were overall very similar and are reported in Supplementary Material, Table T1. The selective sensing capability of L176F for the different cations was clearly visible in the near UV spectra (Fig. 5B and Supplementary Material, Fig. S2B), where the dichroic signal was completely positive in contrast to that previously observed for the WT (22,23). This observation is most likely due to the addition of an aromatic residue, with consequent perturbation of the F band. Slight conformational rearrangements were observed for nmL176F by the addition of 1 mM Mg^{2+} especially in the F band (Supplementary Material, Fig. S2A), and changes became more apparent upon addition of saturating Ca^{2+} for both variants, with significant increases in ellipticity in the Y and W bands (Fig. 5B and Supplementary Material, Fig. S2A).

By taking advantage of the all-α helix secondary structure of the protein we could monitor the thermal stability of L176F over the 20–96 °C range by monitoring the ellipticity at 208 nm (Fig. 5C and Supplementary Material, Fig. S2C). While the apo forms of m/nmL176F showed a similar transition temperature (T_m = 48.2 °C and 47.6 °C respectively, Supplementary Material, Table T1), the Mg^{2+}-bound form of mL176F was approximately 6 °C more stable than nmL176F. However, the addition of saturating Ca^{2+} stabilized more significantly mL176F, for which no transition could be detected, at odds with nmL176F, for which the transition was estimated to occur at 71.8 °C (Supplementary Material, Table T1).

Changes in hydrodynamic size of L176F following Ca^{2+} binding

We monitored the effects that Ca^{2+} binding exerted on the hydrodynamic properties of both mL176F and nmL176F by performing Ca^{2+}-titration experiments and measuring the protein hydrodynamic diameter by dynamic light scattering. Overall, DLS data were consistent with a monomeric protein, substantially monodispersed (PDI 0.17 to 0.37) and showing satisfactory colloidal properties. Examples of average DLS spectra obtained for m/nmL176F at different free [Ca^{2+}] are reported in the Supplementary Material, Fig. S3.

Results of Ca^{2+} titrations starting from suspended Ca^{2+}-free protein in the presence of 1 mM Mg^{2+} are reported in Fig. 6. Non-monotonic changes in the hydrodynamic diameter were observed for mL176F below 120 μM [Ca^{2+}] where a maximum was observed at 60–90 μM Ca^{2+} corresponding to a diameter of approx 7.1 nm (Fig. 6, black line), thus significantly different from that (≈6.4 nm) measured in the absence of Ca^{2+}. The size monotonically decreased above 150 μM Ca^{2+} to reach a stable diameter of approx. 6.6 nm. Similarly, nmL176F showed an

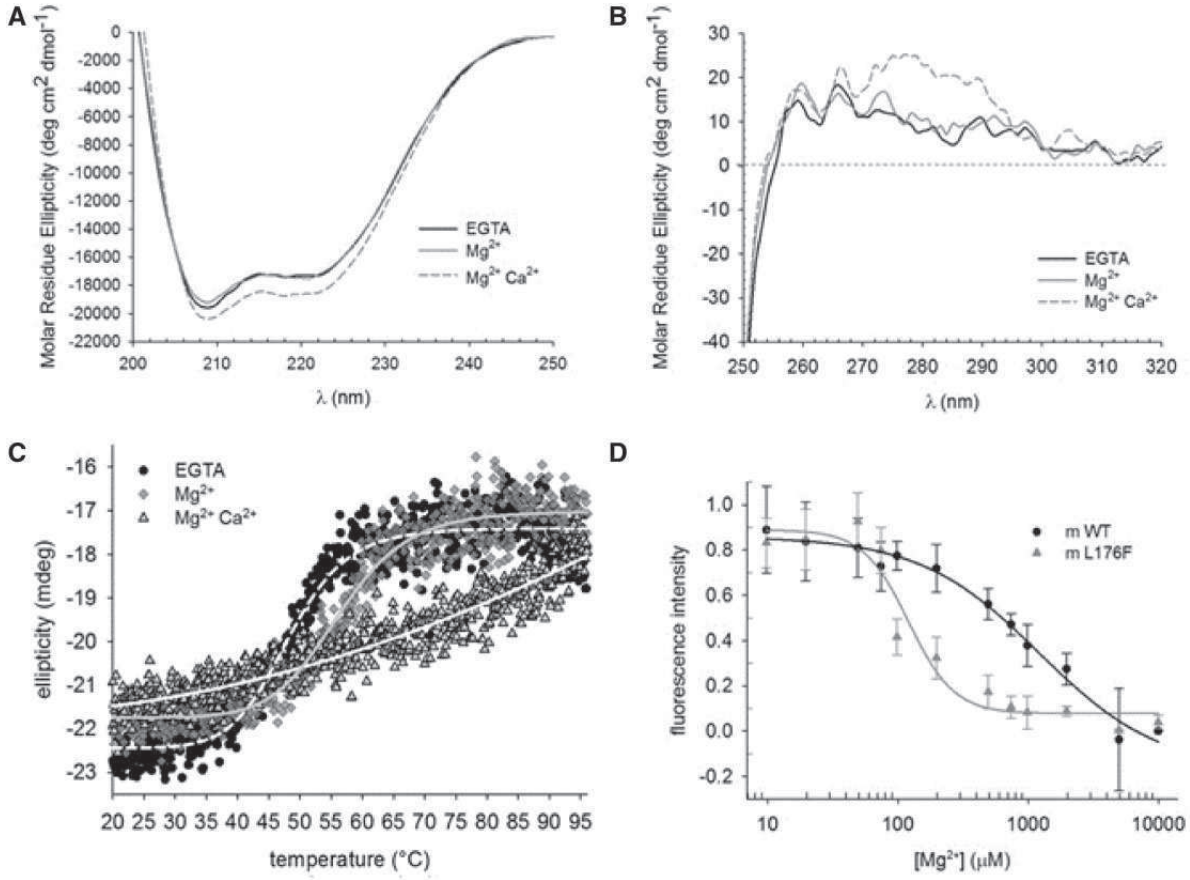

Figure 5. Structural changes occurring in mL176F upon binding of Ca^{2+} and Mg^{2+} monitored by CD spectroscopy and intrinsic fluorescence emission. (**A**) Far UV CD spectra of 5 μM mL176F in 200 μM EGTA (black, solid line); after addition of 1 mM Mg^{2+} (gray, solid line) and further addition of 200 μM free Ca^{2+} (gray, dashed line). (**B**) Near UV CD spectra of 22 μM mL176F in 400 μM EGTA (black, solid line); after addition of 1 mM Mg^{2+} (gray, solid line) and further addition of 400 μM free Ca^{2+} (gray, dashed line). (**C**) Thermal denaturation profiles over the 20–96 °C range temperature of ~10 μM mL176F in the presence of 200 μM EGTA (black circles), 1 mM Mg^{2+} (gray diamonds) and further addition of 200 μM free Ca^{2+} (gray triangles). Denaturation was followed by monitoring the ellipticity signal at 208 nm; experimental data were fitted with a four-parameter Hill sigmoidal function, estimated values are reported in Supplementary Material, Table T1. (**D**) Mg^{2+} titration of mL176F (λ_{em} = 342 nm) and mWT (λ_{em} = 340 nm) performed by exciting W residues (λ_{ex} = 290 nm) and monitoring the intrinsic W fluorescence emission. Three replicates were accumulated and results are shown as an average ± standard deviation. Data were fitted to a four-parameter Hill sigmoidal function.

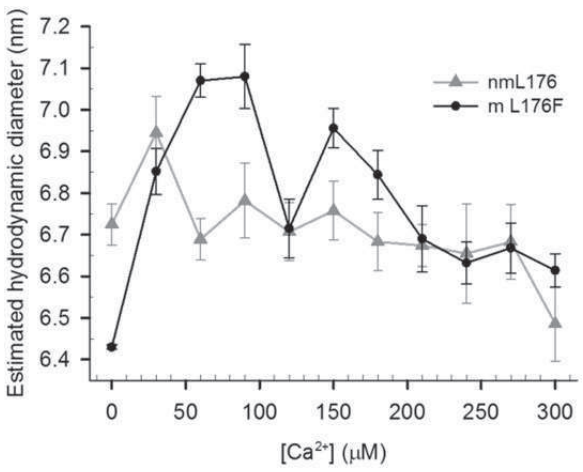

Figure 6. Ca^{2+} titration effects on the average hydrodynamic size measured by Dynamic Light Scattering for 44 μM mL176F (black) and 33 μM nmL176F (gray). All experiments were performed at T = 25 °C in 5 mM Tris-HCl pH 7.5, 150 mM KCl, 500 μM EGTA, 1 mM Mg^{2+}. Both profiles are an average of at least 14 runs, each of which was an accumulation of at least 13 measurements.

initial increase of hydrodynamic size from ≈6.7 nm up to 6.9 nm (at 30 μM Ca^{2+}), but overall the observed changes were lower compared to mL176F (Fig. 6, gray line).

Response of L176F to Mg^{2+}

While the presence of 1 mM Mg^{2+} did not significantly affect the Ca^{2+}-affinity of mL176F (Fig. 3 and Table 2), thermal denaturation studies suggest a significant stabilization in the presence of Mg^{2+}. This prompted us to investigate specifically the binding of Mg^{2+} by monitoring the intrinsic W fluorescence emission, in comparison with WT GCAP1. Fluorescence patterns of m/nmL176F were all compatible with those of a Mg^{2+}-binding protein, with significantly different affinities from the WT form (Fig. 5D and Supplementary Material, Fig. S2D). Binding of Mg^{2+} to mL176F occurred with 10-fold higher affinity than to mWT (K_d^{app} ≈ 120.6 μM vs. 1.22 mM; Fig. 5D) and with significantly higher cooperativity (Hill coefficient h^{L176F} = 2.47 vs. h^{WT} = 0.94). Binding parameters of nmL176F differed as affinity for Mg^{2+} was approximately 5-fold higher than for nmWT (K_d^{app} ≈ 218 μM vs. 1.17 mM; Supplementary Material, Fig. S2), and the binding process showed low cooperativity (h^{L176F} = 0.55;

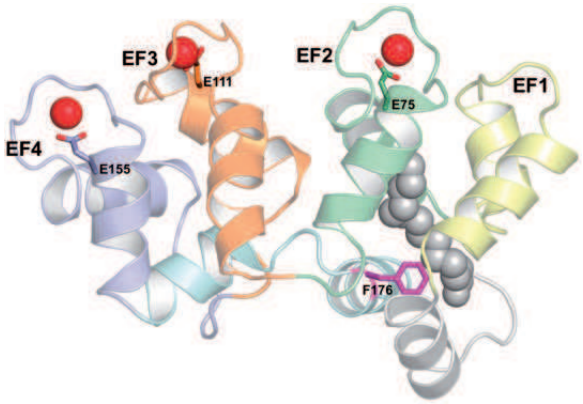

Figure 7. Three-dimensional cartoon representation of the homology model of human L176F GCAP1 mutant. EF1 is colored in yellow, EF2 in green, EF3 in orange and EF4 in blue. N- and C-terminals are colored in pale grey and pale cyan, respectively, the myristoyl group is represented as grey spheres, Ca^{2+} ions are shown as red spheres, F176 is represented in magenta sticks, bidentate Ca^{2+}-coordinating residues are shown in sticks colored like the EF-hand they belong to.

$h^{WT} = 1.72$;) . Both mL176F and nmL176F forms thus exhibited a remarkable affinity for Mg^{2+}.

Molecular dynamics simulations

In order to gain structural insights into the dynamic properties of the different GC-regulatory states of mL176F, we performed 200 ns molecular dynamics simulations and compared the results with those for mWT. Similar to what was done in previous studies (17), proteins were simulated in their GC-inhibiting and activating states. It is well established that the maximal GC inhibition by GCAP1 is achieved when each canonical EF hand is occupied by a Ca^{2+} ion (17,19–21,24). We therefore simulated the GC-inhibiting state $EF2^{Ca}EF3^{Ca}EF4^{Ca}$. The GC-activating states are instead associated to GCAP1 with a Mg^{2+} ion bound in EF2, and possibly in EF3 too (19,20,23), we therefore simulated also the activating states $EF2^{Mg}$ and $EF2^{Mg}EF3^{Mg}$.

As observed in other GCAP1 mutants as well as in the WT (17,23), molecular dynamics simulations highlighted slightly different local dynamics according to the specific cation-bound state. In particular, the Root-Mean Square Fluctuation (RMSF), an index representative for local protein flexibility, was generally reduced for L176F compared to WT in the $EF2^{Ca}EF3^{Ca}EF4^{Ca}$ state (Supplementary Material, Fig. S4A). This indicated a lower flexibility of the mutant structure in the GC-inhibiting state, in particular in the entering helix of EF2 and in its cation-binding loop, and in the exiting helix of the EF3 motif. On the contrary, the L176F form with just one Mg^{2+} ion bound to EF2 was extremely flexible throughout the primary structure, compared to the WT (Supplementary Material, Fig. S4B). Interestingly, the $EF2^{Mg}EF3^{Mg}$ form showed again a significant rigidity, especially in the Mg^{2+}-binding loop of EF2 (Supplementary Material, Fig. S4C).

While no significant changes in the solvent accessible surface area (data not shown) were detected for L176F compared to the WT in any of the GC-regulatory states, some important differences were observed when analysing the Root-Mean Square Deviation (RMSD). The coordinates of the C_α carbons of the essential bidentate Ca^{2+} coordinating residues in each EF hand structure, namely E75 (EF2), E111 (EF3) and E155 (EF4) (Fig. 7) were calculated with respect to the pre-production phase in the time-frame of the MD simulations. Results are summarized in the Supplementary Material, Table T2. The $EF2^{Mg}$-L176F form showed rather high RMSD values (2.7–2.9 Å; Supplementary Material, Table T2) for each bidentate Ca^{2+} coordinating residue, which is in line with the observed flexibility of this form compared to the WT and to the other cation-bound states in the same mutant. However, two findings deserve particular attention. First, in the $EF2^{Ca}EF3^{Ca}EF4^{Ca}$ state, L176F showed approximately halved RMSD compared to the WT for E111 (1.1 Å vs. 2.0 Å), and approximately 35% lower flexibility for E155 located in EF4 (0.8 vs 1.2 Å). Second, the $EF2^{Mg}$ $EF3^{Mg}$ form, in which the EF4 motif is unloaded, is also significantly less flexible in the L176F (RMSD = 1.2 Å) compared to the WT (RMSD = 2.1 Å).

Discussion

Disturbance of the CGMP-Ca^{2+} homeostasis

The L176F substitution had severe consequences for the key regulatory properties of GCAP1: the Ca^{2+}-sensitive regulation of the target GC1 was shifted from the submicromolar to the micromolar range, the x-fold activation of the GC by GCAP1 reached a value of 91-fold, and the mutant had an apparent higher affinity than the WT for the GC (Fig. 2). Peshenko *et al.* (15) constructed and investigated the L176F mutant in a different context (see also Results section) proposing that the interaction between the myristoyl group and the amino acids in the hydrophobic cavity has a regulatory and therefore functional impact. By screening patients showing clinical symptoms of MD we detected the missense mutation leading to the L176F substitution in the protein. Most of the patients in this study had maculopathy only, although two patients, each from a different family, had some evidence of more widespread photoreceptor involvement. Other reports tend to describe a widespread cone (or cone and rod) involvement (7,25,26), but there are also examples of maculopathy patients in these articles. In other words, there is likely to be a spectrum of phenotypes associated with *GUCA1A* mutations from maculopathy only to cone or cone-rod dystrophy. The message for clinicians is that a *GUCAIA* mutation can be a cause of an ad maculopathy as well as a more widespread retinal disease expression. The present study aimed at combining genotype description, phenotype analysis and molecular investigation of protein properties of this MD causing mutation.

The disturbed regulation of GC1 by L176F is, at least in part, repeating a pattern often observed with other dystrophy-related GCAP1 mutants (16,17,26–31). A prominent feature of these cases is that the Ca^{2+}-sensitive regulation of GC1 is halfmaximal at higher than normal physiological levels of cytoplasmic [Ca^{2+}] making these mutants constitutionally active, which would dramatically affect the Ca^{2+}-cGMP homeostasis in cone and rod cells. However, it is noteworthy that the x-fold activation of the mutant, both the nonmyristoylated and particularly the myristoylated one was very high in comparison to the control WT forms (42-fold and 91-fold, respectively; Fig. 2). In a cell, expressing a constitutively active mutant the permanent synthesis of cGMP would lead to a high percentage of CNG-channels kept open most of the time, thus allowing the passage of Ca^{2+}-ions up to a very high micromolar level. At a certain cytoplasmic [Ca^{2+}] however, the GC activation by the GCAP1 mutant switches back to the non-activated stage and the CNG-channels close during illumination having the consequence

that the cytoplasmic [Ca^{2+}] would decrease again turning on the cGMP synthesis. The high x-fold activation like in the case of the L176F mutant would then immediately replenish the cGMP to a higher value than normal keeping again a high percentage of CNG-channels open.

Dell'Orco *et al.* (22) recently modelled the cellular consequences of a photoreceptor cell expressing 50% WT and 50% mutant for other *GUCA1A*/GCAP1 cone-dystrophy mutations of autosomal dominant inheritance. These investigated mutations shared the constitutive activation profile with L176F and simulated photocurrents showed higher response peak amplitudes, prolongation of response duration and a lower current value after complete photoresponse recovery. However, the overall effects on the photoresponse were not large, but significant enough to cause distortion of normal cell physiology. We predict a similar shaping of the photoresponse in the case of the L176F mutation, but with a stronger impact on the dynamics of the photocurrent's ON- and OFF-states due to the more powerful activation rate of L176F.

Is the perturbation of GC activation and Ca^{2+}-sensitive regulation due to impaired Ca^{2+}-binding of L176F?

Results from chelator assays suggest that L176F is WT-like in terms of affinity for Ca^{2+}, similar to what we reported for another GCAP1 mutant L84F (17). The observed GC perturbation is therefore not due to a reduced Ca^{2+}-sensing capability characteristic of most other COD/CORD mutants (17,18,31). Interestingly, Mg^{2+} affected the Ca^{2+}-affinity of the WT mGCAP1 less than for its mL176F variant. Moreover, fluorescence titrations showed a noteworthy affinity of Ca^{2+}-free L176F for Mg^{2+}. Further, Mg^{2+} had a significant effect on the thermal stability of the myristoylated form, and MD simulations showed that the L176F with two Mg^{2+} bound ($EF2^{Mg}$ $EF3^{Mg}$) was structurally and dynamically more stable than the form with only one Mg^{2+} ion bound to EF2. These results suggest that L176F always harbours a Mg^{2+} ion bound to an EF-hand, presumably EF2, and the GC regulatory activity is triggered by cation exchanges in EF3. Moreover, the GC activating state for this mutant seems to be characterized by two Mg^{2+} ions bound respectively to EF2 and EF3, at odds with the WT where due to the much lower affinity probably only one Mg^{2+} ion is bound to EF2 (23). Thus, the constitutive activation of GC1 associated with the pathogenic L176F seems to be related to a higher propensity of this variant to bind Mg^{2+} rather than to a lower affinity for Ca^{2+}, which was the case for many other COD/CORD GCAP1 mutants.

Conformational dynamics of L176F

Impaired Ca^{2+}-sensitive function of L176F seems to correlate more to changes in protein conformation than to changes in Ca^{2+}-affinity. DLS data showed that L176F conformation dynamically responds to variations in [Ca^{2+}] and its hydrodynamic radius changes until the [Ca^{2+}] is high enough to fully saturate the three protein binding sites. The hydrodynamic diameter of the Ca^{2+}-free versus the Ca^{2+}-saturated form was opposite to what Sulmann *et al.* (32) reported for the myristoylated WT, although Sulmann *et al.* performed DLS measurements in the absence of Mg^{2+}. Changes for the nonmyristoylated form were however less prominent, in line with what was observed for the WT form (32).

Molecular dynamics simulations suggest that the structural/dynamical perturbations introduced by the L176F substitution are not only local and protein flexibility is affected in distal regions. In particular: i) the EF2 motif in the $EF2^{Ca}EF3^{Ca}EF4^{Ca}$ state becomes more rigid; ii) the $EF2^{Mg}$ state becomes significantly more flexible in general; iii) in the $EF2^{Mg}$ $EF3^{Mg}$ state, the EF2 binding loop is again less flexible. Most importantly, MD simulations clearly suggest that the local L176F perturbation reaches also distal residues fundamental for coordinating Ca^{2+} binding. Indeed, even in the absence of Ca^{2+} bound to EF4 ($EF2^{Mg}$ $EF3^{Mg}$ state), the mutation stabilizes the structural dynamics of the EF4 loop through a long-range allosteric effect, presumably modulating its Ca^{2+} sensing capability. This finding is substantially in line with the proposed myristoyl tug mechanism (15). A similar allosteric effect is suggested to occur to a lower extent in the $EF2^{Ca}EF3^{Ca}EF4^{Ca}$ state, but it seems to be especially important in the $EF2^{Mg}$ $EF3^{Mg}$ state (likely the GC-activating state for L176F). Indeed, this especially stable state might decrease the capacity of EF4 to bind again a Ca^{2+} ion, which would be essential to restore the GC-inhibiting state, thus contributing to GC constitutive activation.

Materials and Methods

Patient studies

Patients from 3 families with macular dystrophy were included (Table 1). Informed consent was obtained; procedures followed the Declaration of Helsinki and had institutional review board approval. All patients underwent a complete eye examination, genetic analyses, as well as specialized tests of retinal and visual function. DNA isolation and Sanger sequencing of the *GUCA1A* gene was performed as described before (16).

Cloning, protein expression and purification

The sequence variant c.526T > C (p.L176F) was created by PCR site-directed in vitro mutagenesis (primers available upon request). The amplified PCR product was cut with *NdeI* and *NheI* and ligated into the expression vector pET11-bGCAP1-D6 as previously described for other variants (16,17,24). All sequences were verified by DNA sequencing (LGC Genomics, Germany).

Heterologous expression of GCAP1 forms was performed in BL21-CodonPlus *E. coli* cells. Overexpressed proteins were subsequently purified to homogeneity as described before (16,17,24). We co-transformed *E.coli* cells with the plasmid pBB131 containing the gene for yeast (*S. cerevisiae*) N-myristoyl transferase to allow posttranslational modification of WT and mutant GCAP1 with a myristoyl group (24). Proteins were purified after cell lysis using chromatographic procedures exactly as described before for other GCAP1 forms (16,17,24). Methods for determining protein concentration and procedures for gel electrophoresis were done according to standard laboratory protocols exactly as described before (16,17,24).

Cell culture and GC assays

Recombinant human photoreceptor GC1 (assigned as GC-E and alternatively named ROS-GC1, retGC1) was expressed in in HEK flip 293 cells as described (33). Cell membranes were reconstituted with GCAP1 forms and GC activity was measured as described before (33,34). Samples with 10 μM GCAP1 (WT or mutant forms) were incubated at different free [Ca^{2+}] using a Ca^{2+}-EGTA buffer system (11,33,34). The [Ca^{2+}], at which the activation is half-maximal (IC_{50}) was determined. A further way to analyse activation of GC by GCAPs is the x-fold activation

expressed as GC_{max} - GC_{min} divided by GC_{min}; GC_{max} is measured at <10 nM free [Ca^{2+}], GC_{min} at 100 μM free [Ca^{2+}]. Free [Mg^{2+}] is 1 mM. Activity measurements at constant low [Ca^{2+}] and increasing concentrations of GCAP1 forms yielded apparent affinities (EC_{50}-values) of GCAPs for human photoreceptor GC1. Activity values were obtained from at least 4–5 different data sets and were used to calculate the mean ± standard deviation (s.d.).

Ca^{2+}-binding

Calcium binding to GCAP1 variants was monitored by the chelator assay (35,36) exactly as described previously (18). Briefly, Ca^{2+}-free lyophilized proteins (18) were dissolved in the chelator solution at a final concentration of 13–16 μM. The decalcified buffer consisted of 5 mM Tris–HCl pH 7.5, 150 mM KCl. Chelator concentration was between 17–26 μM, while initial Ca^{2+} concentration was 0.9–2.1 μM. The assay is based on the competition for Ca^{2+} between the protein and a chromophoric chelator 5,5'Br_2-BAPTA. Absorbance changes upon Ca^{2+} concentration were measured at λ = 263 nm. Data were fitted using a Newton-Raphson direct least-square fitting procedure implemented in the CaLigator software (35,36) to obtain individual macroscopic binding constants (log K_A, Table 2), which were further used to determine apparent affinity values (K_D^{app}, Table 2; $K_D^{app} = 10^{-(\log K1 + \log K2)/2}$).

Circular dichroism (CD) spectroscopy and thermal denaturation profiles

CD measurements were performed with a Jasco J-710 spectropolarimeter with a Peltier thermostated cell holder. Reported spectra were subtracted with the spectrum of the buffer (5 mM Tris-HCl pH 7.5, 150 mM KCl, 1 mM DTT) and were recorded at 37 °C, using the following parameters: scan rate 50 nm/min, bandwidth 1 nm, response time 4 s, accumulations 5.

Protein concentration for far UV spectra and thermal denaturations was 5–10 μM in 0.1 cm quartz cuvettes, for near UV it was 22–26 μM in 1 cm quartz cuvettes, measured with Bradford assay (37). CD spectra were recorded: (1) in the presence of >15-fold EGTA concentration with respect to the protein concentration, (2) after addition of 1 mM $MgCl_2$, (3) after addition of 2-fold excess $CaCl_2$ with respect to the EGTA concentration. Experimental conditions for thermal denaturations between 20 and 96 °C were substantially the same as for far UV spectra. Setting parameters were as follows: wavelength 208 nm, scan rate 1 °C/min, data pitch 0.1 °C, response time 4 s. Experimental data were fitted for melting temperature estimation to a 4-parameter Hill sigmoid, whose equation is:

$$y = b_f + \frac{|b_f - b_n|T^H}{T_m^H + T^H}$$

Where b_f stands for the value of the folded protein, b_u for the value of the unfolded protein, T for temperature, H for Hill coefficient and T_m for melting temperature.

DLS experiments

DLS measurements were obtained with a Zetasizer Nano-S (Malvern Instruments) using disposable ZEN0112 polystyrene cuvettes. Machine settings were the following: solvent refractive index 1.330, viscosity 0.8872 cP, protein refractive index 1.450, protein absorption 0.001, temperature 25 °C, equilibration 2 min, measurement angle 173° backscatter, analysis model multiple narrow modes. Each experiment consisted of at least 14 runs, each of which was an average of 13 repetitions. Experiments were performed in the following buffer: 5 mM Tris-HCl pH 7.5, 150 mM KCl, 1 mM DTT, 1 mM $MgCl_2$, 500 μM EGTA. Protein concentration was measured (Bradford assays) after filtering with a 0.02 μm Anotop 10 filter (Whatman) and turned out to be 33–44 μM. Ca^{2+} concentration for each titration point was calculated using the Ca-Mg-ATP-EGTA Calculator software with the following settings: database NIST, $T = 25$ °C, pH 7.5, ionic strength 0.15 M (http://maxchelator.stanford.edu/CaMgATPEGTA-NIST.htm). Initial Ca^{2+} concentration was < 5.3 nM, Ca^{2+} titration steps were 30 μM, final Ca^{2+} concentration was 300 μM.

Tryptophan fluorescence titrations

Intrinsic W Fluorescence titrations were performed by two procedures: Ca^{2+}-titration experiments were done on a spectrometer form Photon Technology International (Birmingham, New Jersey, USA) as described before (16,34). Data were normalized to the maximal value (16,34). Spectra of Mg^{2+}-titration experiments were recorded with a Jasco FP-750 spectrofluorimeter in Tris/HCl 5mM, KCl 150 mM, DTT 1 mM, pH 7.5, EGTA 100 μM in 1 cm quartz cuvettes at 25 °C. Parameters were as follows: scan rate 60 nm/min, excitation wavelength 290 nm, emission between 300 and 380 nm, excitation and emission bandwidth 5nm. Mg^{2+} concentration for each titration point was calculated using the Ca-Mg-ATP-EGTA Calculator software with the following settings: database NIST, $T = 25$ °C, pH 7.5, ionic strength 0.15 M (http://maxchelator.stanford.edu/CaMgATPEGTA-NIST.htm). Protein concentration was 0.3 μM for mWT and mL176F, 0.4μM for nmWT and nmL176F for each titration point. Fluorescence emission intensity was monitored at the wavelength corresponding to the maximal emission of the protein in the sole presence of 100 μM EGTA. Initial Mg^{2+} concentration was 9 μM, while it reached 10 mM after complete titration. Due to the experimental set-up we could not absolutely exclude aging of the sample during a titrations set taking place for several hours. Therefore, data were normalized as follows $NF = (F - F_{min})/(F_{max} - F_{min})$, where F is the fluorescence emission at the specific wavelength (340 nm for m/nmWT GCAP1, 342 nm for mL176F, and 343 nm for nmL176F), F_{min} and F_{max} are the minimum and the maximum fluorescence intensity values of the dataset.

Molecular dynamics simulations and analyses

Three-dimensional models and states used for mWT GCAP1 were built using chicken GCAP1 as a template (38) using the same procedure as in (23). Mutation mL176F was generated in silico using the highest-scored rotamer estimated by the 'mutate residue' function of the Maestro (Schrodinger) software using the modelled mWT GCAP1 as a template.

Molecular dynamics simulations were performed using GROMACS 5.0.4 simulation package (39) using the CHARMM27 all-atom force field (40).

All settings for molecular dynamics simulations were taken from Marino *et al.* (23), in which details are provided, with the only difference in the production phase, which in this study consisted of 200 ns of simulations.

Resulting trajectories were subjected to Root-Mean Square Deviation (RMSD) and Root-Mean Square Fluctuations (RMSF) analyses. RMSD of the α-carbon of bidentate Glu residues of EF2, EF3 and EF4 (E75, E111, E155 respectively) was calculated using the 'gmx rms' function implemented in GROMACS 5.0.4 with respect to the starting structure of the production phase. RMSF of the α-carbon of all residues was calculated by the Wordom software (41,42), and represents the time averaged-RMSD with respect to the initial structure of the production phase, and is calculated as follows:

$$RMSF_i = \sqrt{\frac{1}{T}\sum_{t_j=1}^{T} \left| r_i(t_j) - r_i^{ref} 2 \right.}$$

where T is the 200 ns timeframe $r_i(t_j)$ and r_i^{ref} are the atomic coordinates of α-carbon *i* at time t_j and in the structure after 4 ns equilibration, respectively.

Supplementary Material

Supplementary Material is available at *HMG* online.

Acknowledgements

We thank Jutta Appelt for excellent technical assistance and Dr. Dror Sharon, Hebrew University in Jerusalem, Israel, for valuable comments on the manuscript.

Conflict of Interest statement. None declared.

Funding

This work was supported by funding from the Deutsche Forschungsgemeinschaft (DFG grant KO948/10-2 to KWK), from the DFG research training group GRK1885/1, the Italian Ministry for Research and Education (MIUR) via Departmental funding (FUR2013 to DDO), from CINECA through the Italian Super Computing Resource Allocation project (ISCRA Grant HP10CB7L79 to DDO).

References

1. Fritsche, L.G., Fariss, R.N., Stambolian, D., Abecasis, G.R., Curcio, C.A. and Swaroop, A. (2014) Age-related macular degeneration: genetics and biology coming together. *Annu. Rev. Genomics Hum. Genet.*, **15**, 151–171.
2. Armstrong, R.A. and Mousavi, M. (2015) Overview of Risk Factors for Age-Related Macular Degeneration (AMD). *J. Stem Cells*, **10**, 171–191.
3. Lambert, N.G., ElShelmani, H., Singh, M.K., Mansergh, F.C., Wride, M.A., Padilla, M., Keegan, D., Hogg, R.E. and Ambati, B.K. (2016) Risk factors and biomarkers of age-related macular degeneration. *Prog. Retin. Eye Res.*, doi: 10.1016/j.preteyeres.2016.04.003. [Epub ahead of print]
4. Tan, P.L., Bowes, R.C. and Katsanis, N. (2016) AMD and the alternative complement pathway: genetics and functional implications. *Hum. Genomics*, doi: 10.1186/s40246-016-0079-x.
5. Curcio, C.A., Medeiros, N.E. and Millican, C.L. (1996) Photoreceptor loss in age-related macular degeneration. *Invest. Ophthalmol. Vis. Sci.*, **37**, 1236–1249.
6. Berger, W., Kloeckener-Gruissem, B. and Neidhardt, J. (2010) The molecular basis of human retinal and vitreoretinal diseases. *Prog. Retin. Eye Res.*, **29**, 335–375.
7. Kamenarova, K., Corton, M., Garcia-Sandoval, B., Fernandez-San Jose, P., Panchev, V., Avila-Fernandez, A., Lopez-Molina, M.I., Chakarova, C., Ayuso, C. and Bhattacharya, S.S. (2013) Novel GUCA1A mutations suggesting possible mechanisms of pathogenesis in cone, cone-rod, and macular dystrophy patients. *Biomed. Res. Int.*, **2013**, article ID 517570.
8. Mendez, A., Burns, M.E., Sokal, I., Dizhoor, A.M., Baehr, W., Palczewski, K., Baylor, D.A. and Chen, J. (2001) Role of guanylate cyclase-activating proteins (GCAPs) in setting the flash sensitivity of rod photoreceptors. *Proc. Natl. Acad. Sci. U S A*, **98**, 9948–9953.
9. Koch, K.W. and Dell'Orco, D. (2013) A calcium-relay mechanism in vertebrate phototransduction. *ACS Chem. Neurosci.*, **4**, 909–917.
10. Wen, X.H., Dizhoor, A.M. and Makino, C.L. (2014) Membrane guanylyl cyclase complexes shape the photoresponse of retinal rods and cones. *Front. Mol. Neurosci.*, **7**, article 45.
11. Hwang, J.Y., Lange, C., Helten, A., Hoppner-Heitmann, D., Duda, T., Sharma, R.K. and Koch, K.W. (2003) Regulatory modes of rod outer segment membrane guanylate cyclase differ in catalytic efficiency and Ca(2+)-sensitivity. *Eur. J. Biochem.*, **270**, 3814–3821.
12. Peshenko, I.V., Olshevskaya, E.V., Savchenko, A.B., Karan, S., Palczewski, K., Baehr, W. and Dizhoor, A.M. (2011) Enzymatic properties and regulation of the native isozymes of retinal membrane guanylyl cyclase (RetGC) from mouse photoreceptors. *Biochemistry*, **50**, 5590–5600.
13. Makino, C.L., Wen, X.H., Olshevskaya, E.V., Peshenko, I.V., Savchenko, A.B. and Dizhoor, A.M. (2012) Enzymatic relay mechanism stimulates cyclic GMP synthesis in rod photoresponse: biochemical and physiological study in guanylyl cyclase activating protein 1 knockout mice. *PLoS One*, **7**, e47637.
14. Robin, J., Brauer, J., Sulmann, S., Marino, V., Dell'Orco, D., Lienau, C. and Koch, K.W. (2015) Differential nanosecond protein dynamics in homologous calcium sensors. *ACS Chem. Biol.*, **10**, 2344–2352.
15. Peshenko, I.V., Olshevskaya, E.V., Lim, S., Ames, J.B. and Dizhoor, A.M. (2012) Calcium-myristoyl Tug is a new mechanism for intramolecular tuning of calcium sensitivity and target enzyme interaction for guanylyl cyclase-activating protein 1: dynamic connection between N-fatty acyl group and EF-hand controls calcium sensitivity. *J. Biol. Chem.*, **287**, 13972–13984.
16. Kitiratschky, V.B., Behnen, P., Kellner, U., Heckenlively, J.R., Zrenner, E., Jägle, H., Kohl, S., Wissinger, B. and Koch, K.W. (2009) Mutations in the GUCA1A gene involved in hereditary cone dystrophies impair calcium-mediated regulation of guanylate cyclase. *Hum. Mutat.*, **30**, E782–E796.
17. Marino, V., Scholten, A., Koch, K.W. and Dell'Orco, D. (2015) Two retinal dystrophy-associated missense mutations in GUCA1A with distinct molecular properties result in a similar aberrant regulation of the retinal guanylate cyclase. *Hum. Mol. Genet.*, **24**, 6653–6666.
18. Dell'Orco, D., Behnen, P., Linse, S. and Koch, K.W. (2010) Calcium binding, structural stability and guanylate cyclase activation in GCAP1 variants associated with human cone dystrophy. *Cell. Mol. Life. Sci.*, **67**, 973–984.
19. Lim, S., Peshenko, I., Dizhoor, A. and Ames, J.B. (2009) Effects of Ca^{2+}, Mg^{2+}, and myristoylation on guanylyl cyclase activating protein 1 structure and stability. *Biochemistry*, **48**, 850–862.

20. Lim, S., Peshenko, I.V., Olshevskaya, E.V., Dizhoor, A.M. and Ames, J.B. (2016) Structure of guanylyl cyclase activator protein 1 (GCAP1) mutant V77E in a Ca^{2+}-free/Mg^{2+}-bound activator state. *J. Biol. Chem.*, **291**, 4429–4441.
21. Peshenko, I.V. and Dizhoor, A.M. (2006) Ca^{2+} and Mg^{2+} binding properties of GCAP-1. Evidence that Mg^{2+}-bound form is the physiological activator of photoreceptor guanylyl cyclase. *J. Biol. Chem.*, **281**, 23830–23841.
22. Dell'Orco, D., Sulmann, S., Zägel, P., Marino, V. and Koch, K.W. (2014) Impact of cone dystrophy-related mutations in GCAP1 on a kinetic model of phototransduction. *Cell. Mol. Life. Sci.*, **71**, 3829–3840.
23. Marino, V., Sulmann, S., Koch, K.W. and Dell'Orco, D. (2015) Structural effects of Mg^{2+} on the regulatory states of three neuronal calcium sensors operating in vertebrate phototransduction. *Biochim. Biophys. Acta*, **1853**, 2055–2065.
24. Hwang, J.Y. and Koch, K.W. (2002) Calcium- and myristoyl-dependent properties of guanylate cyclase-activating protein-1 and protein-2. *Biochemistry*, **41**, 13021–13028.
25. Michaelides, M., Wilkie, S.E., Jenkins, S., Holder, G.E., Hunt, D.M., Moore, A.T. and Webster, A.R. (2005) Mutation in the gene GUCA1A, encoding guanylate cyclase-activating protein 1, causes cone, cone-rod, and macular dystrophy. *Ophthalmology*, **112**, 1442–1447.
26. Jiang, L. and Baehr, W. (2010) GCAP1 mutations associated with autosomal dominant cone dystrophy. *Adv. Exp. Med. Biol.*, **664**, 273–282.
27. Dizhoor, A.M., Boikov, S.G. and Olshevskaya, E.V. (1998) Constitutive activation of photoreceptor guanylate cyclase by Y99C mutant of GCAP-1. Possible role in causing human autosomal dominant cone degeneration. *J. Biol. Chem.*, **273**, 17311–17314.
28. Sokal, I., Li, N., Surgucheva, I., Warren, M.J., Payne, A.M., Bhattacharya, S.S., Baehr, W. and Palczewski, K. (1998) GCAP1 (Y99C) mutant is constitutively active in autosomal dominant cone dystrophy. *Mol. Cell*, **2**, 129–133.
29. Nishiguchi, K.M., Sokal, I., Yang, L., Roychowdhury, N., Palczewski, K., Berson, E.L., Dryja, T.P. and Baehr, W. (2004) A novel mutation (I143NT) in guanylate cyclase-activating protein 1 (GCAP1) associated with autosomal dominant cone degeneration. *Invest. Ophthalmol. Vis. Sci.*, **45**, 3863–3870.
30. Olshevskaya, E.V., Calvert, P.D., Woodruff, M.L., Peshenko, I.V., Savchenko, A.B., Makino, C.L., Ho, Y.S., Fain, G.L. and Dizhoor, A.M. (2004) The Y99C mutation in guanylyl cyclase-activating protein 1 increases intracellular Ca^{2+} and causes photoreceptor degeneration in transgenic mice. *J. Neurosci.*, **24**, 6078–6085.
31. Behnen, P., Dell'Orco, D. and Koch, K.W. (2010) Involvement of the calcium sensor GCAP1 in hereditary cone dystrophies. *Biol. Chem.*, **391**, 631–637.
32. Sulmann, S., Dell'Orco, D., Marino, V., Behnen, P. and Koch, K.W. (2014) Conformational changes in calcium-sensor proteins under molecular crowding conditions. *Chemistry*, **20**, 6756–6762.
33. Zägel, P., Dell'Orco, D. and Koch, K.W. (2013) The dimerization domain in outer segment guanylate cyclase is a Ca^{2+}-sensitive control switch module. *Biochemistry*, **52**, 5065–5074.
34. Koch, K.W. and Helten, A. (2008). Guanylate cyclase-based signaling in photoreceptors and retina. *Chapter 6 in Signal Transduction in the Retina*. Fliesler S. J., and Kisselev O. G., ed. (Taylor and Francis CRC Press), pp. 121-143
35. Andre, I. and Linse, S. (2002) Measurement of Ca^{2+}-binding constants of proteins and presentation of the CaLigator software. *Anal. Biochem.*, **305**, 195–205.
36. Linse, S. (2002) Calcium binding to proteins studied via competition with chromophoric chelators. *Methods Mol. Biol.*, **173**, 15–24.
37. Bradford, M.M. (1976) A rapid and sensitive method for the quantitation of microgram quantities of protein utilizing the principle of protein-dye binding. *Anal. Biochem.*, **72**, 248–254.
38. Stephen, R., Bereta, G., Golczak, M., Palczewski, K. and Sousa, M.C. (2007) Stabilizing function for myristoyl group revealed by the crystal structure of a neuronal calcium sensor, guanylate cyclase-activating protein 1. *Structure*, **15**, 1392–1402.
39. Hess, B., Kutzner, C., Van Der Spoel, D. and Lindahl, E. (2008) GROMACS 4: Algorithms for Highly Efficient, Load-Balanced, and Scalable Molecular Simulation. *J. Chem. Theory. Comput.*, **4**, 435–447.
40. Bjelkmar, P., Larsson, P., Cuendet, M.A., Bess, B. and Lindahl, E. (2010) Implementation of the CHARMM force field in GROMACS: Analysis of protein stability effects from correction maps, virtual interaction sites, and water models. *J. Chem. Theory. Comput.*, **6**, 459–466.
41. Seeber, M., Cecchini, M., Rao, F., Settanni, G. and Caflisch, A. (2007) Wordom: a program for efficient analysis of molecular dynamics simulations. *Bioinformatics*, **23**, 2625–2627.
42. Seeber, M., Felline, A., Raimondi, F., Muff, S., Friedman, R., Rao, F., Caflisch, A. and Fanelli, F. (2011) Wordom: a user-friendly program for the analysis of molecular structures, trajectories, and free energy surfaces. *J. Comput. Chem.*, **32**, 1183–1194.

SCIENTIFIC REPORTS

OPEN

Allosteric communication pathways routed by Ca^{2+}/Mg^{2+} exchange in GCAP1 selectively switch target regulation modes

Received: 21 July 2016
Accepted: 09 September 2016
Published: 14 October 2016

Valerio Marino[1] & Daniele Dell'Orco[1,2]

GCAP1 is a neuronal calcium sensor protein that regulates the phototransduction cascade in vertebrates by switching between activator and inhibitor of the target guanylate cyclase (GC) in a Ca^{2+}-dependent manner. We carried out exhaustive molecular dynamics simulations of GCAP1 and determined the intramolecular communication pathways involved in the specific GC activator/inhibitor switch. The switch was found to depend on the Mg^{2+}/Ca^{2+} loading states of the three EF hands and on the way the information is transferred from each EF hand to specific residues at the GCAP1/GC interface. Post-translational myristoylation is fundamental to mediate long range allosteric interactions including the EF2-EF4 coupling and the communication between EF4 and the GC binding interface. Some hubs in the identified protein network are the target of retinal dystrophy mutations, suggesting that the lack of complete inhibition of GC observed in many cases is likely due to the perturbation of intra/intermolecular communication routes.

Conformational changes adopted by calcium-sensor proteins in response to Ca^{2+}-binding allow them to selectively recognize and regulate their targets, thereby contributing to the control of several biological processes[1]. For some calcium sensors such as the ubiquitous calmodulin the conformational switch is substantial and associated to a high degree of structural plasticity, which allows the recognition and regulation of a variety of different targets[2,3]. Other Ca^{2+}-sensors, however, are selectively expressed in specific cell types and regulate only a few, sometimes even unique biological targets. This is the case for the neuronal calcium sensors (NCS) family[4,5].

Guanylate cyclase activating proteins (GCAPs) are NCS involved in the early steps of vertebrate vision, which shape the photoresponse of rods and cones under different light conditions, thus contributing to the second messenger-controlled recovery of the phototransduction machinery following light stimulation[6]. By binding up to three Ca^{2+} ions with high, submicromolar affinity and up to two Mg^{2+} ions with lower affinity in their three functional EF-hand motifs, GCAPs show a remarkable and rather unique regulatory capability. The same protein indeed acts as an inhibitor of the membrane bound guanylate cyclase (GC) at high (250–800 nM) intracellular $[Ca^{2+}]$ corresponding to dark-adapted conditions, while it switches to an activator of the enzyme at low (20–100 nM) $[Ca^{2+}]$, thereby stimulating the synthesis of the second messenger cGMP necessary to switch off the light-activated cascade[7–9]. Two to eight GCAP isoforms have been observed in species from fish to human and the role of different GCAPs in rods and cones is well described by a Ca^{2+}-relay model, in which the control of photoreceptor physiological response depends on incremental changes in the cytoplasmic $[Ca^{2+}]$ sensed by GCAPs with slightly different affinity for Ca^{2+} [10–12].

GCAP1 is expressed both in rods and cones and has raised particular interest among other GCAPs as up to fifteen missense mutations in its codifying gene have been associated to retinal dystrophies[13,14], a heterogeneous set of vision-threatening diseases often leading to complete blindness. Biochemical investigations revealed that the majority of GCAP1 molecules carrying the mutations exhibit a more or less severe disturbance in Ca^{2+}-sensing properties, resulting in the constitutive activation of GC over the physiological range of $[Ca^{2+}]$, in which they normally switch between activating and inhibiting regulatory modes[15–20]. Some mutants have been shown to

[1]Department of Neurosciences, Biomedicine and Movement Sciences, Section of Biological Chemistry, University of Verona, strada le Grazie 8, I-37134 Verona, Italy. [2]Centre for BioMedical Computing (CBMC), University of Verona, strada le Grazie 8, I-37134 Verona, Italy. Correspondence and requests for materials should be addressed to D.D.O. (email: daniele.dellorco@univr.it)

affect the binding of Ca^{2+} and Mg^{2+} to one of the three specific EF-hands in GCAP1[15,21], however, in spite of the remarkable deregulation observed in GC activation, some other mutant showed no significant change in metal ion affinity compared to the wild type[18].

Biochemical and biophysical investigations established that it is the selective binding of either Ca^{2+} or Mg^{2+} ions to specific EF-hands that triggers the switch of GCAP1 from its GC inhibitory (three Ca^{2+} ions bound to EF2, EF3 and EF4) to its GC activating form (one Mg^{2+} ion bound to EF2, and putatively to EF3)[7–9]. More recently, it was suggested that the covalent myristoylation at its N-terminal, which controls the affinity of the GCAP1-GC interaction[22,23], is also involved in intramolecular communication with the opposite C-terminal domain by controlling the Ca^{2+} sensitivity of EF4[24,25]. A dynamic connection between the myristoyl moiety and EF4 was thus proposed, which implies a finely regulated allosteric communication between the N and C domains of GCAP1, however the mechanism by which Mg^{2+}/ Ca^{2+} exchange determines the fate of GCAP1 as a Ca^{2+} sensor and GC-regulator remains largely unknown.

We present a thorough structural analysis of both myristoylated and nonmyristoylated GCAP1 based on exhaustive Molecular Dynamics (MD) simulations that unveiled intramolecular communication pathways involved in the specific switch between GC activator/inhibitor states. Our findings suggest that the binding of either Ca^{2+} or Mg^{2+} to specific EF-hands is crucial for routing the information transfer from the ion binding site to distal sites where the interaction with the target GC occurs. Some key residues appear to be especially important to structurally interconnect distal sites via robust allosteric pathways that are only partially overlapped in the activating and inhibitory states. Finally, we found that several residues that are target of retinal dystrophy-associated mutations constitute important intramolecular hubs for the communication routes in GCAP1 thus playing a particularly important role in maintaining its GC inhibitory state. Perturbation of specific intramolecular communication pathways likely results in a lack of complete inhibition of the target GC.

Results

Exhaustive and convergent conformational sampling of GC-inhibiting and activating states of GCAP1 by Molecular Dynamics simulations. Myristoylated and nonmyristoylated GCAP1 (mGCAP1 and nmGCAP1, respectively) were simulated in their GC-inhibiting and activating states. Several independent studies (see Ref. 10 for a review) confirmed that the maximal GC inhibition by GCAP1 is achieved when each canonical EF hand is occupied by a Ca^{2+} ion. We therefore indicate the GC-inhibiting state as $EF2^{Ca}EF3^{Ca}EF4^{Ca}$ throughout this paper. The GC-activating state is instead associated to GCAP1 with a Mg^{2+} ion bound in EF2, and possibly in EF3 too[7–9,26]. We therefore indicate these activating states as $EF2^{Mg}$ and $EF2^{Mg}EF3^{Mg}$, respectively.

Five replicas of 200 ns MD simulations were run for each GCAP1 state and results were considered both individually and by concatenating the trajectories to form a comprehensive 1 μs trajectory. Root-mean square deviation plots calculated on Cα-atoms (RMSD) with respect to the equilibrated structures for the five 200 ns replicas of each simulated state are reported in Supplementary Figure S1. RMSD average values ranged between 2.18 ± 0.29 Å and 2.95 ± 0.67 Å, indicative of good reproducibility across each replica. However, it is well established that independent MD trajectories of the same system at the same temperature may sample slightly different portions of the conformational landscape, therefore RMSD *per se* is not an accurate index for sampling convergence[27]. We therefore performed Principal Component Analysis (PCA) of Cα fluctuations on each individual trajectory in order to define a low-dimensional subspace, in which essential protein dynamics can be better described. Projections of the MD trajectory from each replica along the first two principal components (PC1 and PC2) are shown in Fig. 1. The substantial overlapping of the scatter plots in the PC space sampled is consistent with a homogeneous sampling for each replica.

The similarity and therefore consistency between the conformational subspaces sampled by each replica and, comprehensively, by the concatenated trajectory was probed by computing the Root-Mean-Square Inner Product (RMSIP) of the first 20 PC, representing eigenvectors of the covariance matrix of each replica or of the whole concatenated trajectory (Fig. 2). Satisfactory values were obtained in all cases as proven by RMSIP values approaching unity both when comparing each replica with one another and when the comparison was extended to the concatenated comprehensive 1 μs trajectory. RMSIP values for nonmyristoylated GCAP1 were on average smaller compared to the myristoylated case, however they did not decrease below 0.65 (Fig. 2).

A further proof of conformational sampling convergence was provided by the computation of the cosine content c_1 of the first PC (PC1), which represents a necessary condition for the sampling convergence. It was demonstrated that insufficient sampling could lead to high (close to unity) c_i values, where i refers to any PC_i[27,28]. The c_1 of the six concatenated trajectories of GCAP1 states ranged between 0.0008 and 0.4246, while the average c_1 of the five 200 ns replicas for each simulated GCAP1 state ranged between 0.2490 and 0.6873. Since c_1 relative to the 1 μs concatenated trajectories were found to be lower than the average c_1's of each replica, the conformational sampling achieved when the concatenated trajectory was considered was generally significant and satisfactory.

Overall, these results confirm that each 200 ns MD replica represents an independent and conformationally consistent dynamic description of GCAP1 in all the tested states, and that the concatenated 1 μs trajectories constitute a suitable framework where to exhaustively investigate essential dynamic properties.

Persistent noncovalent interactions along MD trajectories of GCAP1 define a network with specific hubs and intramolecular communication routes. Hydrophobic, electrostatic and H-bond interactions between residues within the protein milieu may be highly transient or significantly persist in time, when they are aimed at maintaining a noncovalent contact necessary to transfer the information intramolecularly. Monitoring the time course of noncovalent interactions along the concatenated 1 μs MD trajectory of GCAP1 hence allowed us to eventually determine whether and how long would contacts persist between groups of interactions, in which amino acids are nodes and interactions are edges or arches in a graph representing the Protein Structure Network (PSN)[29–31].

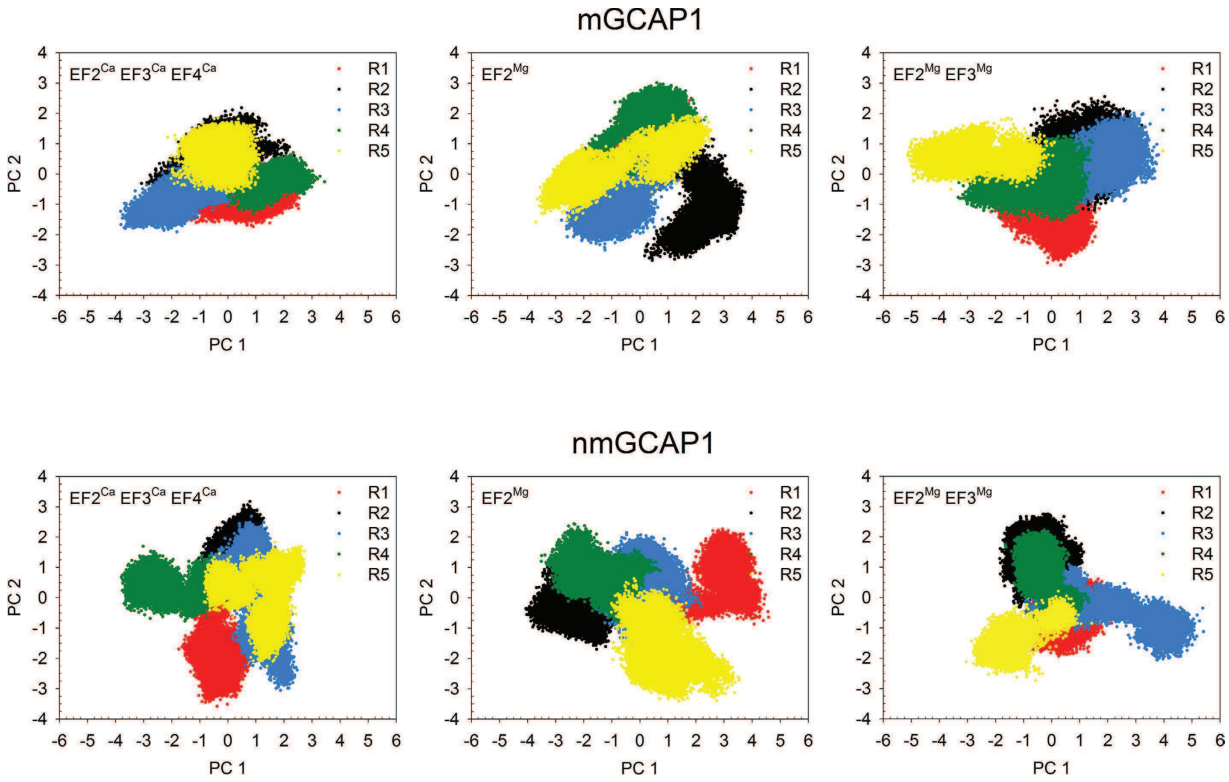

Figure 1. Projections of the frames extracted from each of the five 200 ns MD simulation replicas (R1 to R5) along the first two Principal Components (PC1 and PC2) calculated on the concatenated 1 μs trajectories of mGCAP1 (top panels) and nmGCAP1 (bottom panels) in their $EF2^{Ca}EF3^{Ca}EF4^{Ca}$ (left), $EF2^{Mg}$ (center) and $EF2^{Mg}EF3^{Mg}$ (right) forms. R1 frames are represented in red, R2 frames are black, R3 frames are blue, R4 frames are green, R5 frames are yellow.

The dynamic PSN calculated with the software PyInteraph (see Methods) over 1 μs MD simulations of $EF2^{Ca}EF3^{Ca}EF4^{Ca}$ mGCAP1 is shown in Fig. 3 as an example. The analysis highlighted the presence of some amino acids and ions forming persistent contacts with many neighboring residues, thus constituting hubs for the network. Persistence thresholds (p_T) for each simulated GCAP1 state were estimated (see Methods) in order to filter out transient interactions between residues, and ranged between 19.5% and 28.2%. Persistent interactions represented by edges in the PSN graph connect nodes located in even distal positions within GCAP1 tertiary structure. A thorough analysis of the degree of each hub, representing the number of neighboring residues per hub, as well as its position within the GCAP1 fold revealed important features for mGCAP1 and nmGCAP1 specific for each GC regulatory state. The highest degree hubs (degree = 7 or 8) in $EF2^{Ca}EF3^{Ca}EF4^{Ca}$ mGCAP1 are located in both the N- and C-terminal domains (Fig. 4, top), while they mostly concentrate in the C-domain in the $EF2^{Mg}$ mGCAP1 state. The $EF2^{Mg}EF3^{Mg}$ putative GC activating state of mGCAP1 showed a broader distribution, with 13 high-degree hubs compared to the 7 ones in the $EF2^{Ca}EF3^{Ca}EF4^{Ca}$ and $EF2^{Mg}$ mGCAP1 states (Supplementary Table T1 and Fig. 4, top). Interestingly, D64 and D100, respectively the first Ca^{2+}-coordinator residues of EF2 and EF3 were found among the highest-degree hubs in all mGCAP1 states, while other high-degree hubs varied depending on the GC regulatory state (Fig. 4, Supplementary Table T1). While the same two residues constituted high-degree hubs also for nmGCAP1 in all the three tested GC regulatory states (Supplementary Table T2 and Fig. 4, bottom), the GCAP1 variant lacking the myristoyl modification showed many more high-degree hubs (11 vs. 7) in the $EF2^{Ca}EF3^{Ca}EF4^{Ca}$ state, and less in the $EF2^{Mg}$ and $EF2^{Mg}EF3^{Mg}$ states (5 hubs for nmGCAP1 versus 7 and 13 for mGCAP1, respectively; Supplementary Tables T1 and T2 and Fig. 4).

Interestingly, the analysis of PSN hubs with a degree down to 4 highlighted for both mGCAP1 and nmGCAP1 the presence of several residues target of retinal dystrophies, especially in the $EF2^{Ca}EF3^{Ca}EF4^{Ca}$ GC-inhibitory state (Supplementary Tables T1 and T2). On the contrary, the myristoyl moiety was never found among the high-degree hubs (Supplementary Table T1), indicating the presence of many hydrophobic, yet non-persistent interactions along the 1 μs simulations.

An alternative PSN analysis performed using the elastic network analysis implemented in the WebPSN software (see Methods) overall suggested a similar role for the most important hubs already found by the dynamic analysis (Supplementary Table T3), although the consistency was in general not high.

Intermolecular communication between GCAP1 and its target: information transfer from each EF hand to the putative GC/GCAP1 binding interface. The conformational switch of GCAP1 between GC activating/inhibiting states following the specific exchange of metal ions in its EF-hands must be

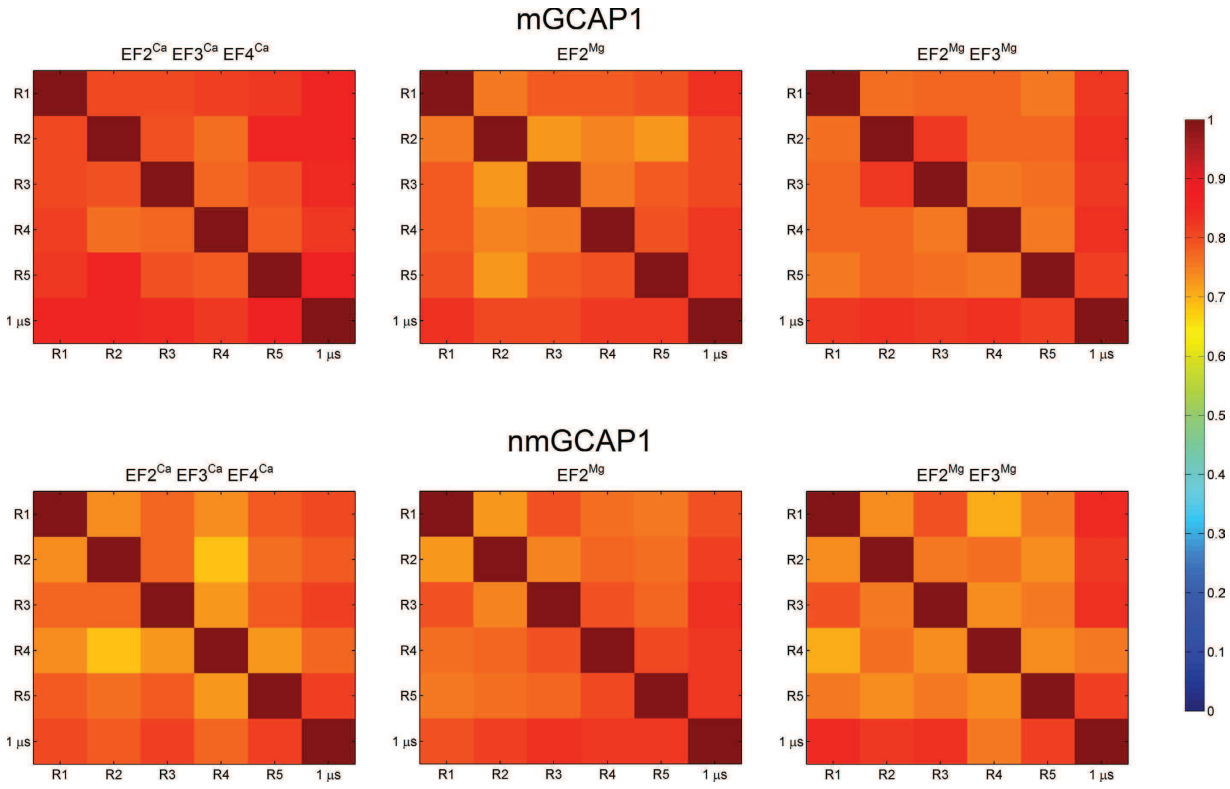

Figure 2. Root-Mean Square Inner Product (RMSIP) of the first 20 Principal Components representing the low frequency motions of each of the five 200 ns MD simulation replicas (R1 to R5) of mGCAP1 (top panels) and nmGCAP1 (bottom panels) in their $EF2^{Ca}EF3^{Ca}EF4^{Ca}$ (left), $EF2^{Mg}$ (center) and $EF2^{Mg}EF3^{Mg}$ (right) forms. The RMSIP is calculated for each replica against each other and against the concatenated trajectory (1 μs) and is represented in a color scale from blue (0) to dark red (1).

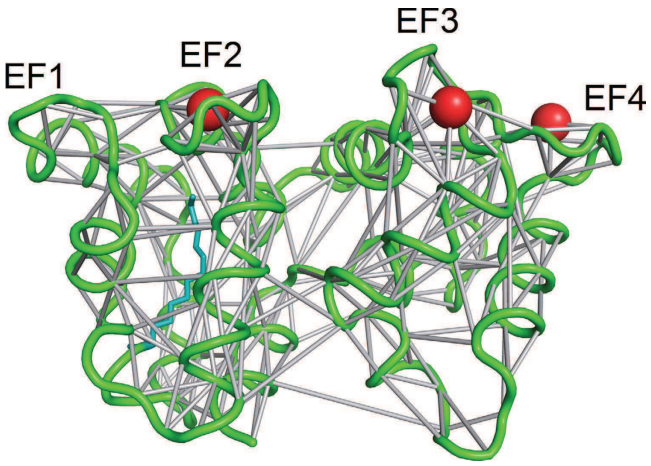

Figure 3. Example of Protein Structure Network calculated with PyInteraph for 1 μs MD simulation of $EF2^{Ca}EF3^{Ca}EF4^{Ca}$ mGCAP1. Secondary structure is represented in green cartoons, Ca^{2+} ions are shown as red spheres, the myristoyl group is represented by teal sticks, edges representing persistent interactions between residues (nodes) are shown as grey sticks connecting Cα-atoms or ions.

communicated to the target via a specific protein-protein interface. Several groups used different techniques to determine the putative GCAP1/GC interface[32–34] and consistently identified specific regions in EF1 and in the exiting helix of EF2 as the main constituents of the binding interface[32–34]. In addition, other residues located in the entering helix of EF3 have been shown to be important for GC binding and activation[32,34].

We considered all the residues suggested to form the putative GCAP1/GC binding interface, which is represented in Fig. 5. Overall, the identified interface shows somewhat disconnected areas, which seems *prima facie* incompatible with a unique GCAP1/GC binding mode. However, it might be possible that the interface follows

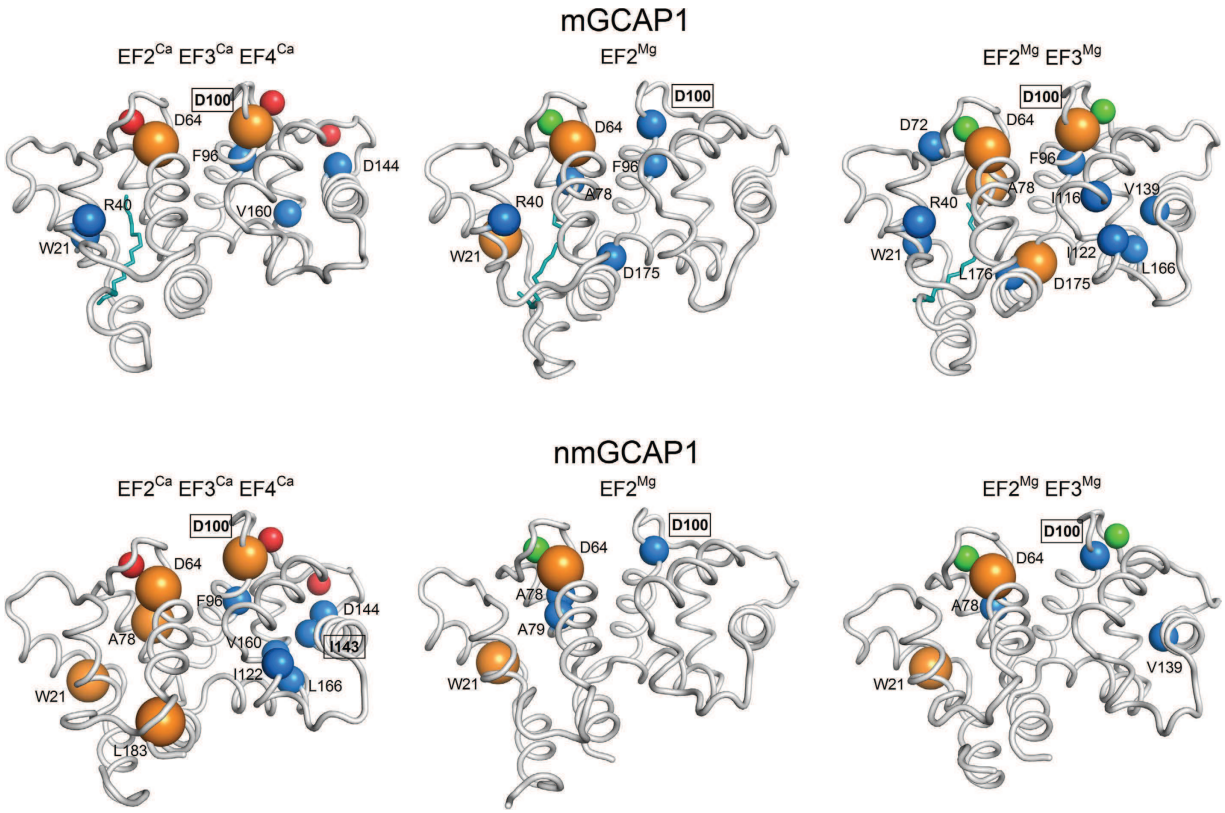

Figure 4. Highest degree hubs identified by PyInteraph in the PSN of mGCAP1 (top panels) and nmGCAP1 (bottom panels) in their $EF2^{Ca}EF3^{Ca}EF4^{Ca}$ (left), $EF2^{Mg}$ (center) and $EF2^{Mg}EF3^{Mg}$ (right) forms. Secondary structure is represented in grey cartoons, Ca^{2+} ions are shown as red spheres, Mg^{2+} ions are shown as green spheres, the myristoyl group is represented as teal sticks, Cα of degree 7 hub residues are represented in blue spheres, Cα of degree 8 hub residues are represented in orange spheres with increased radius. Residues whose mutation is associated with cone, cone-rod or macular dystrophies are labelled in bold and framed.

the conformational switch of GCAP1 between its GC inhibiting/activating states, thereby plastically remodeling itself to cover specific regions in the different regulatory states. We therefore explicitly considered all plausible binding sites between GCAP1 and GC and investigated how the information may route into specific pathways interconnecting each EF-hand to each putative GC binding site.

In order for a communication pathway connecting two nodes A and B to be robust, some requirements should be fulfilled. According to the parsimony principle, the higher the number of shortest paths connecting A and B and the more persistent the noncovalent interactions defining the path itself, the more robust the communication pathway. We translated these requirements into a simple definition of the communication robustness (CR) index defined in Equation 1:

$$CR = \frac{\sigma_{AB} \cdot p_T}{l} \quad (1)$$

where σ_{AB} indicates the number of paths with the shortest length connecting A and B, p_T is the significance threshold for the interaction persistence (see Methods) and l is the length of the shortest paths. The CR index defined above allowed us to systematically investigate the robustness of all identified pathways interconnecting each EF hand, where the Ca^{2+}/Mg^{2+} binding occurs, with each putative GC binding site, in all the GC regulatory states of GCAP1. As a residue representative for the corresponding EF hand we chose to consider the glutamate providing the bidentate oxygen ligands for Ca^{2+}, namely E75 for EF2, E111 for EF3 and E155 for EF4. Results of the analyses for mGCAP1 are reported in Fig. 6.

As a general trend, no particularly high-robustness pathway for GC regulation was found starting from EF2 (E75) considering the relatively short distance between the Ca^{2+}/Mg^{2+} binding region and most of the GC putative binding residues (Fig. 5). The computed CR index indeed never exceeded 0.3, the value observed for E38 in the $EF2^{Mg}$ state, and no major difference was observed for the tested mGCAP1 regulatory states (Fig. 6). In contrast, the highest affinity binding site for Ca^{2+} E111 (EF3) resulted to be more robustly connected to GC interfacial residues, especially in the $EF2^{Ca}EF3^{Ca}EF4^{Ca}$-GC inhibiting state, mostly via the Y22, C29, Y37 and K87 residues (Fig. 6). Switching to GC activating states, either $EF2^{Mg}$ or $EF2^{Mg}EF3^{Mg}$ significantly decreased the communication robustness, except for E38, which showed an opposite trend, where CR increased from 0.14 to 0.24–0.26. E38 thus seems to be an essential residue to mediate target inhibition by ensuring the communication

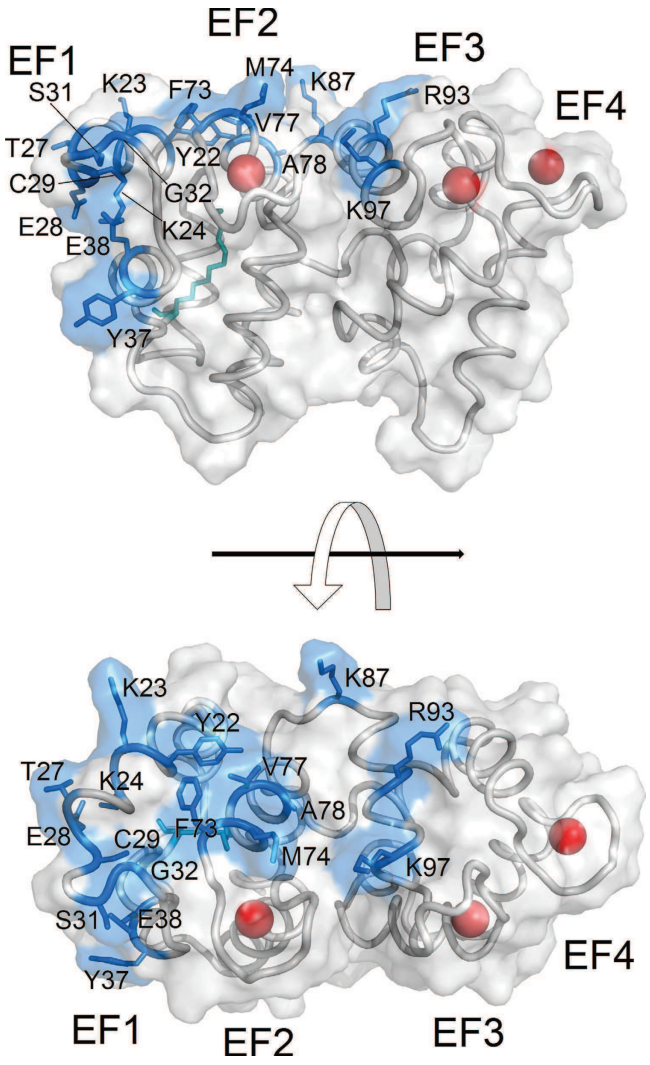

Figure 5. Residues of mGCAP1 involved in the putative interface with the target Guanylate Cyclase. The $EF2^{Ca}EF3^{Ca}EF4^{Ca}$ form is represented in grey cartoons together with its molecular surface, Ca^{2+} ions are shown as red spheres, the myristoyl group is represented in teal sticks, residues belonging to the putative GC interface are represented as blue sticks together with their molecular surface. Residues forming the putative GCAP1/GC interface have been identified in former studies (see text and refs 32,33,34).

of the Ca^{2+}-loaded state of EF3. Interestingly, the relatively high distance between EF4 (E155) and all putative GC binding sites did not prevent the emergence of some particularly robust communication pathways (Fig. 6). While generally E155 showed a low CR index ($\leq$0.1) for many GC interfacial residues, four of them showed remarkably high robustness, namely E38 in its $EF2^{Ca}EF3^{Ca}EF4^{Ca}$ (CR = 0.5) and $EF2^{Mg}$ (CR = 0.7) states, Y22, K23 and C29 in the GC activating states ($EF2^{Mg}$ or $EF2^{Mg}EF3^{Mg}$; CR values between 0.3 and 0.6). The particularly high CR values in the Mg^{2+}-bound states for Y22 and K23 suggest that these two residues are important for communicating to the GC the unloaded status of EF4. In general, the metal-bound state of the distal EF4 motif in mGCAP1 has to be therefore precisely and robustly communicated to specific GC binding residues to ensure the target switch between its operational states.

Interestingly, only a few residues forming the GC binding interface show robust intramolecular communication with all three EF hands in each GC regulatory state. E38, located at the exiting helix in the EF1 motif (Fig. 5) seems to be well connected to both EF2 (CR between 0.25 and 0.30 with E75 in the $EF2^{Ca}EF3^{Ca}EF4^{Ca}$ and $EF2^{Mg}$ states, respectively) and EF3 (CR 0.16–0.28 with E111), and as noticed extremely well connected to EF4, giving the highest CR index in this case (CR 0.5–0.7 with E155) (see Fig. 6). Therefore, E38 seems to be an essential residue to communicate to the target GC about the loading status of the distal EF-hand 4. Particularly apparent was also the robustness of the communication pathways found between EF3 and C29 (Fig. 6), located in the entering helix in EF1 not far from E38, however robustness was limited to the $EF2^{Ca}EF3^{Ca}EF4^{Ca}$ state (CR = 0.48 vs. 0.12 in the $EF2^{Mg}$ state). This could imply that the contact between GC and C29 is necessary to keep the target in its inhibiting state. Other specific patterns of less robust communication could be observed between each EF hand and GC interfacial site (Fig. 6).

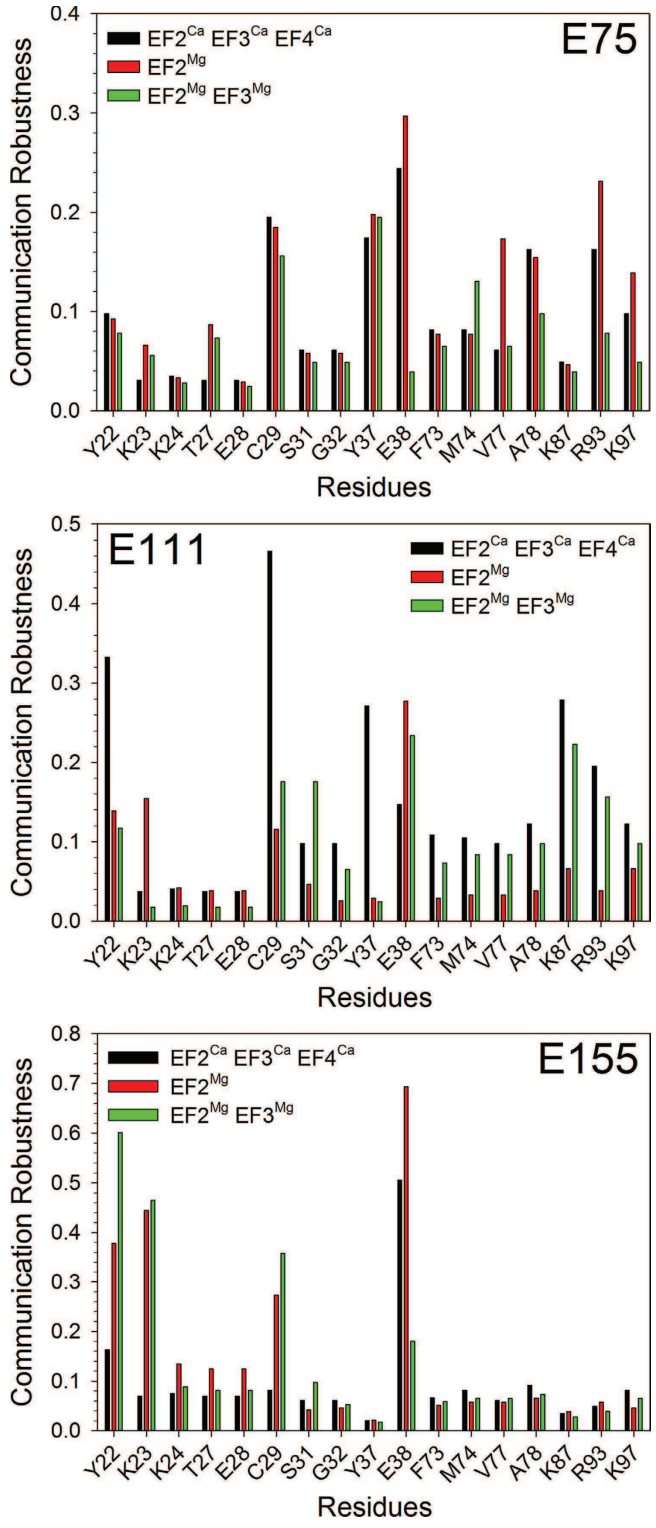

Figure 6. Communication Robustness between bidentate Glu residues of EF2 (top), EF3 (middle), EF4 (bottom) and residues belonging to the GC binding interface of mGCAP1 in its $EF2^{Ca}EF3^{Ca}EF4^{Ca}$ (black), $EF2^{Mg}$ (red) and $EF2^{Mg}EF3^{Mg}$ (green) forms.

The dynamic PSN analysis further allowed us to determine for each amino acid (or node) the selective betweenness centrality (SB, see Methods), indicative of the number of shortest paths between specific vertices that pass through that node. Figure 7 and the Supplementary Videos V1, V2 and V3 show the pathways identified by nodes with the highest SB connecting each EF hand bidentate ligand with the residue in the putative GC binding interface, for which the CR was maximal. As seen above (Fig. 6), EF2 (E75 residue) was mostly connected to E38 (Fig. 7, top) in both GC activating (blue path) and inhibiting (yellow path) states, while EF3 (E111 residue)

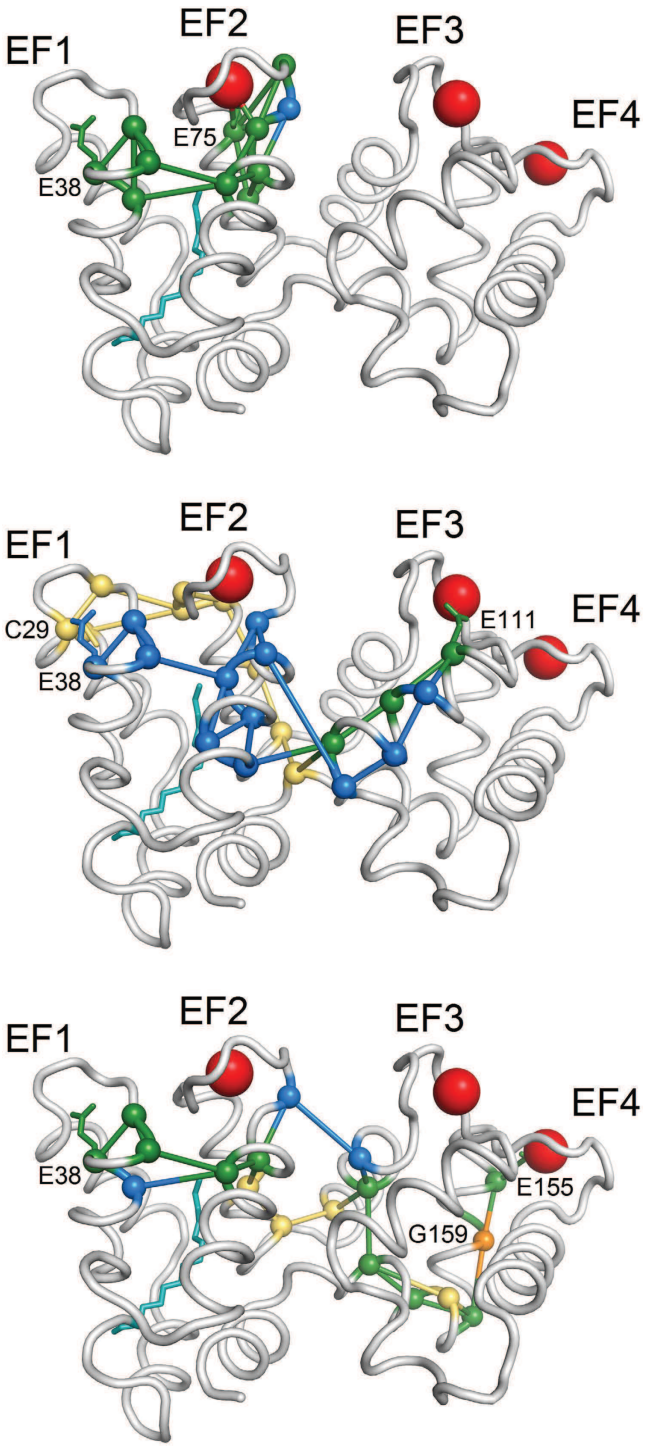

Figure 7. Paths constituted by nodes with the highest selective betweenness connecting bidentate Glu residues of EF2 (top), EF3 (middle) and EF4 (bottom) and the residues belonging to the GC binding interface with the highest CR. Secondary structure is represented in grey cartoons, Ca^{2+} ions are shown as red spheres, the myristoyl group is shown as teal sticks, Cα of the residues belonging to the paths are shown as spheres, edges are shown as sticks, the sidechains of the extremes of the paths are represented as sticks. Nodes and edges specific of the $EF2^{Ca}EF3^{Ca}EF4^{Ca}$ form are represented in yellow, those specific of the $EF2^{Mg}$ form are blue, those in common are green. Residue G159, whose mutation in V is associated with retinal dystrophies, is represented in orange.

showed higher robustness in communication with C29 (Fig. 7, middle) in the GC inhibiting state (yellow path) and with E38 in the GC activating state (blue path). Finally, EF4 (E155 residue) was robustly connected to E38

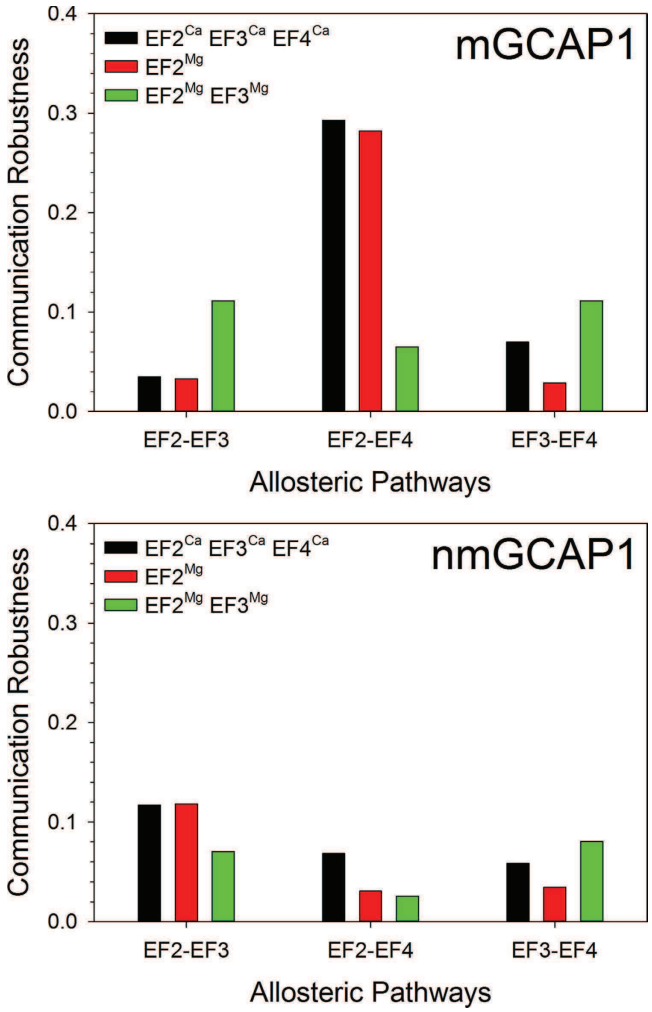

Figure 8. Communication Robustness among bidentate Glu residues of EF2, EF3 and EF4 of mGCAP1 (top) and nmGCAP1 (bottom) in their $EF2^{Ca}EF3^{Ca}EF4^{Ca}$ (black), $EF2^{Mg}$ (red) and $EF2^{Mg}EF3^{Mg}$ (green) forms.

(Fig. 7, bottom) in both the GC activating (blue path) and inhibiting (yellow path) states. It is worth noting that the individuated communication pathways can be partly overlapped (green paths), meaning that some residues are important both for transferring the information to the proper GC binding site in the GC activating and inhibiting states of GCAP1 (Fig. 7).

Intramolecular communication between EF hands in mGCAP1. The analysis of intramolecular communication in GCAP1 in its various GC regulatory states was performed also to unveil potential allosteric mechanisms involving the metal ion-binding sites. We therefore calculated the CR index along the 1 μs MD trajectory between each bidentate ion ligand in EF2, EF3 and EF4. Results for mGCAP1 are shown in Fig. 8 (top). No significantly robust communication pathway could be identified that connects EF2 with the contiguous EF3 or EF3 with EF4. Surprisingly, a significantly high CR (approximately 0.3) was detected for the connection between EF2 and EF4, both in the $EF2^{Ca}EF3^{Ca}EF4^{Ca}$-GC inhibiting and $EF2^{Mg}$-GC activating states. The connection lost robustness in the $EF2^{Mg}EF3^{Mg}$ state ($CR \approx 0.06$; Fig. 8, top).

Role of myristoyl in mediating allosteric communications and GC interactions. The GCAP1 form lacking the myristoyl moiety showed a somewhat different pattern of intramolecular communication robustness concerning the connections between EF hands and putative GC binding sites (Supplementary Figure S4). While a general trend of decreased robustness could be observed in all the tested GCAP1 states (compare Fig. 6 and Supplementary Figure S4), the most apparent differences are the following: a) an almost complete loss of robust communication pathways between EF4 (E155) and the putative GC-binding sites was found for nmGCAP1 (Supplementary Figure S4, bottom), the only exceptions being the mildly robust communication with E38 and G32 in the $EF2^{Mg}EF3^{Mg}$ state; b) the highly robust communication pathways identified between EF3 (E111) and some GC-interface residues in the GC-inhibiting state were replaced by some lower robustness communication pathways with G32, Y37 and F73 (Supplementary Figure S4, middle) in the $EF2^{Mg}$, GC-activating state; c) the interaction between E38 and EF2 (E75) remained highly robust for nmGCAP1 ($CR = 0.32$) only in the

$EF2^{Ca}EF3^{Ca}EF4^{Ca}$-GC inhibiting state, at odds with the myristoylated form, for which both GC regulatory states had robust connections (Supplementary Figure S4, top, vs Fig. 6, top).

Significant differences could be observed for nmGCAP1 compared to the myristoylated form also regarding the inter EF-hand communication (Fig. 8, bottom). Interestingly, no significantly robust communication was observed between either couple of EF-hands in each tested GC regulatory state for nmGCAP1, in particular the distal robust communication between EF2 and EF4 observed for mGCAP1 in both GC activating and inhibitory states was completely lost (Fig. 8, bottom).

We also checked whether robust communication pathways could be identified between the myristoyl moiety and the putative GC binding site. Results reported in Supplementary Figure S2 (top) showed that this is not generally the case. Indeed, except for M74 in the $EF2^{Ca}EF3^{Ca}EF4^{Ca}$ and $EF2^{Mg}EF3^{Mg}$ states (CR ≈0.18), R93 in both Mg^{2+}-bound states (CR≈0.14) and Y37 in the $EF2^{Ca}EF3^{Ca}EF4^{Ca}$ state (CR ≈0.12) all other residues were not connected to the myristoyl by robust pathways. Mildly robust communication pathways were detected between the myristoyl and EF2 in the $EF2^{Ca}EF3^{Ca}EF4^{Ca}$ state (CR ≈0.25), however CR was halved in both Mg^{2+}-bound states (Supplementary Figure S2, bottom). Except for the GC-inhibiting state, for which a significant CR was detected for the communication with EF3 (E111) no other state showed significant values for the communication robustness, in particular no robust path could be identified that connects the myristoyl moiety with EF4 (Supplementary Figure S2, bottom).

Discussion

GCAPs share their general three-dimensional fold with the other members of the NCS family. However, they show the rather unique feature of being at the same time activators and inhibitors of their biological GC target depending on the level of intracellular calcium. Understanding the mechanism by which relatively small protein conformational changes result in such diverse biochemical properties is not trivial, and yet it would be crucial to shed light on the molecular basis of some inherited retinal diseases caused by the deregulation of second messenger homeostasis in photoreceptors. This is especially true for GCAP1, for which up to 15 point mutations have been found to date that cause cone, cone/rod and/or macular dystrophies[13–20].

We performed exhaustive MD simulations of both myristoylated and nonmyristoylated GCAP1 in each GC regulatory state. A comprehensive and consistent sampling of the conformational space has been achieved by the analysis of protein essential dynamics (Figs 1 and 2), which focuses on collective motions to unveil protein conformational transitions[35]. Previous MD studies by us[8,36] and others[37] as well as dedicated biophysical experiments[38,39] showed that the Ca^{2+} binding induces relatively small conformational changes in GCAP1, and that its replacement with Mg^{2+} in specific binding sites may significantly perturb protein compactness and flexibility[8]. In the present study we investigated the details of GCAP1 structural dynamics by carrying out a set of more extensive MD simulations. We concatenated the trajectories from five 200 ns replicas of GCAP1, thus ending up in a consistent 1 μs trajectory where we could perform network-level analyses and highlight long-range communication pathways. The PSN paradigm applied to sufficiently long and convergent MD trajectories has a great potential to find out connections between conformational dynamics and allostery mechanisms, as it has been shown recently in other protein systems[30,40].

An important finding in our study is that the Mg^{2+}/Ca^{2+} exchange in specific EF hands creates selective intramolecular pathways connecting directly the metal ion binding sites with the GC binding sites. According to the PSN paradigm, in which amino acids are nodes and the interaction among them edges, some residues acquire the role of hubs for they mediate many persistent interactions (Figs 3 and 4). The number and the distribution of high degree hubs was shown to depend on the specific GC regulating state and the presence or absence of the myristoyl modification (Fig. 4 and Supplementary Tables T1-T3). The dynamic analysis performed with PyInteraph highlighted the constant presence of D64 and D100 among the highest-degree hubs, a particularly important result since D100 is the target of the cone-dystrophy related D100E/G mutations[17,41]. Other residues target of retinal dystrophy-associated point mutations were found among high-degree hubs both in the GC activating and inhibiting states of mGCAP1 and, to a lower extent, of nmGCAP1 (Supplementary Tables T1 and T2). Partly consistent results were found when the elastic network/PSN analysis was carried out with the WebPSN tool (Supplementary Table T3). Some level of discrepancy with the results obtained by PyInteraph is indeed not surprising, as WebPSN is based on a simple armonic potential applied to a static starting structure, therefore the approach keeps a memory of such initial conditions. Nonetheless, the method suggested a similar role for the most important hubs (Supplementary Table T3).

The communication pathways in GCAP1 are determined by the persistent contacts between contiguous amino acids, which define specific routes extending within the protein structure. These selective routes stabilize specific interaction patterns that are necessary for achieving GC inhibition or activation. This concept may help solving the puzzling evidence of disconnected GC/GCAP1 interfacial areas observed in independent studies[32–34]. According to the Mg^{2+}/Ca^{2+} loading status of each EF-hand, specific communication routes are created within GCAP1 structure that end up in appropriate residues to communicate and trigger GC activation or inhibition. As a consequence, the GCAP1/GC interface might therefore "plastically" adapt to the specific GCAP1 status in order to optimize the protein-protein contacts for proper information transfer. The close proximity of such residues (Fig. 5) would allow the interface optimization to occur without major conformational changes.

Our network-level analysis permitted the identification of specific long range communication pathways connecting distal GCAP1 regions belonging to the N- and C-terminal domains, and to assess the role of myristoylation in mediating such interactions. In spite of the relatively long distance from the putative GC binding sites, EF4 has been shown to robustly communicate with some residues at the GC interfacial region, including the spatially close E38 and C29 (Fig. 5), which are also the ending points of very robust intramolecular routes originated in EF3 and, to a lower extent, EF2 (Figs 6 and 7). Pathways made up of nodes with the highest SB route the information transfer to close or identical interfacial residues of mGCAP1 in its different GC regulatory states, however

they are only partly overlapped (Fig. 7). The pattern of intramolecular communication pathways was shown to be considerably different for nmGCAP1 (Supplementary Figure S4). In general, no significantly robust communication was observed in this case between EF4 and the GC putative binding sites (Supplementary Figure S4, bottom). The myristoyl group was never found among the highest-degree hubs (Supplementary Tables T1-T3), and its communication robustness with the GC putative binding sites was modest in each simulated mGCAP1 state (Supplementary Figure S2, top). The fact that the communication robustness with GCAP1 EF hands was found to be significant only for the nearby EF2 in its GC-inhibiting state (Supplementary Figure S2, bottom) suggests that the myristoyl is a transient connector of important intramolecular interactions rather that a central hub. Its presence is however essential to guarantee the correct routing of the information transfer about the loading state from EF4 to the GC binding site. This finding is substantially in line with the "tug" mechanism proposed by Peshenko *et al.*[25], in which a dynamic connection between the myristoyl and EF4 was hypothesized to attenuate the efficiency of GC activation in exchange for optimal Ca^{2+} sensitivity. The importance of Ca^{2+} binding to EF4 in propagating the conformational information to the GC binding interface, thus leading to the inhibiting/activating switch was recently highlighted by Lim *et al.* in an NMR study, in which the largest Ca^{2+}-dependent structural differences were observed in the EF4 region and in the adjacent so called "switch helix" composed by the 164–174 stretch[24]. Our results are fully consistent with this observation, as all the pathways constituted by nodes with the highest SB connecting EF4 and GC putative binding interface residues include residues belonging to the switch helix (Fig. 7). Our study thus confirms the role of this helical stretch, which may act as a conduit relaying Ca^{2+}-induced structural changes in EF4 to the GC binding site[24].

Another important result from the dynamic analysis performed here is that a robust long range communication between EF2 and EF4, which are distal metal ion binding motifs belonging to the N- and C-terminal domains respectively, was clearly detected both for the GC activating and inhibiting state of mGCAP1 (Fig. 8). This interdomain allosteric interaction takes place only in the presence of the N-terminal myristoylation (Fig. 8), and is likely crucial for GCAP1 switch function as it connects the two metal ion binding sites with intermediate (EF4) and lowest (EF2) affinity for Ca^{2+}, which have respectively negligible and highest affinity for Mg^{2+} [7,9]. It has been long established that the Ca^{2+}-mediated activation of GC by GCAPs is highly cooperative[42] although biophysical evidence strongly suggests that Ca^{2+} binding to GCAP1 occurs without any apparent cooperativity[15,43], except for one case (L84F mGCAP1) in which cooperativity was observed[18]. Our data show that an allosteric mechanism may connect two metal ion binding sites without observed cooperative effects on the binding affinity. The presence or the absence of a specific ion bound to an EF hand can then be communicated to a distal EF hand without affecting the metal ion affinity of this latter.

In conclusion, our analysis suggests that GCAP1 capability of switching between different GC regulatory states depends on the Mg^{2+}/Ca^{2+} binding states and the way the information is transferred to specific residues at the interface with the target. Post translational myristoylation is fundamental to mediate long range allosteric interactions although the fatty acid *per se* is not a hub for intramolecular interactions. Some amino acids with high selective betweenness centrality in the PSN may largely perturb the intramolecular communication pathways necessary for switching between GCAP1 regulatory modes, and the fact that some hubs are target of retinal dystrophy mutants suggests that the lack of complete inhibition of the target GC observed in many cases is likely due to the perturbation of these intermolecular routes. More in general, our computational approach can be applied to other NCS proteins and extended to investigate intermolecular as well as intramolecular communication, thus being of great potential for unveiling poorly understood molecular mechanisms under physiological and altered conditions.

Methods

Molecular Dynamics simulations of GCAP1 in its GC activating/inhibiting states. The homology model of human mGCAP1 in its $EF2^{Ca}EF3^{Ca}EF4^{Ca}$ state was built using the structure of chicken mGCAP1[44] as template using a previously elucidated protocol[15]. Models of nmGCAP1 were built by removing the myristoyl group, $EF2^{Mg}$ and $EF2^{Mg}EF3^{Mg}$ m/nmGCAP1 states were modeled either by removing Ca^{2+} ions from the respective EF-hand or by replacing them with Mg^{2+} ions as reported in ref. 8.

MD simulations of all GCAP1 states were performed using GROMACS 5.0.4 simulation package[45] with the CHARMM27 all-atom force field[46]. All settings for MD simulation and CHARMM27 parameters for the myristoyl group were the same as in ref. 8, in which details are provided. All structures were subjected to energy minimization, first with the steepest descent ($F_{max} = 1000\,kJ\,mol^{-1}\,nm^{-1}$), then with the conjugate gradients ($F_{max} = 500\,kJ\,mol^{-1}\,nm^{-1}$) algorithm, by keeping the position of backbone atoms and ions fixed in both cases. The systems were equilibrated at 310 K for 2 ns of backbone position-restrained MD simulations and then at 310 K for 2 ns of unrestricted MD simulations. After equilibration, all systems underwent 200 ns unrestrained isothermal-isobaric (NPT ensemble, T = 310 K, P = 1 atm) MD simulation. To achieve an exhaustive sampling of the conformational space, five independent replicas of each system were generated by changing the random seed for the generation of initial velocities of the two equilibration and the production phases.

In order to assess the stability of the simulations, the RMSD for the five 200 ns replicas of each state was calculated on Cα atoms with respect to the relative structure after 4 ns equilibration. The average RMSD values ranged between 2.18 and 2.95 Å in the tested GCAP1 states.

Principal Component Analysis. PCA is a widely-known tool to filter high-frequency motions in MD trajectories, taking advantage of the eigenvectors and eigenvalues of the mass-weighted covariance matrix (C) of the atomic positional fluctuations[47]. The C matrix was calculated for each state on protein alpha-carbons (Cα) of each replica and of the concatenated trajectories after superimposition to a reference structure, which was chosen as the conformation observed after the 4 ns equilibration phase in one of the five different replicas.

The PCA technique is based on the diagonalization of matrix C allowing for the identification of a set of eigenvectors and eigenvalues describing, respectively, direction and amplitude of the collective atomic motions or principal components (PC). Eigenvalues are ranked in decreasing order, therefore PC1 is the direction which describes the largest collective motion of the system, PC2 accounts for the second largest motion and so on. In order to analyze the consistency of the conformational space sampled by each replica, we projected the simulated trajectories on the first two PCs for the comparison of the main collective motions (Fig. 1).

It is possible to define the Essential Subspace (ES) as a subset of PCs which accounts for a percentage of total motion, in order to remove the noise represented by high frequency motions. Such percentage can be computed as the ratio between cumulative eigenvalues relative to the eigenvectors belonging to the ES and the sum of all eigenvalues of the system. The ES was defined by the first 20 PC of each replica and concatenated trajectories, describing at least 80% of the variance.

The sampling convergence of each individual MD replica as well as the concatenated trajectories was assessed by computing both the cosine content and the RMSIP indexes for each GCAP1 simulated state. The cosine content (c_1)[48] of the first PC (p_1) of C defining the ES was calculated as defined in Equation 2:

$$c_1 = \frac{2}{T}\left(\int_0^T \cos\left(\frac{\pi t}{T}\right) p_1(t)\,dt\right)^2 \left(\int_0^T p_1^2(t)\,dt\right)^{-1} \tag{2}$$

where T is the total simulation time.

The RMSIP index, a measure of similarity between the ES describing each replica and concatenated trajectory[49], was computed as defined in Equation 3:

$$RMSIP = \left(\frac{1}{S}\sum_{i=1}^{S}\sum_{j=1}^{S}\left(n_i^A \cdot n_j^B\right)^2\right)^{\frac{1}{2}} \tag{3}$$

where $n^A{}_i$ and $n^B{}_j$ are the eigenvectors of the ES of the replicas A and B to be compared and S is the dimensionality of the ES (S=20 in this case).

RMSD matrices and cluster analysis. The average structure for each concatenated trajectory was computed. For each frame of the concatenated trajectory the Cα -RMSD with respect to the average structure was calculated and the average RMSD value (ranging between 1.72 and 2.32 Å in all the tested GCAP1 states) was adopted as the cutoff for the cluster analysis.

Cα-RMSD matrices were computed with respect to the reference average structure defined above to perform cluster analysis of the concatenated trajectories. In order to reduce matrix dimensionality (originally 100,000 × 100,000 frames), 1 out of 4 frames of the concatenated trajectories were considered for the computation of the matrix. RMSD matrices were then processed using the Linkage[50] and Gromos[51] clustering algorithms, using the aforementioned average RMSD value as the cutoff. The Linkage and Gromos algorithms gave different results in terms of number of identified clusters. The Linkage algorithm identified only one cluster, at odds with the Gromos algorithm, which identified 20 to 38 clusters, depending on the state. Since the most populated cluster identified by Gromos algorithm always contained the cluster centers identified by Linkage algorithm, these latter only were used for the analyses done by WebPSN and for structural representations in Figs 3, 4, 5 and 7.

PyInteraph. Concatenated trajectories were subjected to a dynamic network analysis provided by PyInteraph[52], a software that generates a graph of intramolecular connections based on different types of interactions, namely salt bridges, H-bonds and hydrophobic interactions. The software computes an index of persistence of interaction based on the percentage of frames, for which distance cutoff constraints for the specific interaction are satisfied. Parameters for hydrophobic and electrostatic interactions for ions and the myristoyl group were generated manually and are available upon request. The cutoffs for distance and angle of H-bonds were set to default values (3.5 Å and 120° respectively), as well as that for electrostatic interactions (4.5 Å). The cutoff for the distance between the center of mass of the hydrophobic residue-side chains (including the myristoyl group) was set to 5.5 Å; the mass for each single atom was defined according to the CHARMM27 force field. The size of largest hydrophobic connected component (cluster) is the most restrictive constraint for the creation of the PSN[53], therefore its value was calculated at 5% persistence intervals to determine the significance threshold for interaction persistence p_T, which was computed as shown in Supplementary Figure S3. The p_T parameter was calculated for each GCAP1 simulated state (Supplementary Figure S3) and used to filter all three respective interaction graphs (e.g., electrostatic, H-bonds and hydrophobic), which were then joined in a single PSN representing the specific GCAP1 state.

Network analysis representation. Selective betweenness (SB) was computed based on the definition of betweenness, taking into account only the shortest paths between residues A and B (σ_{AB}) and not all possible shortest paths between all nodes of the PSN. In detail, SB was defined as in Equation 4:

$$SB(v) = \frac{\sigma_{AB}(v)}{\sigma_{AB}} \tag{4}$$

where $\sigma_{AB}(v)$ is the number of shortest paths between residues A and B that pass through residue v.

WebPSN. The cluster centers identified for each GCAP1 simulated state were used as reference structures for the analysis performed by the WebPSN server[54]. The software employs an Elastic Network Model – Normal

Mode Analysis (ENM-NMA) strategy to generate a PSN to investigate network properties of macromolecules. ENM-NMA was computed based on Cα atoms of the residues, Ca^{2+} and Mg^{2+} ions and the carbonyl C of the myristic group using 50 modes and Kovacs potential. The normalization factors for ions and the myristoyl group were computed based on the pdb structure, the distance cutoff for PSN calculation was set to 4.5 Å. Relationship between adjacent residues and N- and C-terminal residues were excluded and the minimum degree for the definition of a hub residue was set to 3.

References

1. Berridge, M. J., Bootman, M. D. & Roderick, H. L. Calcium signalling: dynamics, homeostasis and remodelling. *Nat Rev Mol Cell Biol* **4,** 517–529, doi: 10.1038/nrm1155nrm1155 (2003).
2. Vetter, S. W. & Leclerc, E. Novel aspects of calmodulin target recognition and activation. *Eur J Biochem* **270,** 404–414, doi: 3414 (2003).
3. Ikura, M. & Ames, J. B. Genetic polymorphism and protein conformational plasticity in the calmodulin superfamily: two ways to promote multifunctionality. *Proc Natl Acad Sci USA* **103,** 1159–1164, doi: 10.1073/pnas.0508640103 (2006).
4. Burgoyne, R. D. Neuronal calcium sensor proteins: generating diversity in neuronal Ca^{2+} signalling. *Nat Rev Neurosci* **8,** 182–193, doi: 10.1038/nrn2093 (2007).
5. Philippov, P. & Koch, K.-W. *Neuronal Calcium Sensor Proteins;* ISBN:1-59454-978-8 (2006).
6. Koch, K. W. & Dell'Orco, D. Protein and Signaling Networks in Vertebrate Photoreceptor Cells. *Front Mol Neurosci* **8,** 67, doi: 10.3389/fnmol.2015.00067 (2015).
7. Dizhoor, A. M., Olshevskaya, E. V. & Peshenko, I. V. Mg^{2+}/Ca^{2+} cation binding cycle of guanylyl cyclase activating proteins (GCAPs): role in regulation of photoreceptor guanylyl cyclase. *Mol Cell Biochem* **334,** 117–124, doi: 10.1007/s11010-009-0328-6 (2010).
8. Marino, V., Sulmann, S., Koch, K. W. & Dell'Orco, D. Structural effects of Mg(2)(+) on the regulatory states of three neuronal calcium sensors operating in vertebrate phototransduction. *Biochim Biophys Acta* **1853,** 2055–2065, doi: 10.1016/j.bbamcr.2014.10.026 (2015).
9. Peshenko, I. V. & Dizhoor, A. M. Guanylyl cyclase-activating proteins (GCAPs) are Ca^{2+}/Mg^{2+} sensors: implications for photoreceptor guanylyl cyclase (RetGC) regulation in mammalian photoreceptors. *J Biol Chem* **279,** 16903–16906, doi: 10.1074/jbc.C400065200 (2004).
10. Koch, K. W. & Dell'Orco, D. A calcium-relay mechanism in vertebrate phototransduction. *ACS Chem Neurosci* **4,** 909–917, doi: 10.1021/cn400027z (2013).
11. Makino, C. L. *et al.* Enzymatic relay mechanism stimulates cyclic GMP synthesis in rod photoresponse: biochemical and physiological study in guanylyl cyclase activating protein 1 knockout mice. *PLoS One* **7,** e47637, doi: 10.1371/journal.pone.0047637 (2012).
12. Mendez, A. *et al.* Role of guanylate cyclase-activating proteins (GCAPs) in setting the flash sensitivity of rod photoreceptors. *Proc Natl Acad Sci USA* **98,** 9948–9953, doi: 10.1073/pnas.171308998 (2001).
13. Behnen, P., Dell'Orco, D. & Koch, K. W. Involvement of the calcium sensor GCAP1 in hereditary cone dystrophies. *Biol Chem* **391,** 631–637, doi: 10.1515/BC.2010.063 (2010).
14. Kamenarova, K. *et al.* Novel GUCA1A mutations suggesting possible mechanisms of pathogenesis in cone, cone-rod, and macular dystrophy patients. *Biomed Res Int* **2013,** 517570, doi: 10.1155/2013/517570 (2013).
15. Dell'Orco, D., Behnen, P., Linse, S. & Koch, K. W. Calcium binding, structural stability and guanylate cyclase activation in GCAP1 variants associated with human cone dystrophy. *Cell Mol Life Sci* **67,** 973–984, doi: 10.1007/s00018-009-0243-8 (2010).
16. Dizhoor, A. M., Boikov, S. G. & Olshevskaya, E. V. Constitutive activation of photoreceptor guanylate cyclase by Y99C mutant of GCAP-1. Possible role in causing human autosomal dominant cone degeneration. *J Biol Chem* **273,** 17311–17314, doi: 10.1074/jbc.273.28.17311 (1998).
17. Kitiratschky, V. B. *et al.* Mutations in the GUCA1A gene involved in hereditary cone dystrophies impair calcium-mediated regulation of guanylate cyclase. *Hum Mutat* **30,** E782–796, doi: 10.1002/humu.21055 (2009).
18. Marino, V., Scholten, A., Koch, K. W. & Dell'Orco, D. Two retinal dystrophy-associated missense mutations in GUCA1A with distinct molecular properties result in a similar aberrant regulation of the retinal guanylate cyclase. *Hum Mol Genet* **24,** 6653–6666, doi: 10.1093/hmg/ddv370 (2015).
19. Sokal, I. *et al.* A novel GCAP1 missense mutation (L151F) in a large family with autosomal dominant cone-rod dystrophy (adCORD). *Invest Ophthalmol Vis Sci* **46,** 1124–1132, doi: 10.1167/iovs.04-1431 (2005).
20. Sokal, I. *et al.* GCAP1 (Y99C) mutant is constitutively active in autosomal dominant cone dystrophy. *Mol Cell* **2,** 129–133, doi: 10.1016/S1097-2765(00)80121-5 (1998).
21. Dell'Orco, D., Sulmann, S., Zagel, P., Marino, V. & Koch, K. W. Impact of cone dystrophy-related mutations in GCAP1 on a kinetic model of phototransduction. *Cell Mol Life Sci* **71,** 3829–3840, doi: 10.1007/s00018-014-1593-4 (2014).
22. Hwang, J. Y. *et al.* Regulatory modes of rod outer segment membrane guanylate cyclase differ in catalytic efficiency and $Ca^{(2+)}$-sensitivity. *Eur J Biochem* **270,** 3814–3821, doi: 10.1046/j.1432-1033.2003.03770.x (2003).
23. Peshenko, I. V., Olshevskaya, E. V. & Dizhoor, A. M. Interaction of GCAP1 with retinal guanylyl cyclase and calcium: sensitivity to fatty acylation. *Front Mol Neurosci* **5,** 19, doi: 10.3389/fnmol.2012.00019 (2012).
24. Lim, S., Peshenko, I. V., Olshevskaya, E. V., Dizhoor, A. M. & Ames, J. B. Structure of Guanylyl Cyclase Activator Protein 1 (GCAP1) Mutant V77E in a Ca^{2+}-free/Mg^{2+} -bound Activator State. *J Biol Chem* **291,** 4429–4441, doi: 10.1074/jbc.M115.696161 (2016).
25. Peshenko, I. V., Olshevskaya, E. V., Lim, S., Ames, J. B. & Dizhoor, A. M. Calcium-myristoyl Tug is a new mechanism for intramolecular tuning of calcium sensitivity and target enzyme interaction for guanylyl cyclase-activating protein 1: dynamic connection between N-fatty acyl group and EF-hand controls calcium sensitivity. *J Biol Chem* **287,** 13972–13984, doi: 10.1074/jbc.M112.341883 (2012).
26. Lim, S., Peshenko, I., Dizhoor, A. & Ames, J. B. Effects of Ca^{2+}, Mg^{2+}, and myristoylation on guanylyl cyclase activating protein 1 structure and stability. *Biochemistry* **48,** 850–862, doi: 10.1021/bi801897p (2009).
27. Papaleo, E., Mereghetti, P., Fantucci, P., Grandori, R. & De Gioia, L. Free-energy landscape, principal component analysis, and structural clustering to identify representative conformations from molecular dynamics simulations: the myoglobin case. *J Mol Graph Model* **27,** 889–899, doi: 10.1016/j.jmgm.2009.01.006 (2009).
28. Hess, B. Similarities between principal components of protein dynamics and random diffusion. *Phys Rev E Stat Phys Plasmas Fluids Relat Interdiscip Topics* **62,** 8438–8448, doi: 10.1103/PhysRevE.62.8438 (2000).
29. Atilgan, A. R., Akan, P. & Baysal, C. Small-world communication of residues and significance for protein dynamics. *Biophys J* **86,** 85–91, doi: 10.1016/S0006-3495(04)74086-2 (2004).
30. Papaleo, E. Integrating atomistic molecular dynamics simulations, experiments, and network analysis to study protein dynamics: strength in unity. *Front Mol Biosci* **2,** 28, doi: 10.3389/fmolb.2015.00028 (2015).
31. Vendruscolo, M., Dokholyan, N. V., Paci, E. & Karplus, M. Small-world view of the amino acids that play a key role in protein folding. *Phys Rev E Stat Nonlin Soft Matter Phys* **65,** 061910, doi: 10.1103/PhysRevE.65.061910 (2002).
32. Peshenko, I. V., Olshevskaya, E. V., Lim, S., Ames, J. B. & Dizhoor, A. M. Identification of target binding site in photoreceptor guanylyl cyclase-activating protein 1 (GCAP1). *J Biol Chem* **289,** 10140–10154, doi: 10.1074/jbc.M113.540716 (2014).

33. Lim, S., Peshenko, I. V., Dizhoor, A. M. & Ames, J. B. Structural insights for activation of retinal guanylate cyclase by GCAP1. *PLoS One* **8,** e81822, doi: 10.1371/journal.pone. (2013).
34. Schrem, A., Lange, C., Beyermann, M. & Koch, K. W. Identification of a domain in guanylyl cyclase-activating protein 1 that interacts with a complex of guanylyl cyclase and tubulin in photoreceptors. *J Biol Chem* **274,** 6244–6249, doi: 10.1074/jbc.274.10.6244 (1999).
35. Narzi, D., Daidone, I., Amadei, A. & Di Nola, A. Protein Folding Pathways Revealed by Essential Dynamics Sampling. *J Chem Theory Comput* **4,** 1940–1948, doi: 10.1021/ct800157v (2008).
36. Robin, J. *et al.* Differential Nanosecond Protein Dynamics in Homologous Calcium Sensors. *ACS Chem Biol* **10,** 2344–2352, doi: 10.1021/acschembio.5b00278 (2015).
37. Orban, T. *et al.* Conformational changes in guanylate cyclase-activating protein 1 induced by Ca^{2+} and N-terminal fatty acid acylation. *Structure* **18,** 116–126, doi: 10.1016/j.str.2009.11.008 (2010).
38. Dell'Orco, D., Sulmann, S., Linse, S. & Koch, K. W. Dynamics of conformational Ca^{2+} -switches in signaling networks detected by a planar plasmonic device. *Anal Chem* **84,** 2982–2989, doi: 10.1021/ac300213j (2012).
39. Sulmann, S., Dell'Orco, D., Marino, V., Behnen, P. & Koch, K. W. Conformational changes in calcium-sensor proteins under molecular crowding conditions. *Chemistry* **20,** 6756–6762, doi: 10.1002/chem.201402146 (2014).
40. Guo, J., Pang, X. & Zhou, H. X. Two pathways mediate interdomain allosteric regulation in pin1. *Structure* **23,** 237–247, doi: 10.1016/j.str.2014.11.009 (2015).
41. Nong, E., Lee, W., Merriam, J. E., Allikmets, R. & Tsang, S. H. Disease progression in autosomal dominant cone-rod dystrophy caused by a novel mutation (D100G) in the GUCA1A gene. *Doc Ophthalmol* **128,** 59–67, doi: 10.1007/s10633-013-9420-z (2014).
42. Koch, K. W. & Stryer, L. Highly cooperative feedback control of retinal rod guanylate cyclase by calcium ions. *Nature* **334,** 64–66, doi: 10.1038/334064a0 (1988).
43. Peshenko, I. V. & Dizhoor, A. M. Ca^{2+} and Mg^{2+} binding properties of GCAP-1. Evidence that Mg^{2+}-bound form is the physiological activator of photoreceptor guanylyl cyclase. *J Biol Chem* **281,** 23830–23841, doi: 10.1074/jbc.M600257200 (2006).
44. Stephen, R., Bereta, G., Golczak, M., Palczewski, K. & Sousa, M. C. Stabilizing function for myristoyl group revealed by the crystal structure of a neuronal calcium sensor, guanylate cyclase-activating protein 1. *Structure* **15,** 1392–1402, doi: 10.1016/j.str.2007.09.013 (2007).
45. Hess, B., Kutzner, C., Van Der Spoel, D. & Lindahl, E. GROMACS 4: Algorithms for Highly Efficient, Load-Balanced, and Scalable Molecular Simulation. *J Chem Theory Comput* **4,** 435–447, doi: 10.1021/ct700301q (2008).
46. Bjelkmar, P., Larsson, P., Cuendet, M. A., Bess, B. & Lindahl, E. Implementation of the CHARMM force field in GROMACS: Analysis of protein stability effects from correction maps, virtual interaction sites, and water models. *Journal of Chemical Theory and Computation* **6,** 459–466, doi: 10.1021/ct900549r (2010).
47. Amadei, A., Linssen, A. B. & Berendsen, H. J. Essential dynamics of proteins. *Proteins* **17,** 412–425, doi: 10.1002/prot.340170408 (1993).
48. Hess, B. Convergence of sampling in protein simulations. *Phys Rev E Stat Nonlin Soft Matter Phys* **65,** 031910, doi: 10.1103/PhysRevE.65.031910 (2002).
49. Amadei, A., Ceruso, M. A. & Di Nola, A. On the convergence of the conformational coordinates basis set obtained by the essential dynamics analysis of proteins' molecular dynamics simulations. *Proteins* **36,** 419–424, doi: 10.1002/(SICI)1097-0134(19990901)36:4<419::AID-PROT5>3.0.CO;2-U (1999).
50. Ross, G. Algorithm AS 15: single Linkage cluster analysis *Appl. Stat.* **18,** 106–111 (1969).
51. Daura, X. *et al.* Peptide Folding: When Simulation Meets Experiment. *Angew. Chem. Int. Ed* **38,** 236–240, doi: 10.1002/(SICI)1521-3773(19990115)38:1/2<236::AID-ANIE236>3.0.CO;2-M (1999).
52. Tiberti, M. *et al.* PyInteraph: a framework for the analysis of interaction networks in structural ensembles of proteins. *J Chem Inf Model* **54,** 1537–1551, doi: 10.1021/ci400639r (2014).
53. Vishveshwara, S., Ghosh, A. & Hansia, P. Intra and inter-molecular communications through protein structure network. *Curr Protein Pept Sci* **10,** 146–160, doi: 10.2174/138920309787847590 (2009).
54. Seeber, M., Felline, A., Raimondi, F., Mariani, S. & Fanelli, F. WebPSN: a web server for high-throughput investigation of structural communication in biomacromolecules. *Bioinformatics* **31,** 779–781, doi: 10.1093/bioinformatics/btu718 (2015).

Acknowledgements

This work was supported by grants from the Italian Ministry for Education and Research via departmental funding (FUR2015 to DDO) and via support from CINECA through the Italian Super Computing Research Allocation project (ISCRA Grant: HP10CB7L79 to DDO).

Author Contributions

D.D.O. conceived and directed the study, V.M. carried out MD simulations, both authors analyzed the data. D.D.O. drafted the manuscript with the contribution of V.M. Both authors reviewed the final version of the manuscript.

Additional Information

Supplementary information accompanies this paper at http://www.nature.com/srep

Competing financial interests: The authors declare no competing financial interests.

How to cite this article: Marino, V. and Dell'Orco, D. Allosteric communication pathways routed by Ca^{2+}/Mg^{2+} exchange in GCAP1 selectively switch target regulation modes. *Sci. Rep.* **6**, 34277; doi: 10.1038/srep34277 (2016).